ORNL-2080 (Del.)

Contract No. W-7405-eng-26

METALLURGY DIVISION

SEMIANNUAL PROGRESS REPORT

for Period Ending April 10, 1956

J. H. Frye, Jr., Director
W. D. Manly, Associate Director
J. E. Cunningham, Assistant Director

Photostat Price $ 35.70

Microfilm Price $ 9.30

Available from the
Office of Technical Services
Department of Commerce
Washington 25, D. C.

DATE ISSUED

NOV 2 1956

OAK RIDGE NATIONAL LABORATORY
Operated by
UNION CARBIDE NUCLEAR COMPANY
A Division of Union Carbide and Carbon Corporation
Post Office Box P
Oak Ridge, Tennessee

DISCLAIMER

Reports previously issued in this series are as follows:

ORNL-28	Period Ending March 1, 1948
ORNL-69	Period Ending May 31, 1948
ORNL-407	Period Ending July 31, 1949
ORNL-511	Period Ending October 31, 1949
ORNL-583	Period Ending January 31, 1950
ORNL-754	Period Ending April 30, 1950
ORNL-827	Period Ending July 31, 1950
ORNL-910	Period Ending October 31, 1950
ORNL-987	Period Ending January 31, 1951
ORNL-1033	Period Ending April 30, 1951
ORNL-1108	Period Ending July 31, 1951
ORNL-1161	Period Ending October 31, 1951
ORNL-1267	Period Ending January 31, 1952
ORNL-1302	Period Ending April 30, 1952
ORNL-1366	Period Ending July 31, 1952
ORNL-1437	Period Ending October 31, 1952
ORNL-1503	Period Ending January 31, 1953
ORNL-1551	Period Ending April 10, 1953
ORNL-1625	Period Ending October 10, 1953
ORNL-1727	Period Ending April 10, 1954
ORNL-1875	Period Ending October 10, 1954
ORNL-1911	Period Ending April 10, 1955
ORNL-1988	Period Ending October 10, 1955

METALLURGY DIVISION
AT
THE OAK RIDGE NATIONAL LABORATORY

AUGUST 1, 1956

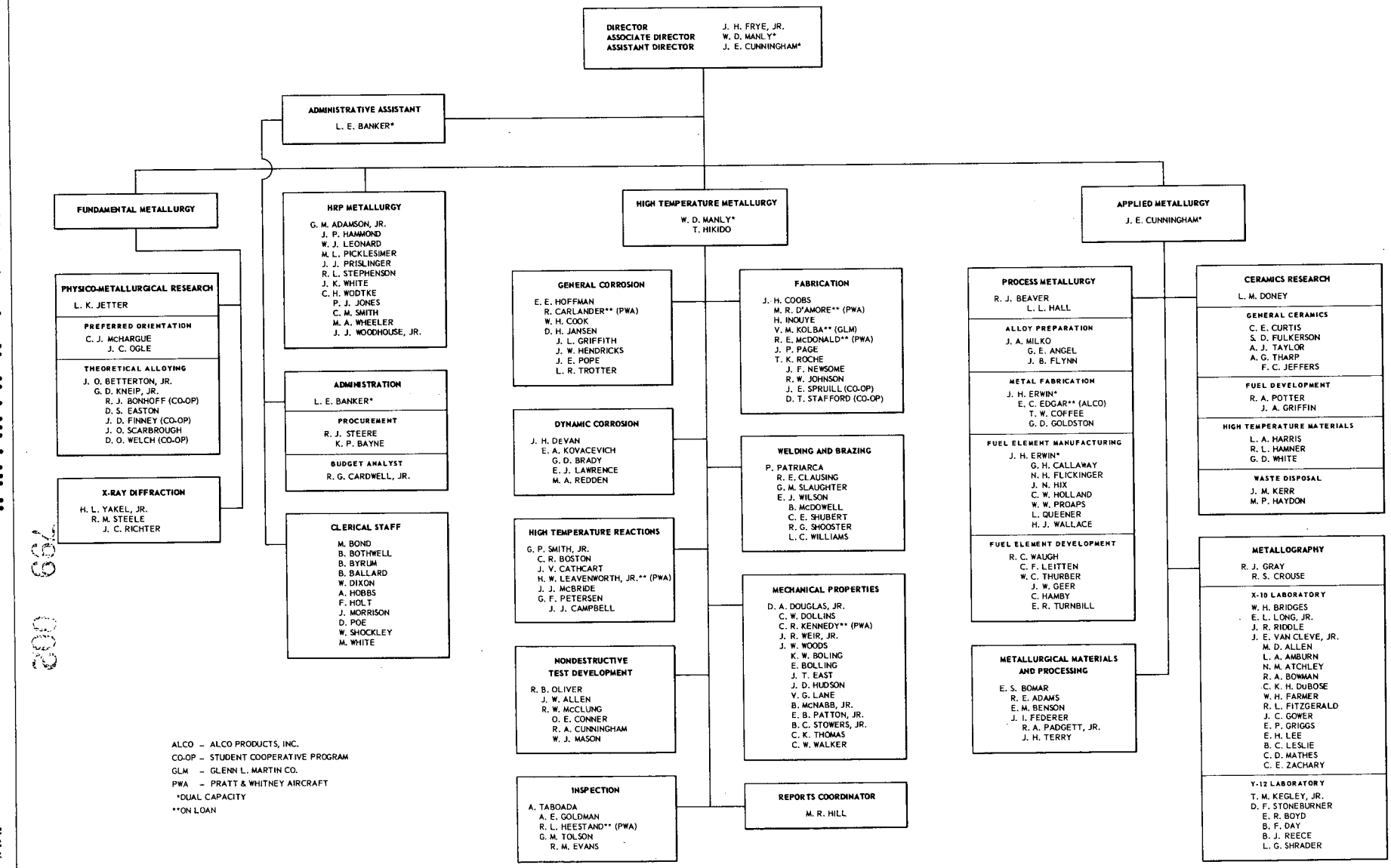

ALCO – ALCO PRODUCTS, INC.
CO-OP – STUDENT COOPERATIVE PROGRAM
GLM – GLENN L. MARTIN CO.
PWA – PRATT & WHITNEY AIRCRAFT
*DUAL CAPACITY
**ON LOAN

CONTENTS

PUBLICATIONS xv

SUMMARY xvii

ANP METALLURGY

GENERAL CORROSION 3

Thermal-Convection-Loop Test of Brazing Alloy 3

Static Tests of Braze Buttons 4

Brazing Alloys on Inconel T-Joints Tested in Sodium and in Fuel Mixtures 6

Corrosion Resistance of Various Brazing Alloys on Inconel and Stainless Steel 7

Brazing Alloys on "A" Nickel 7

Corrosion of Low-Neutron-Cross-Section Brazing Alloys in NaK, Sodium, and $NaF-ZrF_4-UF_4$ 13

Corrosion Testing of Thermocouple Wells 16

Ruthenium-Plated-Inconel Tensile-Test Specimens 17

Effect of an Air Leak into an Inconel–Fused-Salt Test System 19

High-Temperature Tests of Molybdenum in Contact with $NaF-ZrF_4-UF_4$ 19

Decarburization of Plain Carbon Steel by Static Sodium 21

Penetration of Sodium into Beryllium 21

Beryllium-Sodium-Inconel Spacer Tests 23

Thermal-Convection-Loop Test of Beryllium-Sodium-Inconel System 25

Beryllium-Sodium-Hastelloy B Spacer Tests 27

Inconel Loop Experiment with Boiling Sodium 27

Type 348 Stainless Steel Loop Experiments with Boiling Sodium 30

Type 316 Stainless Steel Thermal-Convection Loop Experiments with Sodium 30

Cathalloy A-31 Tested in Static Sodium 32

Corrosion Tests of Alfenol in Various Media 32

Corrosion of Special Alloys in Contact with Dehydrated Sodium Hydroxide 36

Rare-Earth Oxides and Inconel in Static Sodium 48

Apparent Porosity of a Porous Rare-Earth-Oxide Body to Water and to Liquid Sodium 49

DYNAMIC CORROSION 53
Forced-Circulation Loops 53
Loop Design 53
Sodium in Inconel Pump Loops 63
NaK (56-44 wt %) in Inconel 66
Sodium in Type 316 Stainless Steel 67

Effect of ZrH_2 Additions to Fluoride Mixtures 67
Effect of UF_3 Additions to Alkali-Base Fluoride Mixtures 69
Loops Constructed of Hastelloy B 70
Loops Constructed of Nickel-Molybdenum Alloys 72

MECHANICAL PROPERTIES 74
Results of the Hastelloy W Testing Program 74
Inconel Testing Program 75
Creep-Test Results 75
Biaxial Stress Tests 76
Effect of Corrosion on Stress-Rupture Properties of Inconel 77

NONDESTRUCTIVE TESTING 88

WELDING AND BRAZING 99
Metallographic Examination of Failures Occurring in NaK-to-Air Radiators 99
ORNL Radiator No. 1 and York Radiator No. 1 99
Other Radiators 104
Metallographic Examination of High-Conductivity-Fin Radiator Tube-to-Fin Joints 105
Fabrication of Air-Cooled Radiator 7503 107
Measurement of Weld Shrinkage 109
PK Pump Fabrication Experiments 111
Cermet-to-Metal Joining 114
Brazing-Alloy Development 115
Development of Low-Cross-Section Alloys for Fuel-to-NaK Service 115
Oxidation of Coast Metals 52 Alloy 115

FABRICATION 118

Alloy Development 124
Fabricability Studies on Nickel-Molybdenum-Base Alloys 124
Effect of Melting Practice on Nickel-Molybdenum-Base Alloys 125

Chromium-Molybdenum-Nickel Alloys 125
Special Alloys 126
Iron-Zirconium Alloys 126
Extrusion Experiments 127

Control-Rod Fabrication 132
Feasibility of $(Gd\text{-}Sm)_2O_3$ in Metal Matrices 132
Tubular Control Rods 133
Shield Plug for ART Pump 133

PHYSICAL CHEMISTRY OF CORROSION 135
Mass Transfer in Liquid Metals 135
High-Temperature Spectrophotometry 135
The Transformation of $NaNiO_2$ 135
Film Formation on Metals 137
Oxidation of the Alkali Metals 137

HRP METALLURGY

HRP METALLURGY 145
Physical Metallurgy 145
Physical Metallurgy of Zircaloy-2, -2W, -3A, -3B, and -3C 145
Zirconium-Hydrogen and Zircaloy-Hydrogen Alloys 146
Stress Corrosion of Stainless Steels 152
Mechanical Metallurgy 152
Zirconium Alloys 152
Welding Development 152
Titanium Alloys 152
Corrosion Tests of Simulated Weld Metal 155

APPLIED METALLURGY

PACKAGE POWER REACTOR PROGRAM 172
Irradiation Test of Miniature APPR Fuel Plates in the MTR 172
Fabrication of Composite Stainless Steel APPR Fuel Plates 172
Fuel-Melting Experiment 172
Metal-Water-Reaction Experiment 172
Application of Roller Leveler to the Flattening of Fuel Plates 172
Powder-Metallurgy Blending Studies 172
APPR Absorber 172
Examination of 18-Plate APPR Element Irradiated in the MTR 174
Examination of Miniature APPR Plates Irradiated in the MTR 174
Component Assembly by Brazing 174
METALLURGICAL MATERIALS AND PROCESSING 178
Thorium – Metallex Process 178
Differential Thermometry 178
Consolidation Experiments 179
Future Work 180
Growth of ORNL Graphite-Reactor Slugs 180
Metallurgical Processing of Spent Fuel Elements 181
METALLOGRAPHY 183
Nickel-Molybdenum System 183

CERAMICS RESEARCH

CERAMICS 187
UO_3 Crystal Production 187
Si-SiC Development 187
Yttrium Oxide 188
Thorium Oxide Suspensions in Water 189
Uranium Ore Samples 189
Petrographic Examination of Fluorides 191
Spodumene 191
Waste Disposal 191
Fixation of Radioisotopes in Ceramic Bodies 191
Heat Experiments 198

Enthalpy Data from 0 to 1200°C for Physical-Property Studies of Ceramic Materials 200
Fabrication of Cermets Composed of a Metal and a Rare-Earth Oxide for Extruded Control Rods 208
Fabrication of Rare-Earth-Oxide Compacts for Control Rods 208

FUNDAMENTAL METALLURGY

FUNDAMENTAL PHYSICO-METALLURGICAL RESEARCH 211
Preferred Orientation in Extruded Thorium Rod 211
Preferred Orientation in Zircaloy-2 Plate 216
The Constitution of Zirconium-Rich Alloys of the Silver-Zirconium System 218
Lattice Spacings of the Alpha-Phase Region 218
Annealing Experiments on Zirconium Alloys Containing 0 to 28 at. % Silver 219
Preliminary Investigation of the Lattice Spacings of the Alpha Phase in the Indium-Zirconium System 227
Dependence of the Axial Ratio of the Alpha Phase of Zirconium Alloys Upon Electron Concentration 228
Zone Refining of Zirconium 230
Zone-Refining Theory for Finite-Length Passes 230
Experimental Method 232
Metallographic Evidence of Purification 233
Activation Analyses of Purified Rods 234
Summary 237

PUBLICATIONS

W. H. Bridges, J. V. Cathcart, and G. P. Smith, "An Isothermal Bath for Use in the Temperature Range 200–500°C," *J. Sci. Instr.* **32**, 139 (1955).

J. V. Cathcart and W. D. Manly, "The Mass Transfer Properties of Various Metals and Alloys in Liquid Lead," *Corrosion* **12**(2), 43 (1956); also, ORNL-2008 (Jan. 10, 1956). Paper presented at Engineers Joint Council Nuclear Engineering and Science Congress, Cleveland, Ohio, Dec. 12–16, 1955.

L. K. Jetter, C. J. McHargue, and R. O. Williams, "Method of Representing Preferred Orientation Data," *J. Appl. Phys.* **27**, 368 (1956).

E. E. Hoffman, *et al., An Evaluation of the Corrosion and Oxidation Resistance of High-Temperature Brazing Alloys*, ORNL CF-55-8-138 (Aug. 24, 1955).

J. R. Johnson, *et al., The Technology of Uranium Dioxide–A Reactor Material*, ORNL-2011 (Feb. 21, 1956).

J. R. Johnson, *Development of a Cubic Oxide Protective Film on Zirconium*, ORNL-2029 (Feb. 12, 1956).

J. R. Johnson and C. E. Curtis, "The Technology of UO_2 and ThO_2," *Proceedings of International Conference on the Peaceful Uses of Atomic Energy, Geneva, Switzerland, August 1955*, vol 9, p 169, United Nations, New York.

M. T. Cory, A. J. Taylor, and J. R. Johnson, *Graph-I-Tite and Graphite in High Velocity Hydrogen at 2400°C*, ORNL CF-55-8-27 (Aug. 4, 1955).

G. D. Kneip, Jr., and J. O. Betterton, Jr., "Floating-Zone Purification of Zirconium," *J. Electrochem. Soc.* **102**, 228C (1955). Paper presented at Electrochemical Society Meeting, Pittsburgh, Pa., Oct. 9–13, 1955.

L. Mitchell, *Packaging of Radioactive Waste in Ceramic Bodies*, ORNL CF-56-1-131 (Jan. 30, 1956).

G. P. Smith, "Corrosion of Materials in Fused Hydroxides," *Am. Inst. Mining Met. Engr., Inst. Metals Division Special Report Series No. 2*, p 71 (1956); also, ORNL-2048 (March 27, 1956). Paper presented at Symposium on Nuclear Metallurgy, Annual Meeting Am. Inst. Mining Met. Engr., New York, N. Y., Feb. 20, 1956.

G. P. Smith, M. E. Steidlitz, and L. L. Hall, "Reaction at High Temperatures Between Air and Liquid Metal Solutions Containing Sodium. Effect of Solution Composition," *J. Am. Chem. Soc.* **77**, 4533 (1955).

J. M. Warde and J. R. Johnson, "Recent Developments in the Technology of Ceramic Materials for Nuclear Energy Service," *J. Franklin Inst.* **260**, 455 (1955). Paper presented at First Annual Meeting of the Am. Nuclear Soc., The Pennsylvania State University, University Park, Pa., June 27, 1955.

J. M. Warde and R. H. Richardson, "Waste Disposal–Vital to Atomic Power Development," *Mining Eng.* **7**, 458 (1955).

J. M. Warde, "Refractories for Nuclear Energy," *Refractories Inst. Tech. Bull. No. 94* (Feb. 1956).

H. L. Yakel, Jr., "On the Structures of Some Compounds of the Perovskite Type," *Acta Cryst.* **8**, 394 (1955).

H. Inouye, *Scaling of Columbium in Air*, ORNL-1565 (Sept. 24, 1953). Paper presented at Am. Inst. Mining Met. Engr. Reactive Metal Conference, Buffalo, N. Y., March 19–21, 1956.

METALLURGY DIVISION
SEMIANNUAL PROGRESS REPORT

SUMMARY

ANP METALLURGY

General Corrosion. – Operation of a thermal-convection loop containing NaF-ZrF_4-UF_4 (50-46-4 mole %) was terminated after 1000 hr. The hot leg of the loop was made up of six Inconel segments brazed with Coast Metals 52. The brazing alloy showed good corrosion resistance to the fused salts. Maximum attack on the Inconel inserts was 4 mils.

A series of brazing-alloy buttons was tested in static NaF-ZrF_4-UF_4 (50-46-4 mole %), NaOH, and sodium at 1500°F for 100 hr. The high-nickel-content alloys, Coast Metals 52 (89% Ni–5% Si–4% B–2% Fe) and General Electric 81 (66% Ni–19% Cr–10% Si–4% Fe–1% Mn), showed good and fair resistance, respectively, to corrosion by sodium. The 60% Pd–40% Ni alloy tested in the fused salt and NaOH showed good corrosion resistance to both media.

A series of brazing alloys on Inconel T-joints was seesaw-tested in sodium and NaF-ZrF_4-UF_4 (53.5-40-6.5 mole %) at 1500°F. The 80% Ni–10% P–10% Cr and the 75% Ni–25% Ge alloys showed good to fair corrosion resistance to both media. An 80% Au–20% Cu alloy showed fair resistance to attack in the fused-salt bath.

A series of type 304 stainless steel and Inconel T-joints brazed with alloys submitted by the Wall Colmonoy Corporation was tested in static sodium and NaF-ZrF_4-UF_4 (53.5-40-6.5 mole %). The 76.8% Ni–13% Si–10.2% P alloy showed good corrosion resistance to both media. In this series of tests, it was found that brazing alloys having a relatively high percentage of phosphorus appear to have inferior corrosion resistance to sodium, and silicon tends to improve the corrosion resistance of these alloys. On the other hand, alloys having a high percentage of silicon and no phosphorus are heavily attacked in the fused-salt mixture.

A series of brazing alloys on "A" nickel T-joints was tested in sodium, NaF-ZrF_4-UF_4 (53.5-40-6.5 mole %), and NaOH. The alloys 90% Ni–10% P, 80% Ni–10% Cr–10% P, and Nicrobraz (70% Ni–14% Cr–6% Fe–5% B–4% Si–1% C) showed good to fair corrosion resistance to sodium and fluoride salts. The precious-metal alloys 82% Au–18% Ni and 80% Au–20% Cu showed good resistance to corrosion in NaOH.

Seesaw tests have been conducted on a series of four low-cross-section Ni-Cr-Ge-Si alloys. Sodium, NaK, and NaF-ZrF_4-UF_4 (53.5-40-6.5 mole %) at 1500°F were used as the corrosive media. The tests were performed in order to determine the feasibility of using these alloys in the fabrication of NaK-to-fuel heat-exchangers. The nickel content of the alloys ranged from 59 to 70%. Tests to date indicate that the high-nickel-content alloys in this series have the best corrosion resistance to NaK. The 70% Ni–11% Cr–13% Ge–6% Si alloy showed fair corrosion resistance to NaK and the fused-salt mixture.

A number of small Chromel-Alumel thermocouple wells fabricated from Inconel tubes and Chromel-Alumel wires have been seesaw-tested for 100 hr in sodium and NaF-ZrF_4-UF_4 (50-46-4 mole %) at 1500°F. The Chromel-Alumel content of the welded portion of the thermocouple wells was varied. The purpose of the tests was to determine if the corrosion rate on the thermocouple wells would be affected by the high silicon, manganese, and aluminum content of the Alumel. It was found that on increasing the Chromel-Alumel content of the welds their susceptibility to attack by the salt mixture increased.

A ruthenium-plated Inconel specimen has been rupture-tested by the Mechanical Properties Group. Tests to date indicate that ruthenium has no adverse effect on the physical properties of Inconel.

Several tests have been conducted to determine the effect of a small air leak on the corrosion of Inconel in NaF-ZrF_4-UF_4 (50-46-4 mole %). The test capsules were very heavily attacked by the contaminated salt.

Molybdenum specimens tested for 30 min in contact with NaF-ZrF_4-UF_4 (53.5-40.0-6.5 mole %) at 2430°F were unattacked.

The extent to which AISI 1043 plain carbon steel is decarburized by molten sodium at 1000°C in Armco iron and type 304 ELC stainless steel containers was determined after 100 and 400-hr exposures.

Tests conducted for the purpose of determining the extent to which sodium will penetrate beryllium metal during a 1000-hr exposure indicate that the amount of penetration at 1500°F is negligible.

The extent to which beryllium metal mass transfers and/or alloys with Inconel when both metals are immersed for 1000 hr in sodium at 1200°F has been studied as a function of their separation distance. A spacer distance of 20 mils was required in order to prevent compound formation on the surface of the Inconel.

A thermal-convection-loop test to study the compatibility of beryllium and Inconel in sodium at 1300°F revealed that extensive alloying of the Inconel with the beryllium occurred where the surfaces of these metals were in close proximity.

Tests have been conducted for 1000 hr in sodium at 1200°F to study the extent of dissimilar-metal mass transfer of beryllium metal to Hastelloy B as a function of the distance between the two materials. In order to avoid extensive alloying of Hastelloy B with beryllium at 1200°F, a minimum spacer distance of 20 mils is recommended.

An Inconel loop has been tested for 1000 hr with boiling sodium at 1500°F. An appreciable amount of mass-transferred crystals was detected in the cold trap in the condenser pipe. Intergranular cracking to a maximum depth of 25 mils was detected in the center section of the condenser pipe.

Three type 348 stainless steel loops have been operated with boiling sodium for various lengths of time to study the extent of mass transfer in a stainless steel–sodium system in which the oxygen content of the sodium is held to a very low level. No mass-transferred crystals were detected in the cold sections of these systems.

Type 316 stainless steel thermal-convection loops have been tested with sodium in order to study the effect of a diffusion cold trap on the amount of corrosion and mass transfer observed in such a system. In these tests the attack was less, and there were fewer mass-transferred crystals in the loop that had a diffusion-type cold trap.

Cathalloy A-31 (4 wt % tungsten–balance nickel) was found to have good corrosion resistance to static sodium at 1500°F.

Alloys of special compositions have been prepared by the Metallurgy Division and have been subjected to corrosion tests in static sodium hydroxide at 1500°F for 100 hr. The most promising alloy in the group was a 90% Ni–10 Mo composition which experienced less than $\frac{1}{2}$ mil of attack. Further tests are to be conducted on alloys of this composition.

Metallographic examinations on two sets of specimens from four titanium carbide–cobalt cermets did not show any corrosion after having been tested for 100 hr at 4.25 cpm in the seesaw apparatus containing NaF-ZrF_4-UF_4 (53.5-40-6.5 mole %).

Ten titanium carbide cermets with high contents of metal binders, three with cobalt-base alloys and seven with nickel-base alloys, have been tested in NaF-ZrF_4-UF_4 (53.5-40-6.5 mole %). Only two showed attack under metallographic examination. One of the attacked specimens was bonded with a cobalt-base alloy which had a relatively high chromium content, and the other was a nickel-base alloy with aluminum added. Depth of attack was less than 8 mils for both.

Seven tungsten carbide cermets with various alloys as binders were corrosion-tested in sodium and in NaF-ZrF_4-UF_4 (53.5-40-6.5 mole %) and showed no attack on metallographic examination.

Specimens of carbides of boron, titanium, zirconium, and chromium were corrosion-tested in static sodium, NaF-ZrF_4-UF_4 (53.5-40-6.5 mole %),

Relatively dense rare-earth-oxide bodies, one of Sm_2O_3 (5.88 g/cc) and the other of 63.8% Sm_2O_3–26.3% Gd_2O_3–balance primarily other rare-earth oxides (6.58 g/cc), showed good resistance to corrosion by static sodium at 1500°F after 1000 hr, with possibly slight reductions in strength.

A porous body, consisting of 63.8% Sm_2O_3–26.3% Gd_2O_3–balance primarily of other rare-earth oxides, had an apparent porosity of 53.5% to water at room temperature. It had a 52% apparent porosity to static liquid sodium after a 100-hr exposure to the sodium at 1300°F.

A few recheck solid-phase-bonding tests on titanium carbide–nickel cermets tended to confirm the results from original tests. A test was included in which the cermets in the shape of actual valve parts (disk and seat) were used rather than bar-shaped specimens.

Dynamic Corrosion. – Results are reported for several Inconel forced-circulation loops operated to evaluate the corrosive properties of fused-fluoride mixtures. Tests conducted for various times under similar conditions show a rapid initial period of attack followed by a constant rate of attack of 4 mils per 1000 hr. Chromium content of the fluoride appeared to reach an equilibrium value during the stage of rapid attack and remained constant during the remainder of the test.

The effect of wall temperature on the depth of attack was found to be very important in both gas-fired and resistance-heated pump loops. If this temperature is held constant, variations in the maximum temperature of the bulk fluoride mixture have little effect on the extent of corrosion.

Changes in the ratio of hot-leg surface area to volume were investigated in pump loops which contained reservoirs that permitted this ratio to be decreased by a factor of either two or four. The maximum attack which resulted from the smaller decrease, keeping the heater surface constant, was comparable to the attack in a loop of standard volume. However, decreasing the ratio by a factor of four produced a slight increase in attack which was accompanied by a bronze-colored film in the cooler portions of the loop.

Additions of trivalent uranium fluoride to mixtures of $NaF-ZrF_4-UF_4$ (50-46-4 mole %) resulted in some reduction in attack in Inconel pump loops. The operation of such loops with $NaF-KF-LiF-UF_4$ to which similar amounts of UF_3 were added showed a much greater reduction in attack, but a continuous metal deposit of uranium occurred in the colder portions of the loop.

The effect of oxide contamination on mass transfer by sodium has been studied by utilizing Inconel forced-circulation loops. An oxide addition of 0.15 wt % greatly increased the amount of mass transfer in such systems at 1500°F, although an addition of 0.05% had very little effect. Systems containing cold traps and barium additions produced deposits similar to those in loops operated without cold traps and with clean sodium.

An Inconel pump loop which circulated sodium at a relatively low maximum fluid temperature (1000°F) was found to be completely free from deposited metal or hot-leg attack.

Three Inconel pump loops which circulated NaK at 1500°F for 1000 hr produced metal deposits similar to those found in sodium loops. Bypass cold traps used in conjunction with two of the loops were not measurably effective in reducing mass transfer. A pump loop of 316 stainless steel was operated at 1500°F for the purpose of evaluating this material as a container for sodium. Deposits in this loop were fewer than those in Inconel loops operated under similar conditions.

To determine the corrosive effect of fluorides on Inconel containing varying amounts of UF_3, several thermal-convection loops were examined. The results tend to confirm those obtained in the pump-loop studies discussed above in which similar UF_3 additions were used. A series of six Hastelloy B thermal-convection loops, which had their original inside surfaces removed by a reaming operation, were tested with a fluoride-salt mixture and with sodium. Neither system showed significant increases in attack or in amount of metal deposited with increasing operational times. An unreamed Hastelloy B loop operated with sodium showed deposits similar in amount to those in the reamed loops discussed above that were operated under comparable conditions. Two Hastelloy B thermal-convection loops showed good corrosion

resistance in NaF-LiF-KF-UF_4 (11.2-41.0-45.3-2.5 mole %) after 500 and 2000 hr at 1500°F.

A series of nickel-base alloys with various molybdenum contents was tested in NaF-ZrF_4-UF_4 (50-46-4 mole %) at 1500°F. Attack was found to be insignificant in all of these alloys. A 5% chromium addition made to one of the alloys showed no effect on the extent of corrosion.

Mechanical Properties. – The results from creep-rupture tests and tensile tests of Hastelloy W indicate that this alloy has high-temperature-strength properties similar to those of Hastelloy B and that it exhibits better ductility than Hastelloy B in hot tensile tests.

Inconel design curves at 1300, 1500, and 1650°F are presented for both low- and high-temperature-annealed material tested in argon and in fused salts. It is shown that specimens annealed at the higher temperatures, before testing in the fused salts, do not show the marked decrease in creep properties that is evidenced by the material annealed at the lower temperatures.

Analysis of the data from Inconel tube-burst tests shows that the deformation in the direction of the maximum stress is considerably less than the deformation noted in uniaxially stressed Inconel specimens, indicating that the biaxial stress system is reducing the ductility of the material.

Comparison of data obtained at Cornell Aeronautical Laboratory with data obtained at ORNL seems to indicate that the effect of corrosion, of fine-grained Inconel by fluoride fuel No. 30, on the creep strength is somewhat insensitive to the severity or depth of attack and is more dependent on the mechanism of deformation.

Nondestructive Testing. – A brief description and explanation of two types of eddy-current inspection are given.

The advantages of the $\frac{3}{4}$-in. high-resolution transducer are presented, and the necessity for collimation is noted. Metallographic examination has been used to identify several defect types with their respective indications, and corresponding data are presented for (1) a longitudinal crack, (2) intergranular attack, (3) a small gouge, and (4) inside-diameter defects.

A table correlating the number of defects detected by radiography, fluorescent penetrant, and ultrasound in a sample lot of tubing is included.

Welding and Brazing. – Several NaK-to-air radiators that failed are being examined with the intent of making recommendations to correct the causes for these failures. The development of new techniques to be used in the fabrication of subsequent radiators and pumps is also underway. Weld-shrinkage tests are being performed in an effort to predict the shrinkage to be expected in the fabrication of the ART. A study of new low-cross-section brazing alloys is described. Methods of joining cermet valve components to metals are also discussed.

The extrusion of Hastelloy W tube blanks from forged billets was unsuccessful because of hot shortness of the material. Metallographic examination of a cracked extrusion revealed eutectic melting at the base of a crack. Identification of the eutectic was not possible.

The conditions for extrusion of Hastelloy B are still not definite. Three duplex billets of type 316 stainless steel clad with Hastelloy B were extruded but were unsatisfactory because of cracking and roughness resulting from poor lubrication. Attempts to improve the lubrication of Hastelloy B by flame spraying it with a heavy layer of type 304 stainless steel were only moderately successful. A major effort was directed toward improving the melting practice of the Hastelloy alloys and toward developing a more satisfactory technique for lubrication during extrusion. These studies were carried out with fair results on heats of nominal composition of Hastelloy B to which carbon was added in amounts up to 0.1%. The carbon additions were effective in reducing oxide-type inclusions, and the ingots were hot-rolled to sheet successfully. A similar series of melts of Cr-Mo-Ni compositions with carbon additions is being prepared in an effort to improve fabricability of these alloys.

Preliminary work on fabrication of seamless duplex tubing has been completed. Tube blanks of nickel-, Inconel-, and monel-clad type 316 stainless steel were extruded without difficulty.

It was demonstrated that control rods containing 30 vol % of rare-earth oxide can be fabricated by canning a cermet-type core in a capsule of suitable cladding material and hot swaging the composite.

Physical-property data were obtained for extruded control-rod parts containing rare-earth oxides and for the iron-zirconium alloys which were fabricated during the last period.

Encouraging results were obtained on the extrusion of simulated seamless tubular fuel elements; mixtures of Al_2O_3 and stainless steel were used as the cores. Three-ply extrusions at ratios of 9:1 and 21:1 showed fairly uniform cladding and core thickness. Sections have been sent to the Superior Tube Co. for redrawing. A similar technique is planned for the extrusion of control rods containing a mixture of 30% Lindsay oxide–70% nickel in the core.

Several compositions were tested for the fabrication of a high-density, low-thermal-conductivity barrier shield plug for the ART pumps. Fabrication procedures have been established for several suitable materials. A thermal-conductivity apparatus has been constructed and tested, and several specimens have been prepared for conductivity measurements.

Physical Chemistry of Corrosion. – An expression for the activation energy for the rate of solution of a solid metal in a liquid metal has been derived and shown to be equal to the temperature coefficient of the Epstein mass-transfer equation. Measurements of absorption spectra of fused electrolytes continue. Studies of the martensitic transformation in $NaNiO_2$ were completed. Measurements were made of the kinetics of oxidation of alkali metals and of the topography of oxide films formed on niobium.

HRP METALLURGY

A metallographic study of the heat-treated structures obtained in Zircaloys-2, -2W, -3A, -3B, and -3C has been initiated. Conclusions on the temperature range of the $(\alpha + \beta)$ fields, rates of grain

growth, annealing structures, randomization of rolling textures, transformation structures, and stringers in hot-rolled plate have been drawn. A similar study on zirconium-hydrogen and Zircaloy-hydrogen alloys has been initiated, and several conclusions on hydride formation are reported. An identification technique for identifying hydrides in the microstructure has been developed.

Stress-corrosion testing of stainless steels at low stress has continued, but the lack of reproducibility prevents the reporting of data. Cell measurements of annealed and cold-worked 304 stainless steel have shown that the cold-worked specimens are more negative to a calomel electrode than the annealed specimens. Inconel-X heat treated to spring temper was stressed at 90,000 psi in boiling 42 wt % $MgCl_2$ and showed no corrosion.

No embrittling effects on aging Zircaloy-2 for periods up to 1585 hr at 250°C were found in either tensile or impact tests.

A procedure has been developed and tested whereby titanium welds may be made in air with only the inert gas from the torch and backup gas being utilized to protect the weld from contamination. The welds are of high quality and are only slightly harder than welds made in a high-purity-atmosphere box.

Army Package Power Reactor. – Development of the components for the APPR-1 has been essentially completed. Refinements have been made so as to permit manufacture of composite plates and fuel elements within the specifications established. Oak Ridge National Laboratory has been selected to produce 71 fuel elements and 14 absorber sections, sufficient components for 1½ reactor loadings. All pertinent engineering drawings have been received, fuel-element manufacturing procedures have been established, and fabrication of enriched plates is scheduled for April 1, 1956.

Considerable effort has been devoted to the selection of materials and the development of procedures for the processing of absorber plates for the control rod. After evaluation of the various systems in which natural boron was to be utilized, the natural boron was abandoned in favor of the powder-metallurgy iron-boron composite clad with

wrought stainless steel. Several plates containing 3.4 wt % B^{10} in an iron-matrix core and prepared by powder-metallurgy processing have been satisfactorily clad with stainless steel by roll bonding.

Postirradiation examination of APPR fuel plates sectioned from the APPR test assembly irradiated in the MTR revealed no gross damage effects (i.e., blistering, warpage, etc.). Postirradiation evaluation of APPR plate sections in which the UO_2 particle size ranged from 7 to 11 and 88 to 105 μ and which were irradiated in the MTR revealed that fission-fragment damage was more extensive in specimens containing the finer particle sizes. A UO_2 particle size of 44 to 88 μ has been selected for the APPR fuel plates.

Metallurgical Materials and Processing. – Compacts prepared by pressing thorium amalgam from the Metallex process have been examined by differential thermometry. The results indicate that a period of "free" mercury evolution is followed by three arrests, which imply compound decomposition. Sufficient thorium (~20 lb) was prepared by retorting thorium amalgam to permit two extrusion experiments. One billet extruded to give a sound rod; the other yielded a poor rod which resulted because of a surface-conditioning treatment prior to extrusion. Tensile tests of the extruded thorium indicate that extrusion alone will not yield satisfactory rod. Need for arc melting of the retorted product is indicated.

The recording of slug failures in the ORNL Graphite Reactor has been continued. The data continue to support earlier observations that incompletely beta-transformed slugs account for the majority of the slug failures.

Disintegration of type 304 stainless steel has been effected by limited carburization and subsequent treatment with a copper sulfate plus sulfuric acid solution, only 1% of the stainless steel going into solution. Iron-base alloys containing 25% chromium and 5% aluminum have responded to a nitriding treatment and breakdown into a granular powder.

CERAMICS RESEARCH

The production of hydrothermally grown UO_3 has been improved by a study of the variables involved.

The Si-SiC fuel-element development program has been continued by studies of the incorporation of fuel into the compacts, by investigating the causes of cracking in the impregnated plates, and by an increased radiation-damage study program.

A study of yttrium oxide has been carried out, and a paper has been prepared for presentation.

Thoria suspensions in water have been studied in order to discover the cause of settling; the electrical properties of the suspension were noted.

Studies of uranium ores and spodumene have been made for the purpose of contributing to the improved beneficiation of these ores.

Petrographic work on the ANP fluoride fuels continues at a rate of about 100 samples per week.

Various clays and other materials have been investigated for use in the waste-disposal program. A pilot-plant pit has been constructed and placed in operation.

A feasibility study on the autoradiographic behavior of clays has been initiated.

The enthalpy data for various ceramic materials has been determined over a temperature range of 0–1200°C.

Rare-earth-oxide cermets and compacts have been fabricated for control-rod assemblies.

FUNDAMENTAL PHYSICO-METALLURGICAL RESEARCH

The fiber-axis distribution for thorium rod fabricated at 850°C such that the as-extruded rod was partially recrystallized revealed a duplex <111> – <001> texture, whereas that for a completely recrystallized as-extruded rod showed a single <114> texture. Annealing the latter rod at 750°C produced a duplex <115> – <236> texture.

The textures obtained are discussed in terms of present theories, and the need for additional experimental data and for further development of the theories is pointed out.

The preferred orientation in Zircaloy-2 plate was found to be similar to that for zirconium fabricated in a similar manner.

The variation of the α/β boundaries of zirconium and titanium phase diagrams can be reduced in first approximation to a common behavior in terms of electron concentration if a metallic valency of two is used for zirconium and titanium. Recent experimental investigation of the axial ratio of the hexagonal phase of zirconium containing added silver and indium supports this divalency, since comparison of the indium data with that of tin in the literature shows that the effect of tin is twice

as great as that of indium. A metallic valency of 1.5 for titanium has been proposed by Denney on the basis of some theoretical and experimental work on this metal, and these results are also in reasonable agreement with the present results on zirconium. The similarity of titanium and zirconium with respect to the effects of alloying upon the axial ratio of the hexagonal phase is such that if the axial ratios are adjusted slightly to allow for the difference in the pure solvents, the c/a curves plotted against electron concentration are nearly the same in both metals.

The solid solubility of silver and zirconium has been reinvestigated by microscopical means and agrees within experimental error with that found by means of lattice spacings. The effect of iron impurities in the alloys is shown by plotting the phase boundaries of the alpha-phase region of alloys made from iodide zirconium of two different iron contents. A recent investigation has been made of the temperature of the peritectic reaction, β + liquid $\rightleftharpoons Zr_2Ag$, in this system, and the temperature was found to be 1191 ± 2°C.

The investigation of the floating-zone refining of zirconium has been continued. The iron and nickel contents of iodide zirconium have been reduced to less than 2 ppm. The distribution of these two impurities after multiple-pass refining has been established by neutron-activation analyses, and the values agree with the theoretical distributions. The α/β transformation in the purified material takes place over the temperature range 865–873°C, compared with the 16–70°C temperature intervals found in Grade 1 crystal bar.

Preliminary experiments have indicated that a liquid zone can be formed and moved by induction heating a zirconium rod resting on a water-cooled copper hearth. Although the purification efficiency has not been investigated, this method shows promise for the refining of relatively large quantities of zirconium.

ANP METALLURGY

W. D. Manly

GENERAL CORROSION

E. E. Hoffman D. H. Jansen W. H. Cook
Metallurgy Division
R. Carlander
Pratt & Whitney Aircraft

THERMAL-CONVECTION-LOOP TEST OF BRAZING ALLOY

D. H. Jansen

A thermal-convection loop was fabricated of ½-in. sched 40 Inconel tubing; six Inconel segments brazed with Coast Metals 52 (89% Ni–5% Si–4% B–2% Fe) were incorporated in the hot-leg section, and an Inconel jacket was welded around the brazed-segment section (see Fig. 1). Figure 2 is a macrophotograph of two of the Inconel segments. The corrosive medium circulated was NaF-ZrF_4-UF_4 (50-46-4 mole %); duration of the test was 1000 hr; and the hot and cold legs were maintained at 1500 and 1100°F, respectively.

After the test, the inner walls of the Inconel segments and two samples from each brazed joint were examined metallographically for any evidence of attack. Attack on the joints is summarized in Table 1. No evidence of mass transfer was found in the loop.

UNCLASSIFIED
ORNL–LR–DWG 9715

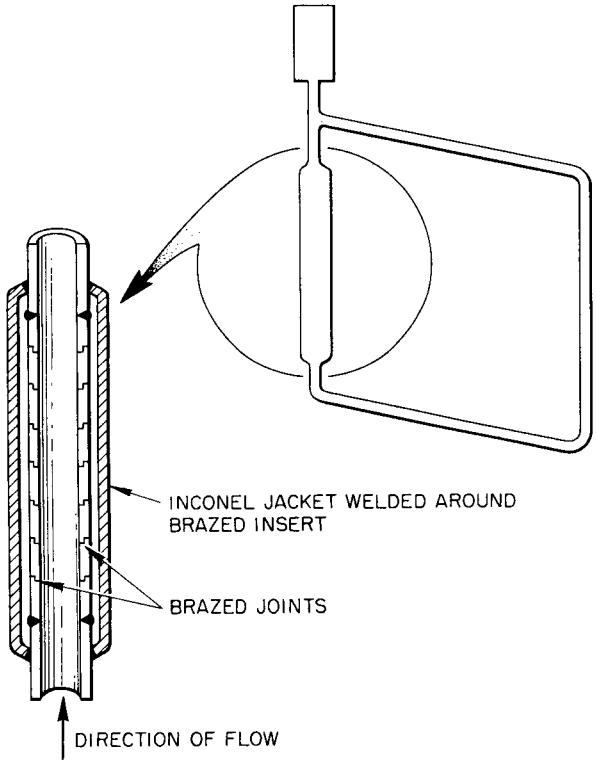

Fig. 1. Diagram of Thermal-Convection Loop Showing Brazed Insert in Hot Leg.

UNCLASSIFIED
Y-16905

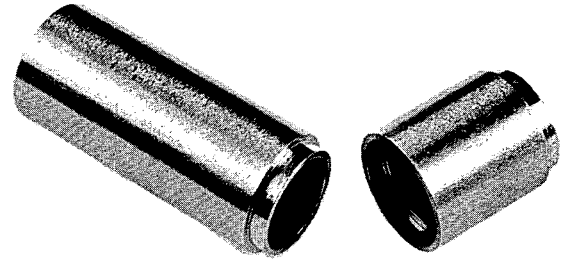

Fig. 2. Inconel Inserts Which Are Brazed Together and Used to Make Up Hot Leg of Loop Illustrated in Fig. 1. 2X. Reduced 47.5%.

TABLE 1. ATTACK ON BRAZED JOINTS AND INCONEL WALL IN HOT LEG OF THERMAL-CONVECTION LOOP

Test Conditions: 1000 hr; hot leg, 1500°F; cold leg, 1100°F

Brazed Joint No.	Attack on Braze (mils)		Attack on Inconel Wall (mils)
1	1.4	1.0	4
2	3	2.0	3
3	0.6	2.0	4
4	1.3	3.5	3
5	9.0	2.0	4

A considerable amount of porosity and an appreciable number of shrinkage voids were observed in most of the brazed joints. Figure 3 shows two brazed joints after having been exposed to the fused salt at 1500°F for 1000 hr.

STATIC TESTS OF BRAZE BUTTONS

D. H. Jansen

Six brazing buttons were corrosion tested under static conditions in sodium, and an identical series was tested in the fused salt NaF-ZrF_4-UF_4 (50-46-4 mole %); two palladium-rich buttons were similarly tested in NaOH and in the fused salt. The buttons were polished on one side and in this condition were used both for testing and for metallographic specimens of as-received material. After testing, the buttons were cut perpendicular to the polished face in order to determine the depth of attack.

The Coast Metals 52 (89% Ni–4% B–5% Si–2% Fe) and General Electric 81 (66% Ni–19% Cr–10% Si–4% Fe–1% Mn) alloys showed good-to-fair corrosion resistance in sodium (Figs. 4 and 5). Buttons of 93% Pd–7% Al tested in the fused salt and in NaOH showed poor resistance to the former medium and very inferior resistance to the latter medium. A Coast Metals 52 button tested in the fused salt showed very deep porosity in only one area; the remainder of the button area exhibited a 0.5-mil attack. This erratic attack is probably due to some isolated segregation, since Coast Metals 52 has exhibited good corrosion resistance to fluorides when used on nickel and Inconel T-joints.

When Coast Metals 52 alloy is tested, a second phase tends to be leached out at the exposed edge. A qualitative microspark traverse on a Coast Metals 52 button tested for 100 hr in the fused salt at 1500°F showed that the boron and silicon concentrations at the edge were one-third of their

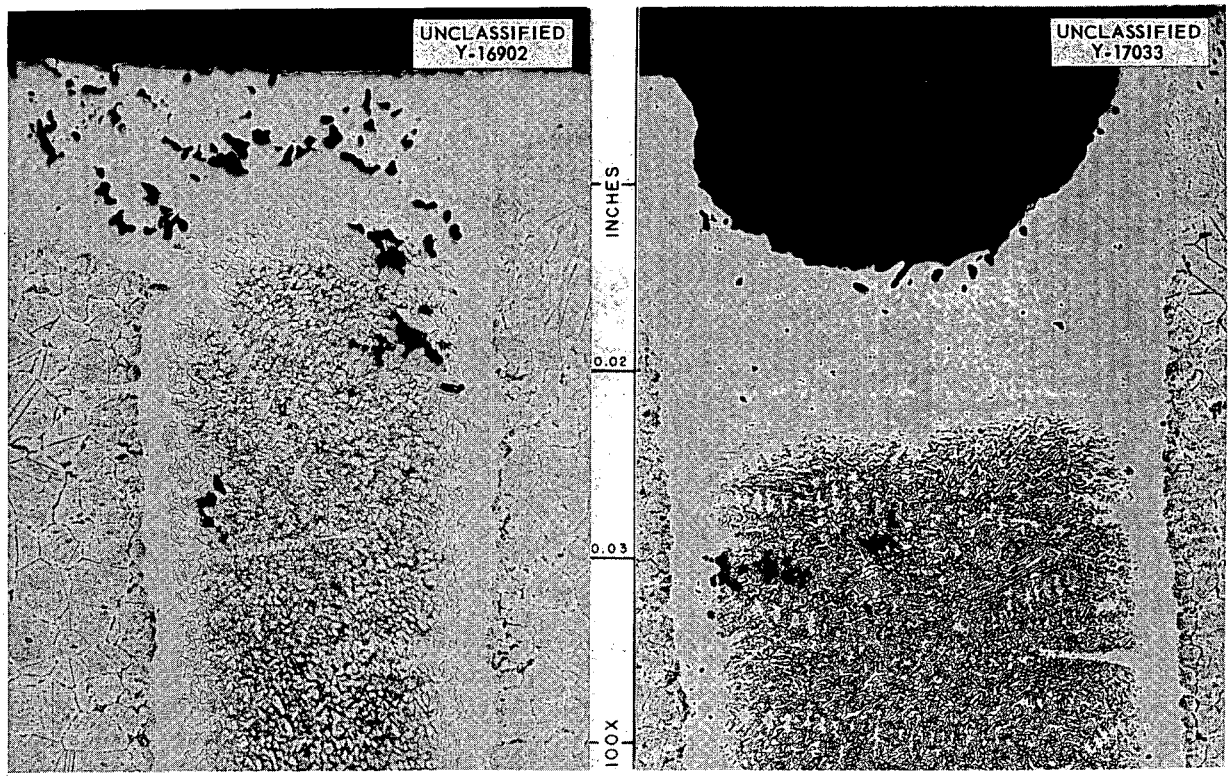

Fig. 3. Two Inconel Joints Brazed with Coast Metals 52 (89% Ni–5% Si–4% B–2% Fe). These brazed joints were exposed for 1000 hr to NaF-ZrF_4-UF_4 (50-46-4 mole %) at 1500°F in a thermal-convection loop. Etchant: oxalic acid. 100X. Reduced 2%. (Secret with caption)

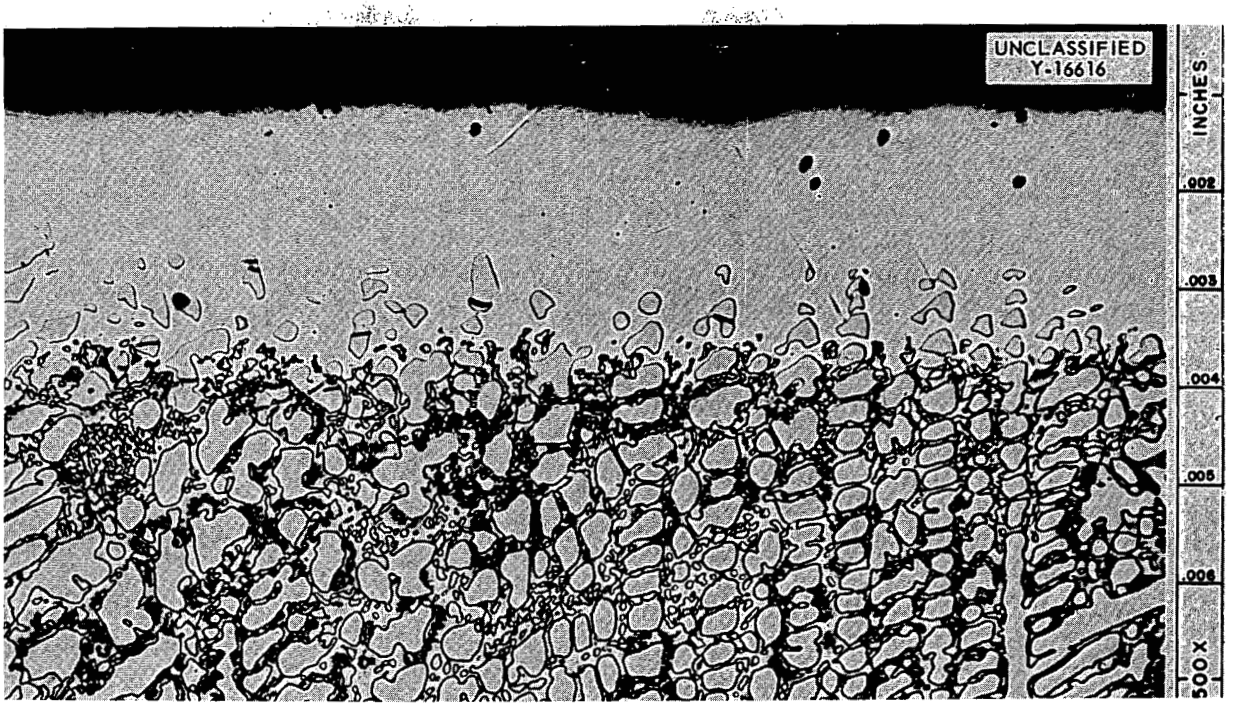

Fig. 4. Coast Metals 52 (89% Ni–5% Si–4% B–2% Fe) Alloy Button After Having Been Tested for 100 hr in Static Sodium at 1500°F. No apparent attack. Note how second phase has been leached out at the surface. Etchant: 10% oxalic acid.

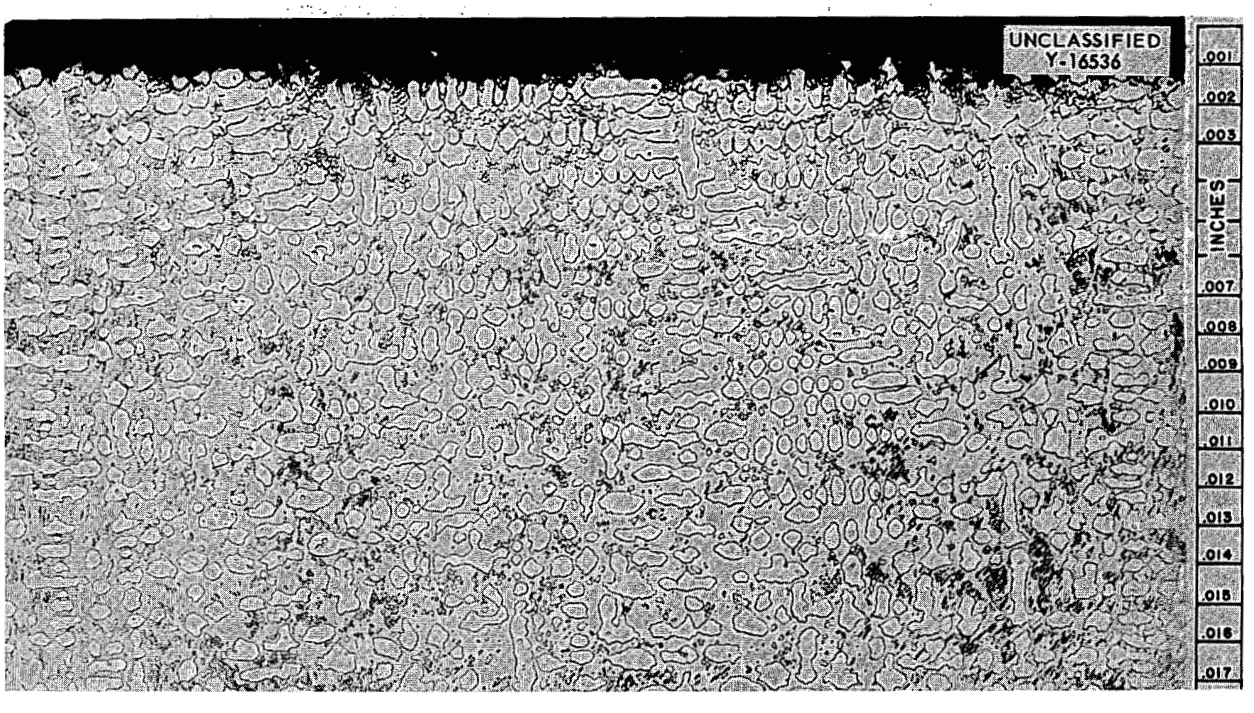

Fig. 5. General Electric 81 (66% Ni–19% Cr–10% Si–4% Fe–1% Mn) Alloy After Having Been Tested for 100 hr in Static Sodium at 1500°F. Attack is 1.5 mils. Etchant: 10% oxalic acid. 200X.

normal values. The concentrations of these elements increased with depth and reached full value at a distance approximately 13 mils from the edge. Microdrillings and chemical analysis of the leached-out area are not complete.

Buttons of 60% Pd–40% Ni tested in the fused salt and in NaOH show good corrosion resistance to both media.

Table 2 lists the brazing buttons tested. The alloys are listed in order of decreasing corrosion resistance.

BRAZING ALLOYS ON INCONEL T-JOINTS TESTED IN SODIUM AND IN FUEL MIXTURES

D. H. Jansen

A series of brazing alloys on Inconel T-joints has been seesaw-tested in sodium and in two NaF-ZrF_4-UF_4 mixtures (53.5-40-6.5 mole % and 50-46-4 mole %). Hydrogen-fired Inconel capsules were used for test containers. Capsules were loaded under an inert atmosphere and were then evacuated and sealed. Duration of the tests was 100 hr, and the hot- and cold-zone temperatures were 1500 and 1100°F, respectively.

TABLE 2. CORROSION OF BRAZING BUTTONS TESTED FOR 100 hr IN STATIC SODIUM, NaOH, AND NaF-ZrF_4-UF_4 (50-46-4 mole %) AT 1500°F

Alloy Composition (wt %)	Weight Change (%)	Metallographic Notes
	Fused-Salt Bath	
60 Pd–40 Ni	−0.043	No attack
89 Ni–5 Si–4 B–2 Fe (Coast Metals 52)	−0.104	0.5-mil attack; considerable porosity in area
65 Ni–25 Ge–10 Cr	−0.22	1.3-mil attack; porosity and subsurface voids in some areas
93 Pd–7 Al	+0.16	3-mil attack
80 Ni–10 Cr–10 P	−0.26	4-mil attack
66 Ni–19 Cr–10 Si–4 Fe–1 Mn (General Electric 81)	−0.37	4-mil attack
55 Mn–35 Ni–10 Cr	−7.3	9-mil stringer attack
60 Mn–40 Ni	−8.4	21-mil stringer attack
	NaOH Bath	
60 Pd–40 Ni	+1.18	No attack
93 Pd–7 Al		Button partially dissolved
	Sodium Bath	
89 Ni–5 Si–4 B–2 Fe (Coast Metals 52)	−0.22	No attack
66 Ni–19 Cr–10 Si–4 Fe–1 Mn (General Electric 81)	−0.047	2-mil attack
65 Ni–25 Ge–10 Cr	−0.083	2-mil attack
80 Ni–10 Cr–10 P	−0.3	3-mil attack
55 Mn–35 Ni–10 Cr	−1.6	4- to 5-mil stringer-type attack
60 Mn–40 Ni	−3.85	Nonuniform attack to a maximum depth of 19 mils

The 80% Ni–10% Cr–10% P and 75% Ni–25% Ge alloys showed good-to-fair corrosion resistance in both the sodium and the fuel mixtures, as shown in Figs. 6 and 7. The results are shown in Table 3. The alloys are listed in order of decreasing corrosion resistance.

CORROSION RESISTANCE OF VARIOUS BRAZING ALLOYS ON INCONEL AND STAINLESS STEEL

C. F. Leitten, Jr. D. H. Jansen

Brazing alloys on type 304 stainless steel and Inconel T-joints submitted by the Wall Colmonoy Corporation have been tested in static sodium and static fuel mixture NaF-ZrF_4-UF_4 (53.5-40-6.5 mole %). These tests were performed in an effort to find a brazing alloy that has good corrosion resistance to both media. The results obtained are summarized in Tables 4 and 5, respectively. The alloys are listed in order of decreasing corrosion resistance. The brazing alloy C-29 (10.2% P–13% Si–76.8% Ni) appears to have the best corrosion resistance to both media.

On comparison of the metallographic results in Tables 4 and 5, it is apparent that brazing alloys containing relatively high percentages of phosphorus appear to be excessively attacked by sodium, but additions of silicon tend to improve their corrosion resistance. On the other hand, brazing alloys having high percentages of silicon and no phosphorus tend to be heavily attacked by the fused salts. The presence of manganese in the brazing alloys appears to reduce their corrosion resistance to both media.

BRAZING ALLOYS ON "A" NICKEL

C. F. Leitten, Jr. D. H. Jansen

Several brazing alloys on "A" nickel T-joints have been submitted by the Welding and Brazing Group for corrosion testing for 100 hr in static sodium and NaF-ZrF_4-UF_4 (53.5-40-6.5 mole %) at 1500°F. Several of the brazing alloys, especially the precious-metal alloys, were also tested in static sodium hydroxide at 1100 and 1500°F for 100 hr. The results of the tests with sodium hydroxide appear in Table 6. The 82% Au–18% Ni alloy showed good corrosion resistance to sodium hydroxide at 1500°F. The 80% Au–20% Cu, 60% Pd–40% Ni, and 60% Pd–37% Ni–3% Si alloys showed good resistance at 1100°F, but these same alloys when tested at 1500°F were heavily attacked. Small additions of silicon to the Pd-Ni alloy tend to improve its resistance to attack at 1100°F. Results of the tests in sodium and in the fused-salt mixture are summarized in Tables 7 and 8, respectively. Since previous tests indicated poor corrosion resistance of the precious metals to

TABLE 3. CORROSION OF BRAZING ALLOYS ON INCONEL T-JOINTS SEESAW-TESTED IN LIQUID SODIUM AND NaF-ZrF_4-UF_4

Test Conditions: 100 hr; hot zone, 1500°F; cold zone, 1100°F

Test Bath	Alloy Composition (wt %)	Weight Change (%)	Resistance	Metallographic Notes
Sodium	80 Ni–10 Cr–10 P	–0.174	Good	No attack
Sodium	75 Ni–25 Ge	–0.052	Fair	2-mil attack
Sodium	50 Ni–25 Ge–25 Mo	–0.252	Poor	Nonuniform attack to a depth of 3.2 mils
Bath 30*	80 Ni–10 Cr–10 P	–0.102	Good	No attack; fillet cracked
Bath 44**	50 Ni–25 Ge–25 Mo	0.0	Good	Erratic attack to a depth of 1 mil
Bath 30*	75 Ni–25 Ge	–0.060	Fair	2-mil attack
Bath 30*	80 Au–20 Cu	–0.072	Fair	Surface voids to a maximum depth of 2 mils
Bath 44**	82 Au–18 Ni	–0.16	Poor	4-mil attack

*Bath 30: 53.5-40-6.5 mole %.
**Bath 44: 50-46-4 mole %.

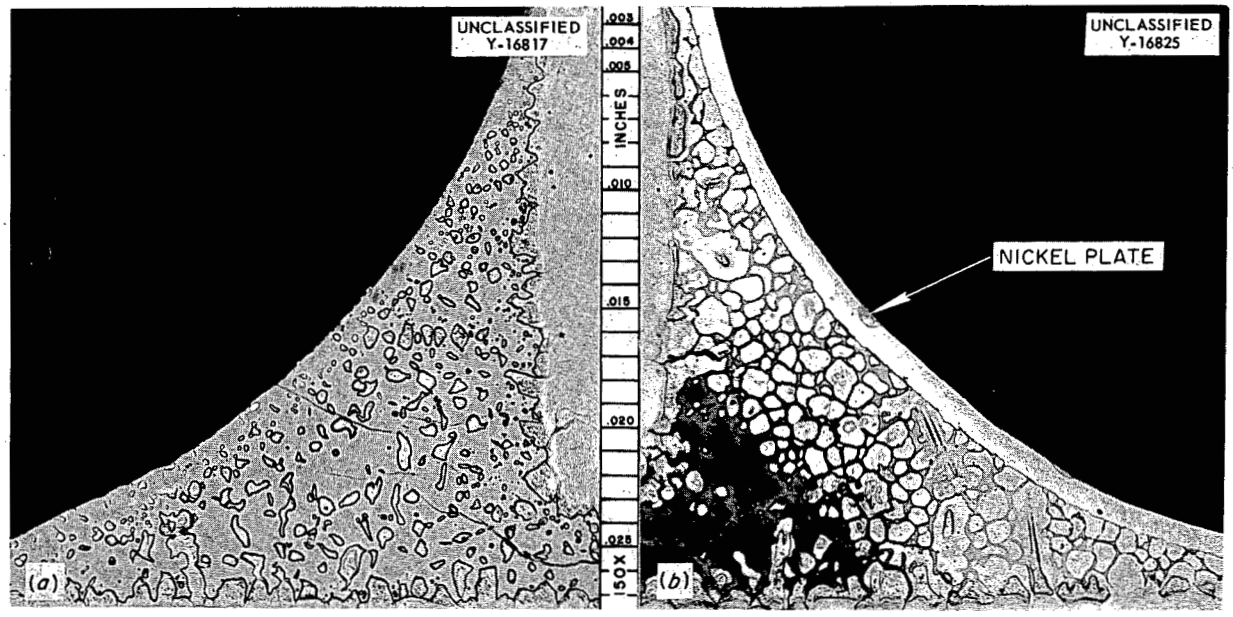

Fig. 6. Alloy 80% Ni–10% P–10% Cr on Inconel T-Joints Seesaw-Tested at 1500°F for 100 hr in (*a*) NaF-ZrF_4-UF_4 (50-46-4 mole %) and (*b*) Sodium. No apparent attack. Specimen (*a*) was nickel-plated after the test in order to preserve the edge during polishing. Etchant: 10% oxalic acid. 150X. Reduced 17%. (Secret with caption)

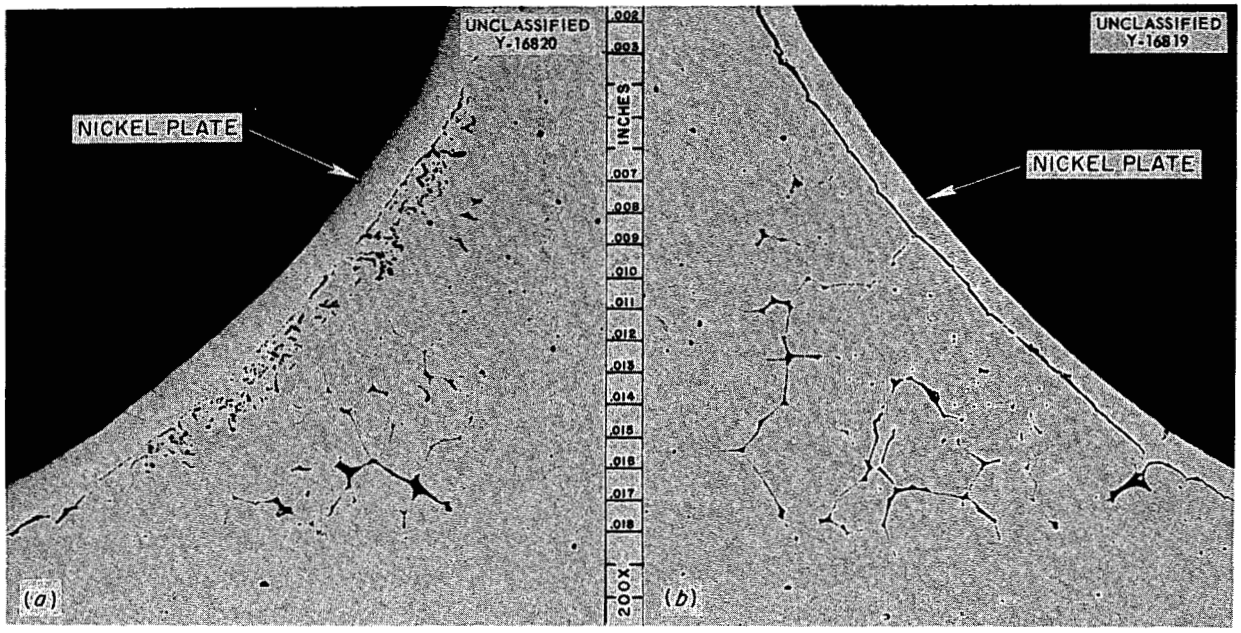

Fig. 7. Brazing Alloy 75% Ni–25% Ge After Seesaw Test at 1500°F for 100 hr in (*a*) Sodium and (*b*) NaF-ZrF_4-UF_4 (50-46-4 mole %). The 2-mil attack which occurred in both media is shown. Both specimens were nickel-plated after the test in order to preserve edges during polishing. Etchant: citric acid. 200X. Reduced 16%. (Secret with caption)

TABLE 4. RESULTS FROM TESTS OF BRAZING ALLOYS ON TYPE 304 STAINLESS STEEL AND ON INCONEL EXPOSED FOR 100 hr TO STATIC SODIUM AT 1500°F

Brazing Alloy*		Base Material	Weight Change		Metallographic Notes
Designation	Composition (wt %)		(g)	(%)	
F-11	9 Si–17.8 Cr–73.2 Ni	304 stainless steel	0	0	No attack along surface of braze fillet
E-11	13 Si–87 Ni	304 stainless steel	–0.0007	–0.068	Surface of braze fillet is unattached
C-29	10.2 P–13 Cr–76.8 Ni	304 stainless steel	+0.0004	+0.054	Less than 0.5 mil of small subsurface voids
B-11	10.8 P–9.2 Si–80 Ni	304 stainless steel	0.0	0.0	Subsurface voids to a depth of 4 mils
A-16	23 P–77 Ni	304 stainless steel	–0.0009	–0.135	Subsurface voids in braze fillet to a depth of 5 mils; attack confined to Ni_3P phase
C-27	9.6 P–2.75 Cr–88.6 Ni	304 stainless steel	–0.0006	–0.086	Subsurface voids to a depth of 5 mils; Ni_3P phase attacked
A-10	12 P–88 Ni	304 stainless steel	–0.0015	–0.141	6-mil attack along entire fillet surface; attack in Ni_3P phase
I-10	11.6 P–6.25 Mn–82.2 Ni	Inconel	–0.0014	–0.135	6-mil nonuniform attack along fillet surface
J-10	9 P–15 Fe–4.5 Cr–71.5 Ni	304 stainless steel	–0.0004	–0.067	Subsurface voids to a depth of 7 mils; Ni_3P removed from fillet zones
B-11	10.8 P–9.2 Si–80 Ni	Inconel	–0.0010	–0.098	4-mil erratic surface attack; subsurface voids to a depth of 9 mils
H-10	10 P–4.3 Mo–85.7 Ni	Inconel	–0.0011	–0.107	9 mils of subsurface voids along fillet surface
I-10	11.6 P–6.25 Mn–82.15 Ni	304 stainless steel	–0.0018	–0.346	Subsurface voids in braze fillet to a depth of 11 mils
H-10	10 P–4.3 Mo–85.7 Ni	304 stainless steel	–0.0006	–0.108	Subsurface voids in braze fillet to a depth of 19 mils
D-11	9.9 P–11.3 Fe–78.8 Ni	304 stainless steel	+0.0006	+0.108	Subsurface voids in braze fillet to a depth of 25 mils

*Brazing alloys listed in order of decreasing corrosion resistance.

TABLE 5. RESULTS FROM TESTS OF BRAZING ALLOYS ON TYPE 304 STAINLESS STEEL AND ON INCONEL EXPOSED FOR 100 hr TO STATIC $NaF-ZrF_4-UF_4$ (53.5-40-6.5 mole %) AT 1500°F

Brazing Alloy*		Base Material	Weight Change		Metallographic Notes
Designation	Composition (wt %)		(g)	(%)	
A-16	23 P–77 Ni	304 stainless steel	−0.0003	−0.042	No attack on braze fillet
C-27	9.6 P–2.75 Cr–88.6 Ni	304 stainless steel	0.0	0.0	No attack on braze fillet
C-29	10.2 P–13 Cr–76.8 Ni	304 stainless steel	+0.0011	+0.180	No attack on braze fillet
I-10	11.6 P–6.25 Mn–82.15 Ni	304 stainless steel	+0.0008	+0.112	No attack on braze fillet
A-10	12 P–88 Ni	304 stainless steel	−0.0031	−0.30	No attack on braze fillet
D-11	9.9 P–11.3 Fe–78.8 Ni	304 stainless steel	+0.0015	+0.304	No attack on braze fillet
J-10	9 P–15 Fe–4.5 Cr–71.5 Ni	304 stainless steel	+0.0007	+0.153	Small subsurface voids in fillet to a depth of 0.5 mil
H-10	10 P–4.3 Mo–85.7 Ni	Inconel	−0.0016	−0.154	0.5-mil attack along surface of fillet
I-10	11.6 P–6.25 Mn–82.25 Ni	Inconel	−0.0006	−0.157	Surface of fillet attacked to a depth of 0.5 mil
H-10	10 P–4.3 Mo–85.7 Ni	304 stainless steel	+0.0036	+0.730	Maximum attack was 0.5 mil in the form of small subsurface voids
B-11	10.8 P–9.2 Si–80 Ni	Inconel	−0.0018	−0.166	Fillet surface attacked to a depth of 1 mil
B-11	10.8 P–9.2 Si–80 Ni	304 stainless steel	−0.0006	−0.082	Braze fillet attached to a depth of 1 mil in several areas
F-11	9 Si–17.8 Cr–73.2 Ni	304 stainless steel	−0.0052	−0.52	6-mil attack on surface of braze fillet
E-11	13 Si–87 Ni	304 stainless steel	−0.0036	−0.358	Braze fillet completely attacked

*Brazing alloys listed in order of decreasing corrosion resistance.

TABLE 6. RESULTS FROM TESTS OF BRAZING ALLOYS ON "A" NICKEL T-JOINTS EXPOSED FOR 100 hr TO SODIUM HYDROXIDE AT 1100 AND 1500°F

Brazing Alloy* Composition (wt %)	Test Temperature (°F)	Weight Change (g)	Weight Change (%)	Metallographic Notes
82 Au–18 Ni	1500	−0.0040	−0.144	Nonuniform surface attack on braze to a depth of 1 mil
82 Au–18 Ni	1100	−0.0007	−0.022	No attack on surface of braze
80 Au–20 Cu	1500	−0.0106	−0.38	Uniform surface attack over entire braze surface to a depth of 3 mils
80 Au–20 Cu	1100	−0.0050	−0.164	Surface attack on braze to a depth of 1 mil
60 Pd–40 Ni	1500	−0.0015	−0.049	Surface of braze fairly clean; attack, in the form of small stringers, to a depth of 4 mils
60 Pd–40 Ni	1100	−0.0007	−0.028	Surface attack to a depth of 0.5 mil
60 Pd–37 Ni–3 Si	1500	+0.0023	+0.083	Surface attack on braze fillet to a depth of 6 mils
60 Pd–37 Ni–3 Si	1100	+0.0008	+0.028	No attack present on braze surface
100 Cu	1500	−0.0118	−0.408	Braze completely attacked; large voids appear throughout
100 Cu	1100	−0.0011	−0.038	Uniform surface attack on braze to a depth of 3 mils
90 Ni–10 P	1500	−0.0054	−0.15	Braze completely attacked; attack concentrated in brittle Ni_3P phase
90 Ni–10 P	1100	−0.0012	−0.047	Braze completely attacked; attack concentrated in Ni_3P phase
69 Ni–20 Cr–11 Si	1500			Braze failed completely
69 Ni–20 Cr–11 Si	1100	+0.0024	+0.093	Braze completely attacked

*Brazing alloys listed in order of decreasing corrosion resistance.

sodium, no brazing alloy containing a precious-metal constituent was tested in this medium. The brazing alloys 90% Ni–10% P, 80% Ni–10% Cr–10% P, and Nicrobraz (70% Ni–14% Cr–6% Fe–5% B–4% Si–1% C) showed good-to-fair corrosion resistance to both the sodium and the fused-salt mixture.

After the tests, several of the brazed T-joints, especially those which included copper, gold, or silicon as an alloying element in the braze material, showed numerous voids in the interface between the base material and the braze fillet. The brazing alloy 60% Pd–37% Ni–3% Si showed this phenomenon to the greatest extent. These voids are not considered to be caused by attack by the test media but rather by diffusion of a braze-alloy constituent into the base material. In order to verify this, several T-joints brazed with an alloy containing either copper, gold, or silicon were sealed in evacuated capsules and were tested at 1500°F for 100 hr. Figure 8*a* is a photomicrograph of brazing alloy 60% Pd–37% Ni–3% Si after 100 hr of exposure to the fused-salt mixture at 1500°F. Many voids can be seen along the interface between the base material and the braze fillet, but the surface of the specimen appears to be free of attack. Figure 8*b* shows the results of the annealing process on the same braze material, 60% Pd–37% Ni–3% Si. As was observed for the specimen in Fig. 8*a*, voids were produced at the interface between the base material and the braze fillet. Therefore, the formation of the voids appears to be independent of environment and, thus, is not the result of attack by the fused salts.

TABLE 7. RESULTS FROM TESTS OF BRAZING ALLOYS ON "A" NICKEL T-JOINTS EXPOSED FOR 100 hr TO STATIC SODIUM AT 1500°F

Brazing Alloy* Composition (wt %)	Weight Change (g)	Weight Change (%)	Metallographic Notes
90 Ni–10 P (Electroless Nickel)	−0.0004	−0.018	No attack
90 Ni–4 B–4 Si–2 Fe (Coast Metals 52)	−0.0019	−0.068	0.5-mil surface attack
80 Ni–10 Cr–10 P	−0.0017	−0.061	1-mil nonuniform attack
66 Ni–10 Si–19 Cr–4 Fe–1 Mn (General Electric 81)	−0.0018	−0.078	1-mil attack
69 Ni–5 B–15 Cr–5 Si–5 Fe–1 C (Nicrobraz)	−0.0022	−0.082	1.5-mil layer of small subsurface voids along fillet edge
50 Ni–25 Mo–25 Ge	−0.0009	−0.036	2.5-mil attack
65 Ni–25 Ge–10 Cr	−0.0024	−0.085	3-mil uniform attack
60 Mn–40 Ni	−0.0080	−0.079	9-mil uniform attack
35 Ni–55 Mn–10 Cr	−0.0005	−0.020	Layer of small voids that penetrated 13 mils into the body of the material
68 Ni–32 Sn	−0.0171	−0.540	Complete attack of whole fillet.

*Brazing alloys listed in order of decreasing corrosion resistance

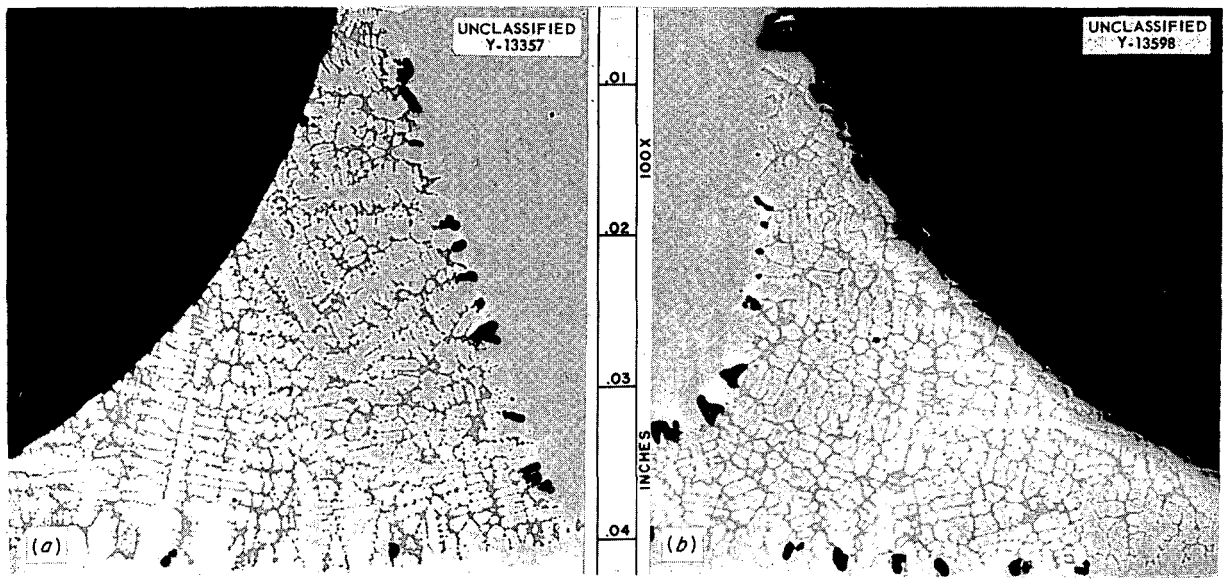

Fig. 8. "A" Nickel T-Joints Brazed with Alloy 60% Pd–37% Ni–3% Si, (a) Tested for 100 hr in NaF-ZrF_4-UF_4 (53.5-40-6.5 mole %) at 1500°F and (b) Annealed in Vacuum for 100 hr at 1500°F. Note similar occurrence of interfacial voids in both specimens. As polished. 100X. Reduced 20%. (Secret with caption)

TABLE 8. RESULTS FROM TESTS OF BRAZING ALLOYS ON "A" NICKEL T-JOINTS EXPOSED FOR 100 hr TO STATIC $NaF-ZrF_4-UF_4$ (53.5-40-6.5 mole %) AT 1500°F

Brazing Alloy* Composition (wt %)	Weight Change (g)	Weight Change (%)	Metallographic Notes
82 Au–18 Ni	−0.0010	−0.036	No attack
60 Pd–40 Ni	−0.0016	−0.06	No attack
60 Pd–37 Ni–3 Si	+0.0008	+0.027	No attack
80 Ni–10 Cr–10 P	0.0	0.0	No attack
50 Ni–25 Mo–25 Ge	0.0	0.0	No attack
70 Ni–14 Cr–6 Fe–5 B–4 Si–1 C (Nicrobraz)	−0.0004	−0.016	No attack
80 Au–20 Cu	−0.0007	−0.026	No attack
90 Ni–10 P (Electroless Nickel)	−0.0004	−0.013	No attack
100 Cu	−0.0006	−0.019	0.5-mil attack
65 Ni–25 Ge–10 Cr	0.0	0.0	Small subsurface voids to a depth of 0.5 mil along brazed fillet
90 Ni–4 B–4 Si–2 Fe (Coast Metals 52)	−0.0014	−0.05	Nonuniform attack of 6 mils
69 Ni–20 Cr–11 Si (General Electric 62)	−0.0017	−0.055	Surface attack of 6 mils
66 Ni–10 Si–19 Cr–4 Fe–1 Mn (General Electric 81)	−0.0003	−0.012	Nonuniform attack of 12 mils
35 Ni–55 Mn–10 Cr	−0.0111	−0.48	Complete attack of braze fillet
60 Mn–40 Ni	−0.0159	−0.59	Complete attack of braze fillet
68 Ni–32 Sn	−0.0998	−3.49	Joint partially dissolved at fillet surface

*Brazing alloys listed in order of decreasing corrosion resistance.

"A" nickel T-joints (see Figs. 9*a* and 9*b*) brazed with 60% Pd–37% Ni–3% Si were tested in sodium hydroxide for 100 hr at 1100 and 1500°F, respectively. In Fig. 9*a* it can be seen that no attack occurred along the braze fillet of the specimen tested at 1100°F and that very few diffusion voids were present. However, as can be seen in Fig. 9*b*, the specimen tested at 1500°F showed a 6-mil surface attack and, also, several small interfacial voids. The absence of interfacial voids in the one case, as compared to the presence of the interfacial voids in the other, is probably caused by the difference in diffusion rates at the two temperatures.

CORROSION OF LOW-NEUTRON-CROSS-SECTION BRAZING ALLOYS IN NaK, SODIUM, AND $NaF-ZrF_4-UF_4$

D. H. Jansen

Seesaw tests using NaK (56-44 wt %), sodium, and $NaF-ZrF_4-UF_4$ (53.5-40.0-6.5 mole %) as corrosion media have been conducted on Inconel tube-to-header joints brazed with Ni-Cr-Ge-Si low-neutron-cross-section brazing alloys. A cross section of this type of joint is shown in Fig. 10. The tube-to-header joints used in these tests are more typical of those actually used in fabrication than are the T-joints used in previous tests. The

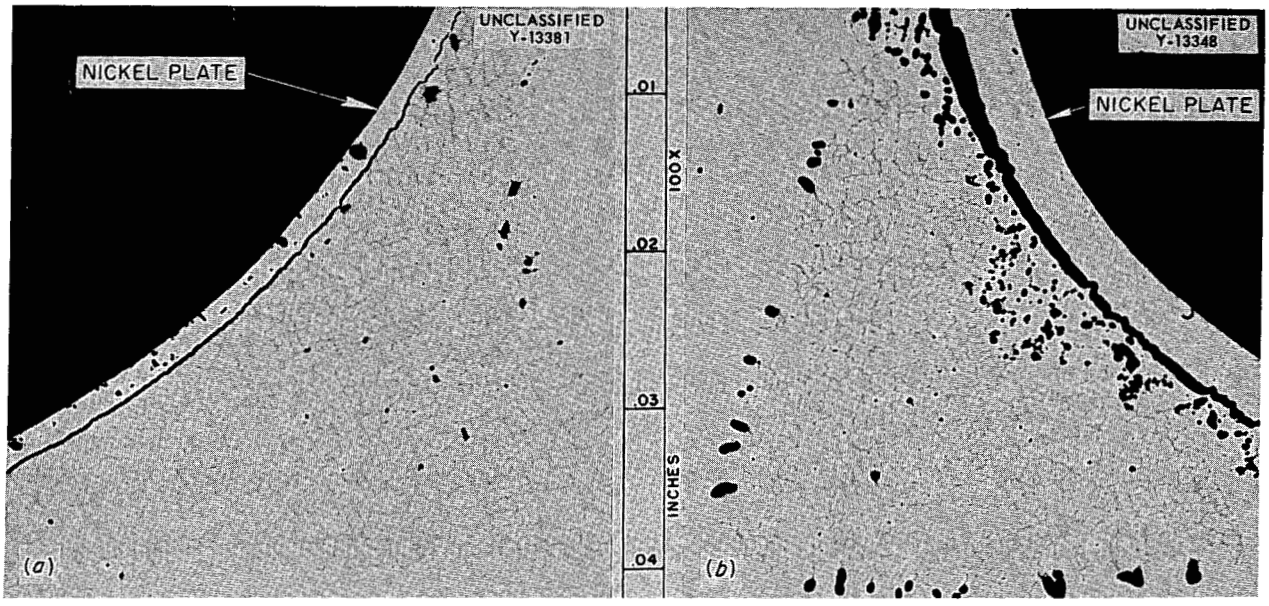

Fig. 9. "A" Nickel T-Joints Brazed with Alloy 60% Pd–37% Ni–3% Si and Tested for 100 hr in Sodium Hydroxide at (*a*) 1100°F and (*b*) 1500°F. Note surface attack and interfacial voids present in specimen tested at higher temperature. 100X. Reduced 18.5%.

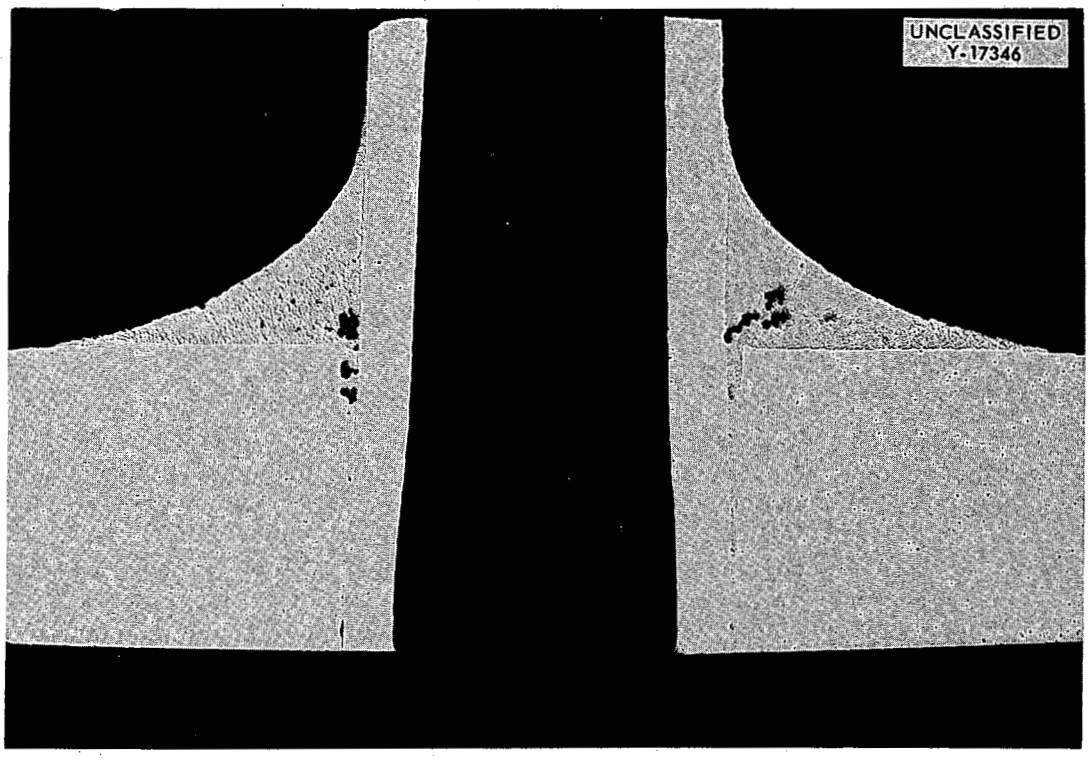

Fig. 10. Cross Section of an As-Brazed Tube-to-Header Joint. Specimen brazed with 89% Ni–5% Si–4% B–2% Fe (Coast Metals 52) alloy. As polished. 10X.

specimens tested to date were given a fast braze (5 min to raise to brazing temperature and 10 min at brazing temperature) and are listed, along with the attack on each brazing alloy, in Table 9. Tests were conducted in hydrogen-fired Inconel capsules with hot- and cold-zone temperatures of 1500 and 1100°F, respectively.

In general, indications are that, of the brazing alloys tested, those containing the highest nickel contents show the best corrosion resistance to NaK. Tube-to-header joints brazed with the above alloys but brought to brazing temperature over a 4-hr period will be tested in the same media in order to determine if brazing time has any effect on corrosion rate. The 70% Ni–11% Cr–13% Ge–6% Si alloy tested in NaK and fused salts is shown in Figs. 11 and 12.

TABLE 9. CORROSION OF BRAZING ALLOYS ON INCONEL TUBE-TO-HEADER JOINTS GIVEN A RAPID BRAZE AND SEESAW TESTED IN SODIUM, NaK (56–44 wt %) AND NaF-ZrF_4-UF_4 (53.5-40-6.5 mole %)

Test Conditions: 100 hr; hot zone, 1500°F; cold zone, 1100°F

Alloy Composition (wt %)	Sodium Attack (mils)	NaK Attack (mils)	Fused-Salt Attack (mils)
70 Ni–11 Cr–13 Ge–6 Si	5	3	3.5
65 Ni–16 Cr–13 Ge–6 Si	6.5	7.5	3
62 Ni–19 Cr–13 Ge–6 Si	7.5	6.5	3
59 Ni–19 Cr–16 Ge–6 Si	8	5	2.5

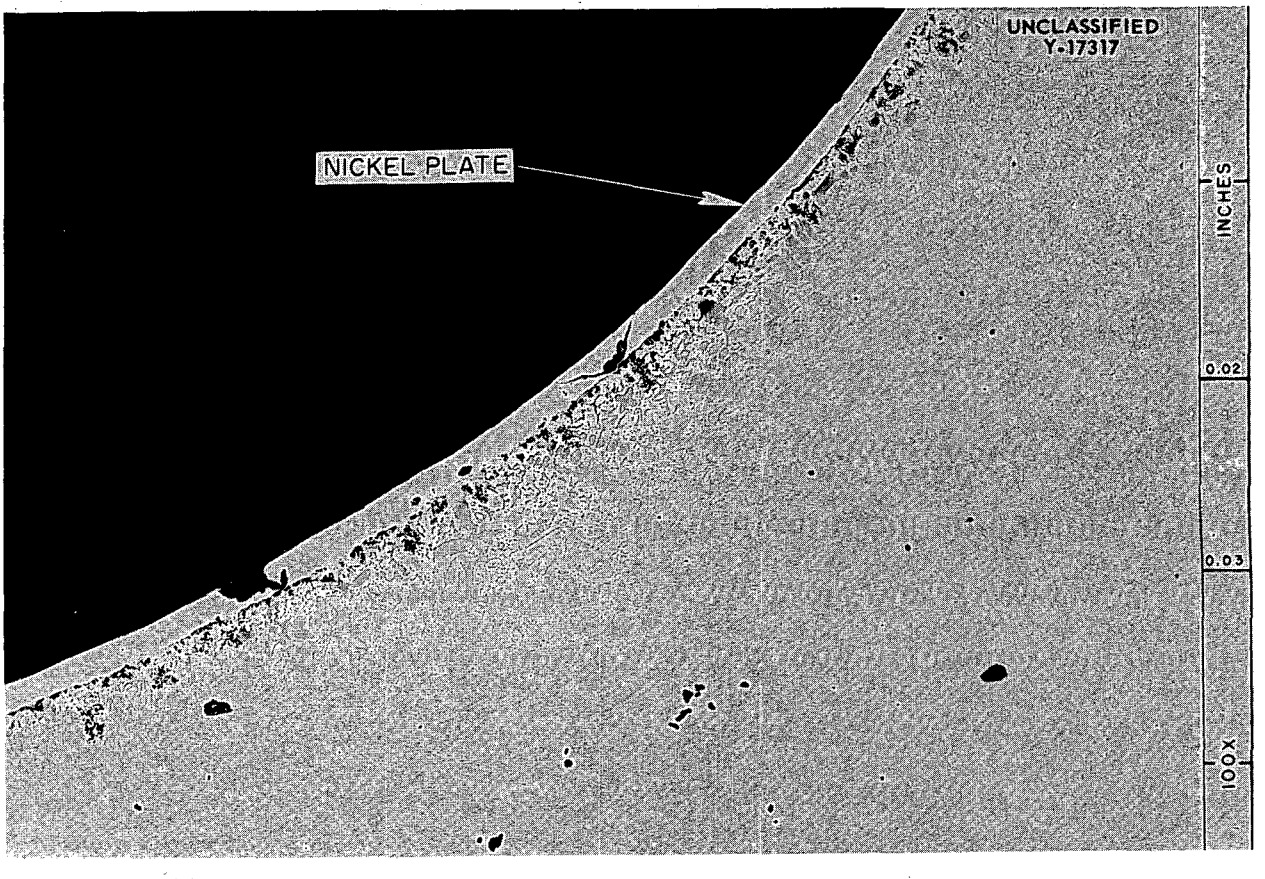

Fig. 11. Brazing Alloy 70% Ni–13% Ge–11% Cr–6% Si on Inconel, Seesaw Tested for 100 hr in NaK (56-44 wt %) with a Hot-Zone Temperature of 1500°F; Nonuniform Attack to a Maximum Depth of 3 mils Is Shown. Specimen nickel-plated following test in order to protect the edge during metallographic polishing. As polished.

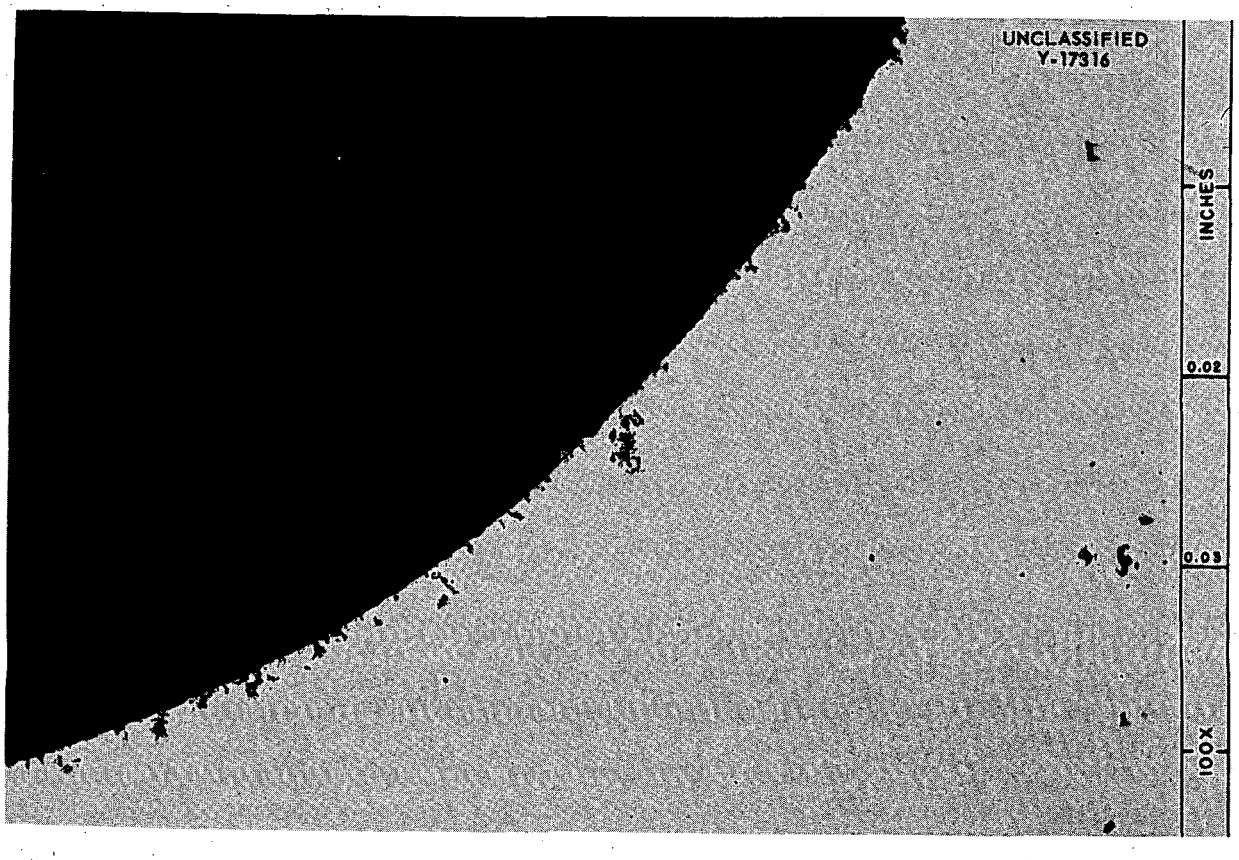

Fig. 12. Brazing Alloy 70% Ni–13% Ge–11% Cr–6% Si on Inconel, Seesaw Tested for 100 hr in $NaF-ZrF_4-UF_4$ (53.5-40-6.5 mole %) with a Hot-Zone Temperature of 1500°F; Nonuniform Attack to Maximum Depth of 3.5 mils Is Shown. As polished. 100X. Reduced 1.5%. (Secret with caption)

Four tube-to-header joints were brazed with the 89% Ni–5% Si–4% B–2% Fe (Coast Metals 52) alloy, two rapidly (10 min) and two slowly (4 hr), and were seesaw-tested for 100 hr in NaK and fused salts at 1500°F to determine whether the brazing time has any bearing on the corrosion rate. Results of the corrosion tests conducted on this alloy are listed in Table 10.

As can be seen from the table, the different brazing rates had no effect on the extent of corrosion on this alloy.

TABLE 10. EFFECT OF BRAZING TIME ON CORROSION OF 89% Ni–5% Si–4% B–2% Fe ALLOY IN SEESAW TESTS WITH SODIUM AND WITH $NaF-ZrF_4-UF_4$ (53.5-40-6.5 mole %)

Test Conditions: 100 hr; hot zone, 1500°F; cold zone, 1100°F

Specimen	Bath	Metallographic Notes
Slow braze, 4 hr	Fused salt	Nonuniform attack to a depth of 0.5 mil
	NaK	No attack
Rapid braze, 10 min	Fused salt	Nonuniform attack to a depth of 0.5 mil
	NaK	No attack

CORROSION TESTING OF THERMOCOUPLE WELLS

D. H. Jansen

A number of thermocouple wells fabricated from 0.125-in.-OD Inconel tubing and 0.020-in. Chromel-

Alumel wires were supplied by the Welding and Brazing Group for corrosion testing in sodium and $NaF-ZrF_4-UF_4$ (50-46-4 mole %). The Chromel-Alumel content of the weld nuggets on the thermocouples was varied in order to determine whether the high content of silicon, manganese, and aluminum in the nuggets has any bearing on the corrosion rate. Nuggets with a high Chromel-Alumel content were made by melting down part of the thermocouple wires to form the weld; whereas, nuggets low in Chromel-Alumel were made by melting down the Inconel tube around the wires.

The tests conducted on the wells and the extent of corrosion are summarized in Table 11.

The tubes with high Chromel-Alumel content in the weld were more heavily attacked in the nonweld areas than were the tubes with low Chromel-Alumel content. All attack measurements were made prior to etching the specimens. Figures 13 and 14 show the tested welds.

RUTHENIUM-PLATED-INCONEL TENSILE-TEST SPECIMENS

D. H. Jansen

A third ruthenium-plated-Inconel tensile-test specimen has been rupture-tested by the Mechanical Properties Group. Results from an unplated Inconel specimen which was to be used as a standard and which was reported previously[1] are invalidated because the heat treatment prior to test differs from that of other tested specimens.

Results, to date, of rupture tests on Inconel specimens are listed in Table 12.

[1] C. F. Leitten, Jr., and D. H. Jansen, *Met. Semiann. Prog. Rep. Oct. 10, 1955*, ORNL-1988, p 17.

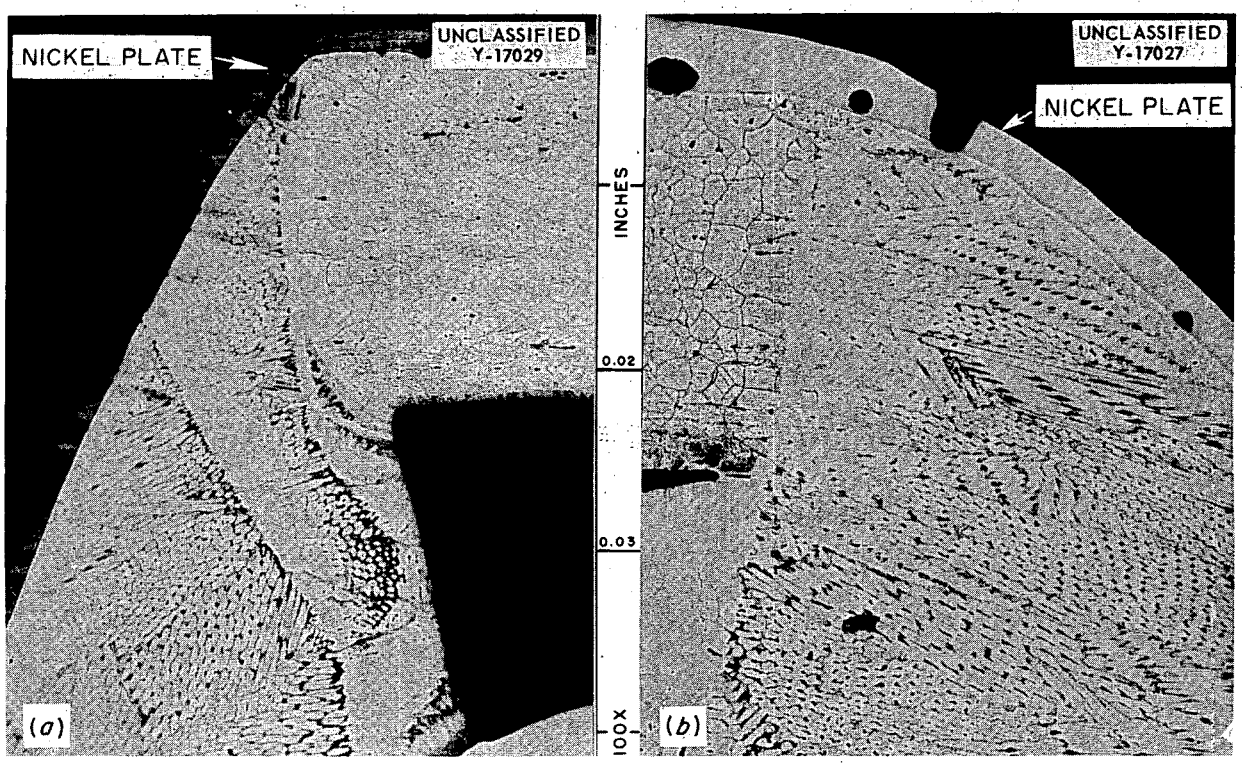

Fig. 13. Inconel Thermocouple Tubes Welded So As to Have Low Chromel-Alumel Content and Seesaw Tested for 100 hr in (a) Sodium and in (b) $NaF-ZrF_4-UF_4$ (50-46-4 mole %) at 1500°F. (*a*) No attack. (*b*) Two-mil attack on thermocouple tube; no apparent attack on weld portion. Attack measurements taken prior to etching specimen. Specimens nickel-plated after test in order to preserve edges during polishing. Etchant: 10% oxalic acid. 100X. Reduced 4%. (Secret with caption)

TABLE 11. THERMOCOUPLE WELLS SEESAW-TESTED FOR 100 hr IN SODIUM AND $NaF-ZrF_4-UF_4$ (50-46-4 mole %) AT 1500°F

Type of Weld		Bath	Attack Area	Attack (mils)
Chromel-Alumel Content	Treatment			
High	Ground flat	Fused salt	Inconel tube	4.5
High	Ground flat	Fused salt	Weld	0.5
High	As-welded	Fused salt	Inconel tube	4.5
High	As-welded	Fused salt	Weld	0.5
Low	As-welded	Fused salt	Inconel tube	2.0
Low	As-welded	Fused salt	Weld	None
Low	As-welded	Sodium	Inconel tube	None
Low	As-welded	Sodium	Weld	None

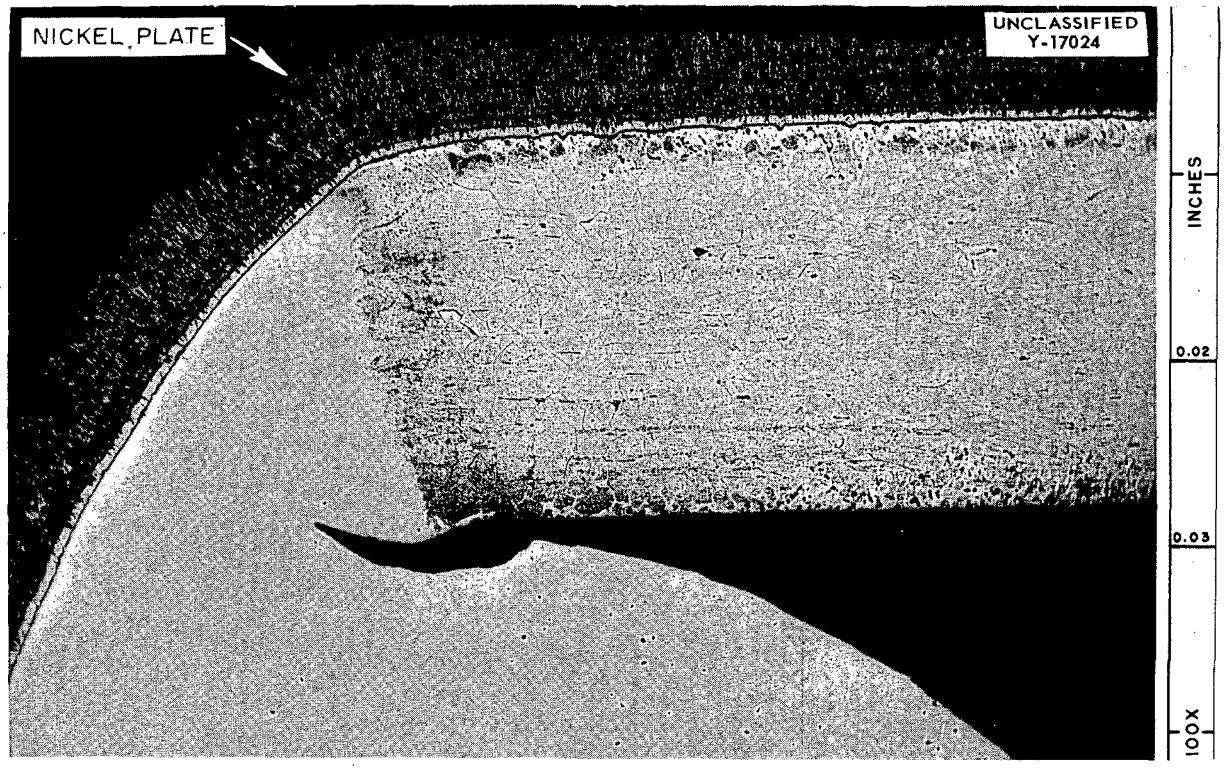

Fig. 14. Inconel Thermocouple Tube Welded So As to Have High Chromel-Alumel Content and Seesaw Tested for 100 hr in $NaF-ZrF_4-UF_4$ (50-46-4 mole %) at 1500°F. Attack: 4.5 mils on thermocouple tube, 0.5 mil on weld portion. Attack measurements taken prior to etching specimen. Specimen nickel-plated after test in order to preserve edge during polishing. Etchant: 10% oxalic acid. 100X. Reduced 1%. (Secret with caption)

TABLE 12. CREEP RUPTURE OF INCONEL AND RUTHENIUM-PLATED-INCONEL TEST SPECIMENS IN A PURIFIED ARGON ATMOSPHERE

Test Conditions: Stress, 3500 psi at 1500°F
Heat treatment prior to test, 100 hr at 1500°F

Specimen No.	Specimen Condition	Time to Rupture (hr)	Final Elongation (%)
1	Unplated (standard)	746	14.0
2	Plated	873	13.4
3	Plated	728	13.6
4	Plated	1200	13.0

Specimen No. 4 and another plated specimen awaiting test were analyzed by the Spectrographic Laboratory, and the results showed positive evidence for the presence of ruthenium plate. After heat treatment and just prior to the test, the shoulders of these specimens were milled to a depth of 2 mils; the milled particles were analyzed and found to contain 1.17% ruthenium.

The plated specimen awaiting test should be rupture-tested before the influence of ruthenium on Inconel can be assessed with finality, although tests to date indicate that ruthenium platings have no adverse effect on the physical properties of Inconel.

EFFECT OF AN AIR LEAK INTO AN INCONEL–FUSED-SALT TEST SYSTEM

R. Carlander

After a 500-hr tube-burst test at 1500°F, an Inconel test capsule was found to be very heavily attacked just above the level of the $NaF\text{-}ZrF_4\text{-}UF_4$ (50-46-4 mole %) test mixture. It was suggested that the attack (see Fig. 15) was due to an air leak in the system; and, therefore, several experiments were performed in which air was admitted into similar test capsules through a small tube. These capsules failed within 24 hr at a temperature of 1500°F. The reaction products found in the fused salt were zirconium oxide and structural-metal fluorides.

Fig. 15. Effect of an Air Leak into Test System Composed of Inconel and $NaF\text{-}ZrF_4\text{-}UF_4$ (50-46-4 mole %). (Secret with caption)

HIGH-TEMPERATURE TESTS OF MOLYBDENUM IN CONTACT WITH $NaF\text{-}ZrF_4\text{-}UF_4$

E. E. Hoffman

Some experiments with molybdenum sheathing have been conducted for the purpose of attempting to devise some type of protection for the cooling jacket of the fused-salt–Inconel pump-loop experiment which is scheduled to go into the MTR. A loop failure would undoubtedly occur in the vicinity of the nose of the loop if the pumping were interrupted for a short period. In the event of such a pump failure, it is possible that the fluorides might reach a temperature as high as 2430°F (1331°C), which has been given as the approximate boiling point of the fluorides. It has been proposed that a sheath of molybdenum around the nose of the loop might afford sufficient protection

for the cooling jacket. It was arbitrarily concluded that 30 min at the test temperature 2430°F (1331°C) would be more than adequate to determine the suitability of molybdenum as a protective sheath.

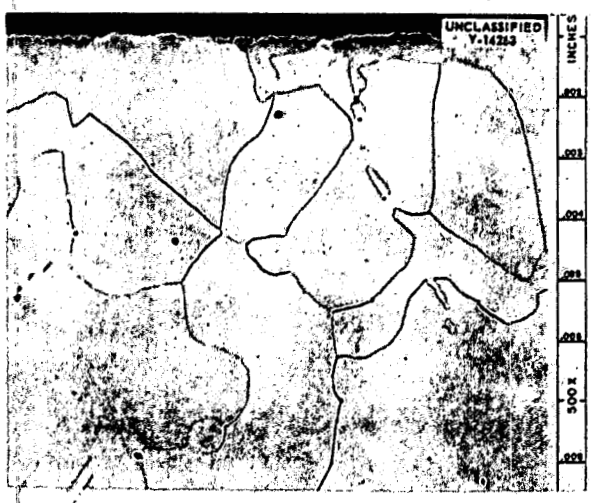

Fig. 16. Surface of Molybdenum Specimen After 30-min Exposure to $NaF-ZrF_4-UF_4$ (53.5-40.0-6.5 mole %) at 1331°C (2430°F). Etched with NH_4OH plus H_2O_2. 500X. Reduced 34%. (Secret with caption)

A molybdenum specimen was placed in a molybdenum container which was filled with $NaF-ZrF_4-UF_4$ (53.5-40-6.5 mole %). In one test, a molybdenum plug was welded into the top of the capsule; while in a second test, the top was left open. In order to prevent oxidation of the molybdenum, these test containers were sealed in Hastelloy B, and then the whole assembly was sealed in quartz. There was no weight change in either specimen as a result of the test. Metallographic examination of these specimens showed no attack (see Fig. 16). The effects of alloying between the molybdenum and the Hastelloy B during this 30-min high-temperature test can be seen in Fig. 17.

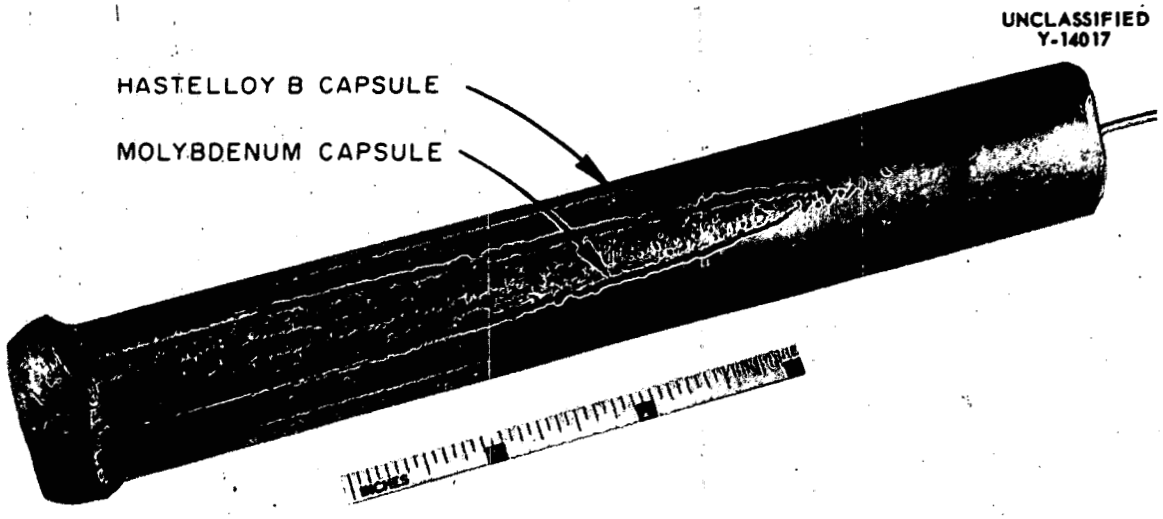

Fig. 17. Hastelloy B and Molybdenum Capsules After Test. Bottom of capsule at left. Note the alloying of the inner molybdenum capsule with the outer Hastelloy B capsule. (Secret with caption)

DECARBURIZATION OF PLAIN CARBON STEEL BY STATIC SODIUM

E. E. Hoffman R. Carlander

It is a well established fact that various metals may be either carburized or decarburized while in contact with sodium at elevated temperatures. The direction and extent of this phenomenon depend on both the original carbon content of the sodium and the carbon content of the metals in contact with the liquid metal.

The purpose of these tests was to determine how far the decarburization of a plain carbon steel might proceed under certain test conditions. Two different types of container materials were used in order to study their effect on the decarburization of AISI 1043 plain carbon steel (0.43% carbon) specimens by the sodium. The capsules were loaded and sealed in an inert atmosphere. The tests were conducted for 100 and 400 hr at 1000°C. Sections of the test components were taken and submitted for metallographic and chemical analyses. The extent to which carbon was transferred in the 100-hr test and in the 400-hr test is shown in Fig. 18.

As expected on the basis of previous investigations, extensive decarburization of the steel specimens occurred in both the Armco iron and the type 304 ELC stainless steel. The extent of decarburization was greater in the 400-hr test (0.43–0.054 wt % carbon) than in the 100-hr test (0.433–0.121 wt % carbon); and, in addition, the vapor zone of the stainless steel capsule was carburized at 400 hr, whereas it was not at 100 hr. The extent of decarburization of the steel specimen tested for 100 hr was greater in the stainless steel capsule, and the decarburization of the steel specimen tested for 400 hr was greater in the Armco iron capsule. Furthermore, the amount of nickel that was mass-transferred to the surface of the steel specimen in the stainless steel capsule was sufficient to cause a phase transformation of 1 to 2 mils in 100 hr and of 2 to 4 mils in 400 hr. Table 14 shows the results of carbon analyses on the various test components. From these results, it is evident that the decarburization of the specimens and the carburization of the capsule walls were greatly increased as the time of testing was increased.

PENETRATION OF SODIUM INTO BERYLLIUM

E. E. Hoffman

The purpose of these tests was to determine the extent to which sodium penetrates beryllium metal in a beryllium-sodium-Inconel static system. These tests were conducted for 1000 hr at 1200 and 1500°F. The beryllium specimens and sodium bath were sealed in Inconel capsules. After the test, five analytical samples, each 10 mils in thickness, were machined from one surface of each

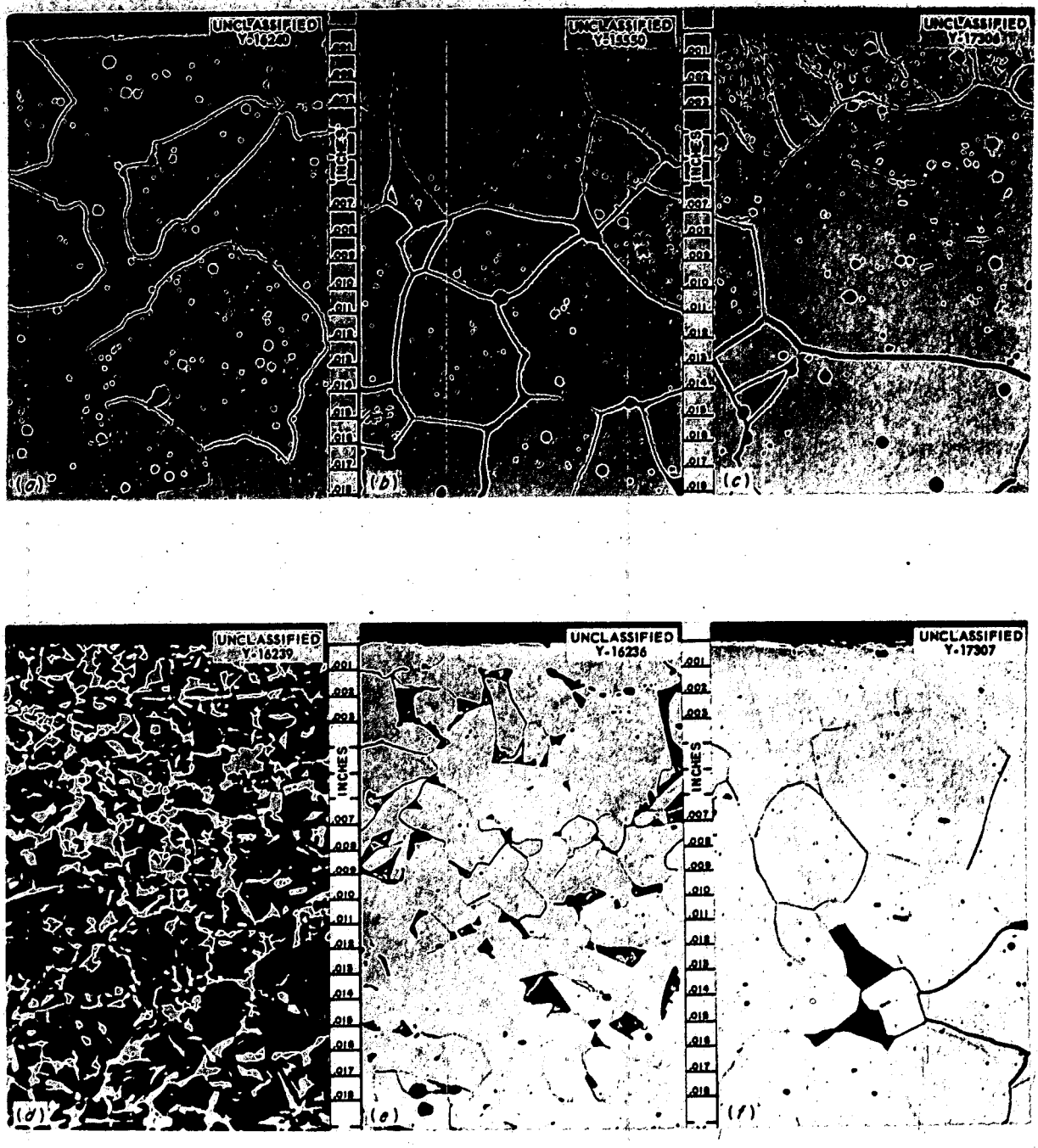

Fig. 18. Decarburization Effect of Sodium at 1000°C on Systems Composed of Armco Iron Capsules and AISI 1043 Plain Carbon Steel Specimens. Armco iron: (*a*) as received, 0.019% carbon; (*b*) tested 100 hr, 0.035% carbon; (*c*) tested 400 hr, 0.024% carbon; etched with 2% nital. AISI 1043 plain carbon steel: (*d*) as received, 0.433% carbon; (*e*) tested 100 hr, 0.121% carbon; (*f*) tested 400 hr, 0.054% carbon; etched with 4% picral in HCl. 200X. Reduced 18%.

TABLE 14. ANALYSES OF VARIOUS COMPONENTS IN SYSTEMS FOR EVALUATING DECARBURIZATION OF TYPE 1043 PLAIN CARBON STEEL BY SODIUM AT 1000°C

Material Analyzed	Carbon (wt %)				Weight Loss ($g/in.^2$)		Nickel (wt %)	
	Before 100-hr Test	Before 400-hr Test	After 100-hr Test	After 400-hr Test	100-hr Test	400-hr Test	Before 400-hr Test	After 400-hr Test
Armco Iron Capsule								
Type 1043 steel	0.433	0.43	0.121	0.054	0.0002	0.0408	0.008	
Armco Iron	0.019	0.018						
Vapor zone			0.019	0.016				
Bath zone			0.035	0.024				
Type 304 ELC Stainless Steel Capsule								
Type 1043 steel	0.433	0.43	0.100	0.074	0.0002	0.0303	0.008	0.090
Type 304 ELC stainless steel	0.022	0.037					11.12	
Vapor zone			0.022	0.162				10.32
Bath zone			0.128	0.200				9.98

specimen. In order to avoid contamination from sodium which adheres to the edges, 50 mils were machined off the surface of each sample. These samples were submitted for spectrographic sodium analysis. The results of these analyses are listed in Table 15.

It appears from these data that very little penetration of beryllium by the sodium bath will occur at a temperature of 1200°F. As can be seen in Fig. 19, the beryllium specimen in this test was attacked irregularly to a maximum depth of 5 mils. In the 1500°F test the specimen was very heavily attacked to a maximum depth of 20 mils, and a 3- to 4-mil porous metallic layer covered the surface of the beryllium specimen. This layer was anisotropic, and it may be either beryllium metal or a beryllium-rich Be-Ni solid solution. No surface layer could be found on the walls of the Inconel capsules used in these tests; however, there was quite a bit of fine precipitate along the surface to a depth of 2 to 3 mils. This precipitate may be either BeNi or $Be_{21}Ni_5$ particles.

TABLE 15. EXTENT OF SODIUM PENETRATION INTO BERYLLIUM AFTER 1000-hr EXPOSURE TO MOLTEN SODIUM

Depth of Penetration (mils)	Sodium Concentration (mg of Na per g of Be)	
	1200°F Test	1500°F Test
0–10	0.2	135
10–20	0.2	29.4
20–30		0.6
30–40	0.3	0.1
40–50	0.02	0.6*

*This apparent increase in sodium concentration is not significant.

BERYLLIUM-SODIUM-INCONEL SPACER TESTS

E. E. Hoffman

Previous tests[2] have revealed that dissimilar-metal mass transfer of beryllium metal to Inconel across small sodium gaps is a serious problem at temperatures in excess of 1200°F. As a result of these findings, a study is underway to determine the effect of temperature and gap size on the alloying of beryllium with Inconel. Layers of BeNi

[2]E. E. Hoffman *et al.*, *ANP Quar. Prog. Rep. Sept. 10, 1954*, ORNL-1771, p 29; G. M. Adamson *et al.*, *ANP Quar. Prog. Rep. Dec. 10, 1954*, ORNL-1816, p 78.

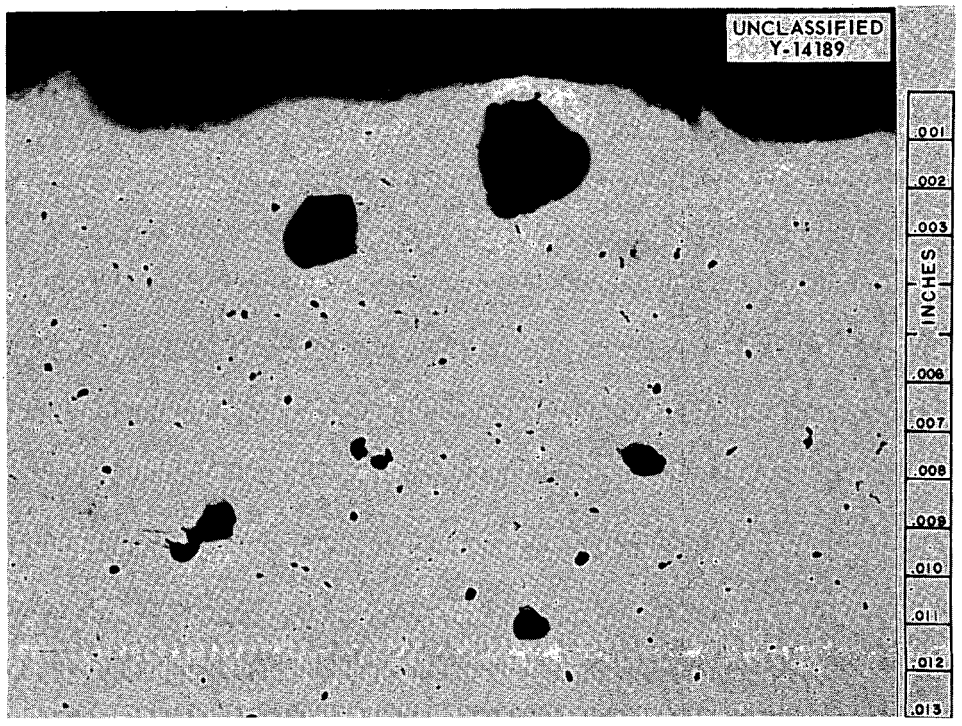

Fig. 19. Surface of a Beryllium Specimen After a 1000-hr Exposure to Static Sodium at 1200°F. Large voids are due to attack by the sodium, while small voids were introduced during metallographic polishing. Unetched. 250X. (Secret with caption)

and $Be_{21}Ni_5$, both of which are very hard and brittle compounds, have been found on Inconel surfaces in past tests. A thermal-convection-loop test which operated for 1000 hr with a hot-zone temperature of 1300°F revealed a $Be_{21}Ni_5$ layer approximately 20 mils in thickness where an Inconel pipe and a beryllium insert were in direct contact.[2] In the same test, in areas where a 6-mil clearance was present between Inconel and beryllium, a ½-mil layer of the Be-Ni compound was found on the surface of the Inconel.

The following tests on beryllium and Inconel specimens were conducted in a static sodium bath, since the maximum attack on beryllium specimens and the only beryllium-nickel-compound layers on Inconel in thermal-convection-loop tests have been found in areas where the bath was fairly stagnant. These areas prevailed in the annular space between the beryllium insert and the Inconel sleeve, which surrounded the beryllium and held it in position in the loops.

The tests completed to date were conducted for 1000 hr at 1200°F and with 0-, 5-, and 20-mil spaces between the Inconel and beryllium. The appearance of these specimens after the test may be seen in Figs. 20, 21, and 22. It can readily be noted that considerable alloying occurred where the specimens were in direct contact. Metallographic examination of the surface of the Inconel specimen separated from the beryllium by the 5-mil space revealed a maximum of 0.2 mils of beryllium-nickel-compound formation. The surface of the Inconel specimen separated from beryllium by the 20-mil space had no beryllium-nickel-compound layers; however, there was an excessive amount of precipitate in the Inconel grains to a depth of 1 mil. Figure 23 shows beryllium and Inconel specimens which were held in direct contact. Figure 24 is a photomicrograph showing the 6-mil layer of $Be_{21}Ni_5$ and BeNi which formed on the surface of the Inconel during this 1000-hr test. Spectrographic analyses of drillings from the

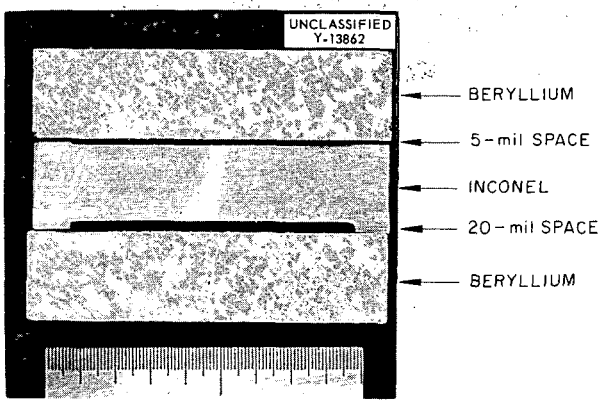

Fig. 20. Inconel and Beryllium Specimens in Positions Occupied During 100-hr Exposure to Sodium at 1200°F. The mating surfaces of these specimens may be seen in Figs. 21 and 22. 3X. Reduced 31%. (Secret with caption)

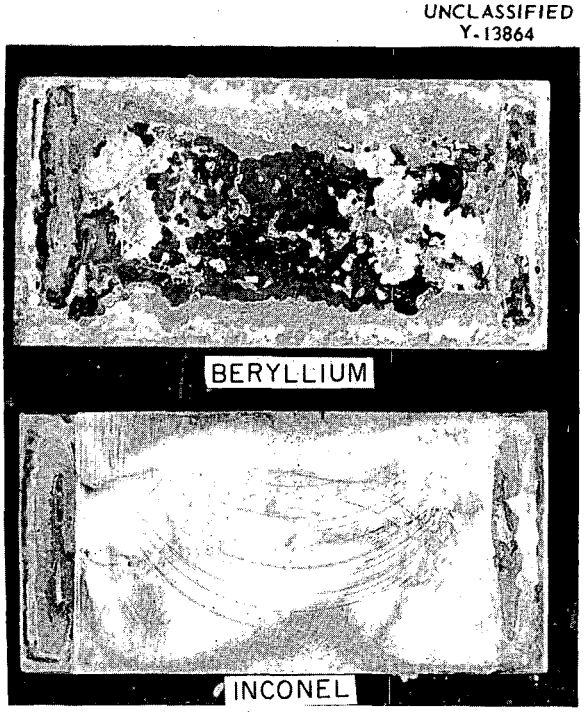

Fig. 21. Surfaces of Beryllium and Inconel Specimens That Were Separated by a 5-mil Space (see Fig. 20). Gray and dark areas on beryllium indicate the formation of BeO. Dark areas on Inconel are locations where Be-Ni alloying occurred. (Disregard areas of direct contact.) Unetched. 3X. (Secret with caption)

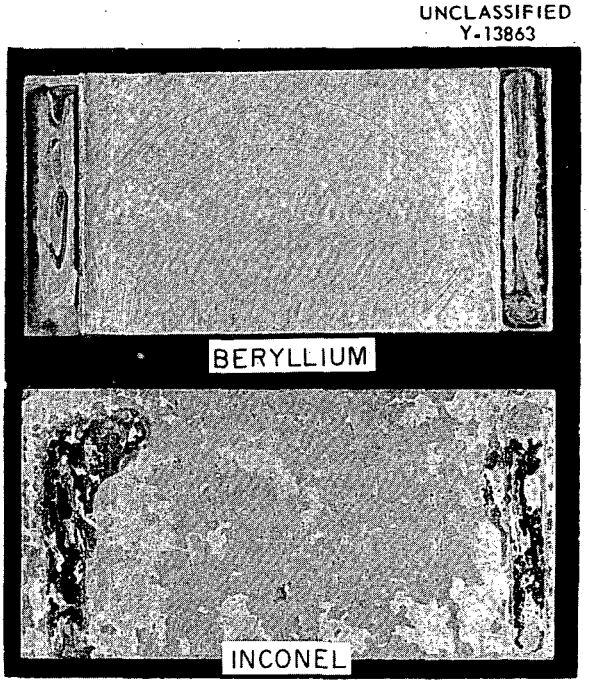

Fig. 22. Surfaces of Beryllium and Inconel Specimens That Were Separated by 20-mil Space (see Fig. 20). Surface discolorations correspond to those described in Fig. 21. Unetched. 3X. (Secret with caption)

surfaces of the Inconel specimens revealed the beryllium concentrations listed below.

Distance Between Inconel and Beryllium (mils)	Beryllium Concentration (10^{-6} g/cm^2)
0	2075–3490
5	5.65
20	0.57

THERMAL-CONVECTION-LOOP TEST OF BERYLLIUM-SODIUM-INCONEL SYSTEM

E. E. Hoffman

In Fig. 25 a beryllium insert and the Inconel sleeve which surrounded it are shown as they appeared after having been exposed to sodium in a recent thermal-convection-loop test. This test was conducted for 1500 hr at a hot-zone temperature of 1300°F, and excessive alloying occurred between the sleeve and the beryllium specimen.

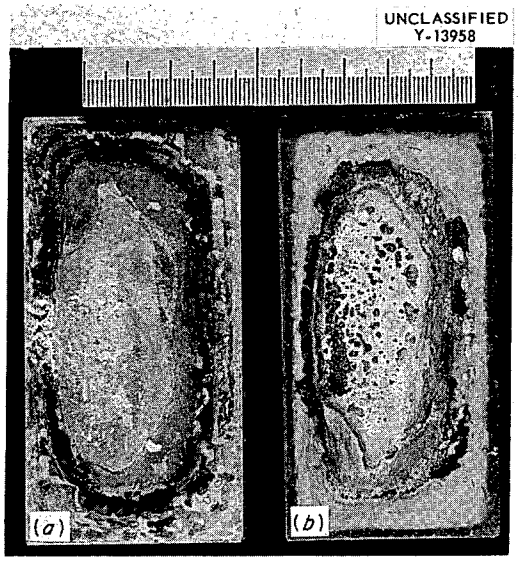

Fig. 23. Mating Surfaces of (a) Beryllium and (b) Inconel Specimens After 1000-hr Exposure to Static Sodium at 1200°F. 3X. Reduced 16%. (Secret with caption)

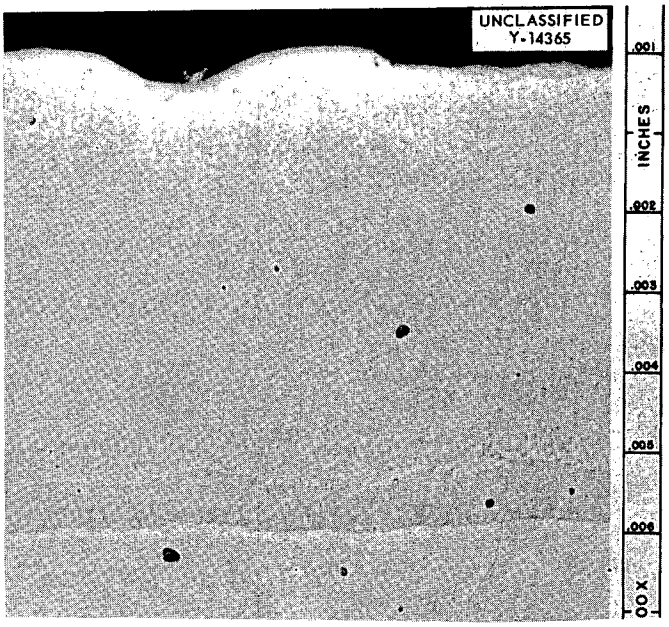

Fig. 24. Layers of BeNi and $Be_{21}Ni_5$ Which Formed on the Inconel Specimen. See caption of Fig. 23 for description of conditions. 500X. Reduced 16%. (Secret with caption)

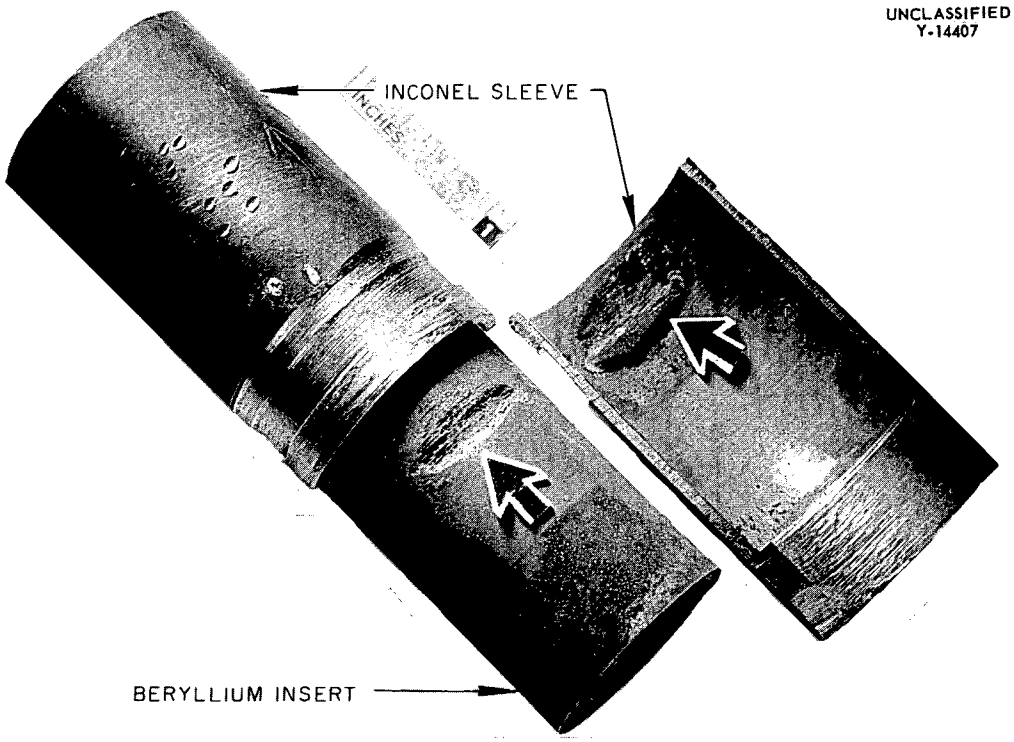

Fig. 25. Inconel Sleeve and Beryllium Insert from Thermal-Convection-Loop Test with Sodium After 1500 hr with Hot Zone of 1300°F. Note alloying (indicated by arrows) which occurred between sleeve and insert. (Secret with caption)

The Inconel and beryllium were separated by a space of approximately 6 mils at the beginning of the test. It can be noted from the photograph that alloying of the beryllium with the Inconel resulted in a metal buildup on the surface of the Inconel and a depression in the beryllium surface. Extensive alloying also occurred between the ends of the beryllium insert and the Inconel pipe, which were in intimate contact during the test. Microdrillings were taken from various sections of the Inconel loop in order to check the beryllium distribution on its surface in various areas. The concentration was found to be 6.0 and 6.4 $\mu g/cm^2$ in two cold-zone areas and 0.25 and 0.97 $\mu g/cm^2$ in two hot-zone areas.

These very low concentrations of beryllium on the cold-leg surfaces of the Inconel loop indicate that the tendency for beryllium metal to undergo temperature-dependent mass transfer under these test conditions is very slight.

BERYLLIUM-SODIUM-HASTELLOY B SPACER TESTS

E. E. Hoffman

Tests have been performed to study the compatibility of Hastelloy B and beryllium in sodium as a function of their distance of separation. The spacing distances employed were 0, 5, 20, 50, and 100 mils. After a 1000-hr test with static sodium at 1200°F, the extent of alloying was observed to be quite similar to that experienced with Inconel, as might be expected, since Hastelloy B and Inconel are both nickel-base alloys. Drillings were taken from the surfaces of the various Hastelloy B specimens, and the beryllium concentrations on the surface of each specimen are as follows:

Distance Between Hastelloy B and Beryllium (mils)	Beryllium Concentration (10^{-6} g/cm^2)
0	8,800
5	6.3
20	1.06
50	0.63
100	0.74

The microscopic appearance of this interaction may be seen in Figs. 26 and 27. Direct contact between beryllium and Hastelloy B (see Fig. 26) resulted in the formation of various extremely hard and brittle phases on the surface of the Hastelloy B specimen. All of these phases have not been identified as yet, but several of them are thought to be Be-Ni intermetallics similar to those found in tests of Inconel in contact with beryllium.[3] Figure 27 shows the extent of transfer of beryllium to the surface of a Hastelloy B specimen when the two materials are separated by a 20-mil sodium gap. The very fine precipitate along the surface is thought to be a Be-Ni compound. From these results, it appears that when in the presence of sodium at 1200°F for long periods of time, beryllium and Hastelloy B surfaces must be separated by more than 20 mils if extensive alloying is to be avoided.

INCONEL LOOP EXPERIMENT WITH BOILING SODIUM

E. E. Hoffman

The results from a test of an Inconel loop which contained boiling sodium and which was terminated after 400 hr because of a pipe failure have been previously reported.[4] Another loop has been operated under similar thermal conditions. The test was conducted under slight vacuum so that the sodium would boil at approximately 1500°F. This loop experiment was terminated after 1000 hr. In the previous test of 400-hr duration, no mass-transferred crystals were detected in the cold trap of the condenser line, but heavy intergranular cracking to a depth of 50 mils was detected in some areas. In the recent test, macroscopically visible quantities of mass-transferred crystals were detected in the cold trap (see Fig. 28).

The intergranular cracks and the deposit of mass-transferred crystals which occurred in the cold trap of this loop are shown in Fig. 29. Various sections from the condenser line were examined metallographically, and the extent of attack and of intergranular cracking was similar to that which was found in the 400-hr test. In the hottest section of the condenser pipe, the attack extended to a depth of 1 to 2 mils and was in the form of small subsurface voids. No intergranular cracking was detected in the hottest and coolest sections of the condenser pipe. However, cracks were found

[3] E. E. Hoffman *et al.*, *ANP Quar. Prog. Rep. March 10, 1955*, ORNL-1864, p 85, Fig. 6.20.

[4] E. E. Hoffman *et al.*, *Met. Semiann. Prog. Rep. Oct. 10, 1955*, ORNL-1988, p 10.

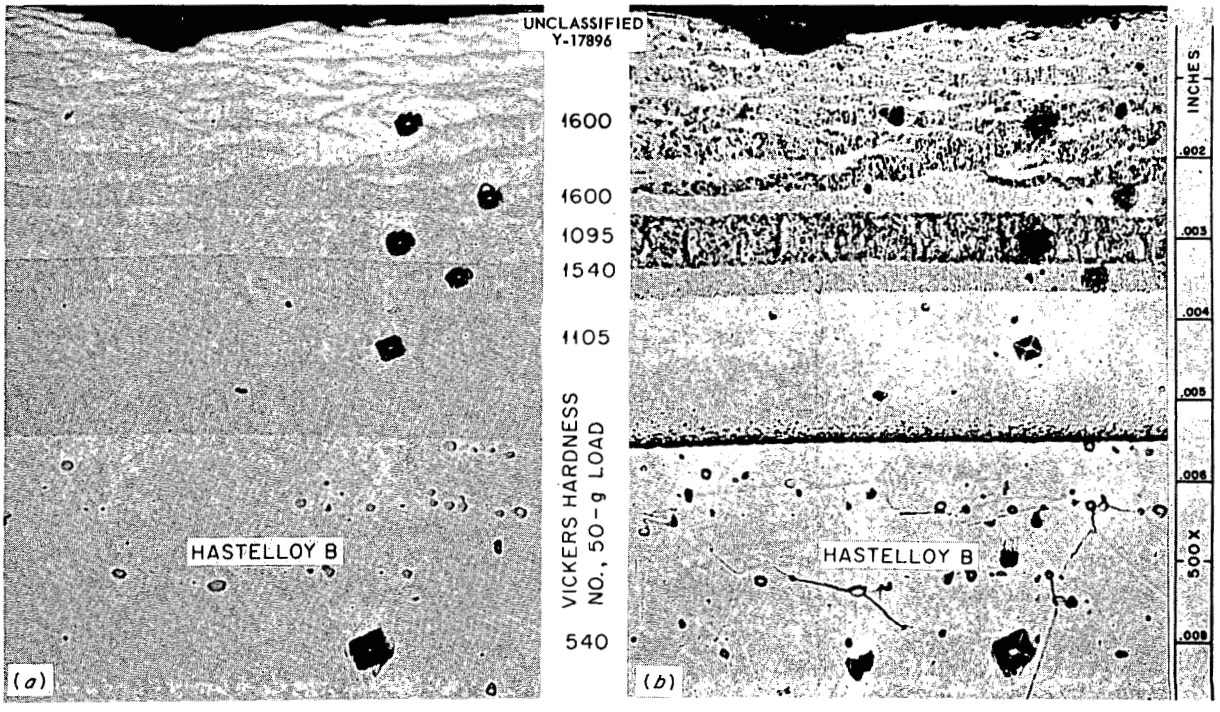

Fig. 26. Edge of Hastelloy B Specimen Which Was in Direct Contact with Beryllium and Was Exposed for 1000 hr to Sodium at 1200°F. (*a*) Unetched. (*b*) Cathodic etch. 500X. Reduced 19%. (Secret with caption)

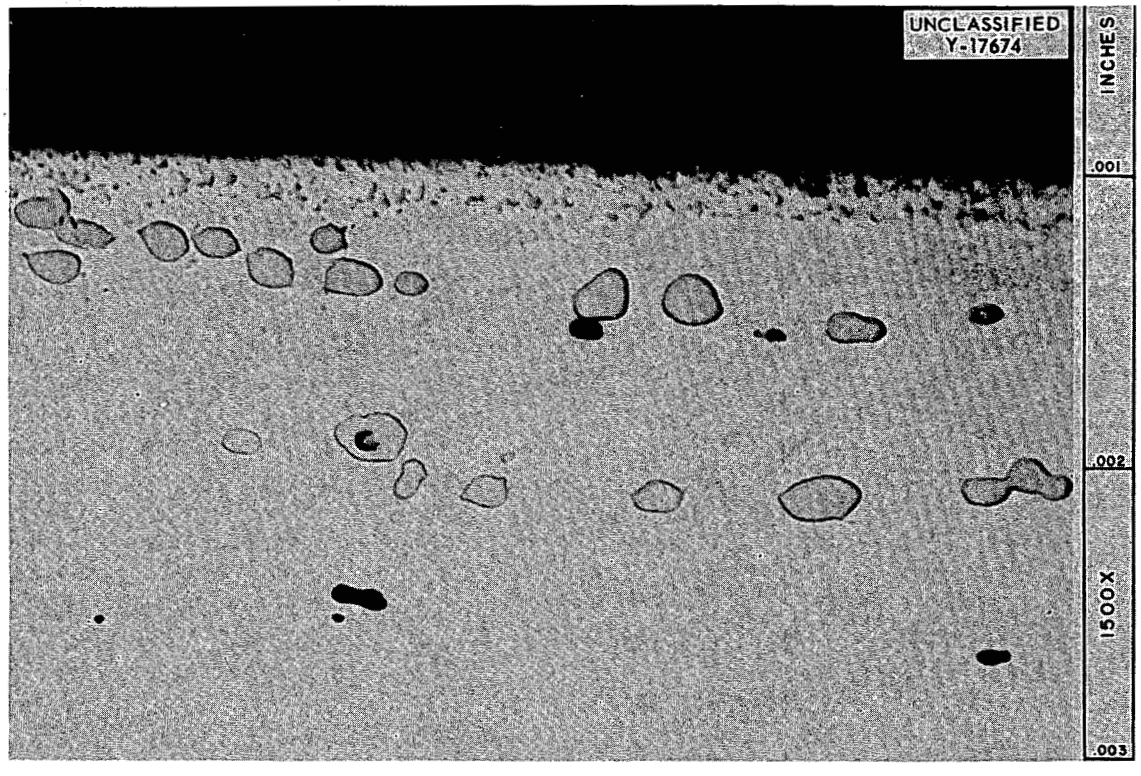

Fig. 27. Edge of Hastelloy B Specimen, Separated from a Beryllium Specimen by a 20-mil Space, After 1000-hr Exposure to Sodium at 1200°F. Note the very fine precipitate along the surface; this is believed to be a beryllium-nickel-intermetallic compound. Unetched. (Secret with caption)

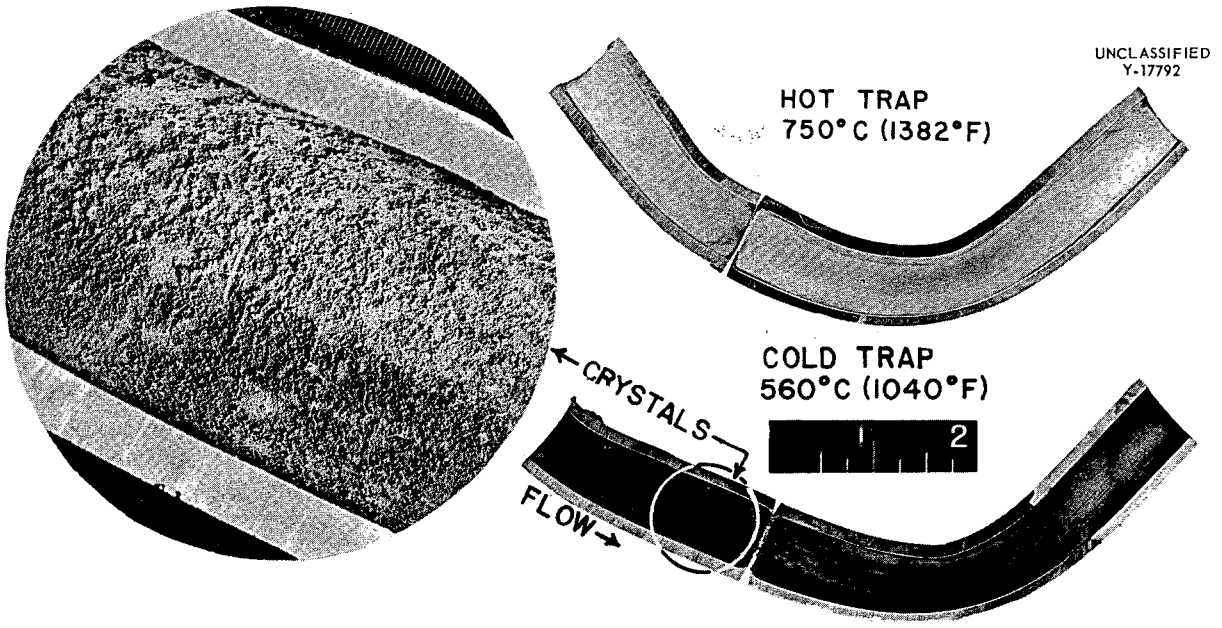

Fig. 28. Inconel Loop No. 3 in Which Sodium Was Boiled for 1000 hr. Note metallic-crystal deposition which occurred on the surface of the cold-trap wall. (See Fig. 29.)

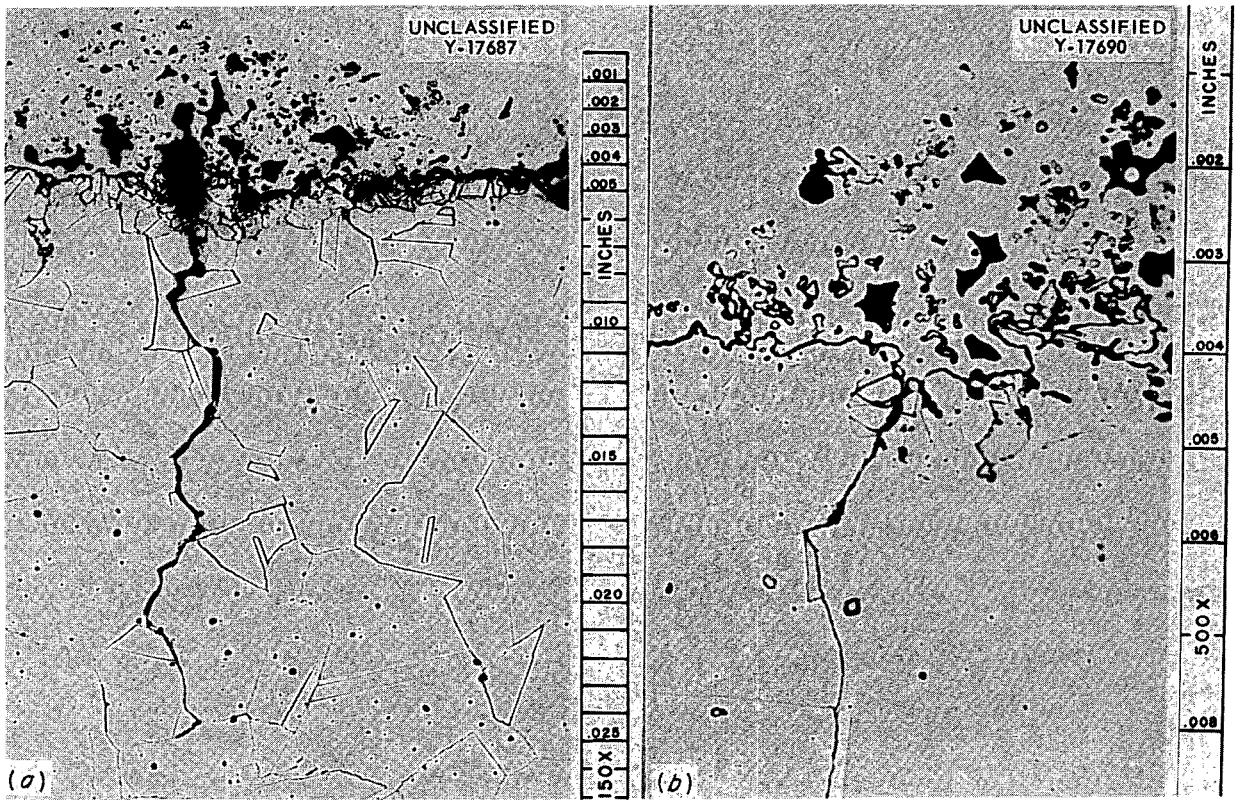

Fig. 29. Wall of Cold Trap from Condenser Section of the Inconel Loop Described in Fig. 28. (*a*) Intergranular cracking and mass-transferred material. (*b*) Enlarged view of the mass-transferred material. Specimens nickel-plated following the test. Etchant: aqua regia. 150X. Reduced 2%.

in the straight section which connected the hot and cold traps; the maximum depth of this cracking was approximately 25 mils, as compared to 50 mils in the earlier 400-hr test. In the areas where cracks were detected, the temperatures varied from 1150 to 1325°F, and metallographic examination indicates that a brittle grain-boundary phase is present in these areas. Periodic thermal excursions caused by the condensing sodium led to severe thermal stresses in the pipe walls which apparently caused the cracks to propagate.

TYPE 348 STAINLESS STEEL LOOP EXPERIMENTS WITH BOILING SODIUM

E. E. Hoffman

Three type 348 stainless steel loops have been operated with boiling sodium for various lengths of time. Type 348 stainless steel is similar in composition to type 347 stainless steel except that the carbon content of type 348 is higher. Each test was terminated before the scheduled shutdown time of 1000 hr because of leaks which developed in various locations in the system. As fabrication techniques improved, the loops operated for longer periods of time: 108, 316, and 740 hr. The tests were run in order to study mass transfer by sodium in a stainless steel system in which the oxygen content of the sodium is held to a very low value and in order to compare the results with those obtained in a similar Inconel system.

The loop as originally designed (for testing Inconel) is shown in a previous report.[5] The design has been modified, and the type used in the work now being reported is shown in Fig. 30. An overflow reservoir and a sampling port were incorporated into the receiver in order to permit samples of the freshly condensed sodium to be taken periodically so that the oxygen concentration could be checked during the course of the run. The nickel sample bucket was lowered through the open valve, and a sample of sodium was taken from the reservoir. The sample bucket was then withdrawn from the loop (a purified helium atmosphere being maintained over the sample) and transferred to a pyrex tube where it was sealed off under vacuum. Although a limited number of samples have been taken to date, the oxygen concentration of the sodium has been found to be approximately 20 ppm; a portion of this may be attributed to contamination during sampling.

The condenser sections of the three loops in this series were sectioned following termination of the tests, and no mass-transferred crystals were found in the cold traps. This is not surprising, since iron-base alloys (stainless steels) have been found to be less susceptible to mass transfer by sodium than nickel-base alloys (e.g., Inconel) in both thermal-convection-loop and pump-loop systems. Heavy intergranular cracking up to 40 mils in depth was detected in the condenser section of each of the loops. Figure 31 is a photomicrograph of a section of the loop which operated for 740 hr.

TYPE 316 STAINLESS STEEL THERMAL-CONVECTION LOOP EXPERIMENTS WITH SODIUM

E. E. Hoffman

Two type 316 stainless steel thermal-convection loops filled with sodium have been tested for 1000 hr with hot- and cold-leg temperatures of approximately 1630 and 1050°F, respectively. The loops were loaded with sodium from the same fill pot, and the test conditions were similar except that a diffusion-type cold trap was placed at the bottom of the cold leg of one loop. Air was blown on one section of the cold leg of each loop so as to induce a very sharp temperature gradient. The tests were performed in order to determine the effect of a diffusion cold trap on the amount of mass transfer observed in a stainless steel system containing sodium. Samples of the sodium used to fill the loops were taken and contained 20 ppm oxygen by analysis. Samples of the sodium were also taken from the loops after the tests: that from loop 26 (no cold trap) contained 25 ppm oxygen, while that from loop 27 (diffusion cold trap) contained 35 ppm oxygen. The difference is attributed to contamination during the sampling operation; however, by present standards, the sodium in both loops was considered to be quite low in oxygen content. The coldest section of each loop was removed after test, and visual inspection revealed a small amount of metallic crystals in each. Although neither loop showed an appreciable amount of crystals, the cold leg which did not have a cold trap definitely had a greater quantity present on its surface. The amount of crystals was insufficient to have an analysis performed.

[5] E. E. Hoffman *et al.*, *Met. Semiann. Prog. Rep. Oct. 10, 1955*, ORNL-1988, p 11, Fig. 5.

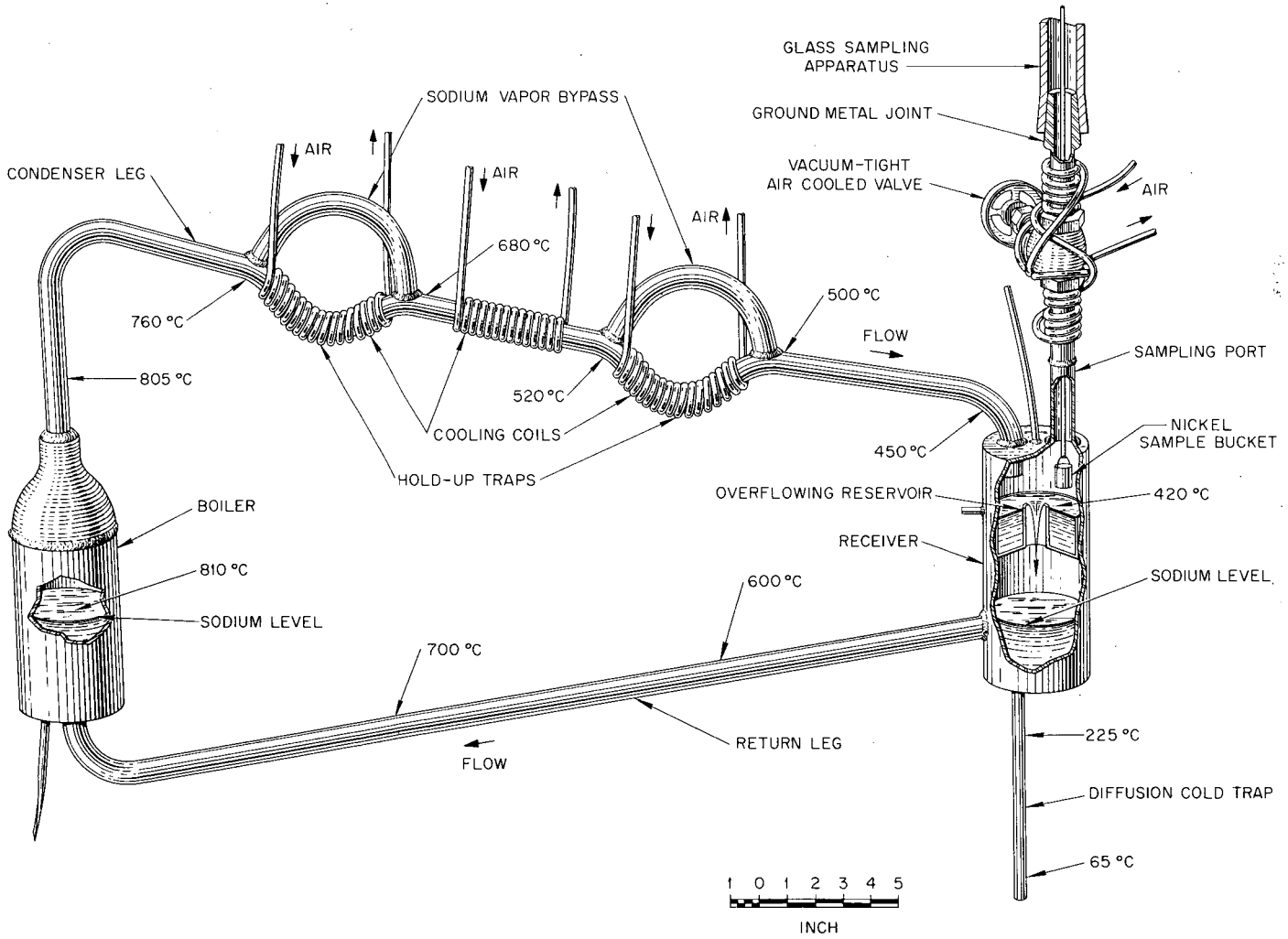

Fig. 30. Stainless Steel Loop for Corrosion Testing with Boiling Sodium.

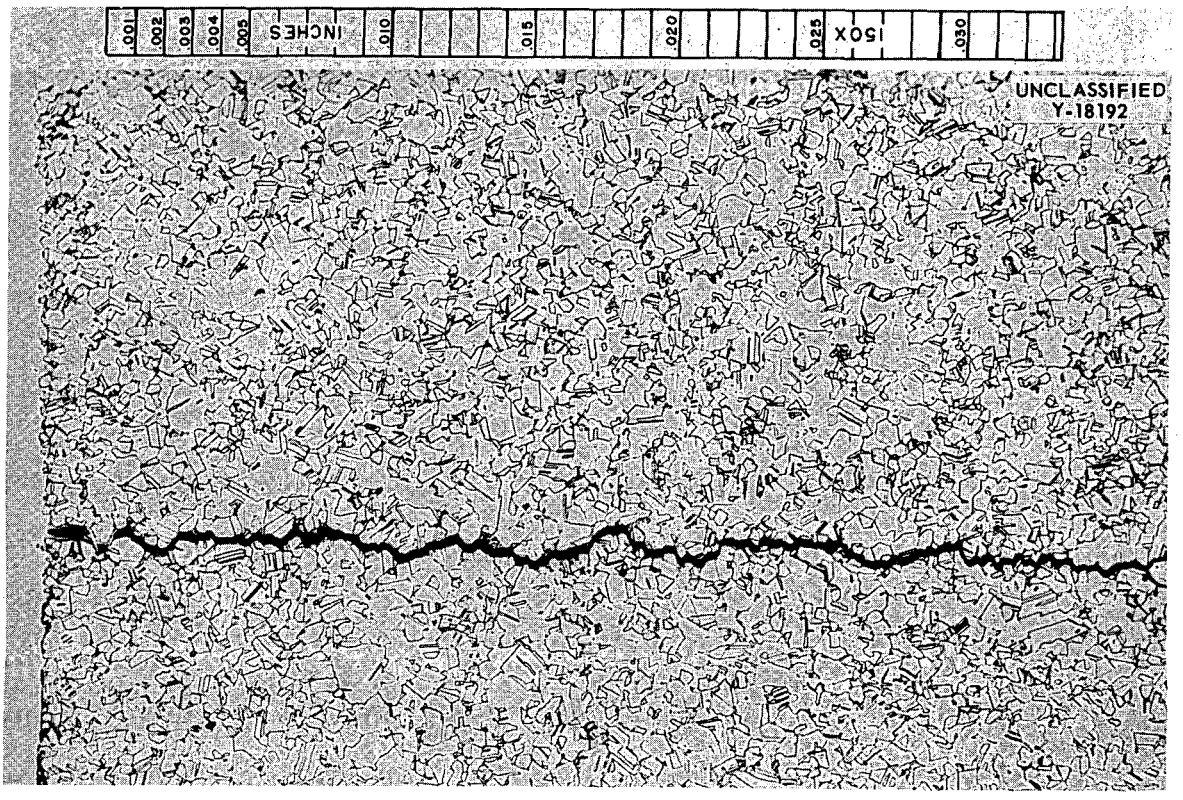

Fig. 31. Wall of Type 348 Stainless Steel Loop Taken from Straight Section of Condenser Pipe Located Midway Between the Holdup Traps (see Fig. 30). Note intergranular cracking. Etchant: aqua regia.

In a similar test of an Inconel thermal-convection loop containing sodium, in which the hot leg reached a maximum temperature of 1500°F (130°F less than in the stainless steel loop tests), the amount of mass transfer observed was approximately ten times that observed in either of the stainless steel tests. The results of metallographic examination are listed in Table 16. These results may be summarized as follows: (1) the attack in the hottest section of loop 26 (without diffusion cold trap) was deeper than that detected in loop 27 (diffusion cold trap) (see Figs. 32 and 33); (2) nickel was preferentially leached from the hot-zone walls by the sodium; (3) deep intergranular cracking was found in the coldest section of the loop with no cold trap, whereas no cracks were observed in the cold leg of the loop which had a diffusion cold trap (see Fig. 33b).

CATHALLOY A-31 TESTED IN STATIC SODIUM

R. Carlander

A 6-in. tube of Cathalloy A-31 (4% W–96% Ni) was half-filled with sodium under a helium atmosphere and tested statically at 150°F for 100 hr. No attack occurred in either the vapor or bath zones of the capsule.

CORROSION TESTS OF ALFENOL IN VARIOUS MEDIA

E. E. Hoffman

Specimens of Alfenol (84% Fe–16% Al), submitted by The Glenn L. Martin Co., have been tested statically at 1500°F in fused-fluoride mixture, lead, lithium, and sodium for 100 hr. Since no Alfenol container tubes were available, Inconel was used as the container material for

Fig. 32. Type 316 Stainless Steel Thermal-Convection Loop No. 26 in Which Sodium Was Circulated but Which Did Not Have a Diffusion Cold Trap. (*a*) Hot leg, 1630°F. (*b*) Cold leg, 1050°F. Note irregularity of hot-leg surface and deep intergranular cracking which occurred in cold leg. Etchant: aqua regia. 500X. Reduced 16.5%.

Fig. 33. Type 316 Stainless Steel Thermal-Convection Loop No. 27 in Which Sodium Was Circulated and Which Had a Diffusion Cold Trap to Lower the Oxygen Content of the Sodium. (*a*) Hot leg, 1630°F. (*b*) Cold leg, 950°F. Note austenite-to-ferrite phase transformation which occurred on surface of hot leg and which was due to preferential leaching of nickel. Etchant: aqua regia. 500X. Reduced 18%.

TABLE 16. RESULTS OF METALLOGRAPHIC EXAMINATION OF SECTIONS FROM TYPE 316 STAINLESS STEEL THERMAL-CONVECTION LOOPS IN WHICH SODIUM WAS CIRCULATED FOR 1000 hr

Section Examined	Operating Temperature of Section (°F)	Metallographic Results	
		Loop 26 – No Cold Trap	Loop 27 – Diffusion-Type Cold Trap
Top of hot leg	1600	Irregular surface attack to a depth of ½ to ¾ mil	Irregular surface attack to a depth of ½ to ¾ mil
Middle of hot leg	1630	Irregular surface attack to a depth of 3 to 3½ mils; on account of preferential leaching of nickel, surface transformed from austenite to ferrite to a depth of ¼ to ½ mil	Attack to a depth of less than 1 mil; on account of preferential leaching of nickel, surface transformed from austenite to ferrite to a depth of ¼ to ½ mil
Middle of cold leg	1330	Attack to a depth of less than ½ mil	Intergranular attack to a depth of ½ to 1 mil
Bottom of cold leg*			
Loop 26	1050	Heavy precipitation of unidentified phase in grains and grain boundaries; quite a few intergranular cracks originating at exposed surface and extending to depths of 10 to 20 mils	Heavy precipitation in exposed grains and grain boundaries; no intergranular cracks detected
Loop 27	950		

*Cooled by air blast.

all tests. The results of these tests were as follows:

1. The specimen tested in $NaF-ZrF_4-UF_4$ (53.5-40-6.5 mole %) was covered with black crystals after the test and showed a 30% increase in weight. The crystals were analyzed and found to be UF_3. The specimen was attacked throughout its thickness by way of the grain boundaries. It appears that the attack was most vigorous in aluminum-rich areas, aluminum being thermodynamically unstable in the molten salt (see Fig. 34).

2. In the test with lead, no weight-change data were taken because particles of lead adhered to the specimen. Metallographic examination revealed attack only in a few scattered areas to a depth of 0.5 mil.

3. The specimen tested in lithium was attacked throughout the grain boundaries, which were apparently aluminum-rich regions. Gentle tapping caused the specimen to break up into individual grains.

4. The specimen tested in sodium lost only 16 mg (0.009%) during the test, and metallographic examination revealed no attack.

[6]E. E. Hoffman *et al.*, *ANP Quar. Prog. Rep. Sept. 10, 1954*, ORNL-1771, p 83.

CORROSION OF SPECIAL ALLOYS IN CONTACT WITH DEHYDRATED SODIUM HYDROXIDE

E. E. Hoffman

Quite a few capsule tests have been conducted in the past on commercially available alloys in static sodium hydroxide at elevated temperatures. After reviewing the past results, G. P. Smith of this division requested that additional tests be performed on nine special alloys. Recent work by M. E. Steidlitz and G. P. Smith has shown that "A" nickel does not exhibit mass transfer in a nonisothermal system provided the maximum temperature in the system does not exceed approximately 1100°F. Pure nickel unfortunately has relatively poor high-temperature strength, and it would be desirable to use a nickel-base alloy, if possible, as a container material for high-temperature sodium hydroxide. In order to increase the severity of the attack the alloys selected (see Table 18) were tested at 1500°F, thereby making less difficult the selection of an alloy for future study in a dynamic system at a lower temperature. Several iron-base alloys were tested in order to compare their corrosion resistance with that of similar commercial alloys.

Nine special alloys were cast and extruded into 1-in.-dia rods by the Fabrication Group. Two capsules, two closure caps, and two specimens were machined from each extruded rod. Duplicate tests were run on all alloys except the 60% Ni–20% Mo–20% Fe alloy. The specimens were weighed before and after the test in order to obtain weight-change data. The sodium hydroxide used in this investigation was dehydrated by heating it at 300°C under vacuum (less than 10 μ) for 6 hr; after which time, the temperature was raised to 360°C and maintained for 20 hr. The individual corrosion-test capsules were placed in a protective capsule and then placed in a furnace where they were held at 1500°F for 100 hr.

The test results are listed in Table 19. Figure 35 shows the 90% Ni–10% Mo alloy after the test; this alloy was the most corrosion resistant of the alloys in this group. On the basis of these tests, the following conclusions may be drawn: (1) iron-base alloys, in general, have poor resistance to corrosion by sodium hydroxide at 1500°F, the resistance decreasing with increasing iron content; (2) additions of chromium tend to decrease the corrosion resistance of the iron-base alloys, whereas additions of nickel are beneficial; (3) nickel-base alloys have good resistance to the hydroxide provided the nickel content is above 80%; (4) the 90% Ni–10% Mo alloy was found to be attacked less than the 85% Ni–15% Mo alloy. Further tests are planned on an alloy similar to the 90% Ni–10% Mo alloy, since the present results indicate that the corrosion resistance of this latter alloy is much better than that of any of the other alloys with good high-temperature strengths which have been tested in the past.

TABLE 18. COMPOSITION OF SPECIAL ALLOYS TESTED IN SODIUM HYDROXIDE

Nominal Composition (wt %)	Elemental Analyses (wt %)							
	Ni	Fe	Mo	Cr	C	Si	Mn	S
85 Ni–15 Mo	86.07		15.09		0.021	0.030	<0.002	<0.0001
90 Ni–10 Mo	89.60		10.23		0.014	0.040	<0.0020	0.0002
80 Ni–10 Mo–10 Fe	78.48	10.14	9.60		0.010	0.040	<0.002	0.0006
60 Ni–20 Mo–20 Fe	59.44	20.38	19.53		0.018	0.040	<0.002	0.0003
70 Ni–15 Fe–15 Mo	71.29	13.83	14.31		0.013	0.023	<0.017	<0.0001
80 Fe–20 Cr		80.91		19.14	0.017	0.060	<0.002	0.021
80 Fe–10 Cr–10 Ni	10.40	79.60		9.93	0.018	0.030	<0.002	0.012
74 Fe–18 Cr–8 Ni	8.11	73.5		18.70	0.022	0.030	<0.002	0.019
60 Fe–20 Cr–20 Ni	19.88	61.43		19.66	0.005	0.040	<0.002	0.013

TABLE 19. CORROSION OF SPECIAL ALLOYS AFTER 100 hr IN STATIC SODIUM HYDROXIDE AT 1500°F

Test No.	Alloy Composition (wt %)	Weight Change (g/cm^2)	Metallographic Notes
		Nickel-Base Alloys	
1	85 Ni–15 Mo	–0.011	Scattered subsurface voids to a depth of 1.5 to 2.5 mils
2	85 Ni–15 Mo	–0.010	Scattered subsurface voids to a depth of 2 to 3 mils
3	90 Ni–10 Mo	–0.005	Attack to a depth of less than ½ mil
4	90 Ni–10 Mo	–0.005	Same as above
5	80 Ni–10 Mo–10 Fe	–0.006	A few scattered subsurface voids to a depth of 1 mil
6	80 Ni–10 Mo–10 Fe	–0.005	Same as above, except that one corner of specimen heavily attacked to a depth of 3 mils
13	60 Ni–20 Mo–20 Fe	–0.003	Very small subsurface voids to a depth of 4 to 5 mils in scattered areas
16	70 Ni–15 Fe–15 Mo	–0.021	Attack in the form of small subsurface voids to a depth of 3 to 4 mils
17	70 Ni–15 Fe–15 Mo	–0.020	Same as above
		Iron-Base Alloys	
7	80 Fe–20 Cr	0.796	Specimen very heavily attacked; thick oxidation-type corrosion product with thin metallic layers at surface; thickness of unattacked material decreased from 250 to 216 mils
8	80 Fe–20 Cr	0.913	Same as above
9	80 Fe–10 Cr–10 Ni	0.045	Heavy oxidation-type attack to a depth of 5 to 6 mils
10	80 Fe–10 Cr–10 Ni	0.042	Same as above
11	74 Fe–18 Cr–8 Ni	0.104	Heavy oxidation-type attack to a depth of 11 mils
12	74 Fe–18 Cr–8 Ni	0.112	Heavy attack to a depth of 12 to 13 mils
14	60 Fe–20 Cr–20 Ni	0.047	Uniform attack to a depth of 5 mils
15	60 Fe–20 Cr–20 Ni	0.032	Uniform attack to a depth of 5.5 mils

RARE-EARTH OXIDES AND INCONEL IN STATIC SODIUM

W. H. Cook

In the considerations pertaining to the use of rare-earth oxides as possible control-rod materials for the ART, it was suggested that sodium be used as the heat-transfer medium to aid in the cooling of the control-rod materials. It was proposed that Inconel be used as the container material for the sodium and the rare-earth oxides. In consequence of these proposals, tests have been conducted on some rare-earth oxides in order to investigate their corrosion resistance to sodium and to determine what effects, if any, occur on their Inconel containers.

One specimen[11] of Sm_2O_3 with a density of 5.88 g/cc and an apparent porosity of 25.4% has been tested for 1000 hr in static sodium at 1500°F in an Inconel capsule. Two specimens from a ceramic body with a density of 6.58 g/cc (apparent porosity, not determined)[11] and consisting of a mixture of rare-earth oxides have been similarly tested, one for 500 hr and the other for 1000 hr; the body, fabricated from a commercially available powder known as Lindsay Mix,[12] had 63.8 wt % Sm_2O_3, 26.3 wt % Gd_2O_3, and the remaining percentage primarily other rare-earth oxides. The results of the tests indicated negligible corrosion attack by the sodium on the three specimens and on their Inconel capsules after 1000 hr, but there may have been some reduction in their strength.

The weight changes and dimensional changes of the three specimens were all positive, as one might expect with porous materials, and were less than 0.5%. The original buff color of the specimens had been altered to gray-black, but this was the only macroscopic change (see Figs. 46 and 47); it was found that the gray-black color extended throughout the specimens and is taken as evidence that the sodium completely penetrated the specimens, probably along the pore spaces.

Powder x-ray diffraction patterns of untested and pieces of the Sm_2O_3 and of the two Lindsay Mix specimens did not reveal any reaction products. Chemical analyses of the sodium baths indicated negligible quantities of chromium, nickel, iron, or the rare earths, which supports the conclusion that the attack on the rare-earth oxides and on the Inconel capsules was negligible. Metallographic polishing and examination of the rare-earth-oxide specimens, untested and tested, indicated that the tested specimens may have been slightly weakened by the tests; however, there was no

[11]The Ceramics Section of the Metallurgy Division fabricated the specimens and determined the density and apparent porosity.

[12]Lindsay Light and Chemical Co., West Chicago, Ill.

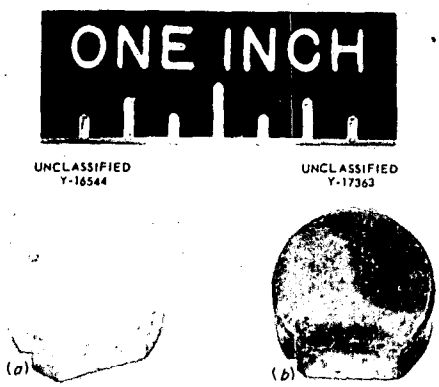

Fig. 46. Samarium Oxide (a) Untested and (b) After Exposure for 1000 hr to Static Sodium at 1500°F.

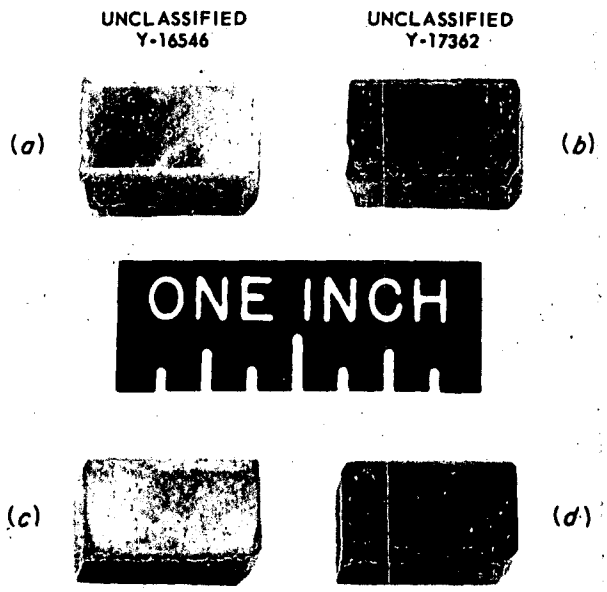

Fig. 47. Specimens Composed of 63.8% Sm_2O_3 Plus 26.3% Gd_2O_3, with Remaining Percentage Primarily Other Rare-Earth Oxides, and Tested in Static Sodium at 1500°F. Specimens (a) before and (b) after 500-hr test. Specimens (c) before and (d) after 1000-hr test.

microscopically visible attack (see Fig. 48).

Metallographic examination of the Inconel capsules that contained the Lindsay Mix specimens revealed only slight surface roughening in spots on the inner walls. There was no surface roughening of the capsule in the Sm_2O_3 test. Spectrographic analyses of the inner surfaces of the three test capsules did not reveal any rare earths. The over-all results from the two Lindsay Mix tests were not significantly different even though one test period was twice as long as the other.

APPARENT POROSITY OF A POROUS RARE-EARTH-OXIDE BODY TO WATER AND TO LIQUID SODIUM

W. H. Cook

The corrosion resistance to liquid sodium shown by the Lindsay Mix body with a density of 6.58 g/cc prompted further tests. These tests were designed to approximate, more closely, expected operating conditions and to use a Lindsay Mix body with the structural characteristics proposed for actual applications in the ART. The purposes of the tests were to determine (1) the relationship between the apparent porosity of the Lindsay Mix body to water versus its apparent porosity to molten sodium and (2) the resistances of the body and of Inconel to corrosion by sodium when separated by only a short distance (approximately 0.05 in.). For these tests, the Ceramics Laboratory fabricated a porous Lindsay Mix body (a hollow cylinder nominally 0.9 in. OD × 0.5 in. ID × 1 in. long) with a density of 3.53 g/cc and an apparent porosity to water of 53.5%. This body had an apparent porosity of 52% to sodium after having been exposed for 100 hr to static sodium at 1300°F under vacuum. Also, it had been slightly weakened; its Moh hardness was changed by the test from 3 to 2.

In order to determine the apparent porosity of the body to sodium, the sodium was allowed to cool and solidify around the body at the end of the 100-hr test period, and the test capsule was transferred to a dry box filled with helium. The test capsule was opened; the excess sodium was removed from the surfaces of the body with plastic scrapers; and the body was weighed. The absorbed sodium was then removed from the body by vacuum distillation, and the body was again weighed. By use of the latter weight, the body density of 3.53 g/cc, the weight of the absorbed sodium, and a sodium density of 0.951 g/cc (at 97.8°C, the melting point of sodium), the apparent porosity of the body to sodium was calculated.

In order to complete the accumulation of information from this test, the sodium bath has been submitted for chemical analysis, and the Inconel that

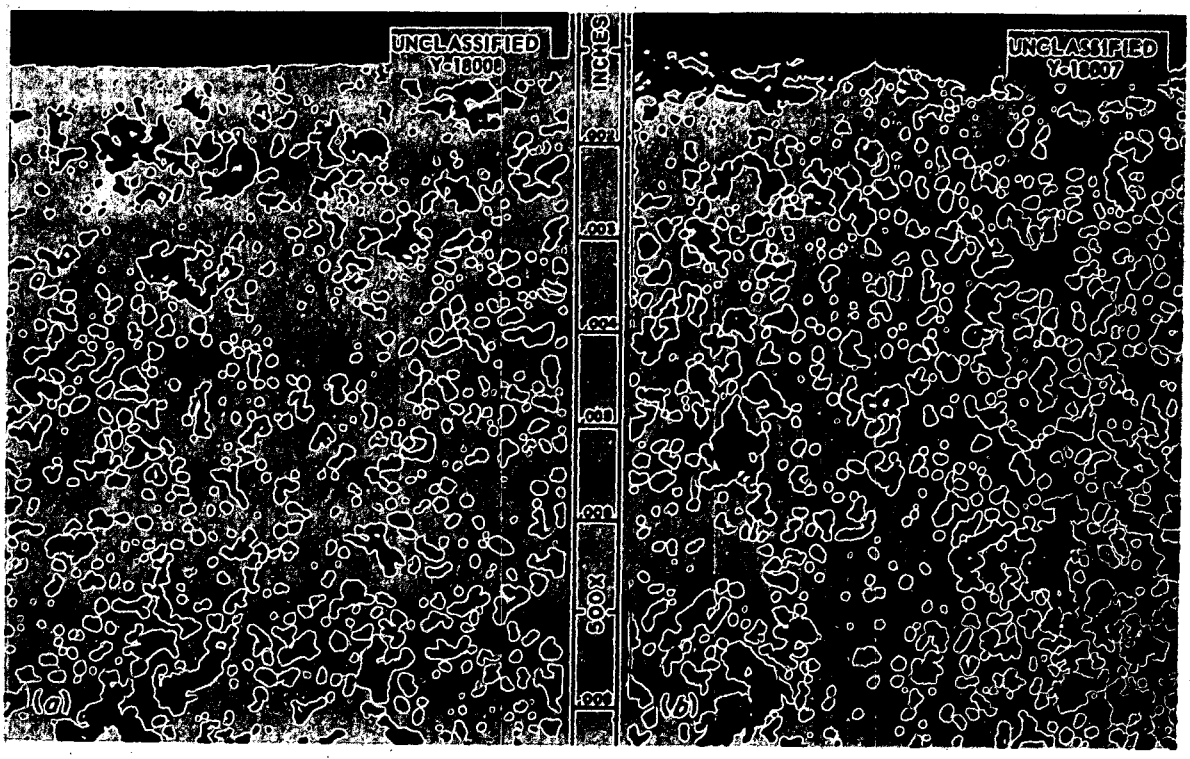

Fig. 48. Specimens of Rare-Earth-Oxide Body (63.8% Sm_2O_3–26.4% Gd_2O_3–Balance, Primarily Other Rare-Earth Oxides) (a) Untested and (b) After Exposure for 500 hr to Static Sodium at 1500°F. Unetched.

was adjacent to the body will be examined metallographically.

Since the 100-hr test was relatively short, similar tests are planned which will be of 1000 hr duration or longer so as to better evaluate the present concept that ceramics with the same chemical compositions become less corrosion resistant as their porosities increase.

DYNAMIC CORROSION

J. H. DeVan E. A. Kovacevich

FORCED-CIRCULATION LOOPS

J. H. DeVan

Loop Design

Several Inconel forced-circulation loops were constructed and operated by the Aircraft Reactor Engineering Division at the request of the Metallurgy Division to study the effect of high velocities and flow rates on corrosion by fluoride salts. The first pump-loop design for these studies incorporated, as reported previously,[1] a coiled hot leg heated by direct resistance. This heating method was found to be unsatisfactory for corrosion studies because of temperature differences across the bends in the coil. Consequently, an improved design, presented in Fig. 50, was developed in which resistance heating is accomplished entirely in straight sections of tubing. An alternate arrangement, shown in Fig. 51, using a gas-fired heat source, has also been employed in order to provide a comparison of heating methods. Both types of loop designs were tested and examined, and the results to date are summarized below.

Effect of Time on Depth of Corrosion. – A series of Inconel loops having identical temperature conditions and loop configurations (Fig. 50) were tested in NaF-ZrF_4-UF_4 (50-46-4 mole %) for various durations of time so as to determine the effect of this variable on fluoride corrosion. Operating conditions for the series are as follows:

Isothermal time, hr	24
Cleaning time, hr	2
Maximum fluoride temperature, °F	1500
Maximum wall temperature, °F	1615–1635
ΔT, fluoride temperature gradient, °F	200
Isothermal temperature, °F	1300
Cleaning temperature, °F	1310
Reynolds number	10,000
Velocity, fps	6.5
No. 1 heater length, ft	6.4
No. 2 heater length, ft	5.6
Total heater length, ft	12
Cooler length, ft	16
Total length, ft	50.5
Ratio of hot-leg surface to loop volume, $in.^{-1}$	1.50

A single loop was used for several tests in the series by replacing the two straight heating sections after each experiment. Those loops designated with a "4-" prefix represent one series in which the pump, the connecting lines, the cooling coil, and the hot bend were reused; whereas loops designated with a "5-" represent a second similar series. New cleaning and operating batches of fluorides were used in each loop test. The cleaning operation, to remove oxide films and other sources of contamination, was performed prior to the test by circulating a fluoride mixture for 2 hr at 1300°F. This mixture was then dumped and replaced by the operating charge, which was circulated isothermally for 24 hr before the temperature differential was applied. The attacks which occurred and the actual test times, during which the systems were operated under the temperature differential, are given below.

Loop No.	Operating Time (hr)	Maximum Attack (mils)
4-A	0	½
5-A	10	3
4-D(1)	20.5	3
4-B	50	3
4-C	100	3½
5-B	241	5
4-D(2)	500	5
5-C(2)	1000	7

The period of isothermal operation at 1300°F was intended to establish chemical equilibrium for that phase of fluoride corrosion associated with reduction of the impurities that are inherent in the fluorides. However, the depth of attack and the chromium concentration were quite low following this isothermal operation. This fact together with the rapid rate of attack during the first 10 hr of nonisothermal operation with a hot-leg temperature of 1500°F indicate either that equilibrium at the lower temperature was not reached or

[1] L. A. Mann, W. B. McDonald, and W. C. Tunnell, *ANP Quar. Prog. Rep. Dec. 10, 1954*, ORNL-1816, p 45, Fig. 3.4.

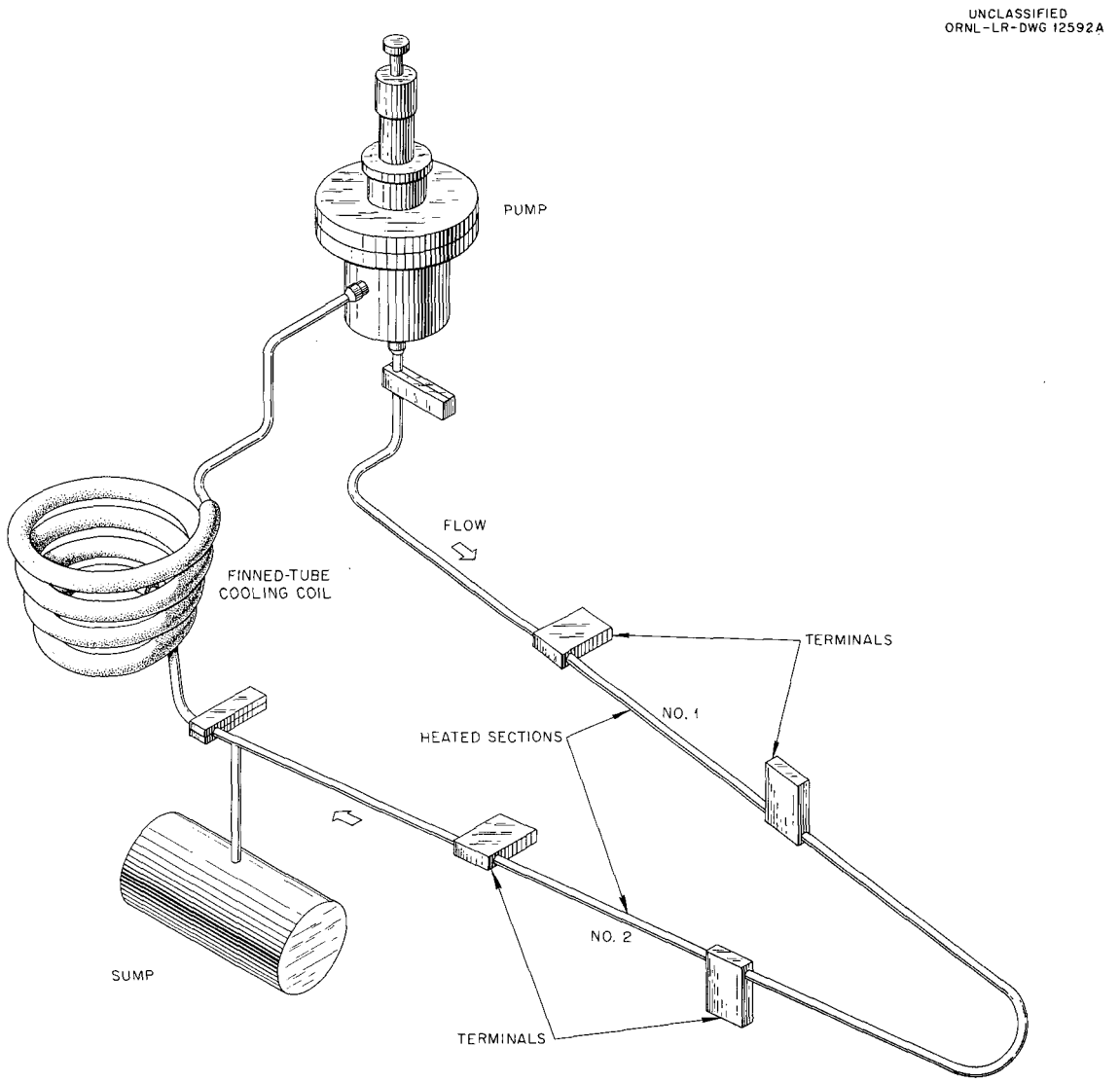

Fig. 50. Schematic Drawing of Fluoride-Fuel Forced-Circulation Loop with Straight Resistance-Heated Sections. (Secret with caption)

that equilibrium shifts rapidly with temperature. After the first 50 hr, the chromium content of the fluoride mixture remained constant, but the depth of attack increased, in confirmation of the mass-transfer data from thermal-convection loops. Beyond 50 hr, a plot of the depth-of-attack vs the time-of-test, shown in Fig. 52, appears to be linear with a slope of between 3 and 4 mils per 1000 hr of circulation. The change in attack with increasing operating time can also be seen in Fig. 53, which shows typical hot-leg sections after several operating time intervals.

Effect of Temperature on Depth of Attack. – The importance of wall temperature as a controlling factor in fluoride corrosion was noted in a previous report[2] in which the results from resistance-heated pump loops with heater sections in the form of coils were discussed. Temperature differences occurred across the bends of the coil, and the extent of attack on the inner radii was quite different from that on the outer radii of the bends,

[2]G. M. Adamson and R. S. Crouse, *ANP Quar. Prog. Rep. June 10, 1955*, ORNL-1896, p 83.

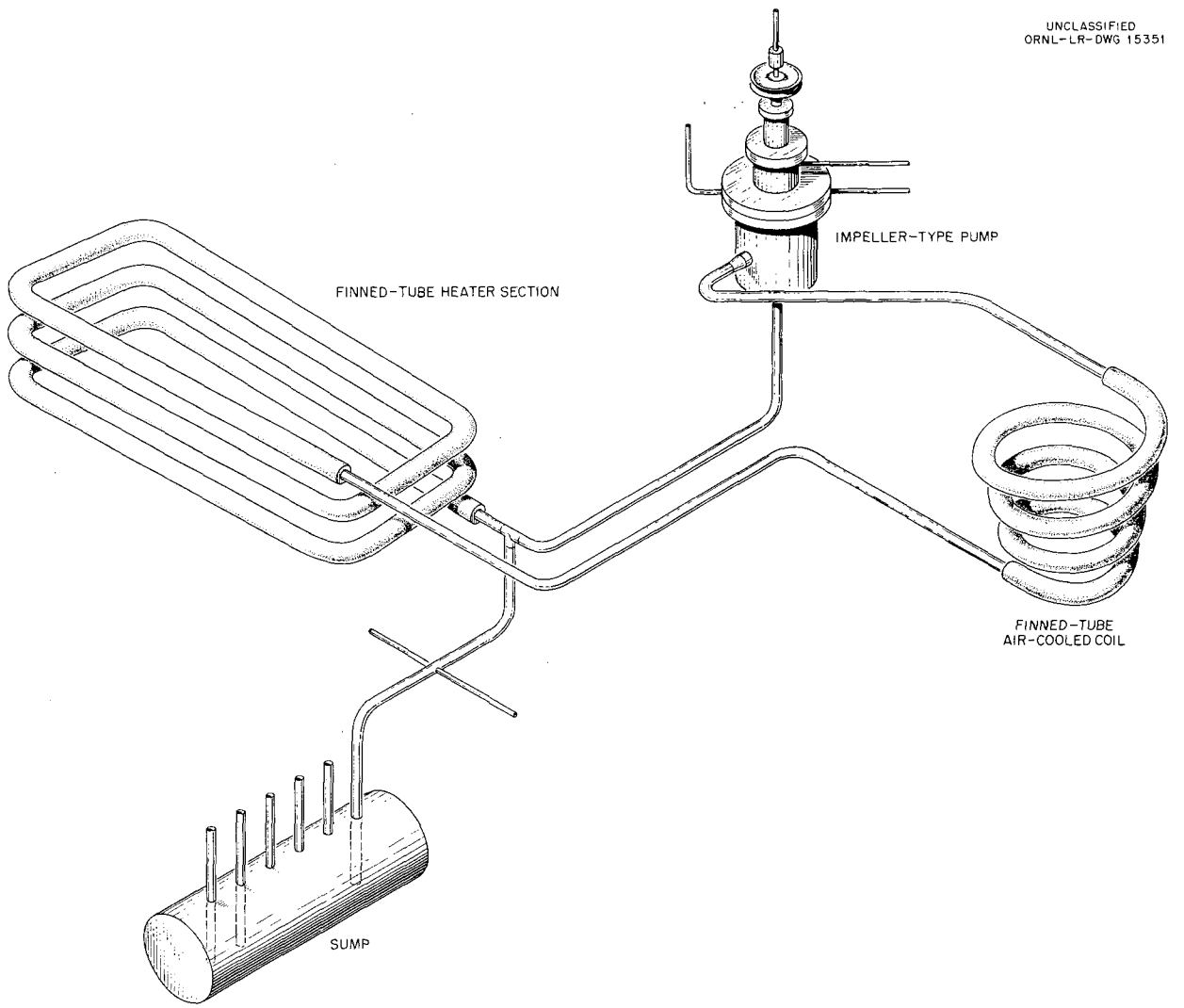

Fig. 51. Schematic Drawing of Gas-Fired Forced-Circulation Loop.

although the temperature of the bulk fluoride over any cross section was the same. A series of tests, now partially completed, was subsequently initiated in which the same bulk-fluoride-mixture temperatures were maintained for all the tests, but the fluid velocities and the distributions of heat to the hot legs were varied in order to change the maximum wall temperatures in the heated sections of the loops. Results obtained to date for this series, together with specific operating conditions, are shown in Table 24.

Gas-fired loop 4935-7, while it did not complete its scheduled operating period, illustrates qualitatively the effect of a high wall temperature (relative to a 1500°F maximum bulk-fluid temperature). This loop shows substantially more attack than two other gas-fired loops, 4935-2 and -5, which operated for longer periods but with maximum wall temperatures that were approximately 100°F lower. The effect of variation in flow rate (Reynolds number) has obviously been neglected in the above considerations; although on the basis of the agreement between attacks in thermal-convection loops and pump loops, this variable, over the ranges of these tests, apparently has little influence on corrosion results.

A similar increase in attack, as a function of wall temperature, was evidenced in a series of

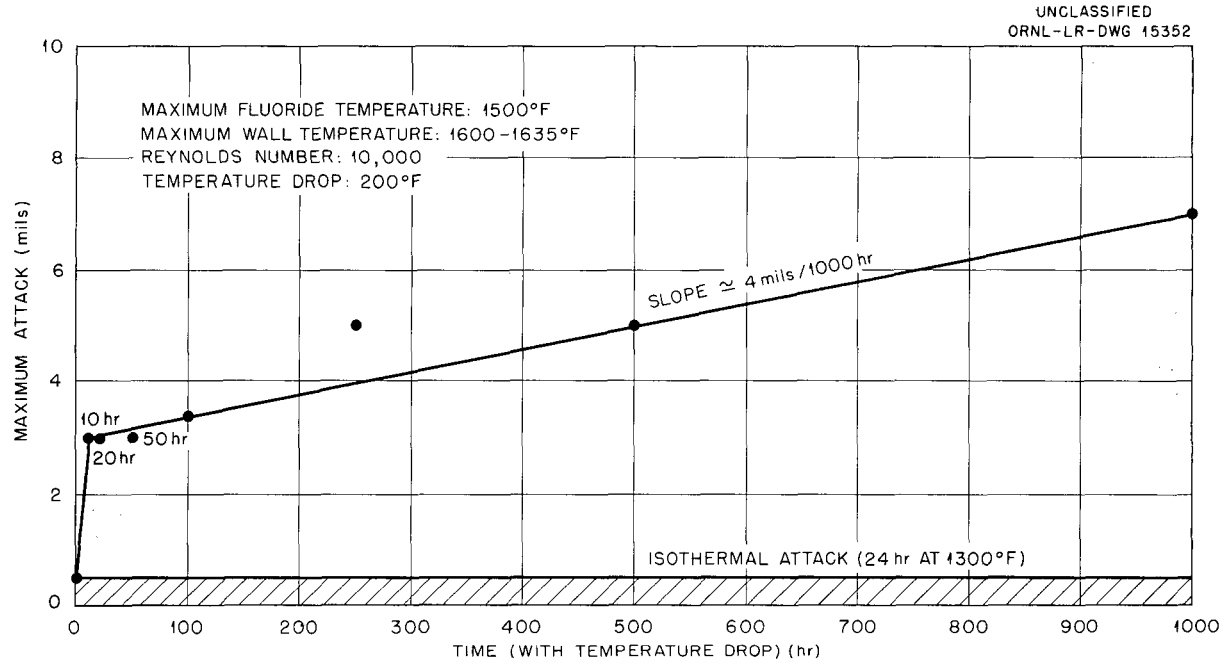

Fig. 52. Corrosion in Inconel Pump Loop as a Function of Time During Which Temperature Differential Was Applied. Time operated with temperature drop, 700 hr. (Secret with caption)

resistance-heated loops, shown in Table 24, which were operated with maximum wall temperatures ranging from 1550 to 1710°F. Maximum fluoride temperature was held constant at 1500°F for all tests. Attacks at the higher and lower extremes of wall temperatures are compared in Fig. 54 and may be seen to have increased considerably both in depth and intensity at 1710°F, as compared to 1550°F. The effect of a 1590°F wall temperature, as evidenced by loop 4950-5, is apparently close to that of the 1550°F wall temperature; although this can only be speculated, since the test at the former temperature was terminated after 640 hr (rather than the intended 1000 hr) because of a power failure.

The operation of loop 7425-41, in which fluid temperature was increased to 1650°F with an accompanying 1700°F maximum wall temperature, lends further support to the importance of maximum wall (or boundary-layer) temperature on the rate of attack in Inconel systems. The maximum attack, which occurred in this loop after 1000 hr, was 10 mils and was quite similar to that for loop 7425-43 (Table 24), which operated with the same maximum wall temperature but with the fluid at a maximum temperature of 1500°F. The amounts of chromium in solution at the two bulk-fluid temperatures, shown in Table 25, were also comparable.

Comparison of Heating Methods. – The results of both gas-fired and resistance-heated pump loops, which were discussed in the preceding section, indicate that the method of heating does not have a large effect on corrosion if other variables are held constant. As shown in Table 25, excellent correlation of attack was found between loops 4935-2 (gas fired) and 4950-2 (resistance heated), which were operated under similar conditions and with similar heater surface areas. Fair correlation is also seen on comparing gas-fired loop 4935-5 with resistance-heated loop 4950-5. Both of these loops operated for similar periods, but the heater lengths were slightly different.

While, in the cases cited above, gas-fired tests were found to compare favorably with resistance-heated tests, considerable difficulty was encountered in effectively measuring and controlling the wall temperatures in several loop tests in which gas-fired furnaces were used. Hot spots

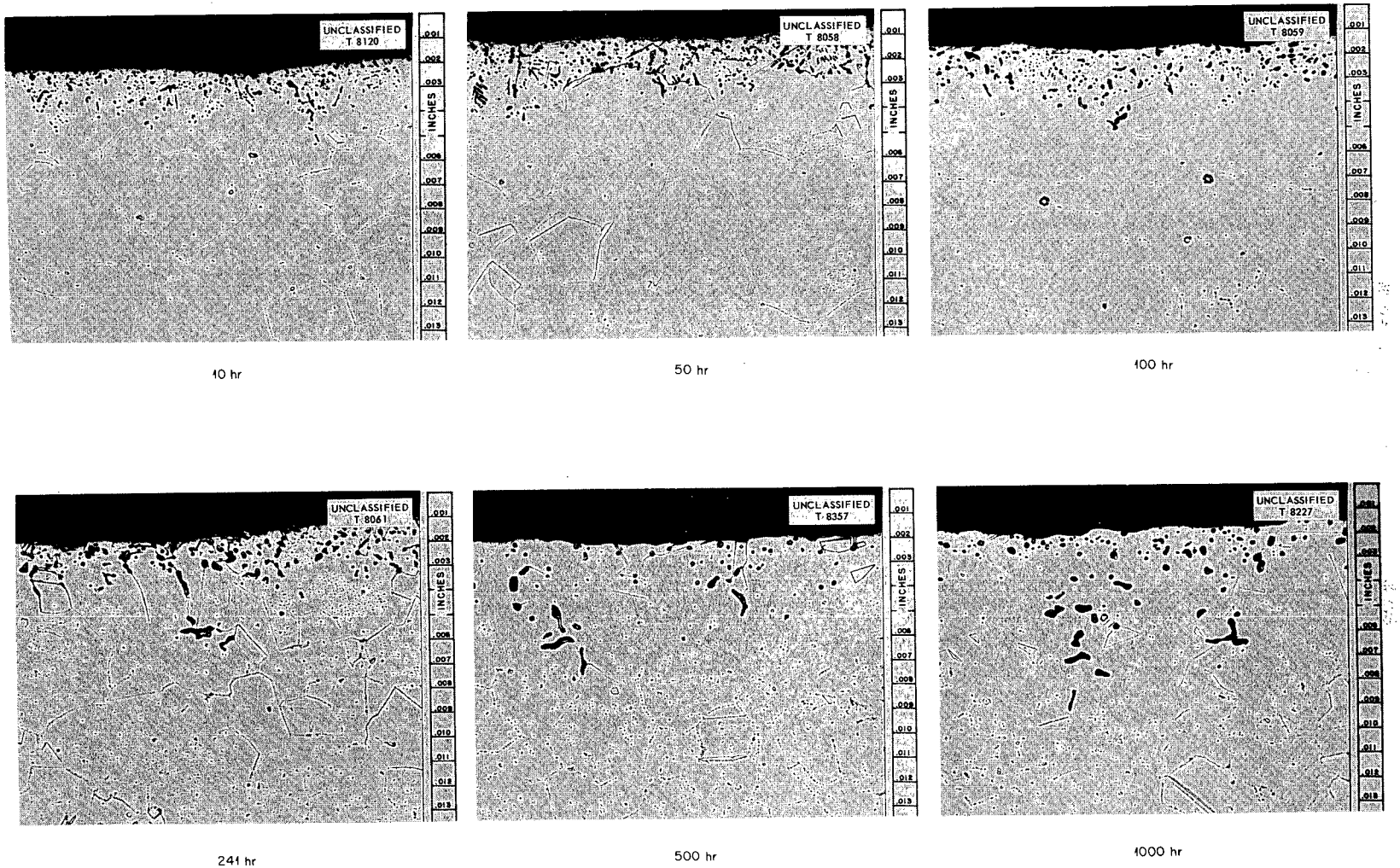

Fig. 53. Effect of Time on Corrosion of Inconel Pump Loops in Which NaF-ZrF_4-UF_4 (50-46-4 mole %) Was Circulated with a Maximum Temperature of 1500°F, a Temperature Differential of 200°F and a Reynolds Number of 10,000. 250X. Reduced 38.5%. (Secret with caption)

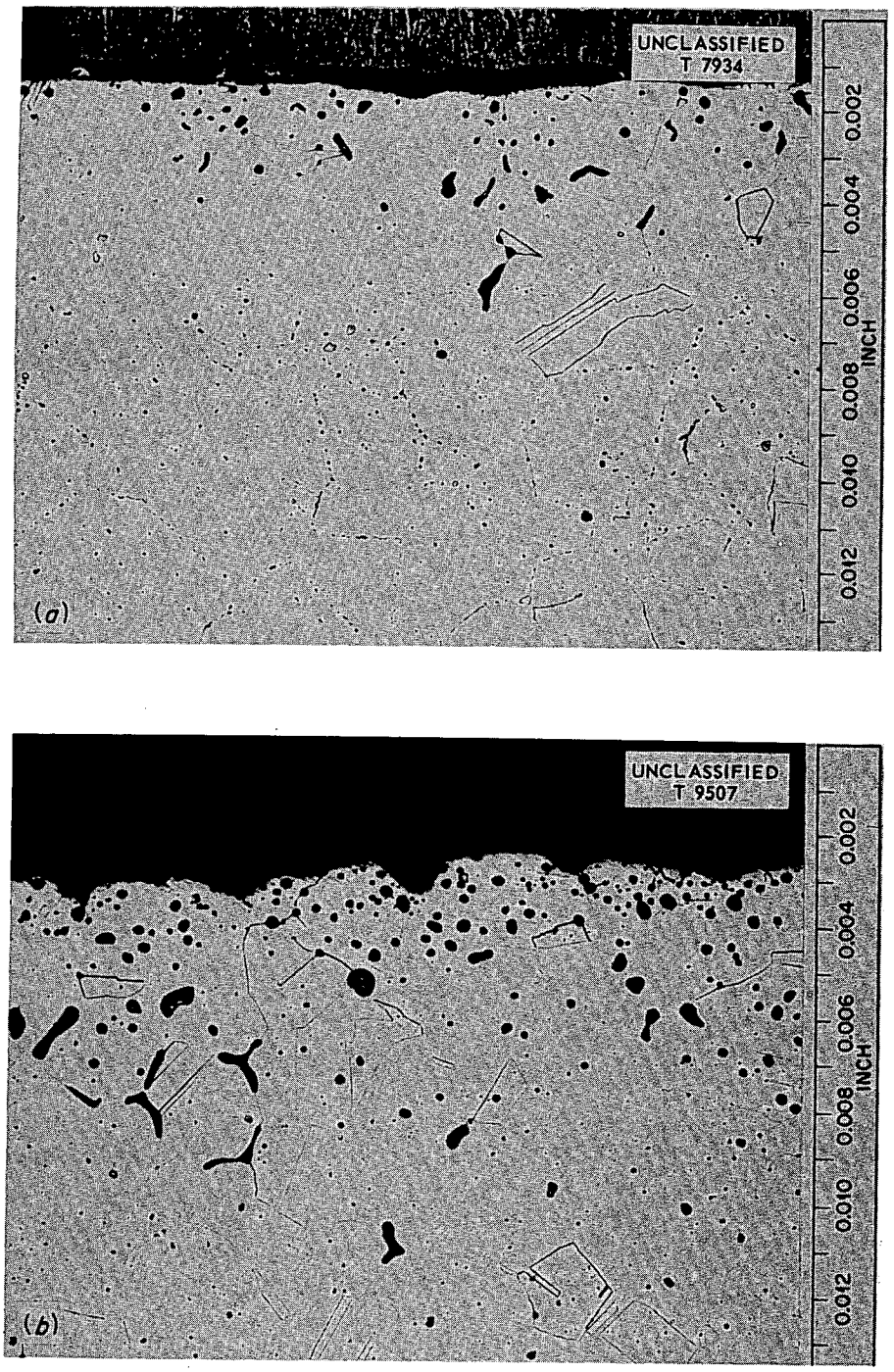

Fig. 54. Effect of Wall Temperature on Maximum Attack in Inconel Pump Loops in Which Fluoride Fuel Was Circulated. (*a*) Loop 4950-2; wall temperature, 1550°F. (*b*) Loop 7425-43; wall temperature, 1710°F. 250X. (Secret with caption)

TABLE 24. EFFECT OF HOT-WALL TEMPERATURE[a] ON CORROSION IN INCONEL PUMP LOOPS CIRCULATING FLUORIDE FUEL NO. 30[b]

	Loop No.					
	4935-2	4935-5	4935-7	4950-2	4950-5	7425-43
Operating time, hr	1000	681	332	1000	640	1000
Maximum fluoride temperature, °F	1500	1500	1500–1510	1500	1500	1500
Maximum tube-wall temperature, °F	>1600[c]	>1582[c]	>1710[c]	1550	1590	1710
Reynolds number	5,000	9,000–10,000	~6,000	10,000	8,000	6,500
Velocity, fps	3.2	6.5	4.6	6.5	5.2	4.5
Length of heated tube, ft	17	23	23	17	17	17
First leg				7.9	7.9	7.9
Second leg				9.1	9.1	9.1
Total length of loop, ft	43	53	53	51	51	51
Heating method	Gas	Gas	Gas	Electrical resistance	Electrical resistance	Electrical resistance
Shape of heated section	Coiled	Coiled	Coiled	Straight	Straight	Straight
Ratio of hot-leg surface to loop volume, $in.^{-1}$	2.38	2.86	2.86	2.10	2.10	2.10
Cause of termination	Scheduled	Power failure	Power failure	Scheduled	Power failure	Scheduled
Maximum depth of attack, mils	5	5	8	5	3	9

[a]Temperature gradient of fluoride mixture around circuit was held constant at 200°F.
[b]$NaF-ZrF_4-UF_4$ (50-46-4 mole %).
[c]Values represent thermocouple readings slightly ahead of point of maximum wall temperature.

TABLE 25. ANALYSIS OF FLUORIDE FUELS USED IN INCONEL PUMP-LOOP EXPERIMENTS IN WHICH THE EFFECT OF HOT-WALL TEMPERATURES WAS STUDIED

Loop No.	Fuel Sample	Analytical Results			
		U (wt %)	Ni (ppm)	Cr (ppm)	Fe (ppm)
7425-41	Before test	8.61	40	105	45
	After test	10.3(?)	40	440	70
7425-43	Before test	9.20	50	55	70
	After test	9.37	100	650	80

resulting from uneven furnace heating were frequently encountered and resulted in quite high attacks in localized areas along the heater length. Consequently, the use of gas-fired furnaces has been discontinued in favor of resistance-heating techniques.

Effect of Changes in the Ratio of Hot-Leg Surface Area to Loop Volume. – In order to determine the effect of variations in the ratio of the surface area of the hot leg to the volume of the loop, two resistance-heated Inconel pump loops, 7425-6 and -7A, were operated with a volume of fluorides greater than that employed in standard tests but with essentially unchanged loop-wall surface areas. The fluoride mixture circulated was NaF-ZrF_4-UF_4 (50-46-4 mole %). Other operating conditions for these loops are shown in Table 26.

The volume in these two loops was increased over that of a standard control loop, 7425-1A, by placing reservoirs, in the form of large cans, at the hairpin turn which connects the No. 1 and No. 2 heaters (see Fig. 50). Since heat is not normally introduced at this hairpin, Calrod heaters placed around the cans maintained the fluid temperature imparted by the first heater section but did not add to that temperature. Therefore, the walls of the can were at the same temperature as the tube walls which comprised the hairpin section in the standard loop; and the temperature distributions around the heaters, as well as around the rest of the loop, were maintained the same for all tests. Fluoride temperatures at the reservoirs were approximately 75°F lower than the maximum fluoride temperature, which was attained immediately past the second heater leg.

It is evident from Table 26 that variations in depth of attack show no particular correlation with loop volume over the ranges investigated. However, the attack of 9 mils which occurred in loop 7425-1A seems high, based on results of comparable standard loops, and would more logically be expected to be in the range of 5 to 7 mils. This estimated value provides a more reasonable comparison with the 6-mil attack reported for loop 7425-6, where the ratio of volume to heating surface was increased by a factor of two, although it still does not indicate any measurable increase in attack as a result of this volume increase.

The 9-mil attack observed in 7425-7A, in which the ratio of volume to heating surface was quadrupled, was accompanied by a thin, continuous, gold-colored layer covering substantial parts of the cold leg, as well as parts of the pump which were in contact with fluorides. This deposit was analyzed to be predominantly titanium, with possibly some zirconium present. The system was carefully examined for materials high in titanium,

TABLE 26. EXPERIMENTAL DATA PERTAINING TO INCONEL PUMP LOOPS OPERATED WITH VARIOUS SYSTEM VOLUMES AND TEMPERATURE DROPS

Total length of each loop: 51 ft
Length of heater: 17 ft
Operating time: 1000 hr (except loop 7425-1A, 1001 hr)

	Loop No.				
	7425-6	7425-7A	7425-1A	7425-3A	4950-6
Maximum fluoride temperature, °F	1500	1500	1500	1532	1520
ΔT, temperature gradient, °F	200	200	200	132	300
Maximum tube-wall temperature, °F	1590	1610	1600	1600	1620
Reynolds number	10,000	10,000	10,000	16,000	~8,000
Velocity, fps	6.5	6.5	6.5	9.9	5.22
System volume, $in.^3$	251	518	80.8	80.8	80.8
Ratio of hot-leg surface to loop volume, $in.^{-1}$	0.98	0.5	7.34	7.34	7.34
Maximum depth of attack, mils	6	9	$9\frac{1}{2}$	$11\frac{1}{2}$	8

but none were found. Preliminary x-ray-diffraction results indicate the deposit may be TiO.

Thus, while the attack has increased approximately 3 mils in this system, compared to the systems with lesser volumes, the significance of the increase cannot be established until the source of the deposits is discovered. However, in the event the increase should prove real, it still appears that system volume, over the ranges studied, has no great effect on corrosive attack over a 1000 hr period.

Effect of Variations in Temperature Drop. – Three Inconel pump loops, 7425-3A, 7425-1A, and 4950-6, which comprised a series to study the effect of temperature gradient around the loop circuit on fluoride corrosion, were operated 1000 hr with the fluoride mixture $NaF-ZrF_4-UF_4$ (50-46-4 mole %). In the operation of these loops, the maximum wall and fluid temperatures were maintained constant insofar as possible, while the fluid velocity and the hot-leg temperature were varied so as to achieve a specified cold-zone temperature and temperature drop in the system. Specific conditions are shown in Table 26. Since varying the Reynolds number or velocity, as discussed in a previous section, has not been observed to affect corrosion appreciably, it was felt that any differences in the corrosion in these three loops could be attributed directly to differences in temperature drop.

The temperature drops employed for the three loops were 132, 200, and 300°F and produced maximum hot-leg attacks of $11\frac{1}{2}$, $9\frac{1}{2}$, and 8 mils, respectively. Thus, the variation of hot-leg attack with temperature drop seems inverted from what would normally be expected. However, other causes may be responsible for the relatively high attacks encountered for the lower temperature drops. As already discussed, the attack in loop 7425-1A appears to be high, relative to similar loops operated with a 200°F temperature drop. A leak developed in this loop, as well as in loop 7425-3A, which necessitated a temporary interruption in the operation after 22 and 120 hr, respectively. Subsequent additions of fresh fluorides upon resumption of the tests may have caused an increase in attack over that which would otherwise have been obtained.

Effect of UF_3 Additions to Fluoride Mixtures. – A series of Inconel pump loops have been operated with the fluoride mixtures $NaF-ZrF_4-UF_4$ (50-46-4 mole %) and $NaF-KF-LiF-UF_4$ (11.2-41.0-45.3-2.5 mole %) to which varying amounts of UF_3 were added. Table 27 shows the analyses of the fluorides circulated, and in Table 28 are given the operating conditions for the loops in this series. The changes expected in the chemical and, concomitantly, the corrosive behavior of these salts, as a result of the UF_3 additions, are discussed in a subsequent section of this report which deals with results of thermal-convection-loop tests in which similar additions were utilized.

Of the two systems investigated, additions made to the alkali-metal-base fluoride produced the most significant effect on corrosion, resulting in a substantial decrease in the depth and number of subsurface voids. Only minor improvements in attack resulted from the addition of UF_3 to the zirconium-base fluorides.

Two of the loops (4695-1 and -2) circulated $NaF-ZrF_4-(UF_4,UF_3)$ (50-46-4 mole %) in which approximately 2 wt % of the uranium had been converted to U^{+++}. The design of loop 4695-1 differed from 4695-2 in that the heated section was in the form of a coil. Operation of this loop (Table 28) was terminated after 385 hr because of a leak at a heating terminal. Examination showed the maximum attack, which was found in a bend in the first heating leg, to be 12 mils. In a straight portion of the heated section, the maximum attack extended to a depth of 9 mils. The depths of attack were, thus, only slightly less than those found in loops discussed in an earlier report,[3] which were of similar design but circulated a mixture containing no trivalent uranium. However, the number of voids appeared to be substantially reduced.

The other loop examined, 4695-2, was fabricated with two straight heating sections connected with a U-bend (Fig. 50) and operated for 887 hr before being terminated because of a pump-bearing failure. The maximum attack was to a depth of 8 mils and was found in the first heated section. A temperature study of this loop showed that the maximum wall temperature occurred in the first heated section; whereas the maximum fluoride-mixture temperature occurred in the second heated section. Thus, the location of the site of maximum attack in this loop again demonstrates the importance of maximum wall temperature in controlling attack, as

[3] *Ibid.*

TABLE 27. ANALYSES OF FLUORIDE FUELS USED IN INCONEL PUMP-LOOP EXPERIMENTS IN WHICH EFFECT OF ADDED U^{+++} WAS DETERMINED

Loop No.	Fuel Sample	Analytical Results				
		U (wt %)	U^{+++} (wt %)	Ni (ppm)	Cr (ppm)	Fe (ppm)
4695-1	Before test	8.40	1.65	20	160	95
	After test	7.95	1.27	10	80	120
	Batch	8.69	2.19	120	175	95
4695-2	Before test	7.76	1.80	40	190	50
	After test	8.02	1.02	3	340	40
	Batch	7.63	1.92	125	200	55
4950-3	Before test	8.27	0.39	9	135	45
	After test	8.03	0.73	8	200	50
	Batch	8.39	0.64	20	130	70
4950-1	Before test	9.21		40	60	30
	After test	10.70		15	330	35
	Batch	8.96		40	70	110
4695-3	Before test	15.1*	0.58	120	35	165
	After test	12.3		25	1640	50
	Batch	12.3		410	500	125
7425-2	Before test	11.9	1.07	135	35	105
	After test	10.7	0.0	275	25	150
	Batch	12.3	1.40	20	15	120
7425-4A	Before test	10.8	0.81	115	40	165
	After test	10.8	0.70	390	155	120
	Batch	11.92	2.01	<1	25	70

*Uranium content unusually high.

discussed earlier in the report. In general, the depth of attack was slightly less than that which occurred in other loops operated under similar temperature conditions but with standard fluoride mixtures. However, a thin deposit, possibly metallic uranium, was found in the final portion of the cold leg.

A third loop, 4950-3, circulated the same fluoride mixture as in the above-mentioned loops but with a lower U^{+++} content. This loop, which was of a U-bend design similar to 4695-2 but with a shorter heating section, showed a maximum attack of 11 mils in the second heating leg. Loop 4950-1, which had a similar heating length, was operated for 1000 hr with an all UF_4 mixture. The maximum attack found in this loop was 18 mils, showing that even though only about 0.5 wt % U^{+++} was present a considerable reduction in attack resulted in loop 4950-3.

Two other Inconel pump loops which circulated NaF-KF-LiF-UF_4 (11.2-41.0-45.3-2.5 mole %) to which UF_3 was added show that the presence of U^{+++} in such mixtures is quite effective in reducing hot-leg attack. However, disproportionation of UF_3 occurred whereby, in the case of both loops, continuous layers of metallic uranium formed along the colder loop walls. Fluoride samples taken from loops 7425-2 and 7425-4A immediately prior to operation were reported to contain approximately 1% U^{+++} (Table 27). Both operated with a 1500°F hot leg, a 200°F temperature drop, and a Reynolds number of 10,000.

Because of pump-motor failure, loop 7425-2 was terminated after 550 hr; maximum attack was

TABLE 28. DATA CONCERNING INCONEL PUMP LOOPS WHICH CIRCULATED FLUORIDE FUELS WITH VARIOUS U^{+++} CONTENTS

	Loop No.						
	4695-1	4695-2	4950-3	4950-1	4695-3	7425-2	7425-4A
Fluoride fuel*	No. 30 + U^{+++}	No. 30 + U^{+++}	No. 30 + U^{+++}	No. 30	No. 107	No. 107 + U^{+++}	No. 107 + U^{+++}
Operating time, hr	385	887	1000	1000	630	550	1000
Isothermal time, hr	50	71	61	62	43	24	44
Maximum fluoride temperature, °F	1500	1530	1500	1500	1500	1500	1500
Maximum tube-wall temperature, °F	>1735	>1670	1690	1650	>1640	1570	1555
ΔT, temperature gradient, °F	300	200	200	200	300	200	200
Reynolds number	10,000	15,000	10,000	5,000	10,000	10,000	10,000
Velocity, fps	6.8	10.1	6.5	3.25	3.3	4.1	4.1
Ratio of hot-leg surface to loop volume, $in.^{-1}$	1.51	1.51	1.19	1.19	1.51	2.15	2.15
No. 1 heater length, ft	5	5	3.9	3.5	5	7.9	7.9
No. 2 heater length, ft	7	7	4.3	4.7	7	9.1	9.1
Total heater length, ft	12	12	8.2	8.2	12	17	17
Attack, mils	12	8	11	18	35	1½	2

*Fuel No. 30: $NaF-ZrF_4-UF_4$ (50-46-4 mole %)
Fuel No. 107: $NaF-KF-LiF-UF_4$ (11.2-41.0-45.3-2.5 mole %)

found, by metallographic means, to be under 1½ mils. In loop 7425-4A, which operated successfully for 1000 hr, only slightly greater attack (reaching a depth of 2 mils) occurred, which is shown in Fig. 55. Analyses of the fuels before and after testing, as reported in Table 27, showed little change in chromium content, which is indicative of the low attacks observed.

These attacks contrast with an attack of 35 mils found in Inconel loop 4695-3, which circulated the same alkali-metal-fluoride mixture but contained no trivalent uranium.

Sodium in Inconel Pump Loops

A series of tests in which the oxide level of sodium was altered through the use of cold traps, deoxidizers, or oxide additions has been conducted in order to study the effect of oxide contamination on mass transfer in sodium-Inconel forced-circulation systems. The operating conditions and test results for this series are given in Table 29. All loops were run with a maximum

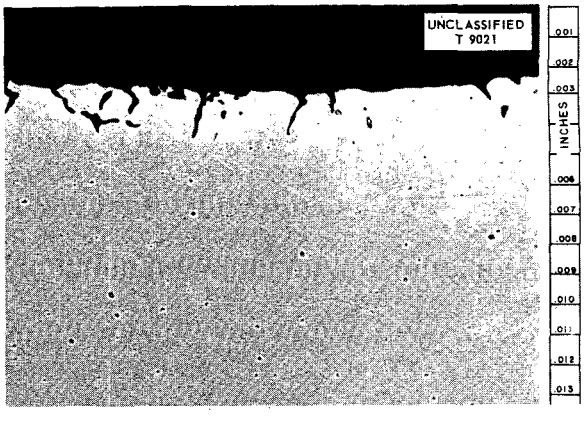

Fig. 55. Maximum Attack Found in Inconel Pump Loop 7425-4A After Circulation of NaF-KF-LiF-(UF_4 + UF_3) (11.2-41.0-45.3-2.5 mole %, 0.81 wt % U as U^{+++}) for 1000 hr. Maximum temperature of fluoride mixture was 1500°F; Reynolds number was 10,000. 250X. Reduced 34.5%. (Secret with caption)

TABLE 29. DATA RELEVANT TO OPERATION OF FORCED-CIRCULATION INCONEL LOOPS IN WHICH SODIUM WITH VARIOUS OXIDE CONTENTS WAS USED

Maximum fluid temperature: 1500°F
Temperature differential: 300°F

Loop No.	System Variables	Operating Time (hr)	Maximum Hot-Leg Attack (mils)	Deposit		Oxide Content	
				Maximum Thickness (mils)	Weight (g)	Initial (wt %)	Final (wt %)
4951-8	Bypass cold trap	1000	2	14	13	0.074	0.035
7426-2	0.05% O_2 added as Na_2O_2	1000	2	20	15	0.035	0.025
4951-5	0.15% O_2 added as Na_2O_2	1000	2	30	26	0.036	0.027
7426-1	Barium added, bypass cold trap	1000	2	20	13		0.035
4951-6	Bypass cold trap	500	1½	11	7	0.041	0.026
4951-9	Barium added, no bypass cold trap	500	1½	18	5	0.051	0.031

fluid temperature of 1500°F, a 300°F temperature drop, and a Reynolds number greater than 15,000. The total weight of mass-transferred deposit provides a convenient parameter for evaluating oxide effects, and it is determined by brushing all deposits from the loop sections after the sodium has been removed. With Inconel-sodium systems, most crystals are lightly adherent so that they are not washed out with the sodium, and they may be mechanically accumulated by brushing for the weight determination.

Loop 4951-8, which contained a circulatory bypass cold trap for oxide removal, as shown in Fig. 56, was operated as the control or standard loop for the 1000-hr test series. Operating temperature of the cold trap was 300°F, and approximately 5% of the fluoride flow was diverted through it. Increases in oxide content, relative to this control loop, were effected by the addition of Na_2O_2, calculated to produce oxygen contents of 0.15% in one and 0.05% in another of the loops in the series. Loop 4951-5, which contained the larger oxide addition, showed a substantial increase in both the depth of and amount of mass-transferred deposit, compared to control loop 4951-8. However, the added 0.05% oxygen in loop 7426-2 resulted in only a slight increase in mass transfer over that shown by the control loop. In both cases, analyses of the sodium from the two sodium-peroxide-containing loops failed to pick up any increase in oxide content as a result of the additions. The explanation for this undoubtedly lies in the difficulties that are encountered in obtaining representative sodium samples for analyses.

The addition of 1.3% barium (as a deoxidizing agent) was made to the sodium circulated in loop 7426-1, but no difference could be observed in the weight of mass-transferred particles in this loop, when compared to control loop 4951-8. The only evidence of any effect attributable to the barium was seen in the hot leg, where the intergranular penetrations which occurred were observed to have, in conjunction with them, a metallic layer distinct from the base metal.

Two 500-hr loops, 4951-6 and 4951-9, were also operated in conjunction with the oxide-contamination series. The former loop, which was discussed in a previous report,[4] contained a bypass cold trap for oxide removal; whereas loop 4951-9 circulated sodium to which 1% barium had been added. In Table 29 a slight decrease in the amount of mass transfer is seen for the loop with the barium addition, compared with the loop containing the cold trap. However, some error exists in determining the weight of the mass-transferred

[4] G. M. Adamson *et al.*, *Met. Semiann. Prog. Rep. Oct. 10, 1955*, ORNL-1988, p 25.

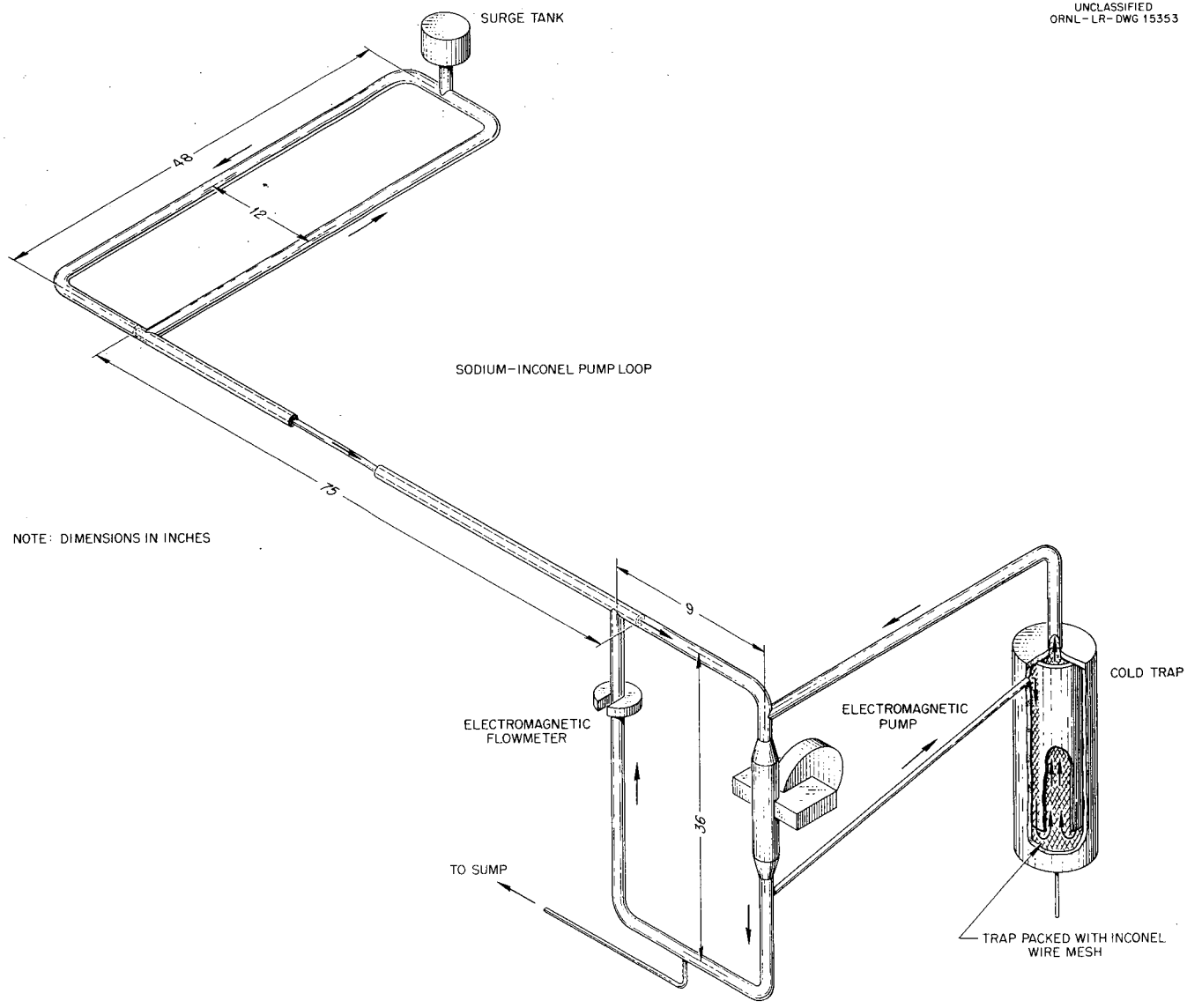

Fig. 56. Location and Design of Cold Trap in Inconel Loops for Forced Circulation of Alkali Metals.

deposit in these loops and could possibly be responsible for this apparent decrease.

Intergranular attack was observed in the hot legs of all loops, reaching a maximum depth of 1½ mils in the 500-hr tests and 2 mils in the 1000-hr tests. Figure 57 illustrates the attack that occurred in loop 4951-8. The oxide and the barium additions appeared to have little effect on the depth of this attack, although additional corrosion in the form of uniform surface removal, which is difficult to evaluate, is, of course, also possible. The deposits in all the loops were quite similar in composition; all fell within the ranges shown in Table 30.

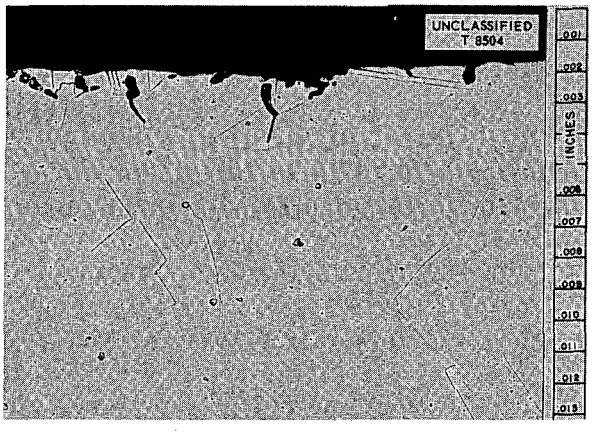

Fig. 57. Hot-Leg Attack in Inconel Pump Loop 4951-8 Operated for 1000 hr with Sodium at 1500°F. 250X. Reduced 32%. (Confidential with caption)

The operation of a pump loop with a 1000°F maximum sodium temperature has shown that the effect of temperature on corrosion in Inconel-sodium systems is very significant. After the loop was operated for 1000 hr with a 200°F temperature drop, visual inspection of the loop revealed that the original oxide film on the Inconel tubing was undisturbed. Metallographic examination showed the loop to be devoid of any deposits and unattacked in the hot leg.

NaK (56-44 wt %) in Inconel

Three Inconel pump loops which circulated NaK instead of sodium have completed 1000 hr of operation; the temperature drop was 300°F, and the maximum fluid temperature was 1500°F. To study the effects of oxide contamination on mass transfer in these systems, the NaK in two of the loops, 7439-1 and 3, was circulated through a bypass cold trap (Fig. 56); while in the other loop 7439-2, no steps other than careful handling were taken to clean up the system. The cold-trap temperature (300°F) in loop 7439-1 compared with that used in sodium systems; while in the case of loop 7439-3, the cold-trap temperature was held to the minimum temperature at which flow of the NaK could be maintained (about 100°F).

TABLE 30. ANALYSES OF MASS-TRANSFERRED DEPOSITS OCCURRING IN INCONEL PUMP LOOPS AFTER CIRCULATING SODIUM AND NaK AT 1500°C

Elements Comprising Deposit	Amount of Element in Deposit (wt %)	
	After Sodium Test	After NaK Test
Nickel*	87–92	90–92
Chromium*	7–10	8–10
Iron*	0.02–3.0	0.1–0.5
Aluminum**	0.2	0.2–0.5
Manganese**	0.2–1.0	0.2–0.5
Titanium**	0.02–0.5	0.2
Silicon**	0.05–0.3	0.2–0.5
Cobalt**	0.05–0.2	0.1–0.5

*Chemical analysis.
**Spectrographic analysis.

As in the case of sodium-filled loops, metal deposits appeared in the economizers and, to a lesser extent, in the cold-leg sections of the loops. Visual and metallographic examination did not reveal any significant difference in the amount or appearance of the deposits formed in the loops with cold traps and that formed in loop 7439-2. Thus, the use of a bypass cold trap in NaK systems, even at the lowest possible temperature, was apparently of little benefit in limiting mass transfer.

The dendritic crystals comprising these deposits were somewhat finer than the crystals observed in sodium-filled loops, were more adherent, and projected from a thin metallic layer integrally bonded to the base metal, as seen in Fig. 58. However, analyses of the deposits, which are listed in Table 30, showed that the compositions

Fig. 58. Layer Deposited in Economizer of Inconel Pump Loop 7439-2 Which Circulated NaK for 1000 hr. 250X. Reduced 11%. (Confidential with caption)

were identical with those found in Inconel-sodium loops. A comparison of the amount of mass transfer in these NaK systems, relative to comparable sodium systems, has not been possible because of difficulties in removing the deposit from the loop for weight determination. The maximum deposit thicknesses were approximately the same in loops that circulated NaK and in loops in which sodium was circulated; although such thickness measurements are not necessarily an effective measure of mass transfer, since the crystals are formed in discrete patches. However, it does appear that the same restriction to flow, as a result of mass transfer, will generally be encountered in both systems.

Hot-leg attack in the form of intergranular penetration was observed to the same degree in all three NaK-tested loops. The manner of attack was identical to that observed in sodium-tested loops, but the depths of penetration were slightly less, reaching a maximum of 1 mil in comparison with the 2 mils for sodium-tested loop 4951-8 illustrated in Fig. 57.

Sodium in Type 316 Stainless Steel

A type 316 stainless steel loop, 7426-5, has completed 1000 hr of operation with sodium as the test fluid. The loop had a hot-leg temperature of 1500°F, had a 300°F temperature drop, and contained a bypass cold trap. Like an earlier type 316 stainless steel loop which operated 476 hr,[5] this loop showed very little evidence of mass transfer either in the economizer or in the cold leg. The amount of deposit which could be scraped out was sufficient only for spectrographic examination, which indicated predominantly nickel and chromium to be present. A few scattered intergranular penetrations to a depth of $\frac{1}{2}$ mil were seen in the hot leg, and there was some slight porosity to a depth of 5 mils below the exposed surfaces.

[5] *Ibid.*, p 28.

Effect of UF_3 Additions to Alkali-Base Fluoride Mixtures

To study further the effect of U^{+++} concentration in fluoride mixtures, a series of Inconel thermal-convection loops was operated with fuel No. 107, NaF-LiF-KF-UF_4 (11.2-41.0-45.3-2.5 mole %), to which varying amounts of UF_3 were added. The UF_3 was added to yield from 1.0 to 3.0 wt % U^{+++}. The compounding of a fuel with a desired U^{+++} content was very difficult, and analyses of the resulting batches showed that the U^{+++} contents very often varied from those which were calculated on the basis of the amount added. Likewise, from Table 32, discrepancies are seen to exist between several of the batch analyses made immediately following the UF_3 additions and the analyses made prior to filling the loops. A reasonable explanation for the decrease in U^{+++} content with time might be that the more stable UF_4 is formed, although the differences between the batch analyses and the fill analyses do not always show this. Consequently, it is believed that the discrepancies are the result of inherent difficulties in analyzing for U^{+++}.

For comparison purposes, loops 507 and 511 were operated with standard fuel compositions, that is, without U^{+++} additions (designated BE fuel). However, the fuel used in these loops differed slightly from the composition corresponding to fuel No. 107 in that the former fuel contained approximately 1.0 wt % less uranium. For corrosion purposes, it was assumed that the two fuels would exhibit similar behaviors.

Comparison of maximum attack in the standard loops with that in the loops having U^{+++} additions is shown in Table 32. The U^{+++} additions have considerably reduced the fluoride attack; values ranged from 1 to 2 mils for all loops in which U^{+++} was added, compared with 13.5 mils in a case where no U^{+++} was added. However, in every case where UF_3 was added, a metallic layer,

TABLE 32. COMPARISON OF CORROSION OF INCONEL THERMAL-CONVECTION LOOPS OPERATED AT 1500°F FOR 500 hr WITH FUEL NO. 107 CONTAINING DIFFERENT AMOUNTS OF UF_3

Loop No.	Amount of U^{+++} (wt %)		Metallographic Results	
	Batch Sample	Fill Sample	Hot-Leg Attack (mils)	Cold Leg
793	1.83	0.88	2	Light layer
796	3.22	0.77	1	0.1-mil layer
797	1.51	2.55	1½	0.1-mil layer
798	0.94	0.70	1½	<0.5-mil layer
799	1.82	3.04	1	0.5-mil layer
507	**	2.43	11	0.5-mil metallic deposit
511	**	1.16	13½	Metallic deposit*

*Analysis indicated predominantly chromium.

**Not reported.

shown in Fig. 60, resulted, which was believed to be uranium.

In the standard loops, metallic crystals, consisting predominantly of chromium, were present in the cold leg. Such a deposit is commonly observed in systems of alkali-base fluorides and Inconel and is the result of mass transfer of chromium from the hot-leg to the cold-leg sections. This deposit was not observed in loops which operated with fuel containing UF_3 additions.

Loops Constructed of Hastelloy B

Test results reported previously[6] have indicated a considerable amount of mass transfer in sodium-Hastelloy B systems which were operated at 1500°F for 1000 hr. In initial tests, deposits of fine nickel crystals formed to an extent sufficient to seriously restrict the flow of sodium. As an outgrowth of these early data, a number of Hastelloy B loops were constructed with the original inside surface removed by reaming so as to ensure a uniform surface composition and also to eliminate surface roughness. Three of these loops, 766, 767, and 768, were operated with sodium at 1500°F for 500, 1000, and 1500 hr, respectively. Metallographic results, as shown in Table 33, indicated no substantial increase in depth of hot-leg attack with increasing operational time; and in all of the tests, the cold legs revealed no metallic deposits and very little attack. A few scattered metallic particles were observed macroscopically in the traps of all loops.

In order to further investigate this apparent effect of surface condition on the mass transfer of Hastelloy B by sodium, loop 875, constructed of unreamed as-received tubing, was operated 1000 hr at 1500°F. This loop showed macroscopically some metallic deposits in the cold leg and the trap area, although the mass-transferred product is considerably less than that which was reported for earlier sodium-Hastelloy B systems.[6]

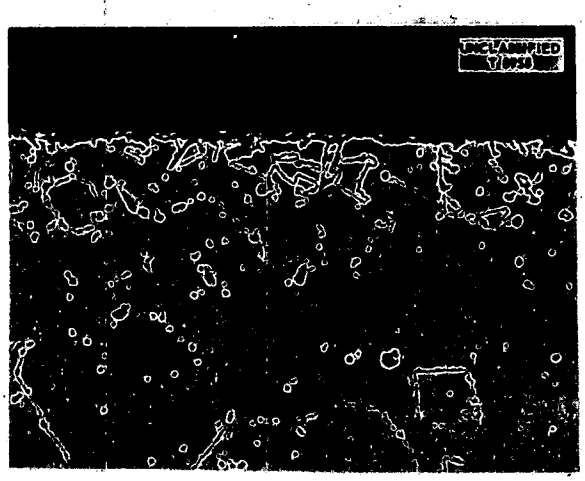

Fig. 60. Layer Present in the Cold Leg of Inconel Thermal-Convection Loop Operated with NaF-LiF-KF-UF_4 (11.2-41.0-45.3-2.5 mole %) to Which Was Added 0.94 wt % U^{+++}. 250X. Reduced 29.5%. (Secret with caption)

[6] G. M. Adamson, A. Taboada, and V. P. Treciokas, *Met. Semiann. Prog. Rep. April 10, 1955*, ORNL-1911, p 54.

TABLE 33. COMPARISON OF REAMED AND UNREAMED HASTELLOY B THERMAL-CONVECTION LOOPS OPERATED WITH SODIUM AT 1500°F

Loop No.	Condition	Time (hr)	Maximum Attack (mils)	Metallographic Results	
				Hot Leg	Cold Leg
766	Reamed	500	½	Light surface attack	No deposit; some attack
767	Reamed	1000	½	Light surface attack	No deposits or attack
768	Reamed	1500	2½	Intergranular attack with surface pitting	No deposits or attack
875	Original	1000	1½	Pitting and surface porosity	No attack; small amount of mass transfer

The reason for the presence of fewer deposits in recent Hastelloy B loops is not entirely clear. Differences in impurities in the sodium, particularly oxide, may possibly have existed in previous loops compared with recent loops, although tests of Inconel loops over a similar time period and with various batches of sodium do not bear this out.

Also, included were three loops, 769, 770, and 771, which were reamed out and were operated at 500, 1000, and 1500 hr, respectively, with fuel No. 30, NaF-ZrF-UF_4 (50-46-4 mole %) at 1500°F. Test results, shown in Table 34, indicated that there was no apparent variation in the amount of attack over the time range employed. The depths of attack were similar to those which occurred in earlier tests of Hastelloy B loops constructed of as-received, or unreamed, tubing, although metallic crystals reported in certain of the earlier loops were completely absent in the later tests.

An unreamed Hastelloy B loop, 866, which was operated with fuel No. 30 at 1650°F for 1000 hr, likewise was found to be free of metallic deposits. Hot-leg attack reached a maximum depth of 5 mils, which is a slight increase over the attack which occurs at 1500°F.

Two thermal-convection loops, 814 and 816, constructed of ½-in. IPS, schedule 40, Hastelloy B pipe were operated at 1500°F with fuel No. 107 NaF-LiF-KF-UF_4 (11.2-41.0-45.3-2.5 mole %). Loop 814, which ran 500 hr, showed a maximum hot-leg attack of 2 mils. This attack appeared as heavy surface pitting and general subsurface void formation and is shown in Fig. 61.

Increasing the operational time to 2000 hr, as evidenced by loop 816, had little effect on the depth of attack, although the extent of void formation was accentuated, as shown in Fig. 62. The attack in the cold legs of these loops differed

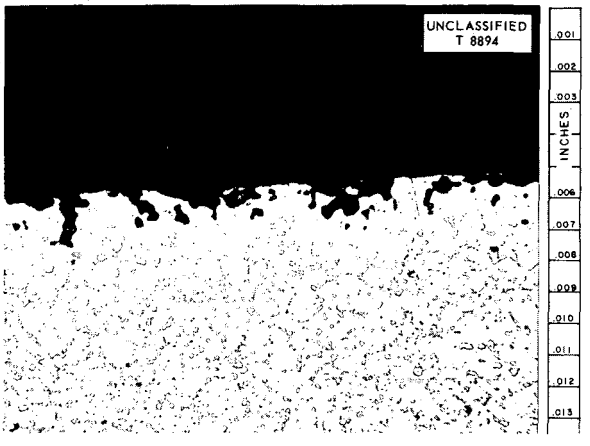

Fig. 61. Maximum Attack in Hastelloy B Thermal-Convection Loop 814 After Circulation of NaF-LiF-KF-UF_4 (11.2-41.0-45.3-2.5 mole %) for 500 hr at 1500°F. 250X. Reduced 32%. (Secret with caption)

TABLE 34. COMPARISON OF REAMED AND UNREAMED HASTELLOY B THERMAL-CONVECTION LOOPS OPERATED WITH FLUORIDE FUEL MIXTURES AT 1500 AND 1650°F

Loop No.	Condition	Fuel No.	Temperature (°F)	Time (hr)	Maximum Attack (mils)	Metallographic Results	
						Hot Leg	Cold Leg
769	Reamed	30	1500	500	1½	Subsurface voids	No attack or deposits
770	Reamed	30	1500	1000	3	Intergranular subsurface voids	No attack or deposits
771	Reamed	30	1500	1500	2	Subsurface voids	Intergranular attack of 2 mils
866	Original	30	1650	1000	5	Subsurface voids	Attack to 1½ mils; no deposits
814	Original	107	1500	500	2	Subsurface voids	Subsurface voids
816	Original	107	1500	2000	2	Subsurface voids	Subsurface voids

very little from that observed in the hot legs; moreover, the cold legs appeared to be completely free of any deposits.

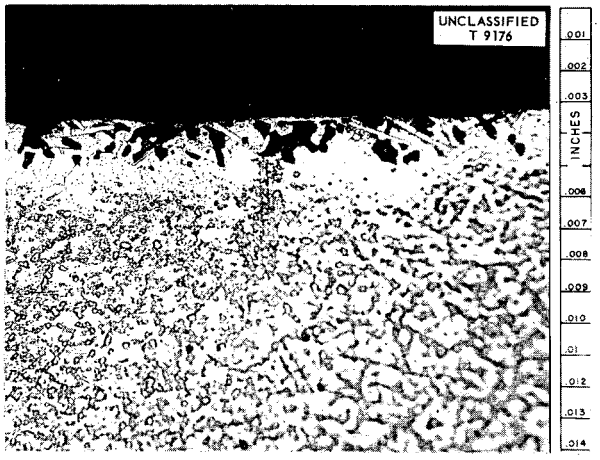

Fig. 62. Maximum Attack in Hastelloy B Thermal-Convection Loop 816 After Circulation of NaF-LiF-KF-UF_4 (11.2-41.0-45.3-2.5 mole %) for 2000 hr at 1500°F. 250X. Reduced 32%. (Secret with caption)

Loops Constructed of Nickel-Molybdenum Alloys

A series of vacuum-melted alloys were prepared by the Fabrication Group in order to permit a study of the corrosion properties of nickel-base – molybdenum alloys having compositions which represented modifications of commercial Hastelloy B. Thermal-convection loops having the compositions shown in Table 35 were operated for 1000 hr at 1500°F with fuel No. 30. After operation, only one loop showed attack that was more than 2 mils in depth in the hot leg. The large attack in this loop, 1008, is believed to be the result of an air leak, which interrupted the test, since loop 1013 of identical composition showed only ½ mil of attack after successfully operating for 1000 hr. Results obtained from these alloys and, for comparison purposes, from Hastelloy B and Inconel are shown in Table 35. The results indicate that corrosion of a nickel-molybdenum alloy in fuel No. 30 at 1500°F is not seriously affected by varying the molybdenum and chromium content. An Inconel loop, 1010, was operated as the control, or standard, in this series and is shown to have incurred a maximum attack of 12 mils. For comparison, the attack in this Inconel loop and that in an 85% nickel–15% molybdenum loop are shown in Fig. 63.

TABLE 35. NICKEL-MOLYBDENUM THERMAL-CONVECTION LOOPS TESTED IN FUEL NO. 30 AT 1500°F

Loop No.	Material	Composition (wt %)	Operating Time (hr)	Maximum Attack (mils)
181	Hastelloy B	29 Mo–65 Ni–5 Fe	1000	1
1004	DPI-30	24 Mo–76 Ni	791*	0
1006	-37	3 Cr–20 Mo–77 Ni	1000	1
1007	-30	15 Mo–85 Ni	1000	1
1008	-40	5 Cr–20 Mo–75 Ni	240*	10
1009	-33	15 Mo–85 Ni	1000	1
1010	Inconel	76 Ni–17 Cr–7 Fe	1000	12
1013	DPI-40	5 Cr–20 Mo–75 Ni	831*	½
1014	-30	24 Mo–76 Ni	1000	2
1015	-30	24 Mo–76 Ni	1000	½

*Terminated because of leak.

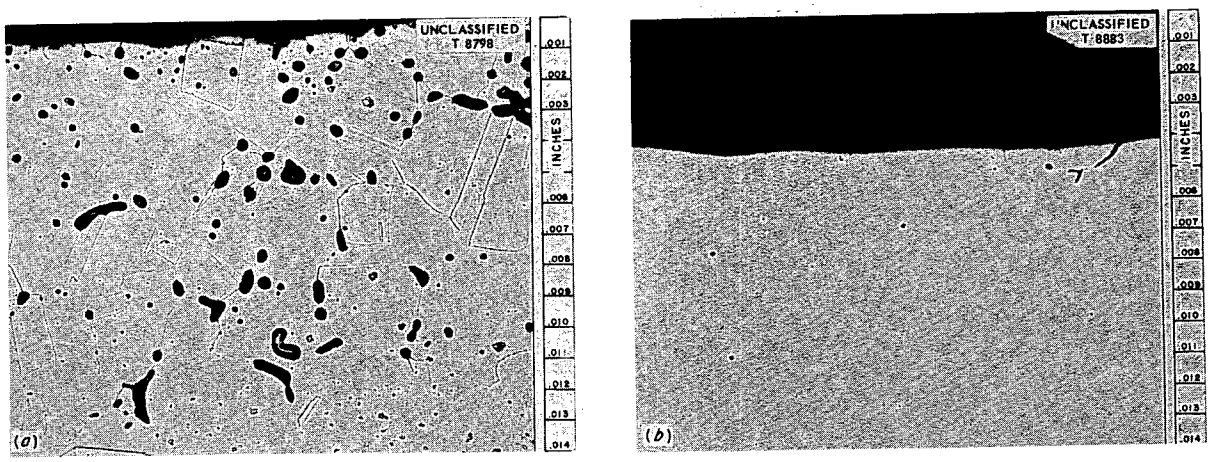

Fig. 63. Comparison of Maximum Attacks as Found in (a) Loop 1009 Constructed of 85% Ni–15% Mo and (b) Loop 1010 Constructed of Inconel Which Were Operated with $NaF-ZrF_4-UF_4$ (50-46-4 mole %) for 1000 hr at 1500°F. 250X. Reduced 10%. (Secret with caption)

MECHANICAL PROPERTIES

D. A. Douglas J. W. Woods
J. R. Weir C. W. Dollins
Metallurgy Division
C. R. Kennedy
Pratt & Whitney Aircraft

RESULTS OF THE HASTELLOY W TESTING PROGRAM

Hastelloy W is a nickel-base alloy which differs from Hastelloy B in that the nickel and molybdenum contents are slightly reduced and about 5% chromium is added. This alloy was originally developed as a welding rod for the joining of Hastelloy alloys with different compositions. Interest in the use of this alloy as a structural material arose because it was thought that the higher chromium content and the slightly lower molybdenum content of the alloy might result in an improvement over Hastelloy B, which has a tendency to age in the 1100 to 1300°F temperature range; thus, a more easily fabricable alloy might result. Creep tests and metallographic examination show that there is a significant decrease in the amount of second phase found in Hastelloy W after tests at 1300°F. Hence, Hastelloy W is a noticeable improvement over Hastelloy B, which is brittle at this temperature. Figures 64 and 65 show the difference in microstructure of Hastelloys

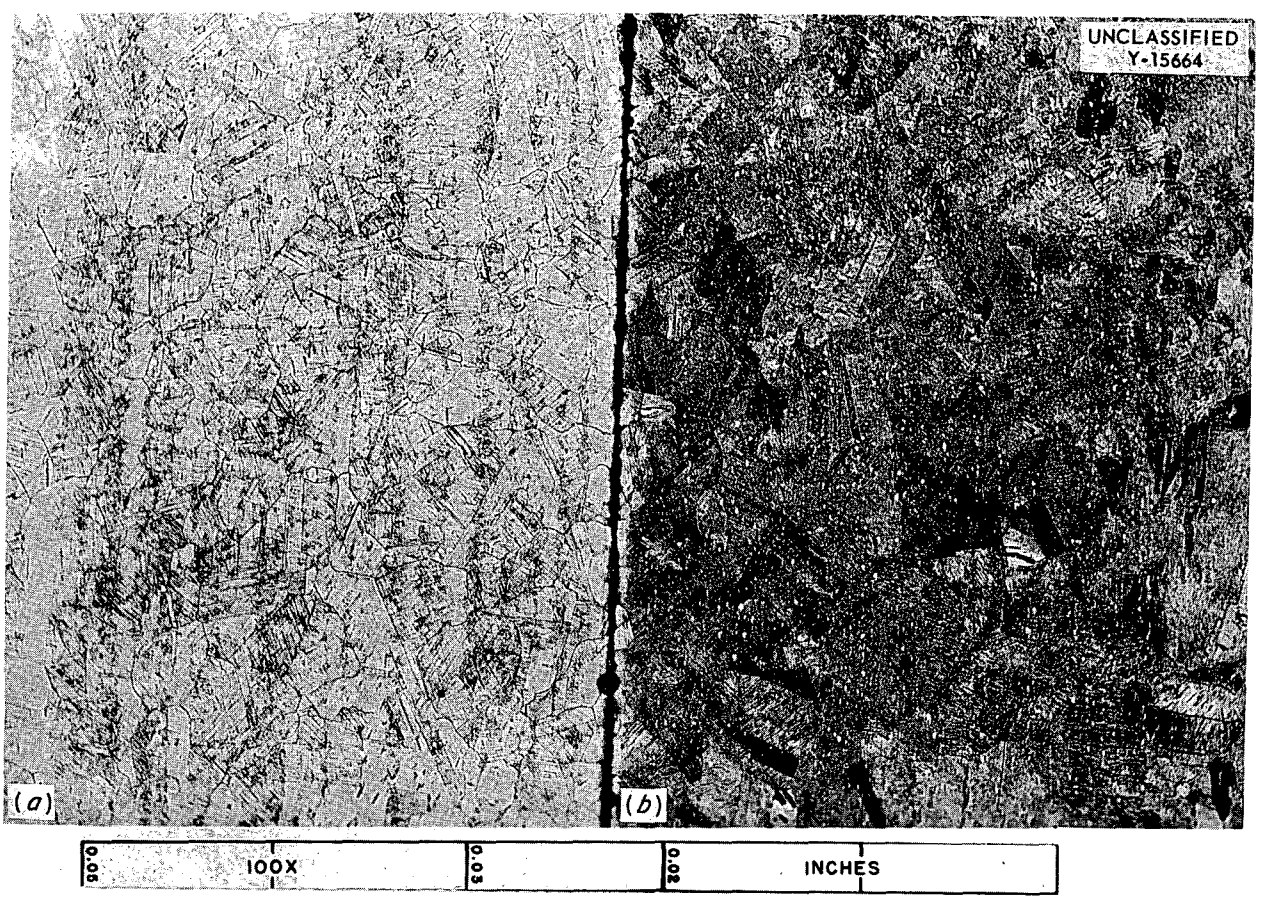

Fig. 64. Photomicrograph of Hastelloy B After Creep Testing at 1300°F and at 30,000 psi. Ruptured in 200 hr. (*a*) Unstressed. (*b*) Stressed.

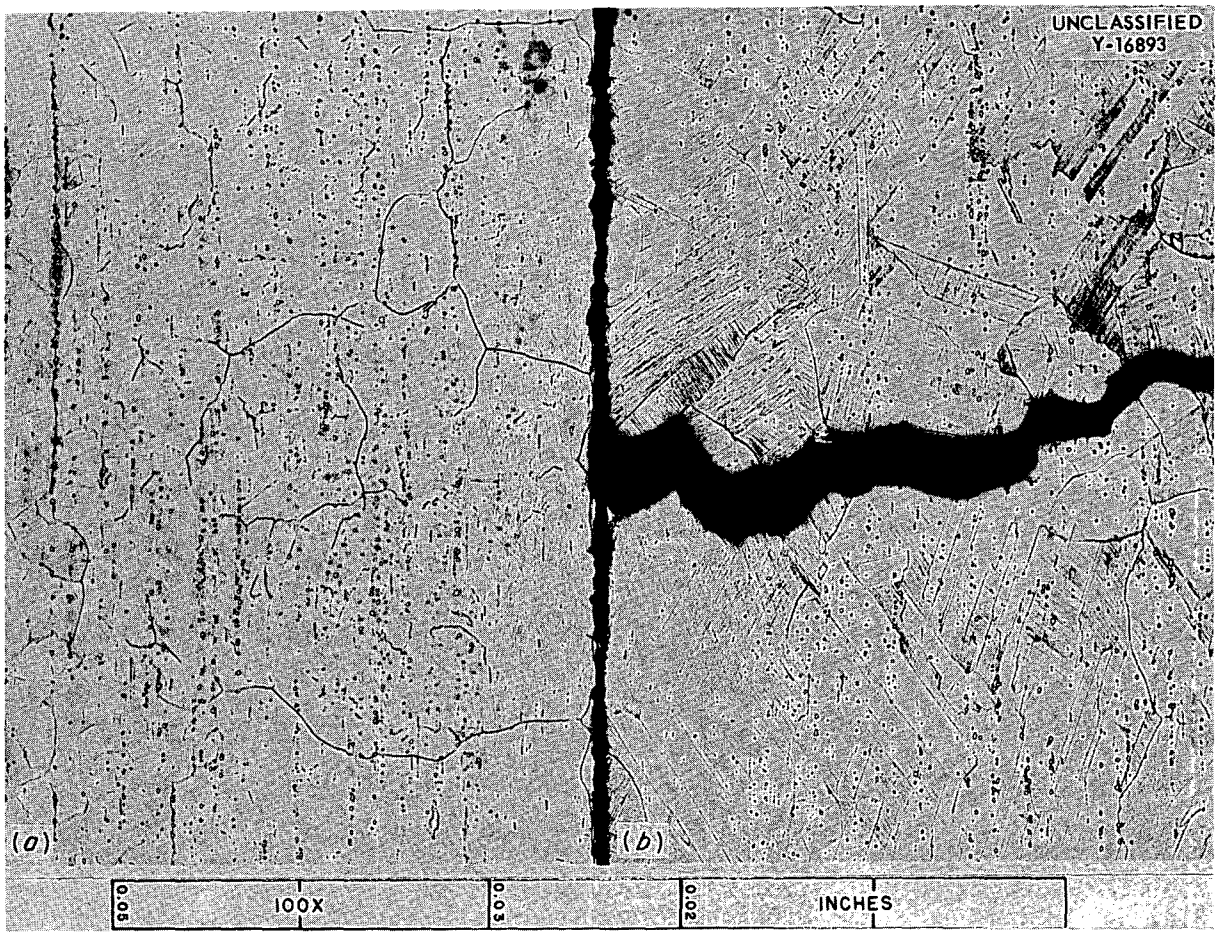

Fig. 65. Photomicrograph of Hastelloy W After Creep Testing at 1300°F and at 35,000 psi. Ruptured in 400 hr. (*a*) Unstressed. (*b*) Stressed.

B and W after 200 hr and 400 hr, respectively, at 1300°F. The strengths and ductilities of the two alloys in tensile tests in the temperature range 1000 to 1800°F are compared in Fig. 66.

In Figs. 67, 68, and 69, the creep-rupture properties of Hastelloys B and W at 1300, 1500, and 1650°F are compared. It is apparent that there is no significant difference in their creep strengths. The corrosion resistance of Hastelloy W in fused-fluoride mixtures has been found to be equal to that of Hastelloy B. The most serious deterrent to the use of Hastelloy W for reactor construction is its loss of ductility after exposure to temperatures in the range from 1200 to 1400°F. Creep tests at 1300°F have indicated a loss of ductility, in that the total strain upon rupture is never over 10%. Room-temperature tensile testing of Hastelloy W aged for 100 hr at 1300°F is now in progress to determine the extent of its loss of ductility.

INCONEL TESTING PROGRAM

Creep-Test Results

Complete design curves for 0.060-in.-thick Inconel sheet specimens in the temperature range and environments of interest are presented in Figs. 70 through 81. Summaries of the stress-rupture results for the coarse-grain (2050°F annealed) material and the fine-grain (1650°F annealed) material tested in argon and in NaF-ZrF_4-UF_4 (50-46-4 mole %) at 1300, 1500, and 1650°F are presented in Figs. 82 and 83. It can be seen that the decrease in rupture strength of

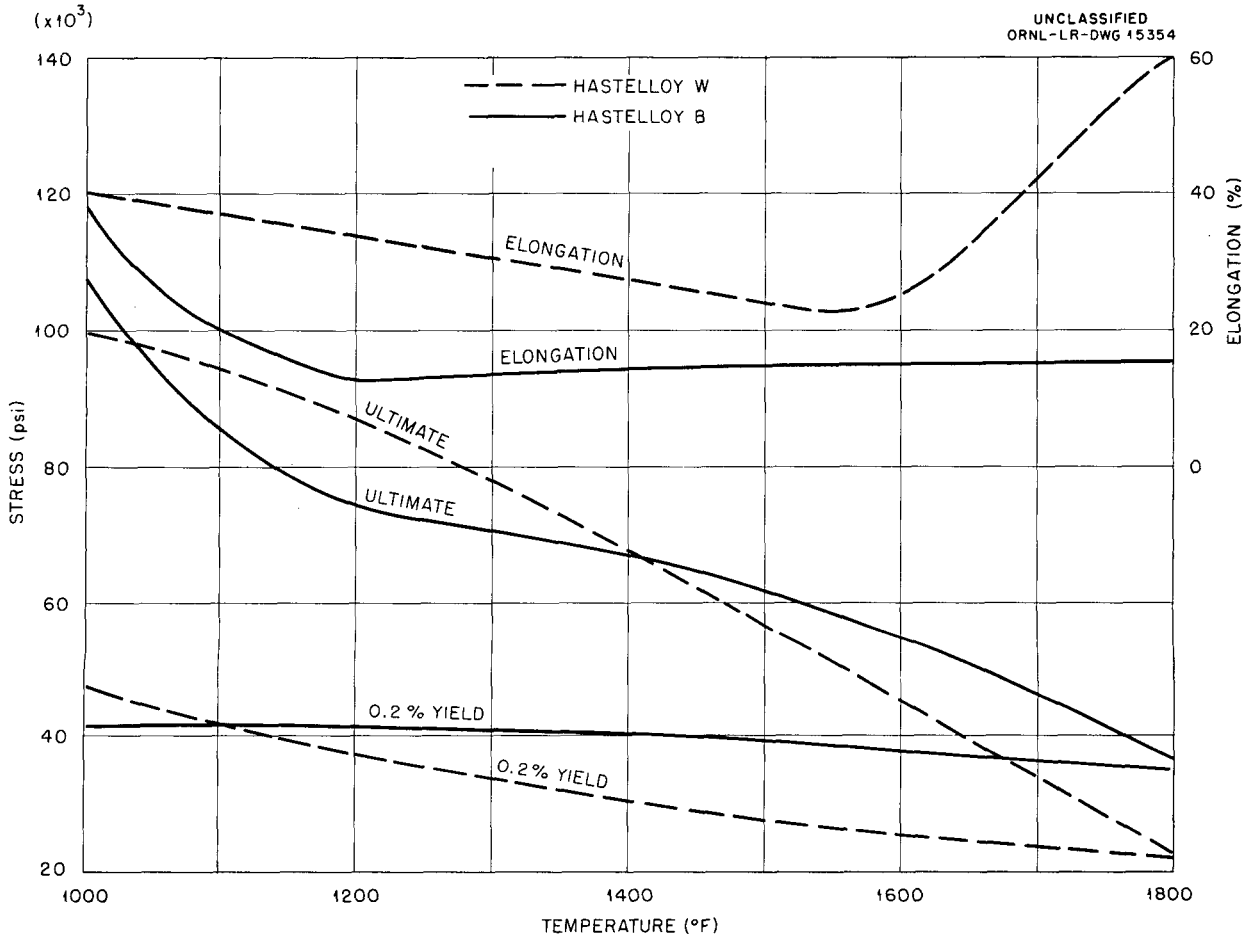

Fig. 66. Strengths and Ductilities of Hastelloy B and Hastelloy W as Functions of Test Temperature.

the coarse-grained material as a result of the corrosive action of the fused fluorides is less than that in the case of the fine-grained material. The loss of creep strength in fused fluorides exhibited by the fine-grain material results in its having poorer properties at 1500°F in this environment than the coarse-grain material; whereas in an argon environment at 1500°F, the reverse is true.

Biaxial Stress Tests

In the previous semiannual report[1] it was pointed out that in a closed-end, internally pressurized tube a stress system is established such that the tangential or hoop stress is twice the axial stress. No apparent effect is noted on the stress-rupture properties of Inconel under this stress distribution, when compared with uniaxially stressed sheet specimens of similar cross section. However, it was noted that the maximum deformation in the direction of the greater stress of the tubular specimens was considerably less than that noted for the specimens tested by conventional creep methods. In Table 36 the total elongations at failure for several tests of each type are compared.

The decrease in ductility shown by the tube-burst-type test may be attributed to the tangential-to-axial stress ratio of two to one which was set up in a closed-end, pressurized tube.

Metals when deformed at room temperature under various states of stress exhibit increasing or decreasing ductility, as compared to uniaxial

[1] J. W. Weir, *Met. Semiann. Prog. Rep. Oct. 10, 1955*, ORNL-1988, p 36.

TABLE 36. COMPARISON OF DEFORMATION AT RUPTURE OF 0.060-in.-SHEET INCONEL WITH THAT OF 0.060-in.-WALL TUBE-TYPE INCONEL

Temperature (°F)	Stress (psi)	Elongation (%)			
		Argon		$NaF-ZrF_4-UF_4$ (50-46-4 mole %)	
		Tube Burst	Sheet	Tube Burst	Sheet
1300	15,000			3	50
1300	12,000	9	70		
1300	10,000			9	40
1300	8,000	13	25		
1500	5,000	9	28	10	17
1500	4,000	5	20	4	13
1500	3,000	2	12	6	8
1500	2,000	1	12		
1650	3,000	7	30	7	19
1650	2,500	4	30	5	16
1650	2,000	4	30	3	15
1650	1,500	3	12	3	8

tensile ductility, depending on whether the stress system tends to increase or decrease the maximum shear stress.[2] In the case of a biaxial tensile-stress system, such as is found in the tube-burst test, the maximum shear stress is decreased by the action of the smaller axial stress so that slip is restricted. Thus, a decrease in the amount of deformation at fracture is noted.

Effect of Corrosion on Stress-Rupture Properties of Inconel

The mechanism by which the fused-fluoride salts corrode Inconel is quite well understood and has been discussed by both the Materials Chemistry Division and the Metallurgy Division in previous ANP Quarterly Reports. The effect of corrosion on the strength properties of the metal is not so well understood, and a number of anomalies have been observed. Intuitively one might expect the strength characteristics of a material to decrease fairly linearly with increasing depth of corrosion attack. However, no such trend is observed. Metallographic examination indicates that the majority of the corrosive attack occurs in the first 100 hr; but very little decrease in creep strength is noted at stresses which produce failure in 100 hr, as compared to similar tests in argon. Conversely, on tests which fail in 1000 hr only a few mils of additional attack can be seen, but there is a drastic reduction in creep strength.

The Cornell Aeronautical Laboratory of Buffalo, New York, has been conducting a creep program for the Wright Air Development Center, Wright-Patterson Air Force Base, Ohio, similar to that of ORNL. Their test equipment differs from that at the Laboratory in that a tubular-type specimen is employed and the fused salt is confined to the inside of the specimen so that accurate strain measurements can be made with conventional extensometers. The surface-area-to-volume ratio in their system is 5 to 1, whereas it is 0.15 to 1 in the test system at the Laboratory. As a result of the smaller volume of salt relative to the surface area of the specimen, only a limited amount

[2] M. Gensamer, *Metal. Progr.* 41, 212 (1941).

of corrosion occurs and very few voids are formed in their specimen; however, they still find a drastic reduction in creep strength in the longer-time tests, as compared to similar tests in argon.[3] Table 37 compares the results of tests both in argon and in the corrosive media, as obtained at the two laboratories.

The ratio of stresses in the two environments to produce rupture in 100 and 1000 hr along with the observed depths of corrosion are given in the Table 38.

It is difficult to arrive at any firm conclusions based on the rather limited data now available; however, it is possible to make a few generalizations. Since the corrosive attack is primarily confined to the grain-boundary regions, the lack of sensitivity to this effect at the high stresses can be explained on the basis that the deformation mechanism at these rapid strain rates is transgranular in nature and, thus, is not so greatly influenced by changes in the grain-boundary regions. It has been observed that salts contaminated with air or moisture produce a catastrophic rate of attack, which greatly reduces rupture life at all stress values; but this type of attack would not be considered normal in this environment. In the long-time tests where the strain rate is low, the area of deformation is confined to the grain-boundary regions. In this case, it would appear that chemical alteration, or grain-boundary instability initiated by the corrosive attack, results in a significant change in the creep properties of the material. The data from Cornell Aeronautical Laboratory would indicate that this effect can be noted, even though the corrosive attack does not penetrate any further than two or three grains into the material.

[3] G. J. Guarnieri, *Cornell Aeronautical Laboratory Quarterly Progress Report No. 3*, KB-935-M-3 (March 14, 1955).

TABLE 38. COMPARISON OF INCONEL TEST DATA AS OBTAINED AT ORNL AND AT CORNELL AERONAUTICAL LABORATORY

	s/a, Stress Ratio*	Depth of Corrosion (mils)
	100-hr Rupture Test	
ORNL	$\frac{7200}{7500} = 0.97$	5–7
Cornell	$\frac{7500}{7500} = 1$	1
	1000-hr Rupture Test	
ORNL	$\frac{2700}{4000} = 0.67$	7–9
Cornell	$\frac{3200}{5000} = 0.64$	2–3

*a = stressed in argon.
s = stressed in fused salt.

TABLE 37. TESTS OF INCONEL SPECIMENS AT 1500°F STRESSED TO RUPTURE IN 100 AND 1000 hr

Time to Rupture (hr)	Stress (psi)			
	Tests at ORNL		Tests at Cornell	
	In Argon	In $NaF-ZrF_4-UF_4$ (50-46-4 mole %)	In Argon	In $NaF-ZrF_4-UF_4$ (50-46-4 mole %)
100	7500	7200	7500	7500
1000	4000	2700	5000	3200

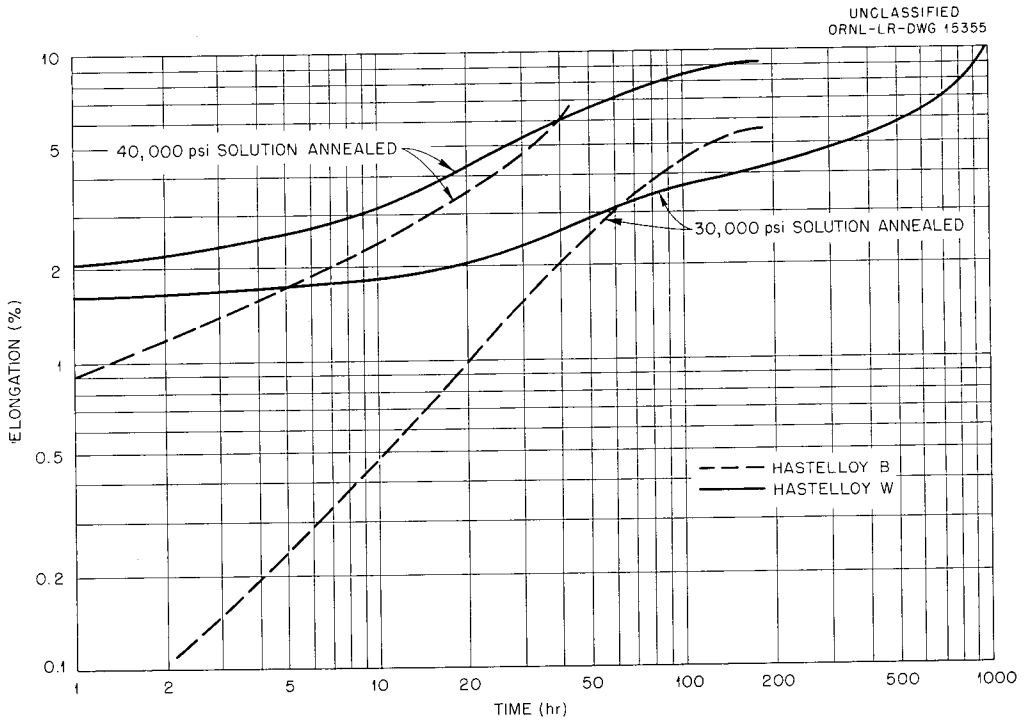

Fig. 67. Creep Curves for Solution-Annealed Hastelloys B and W Tested at 1300°F in Argon.

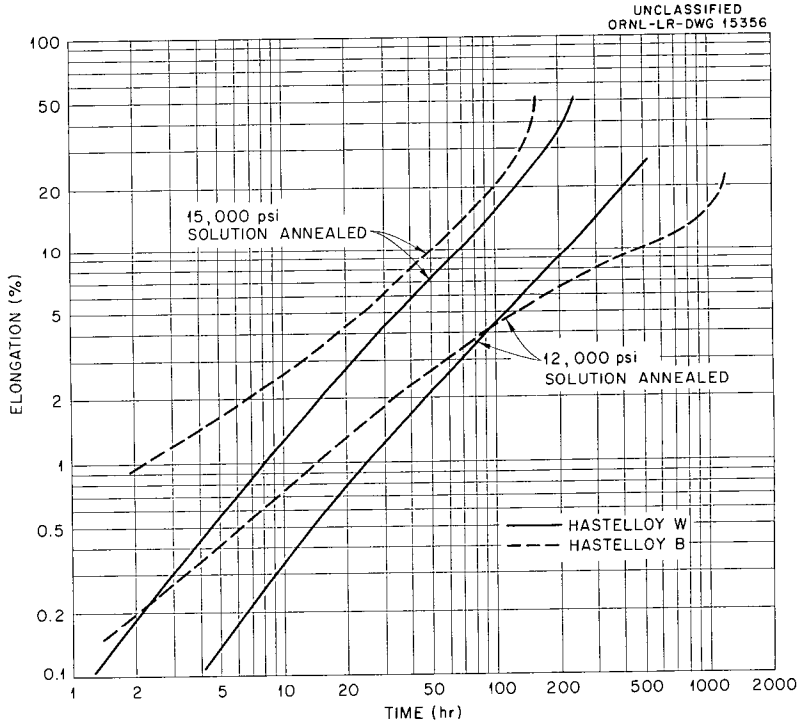

Fig. 68. Creep Curves for Solution-Annealed Hastelloys B and W Tested at 1500°F in Argon.

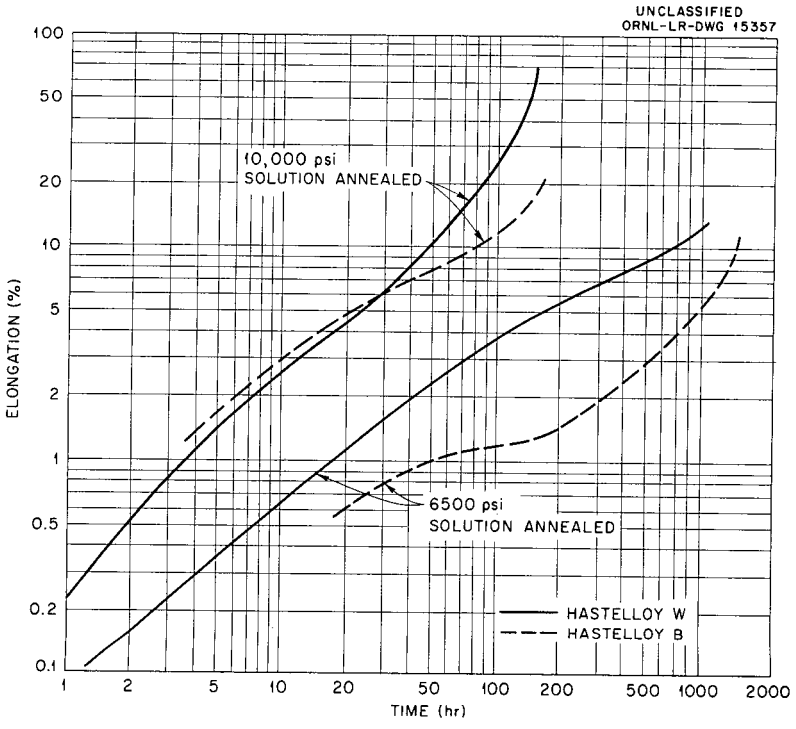

Fig. 69. Creep Curves for Solution-Annealed Hastelloys B and W Tested at 1650°F in Argon.

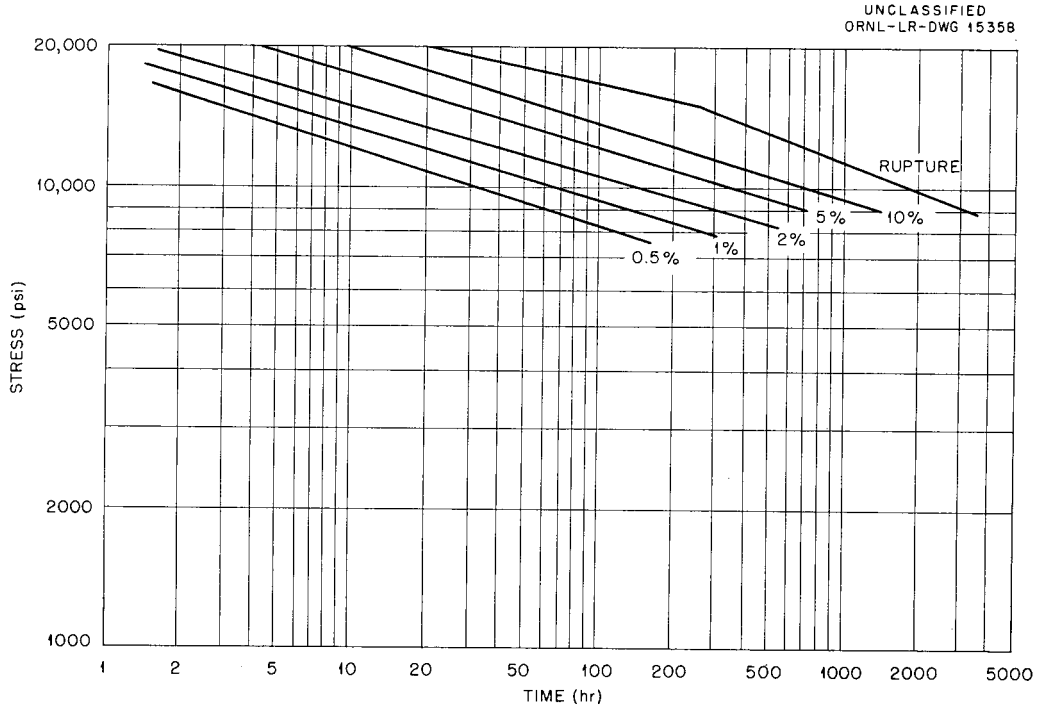

Fig. 70. Design Curves for Inconel Sheet (Heat B) Annealed at 1650°F and Tested in Argon at 1300°F.

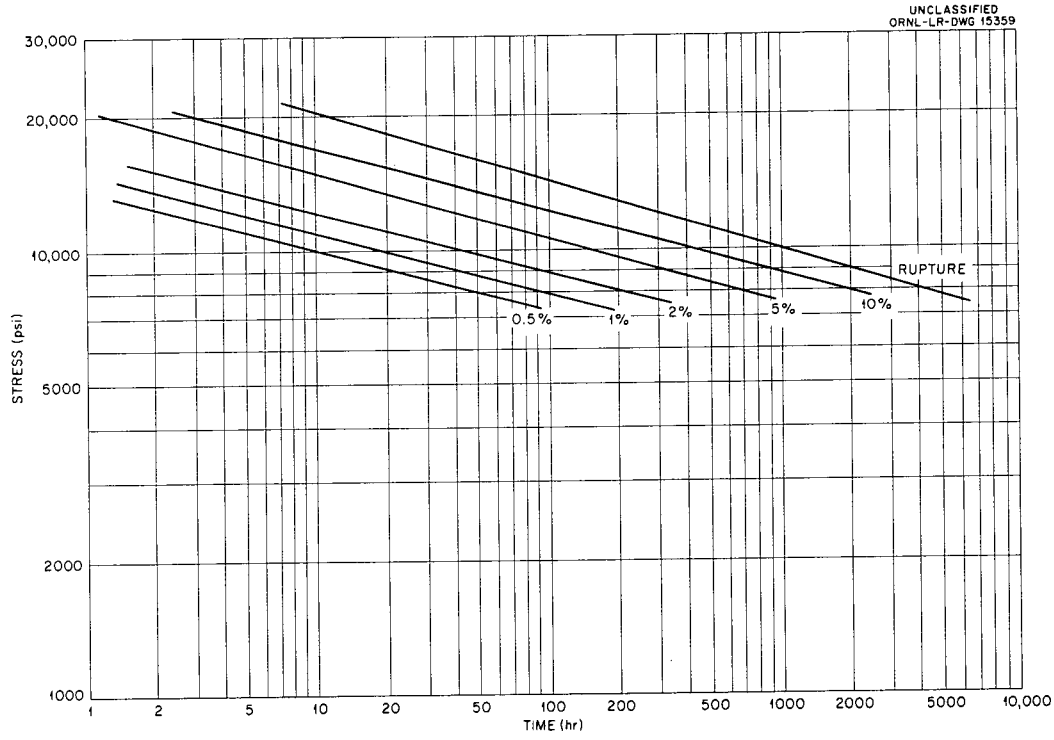

Fig. 71. Design Curves for Inconel Sheet (Heat B) Annealed at 2050°F and Tested in Argon at 1300°F.

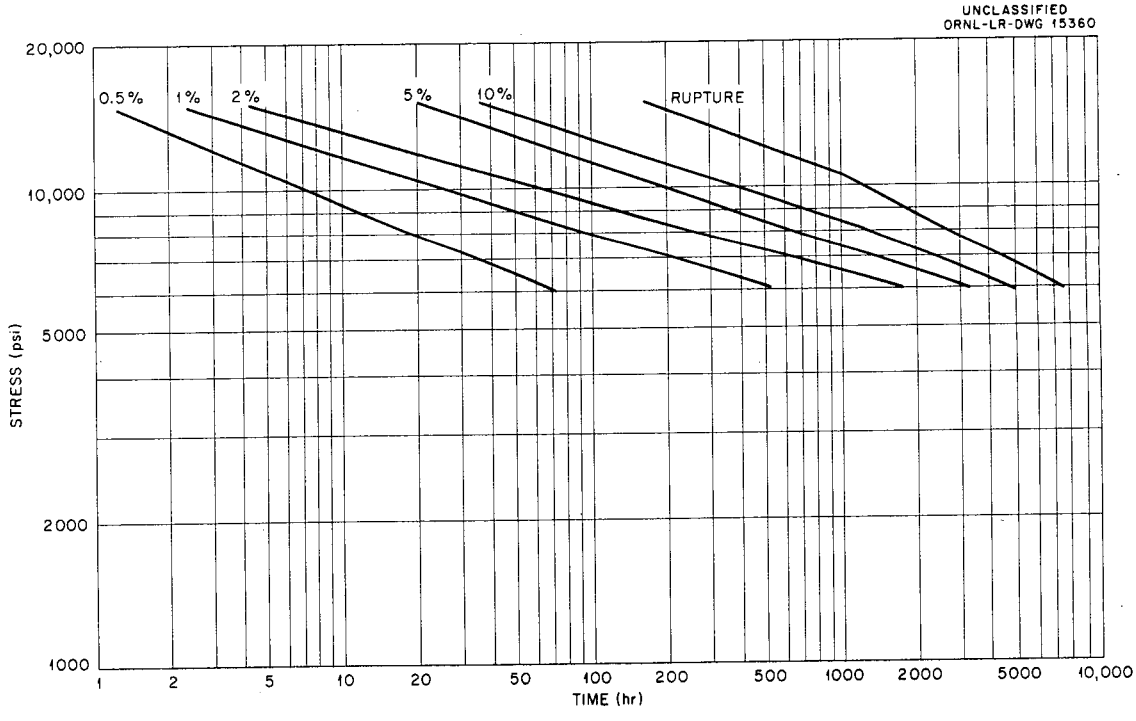

Fig. 72. Design Curves for As-Received Inconel Sheet (Heat B) Tested in NaF-ZrF_4-UF_4 (50-46-4 mole %) at 1300°F. (Secret with caption)

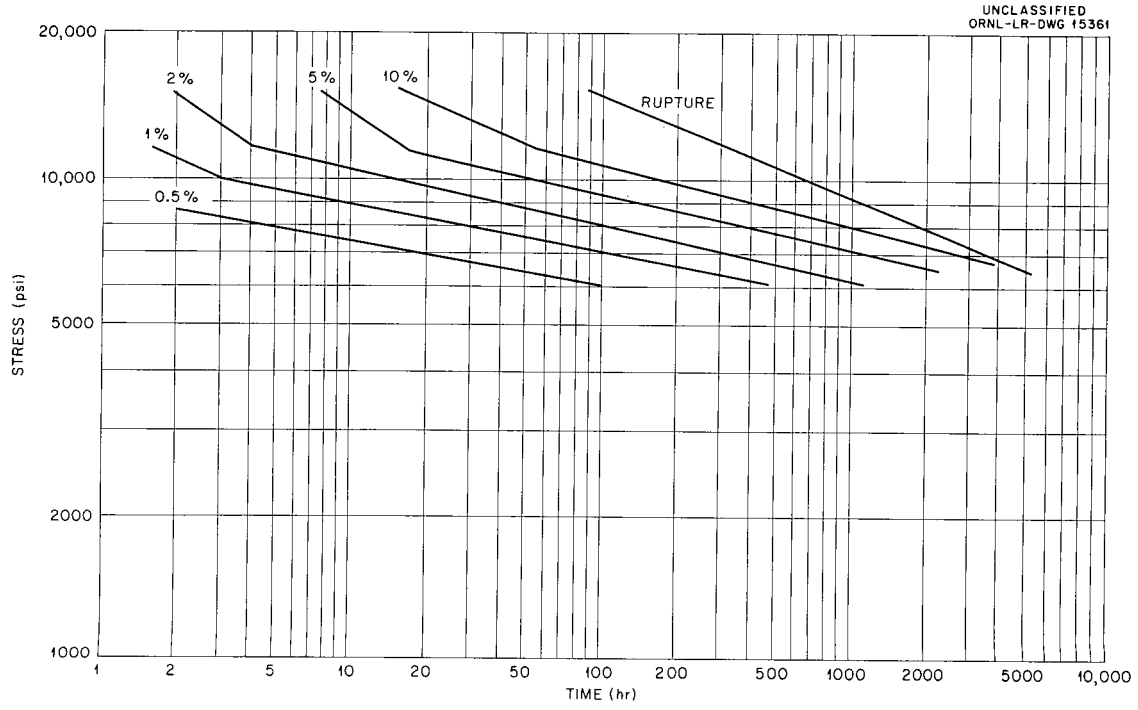

Fig. 73. Design Curves for Inconel Sheet (Heat B) Annealed at 2050°F and Tested in $NaF-ZrF_4-UF_4$ (50-46-4 mole %) at 1300°F. (Secret with caption)

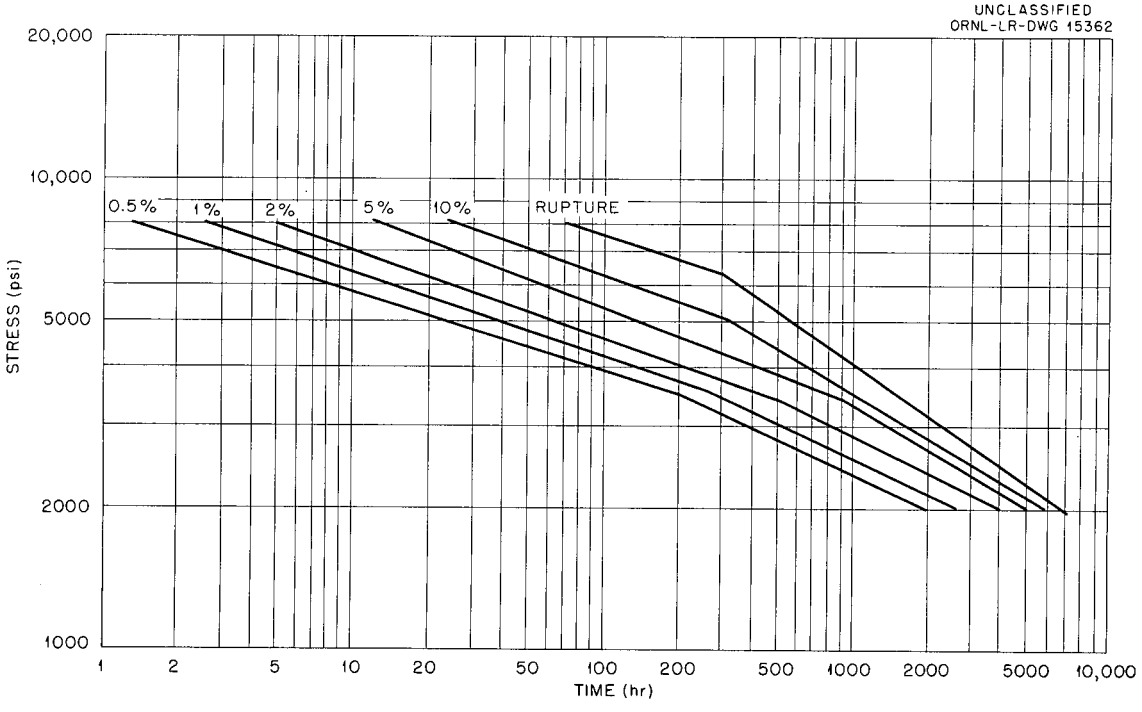

Fig. 74. Design Curves for Inconel Sheet (Heat B) Annealed at 1650°F and Tested in Argon at 1500°F.

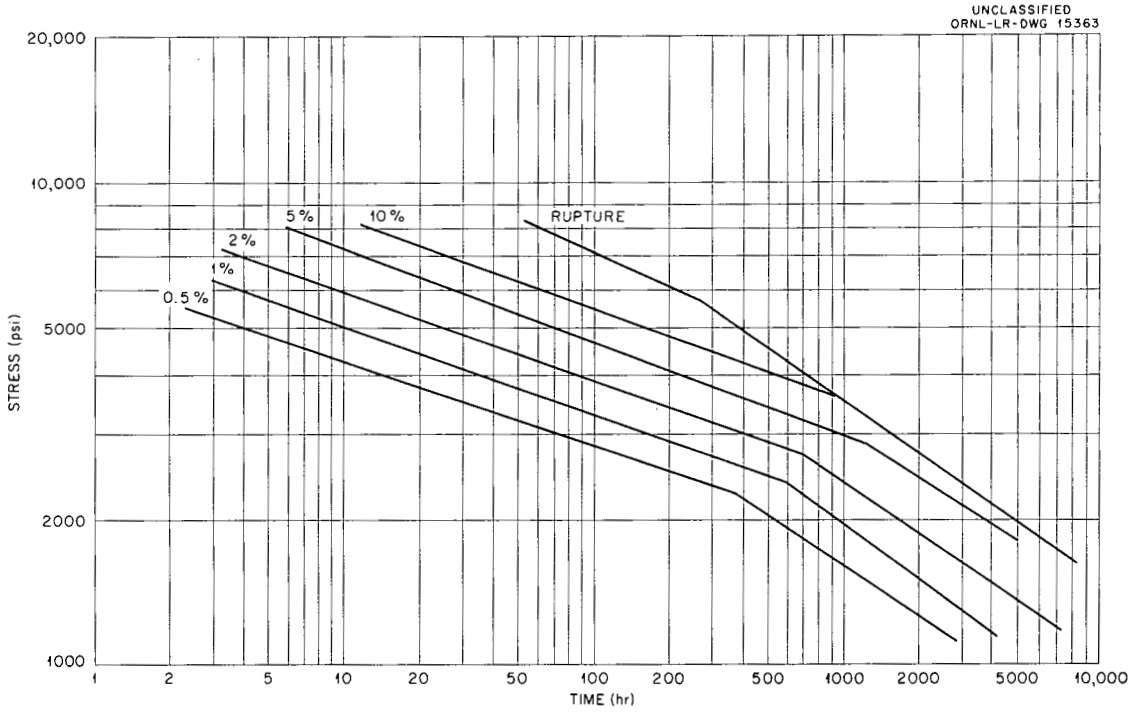

Fig. 75. Design Curves for Inconel Sheet (Heat B) Annealed at 2050°F and Tested in Argon at 1500°F.

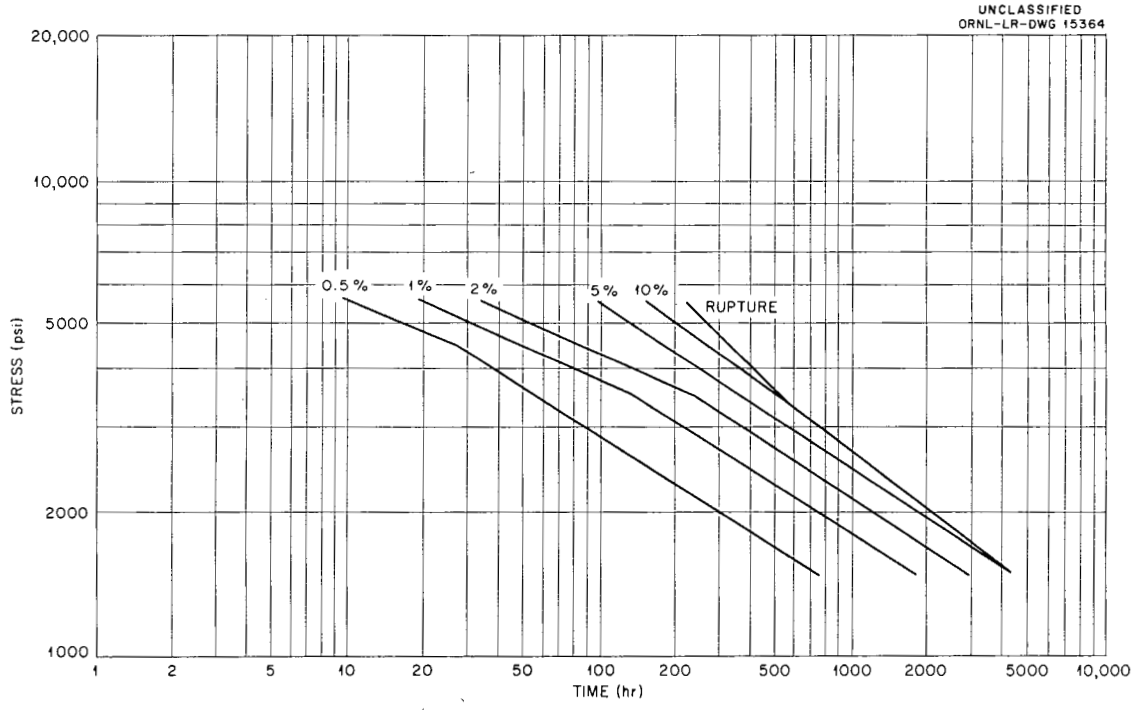

Fig. 76. Design Curves for As-Received Inconel Sheet (Heat B) Tested in NaF-ZrF_4-UF_4 (50-46-4 mole %) at 1500°F. (Secret with caption)

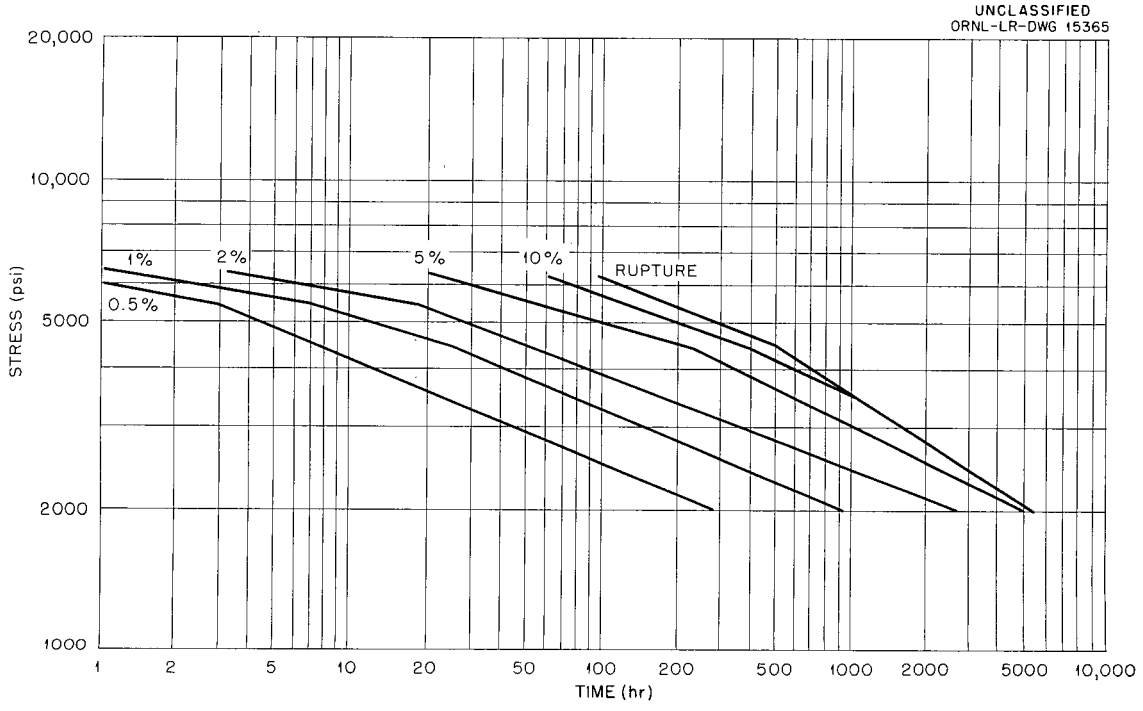

Fig. 77. Design Curves for Inconel Sheet (Heat B) Annealed at 2050°F and Tested in $NaF-ZrF_4-UF_4$ (50-46-4 mole %) at 1500°F. (Secret with caption)

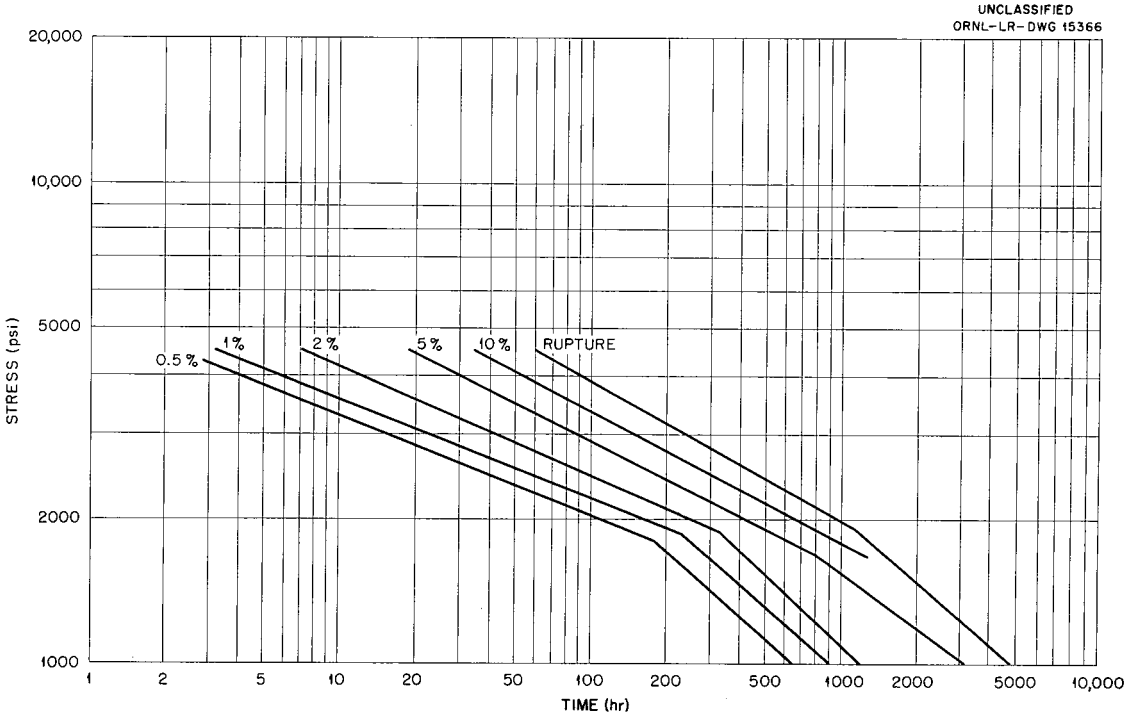

Fig. 78. Design Curves for As-Received Inconel Sheet (Heat B) Tested in Argon at 1650°F.

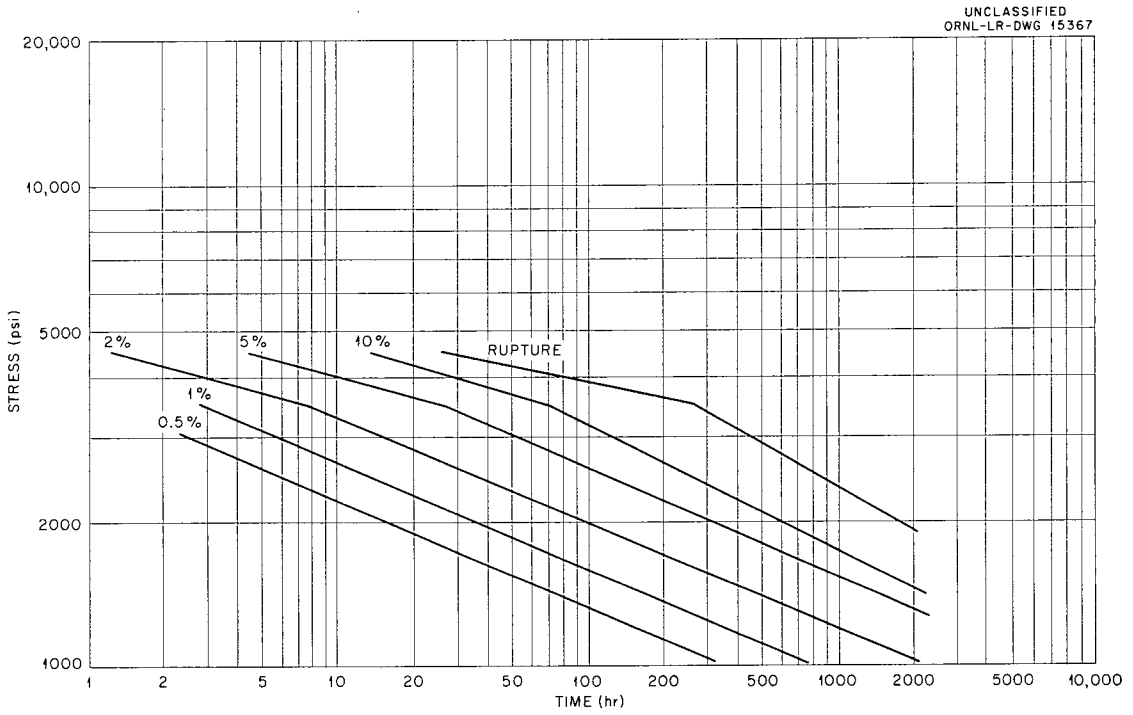

Fig. 79. Design Curves for Inconel Sheet Annealed at 2050°F and Tested in Argon at 1650°F.

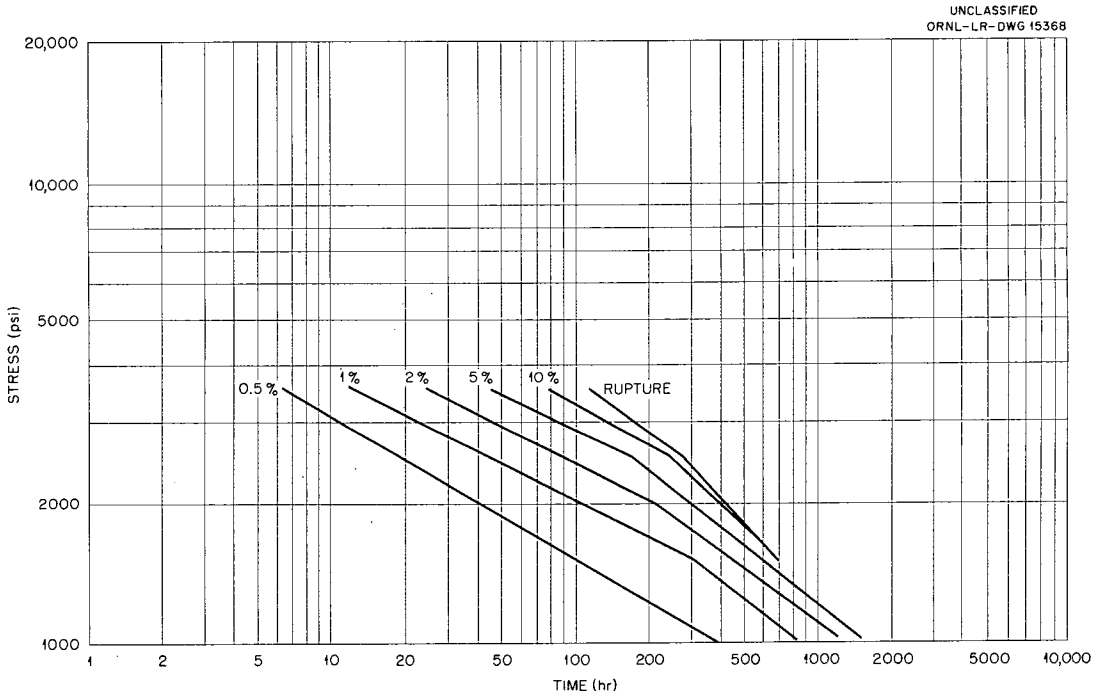

Fig. 80. Design Curves for As-Received Inconel Sheet (Heat B) Tested in NaF-ZrF_4-UF_4 (50-46-4 mole %) at 1650°F. (Secret with caption)

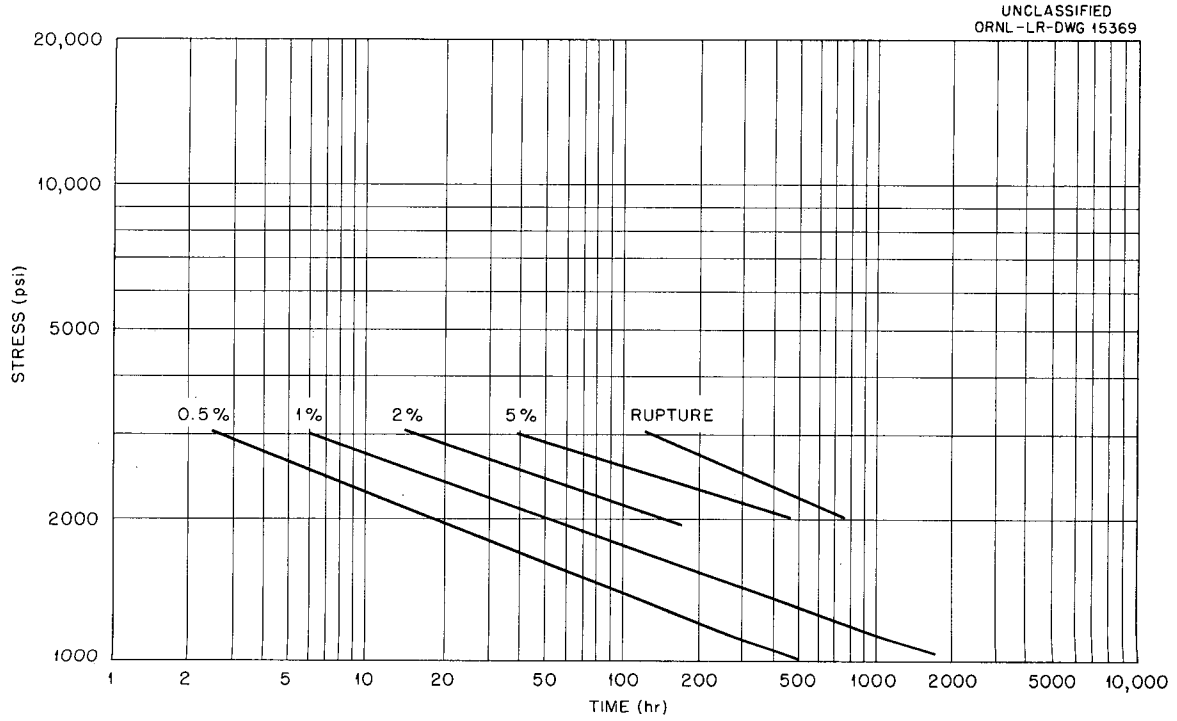

Fig. 81. Design Curves for Inconel Sheet (Heat B) Annealed at 2050°F and Tested in NaF-ZrF_4-UF_4 (50-46-4 mole %) at 1650°F. (Secret with caption)

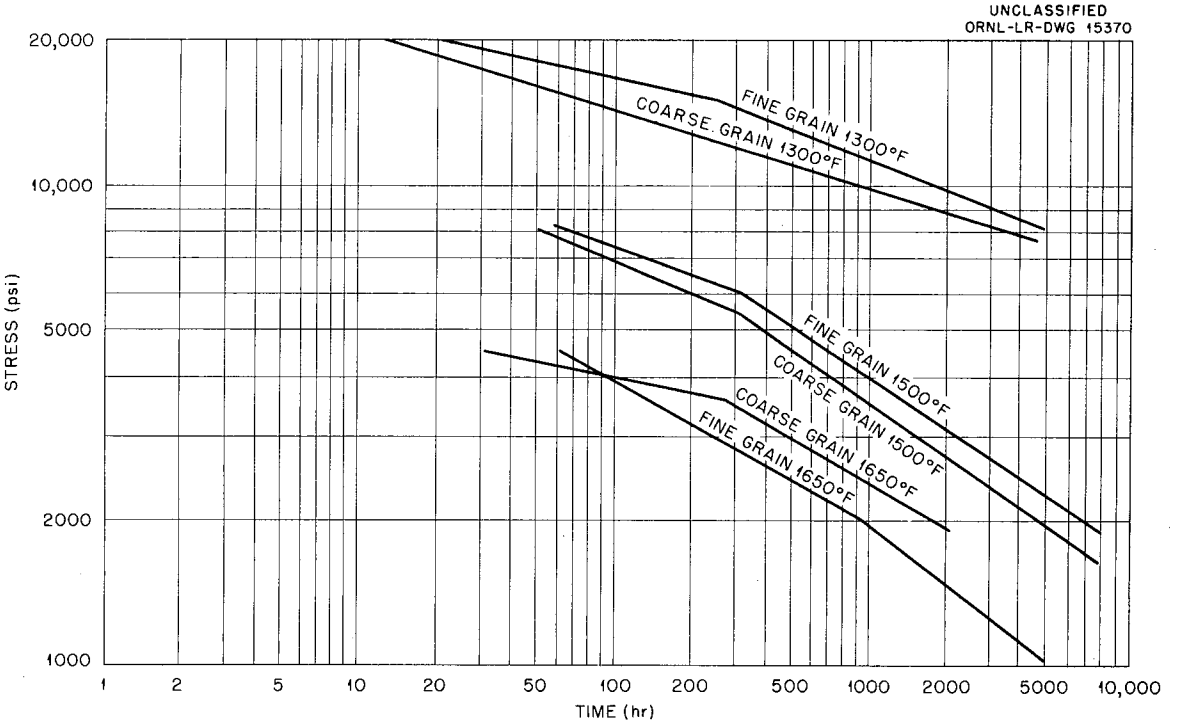

Fig. 82. Comparison of Stress-Rupture Properties of Fine-Grain and Coarse-Grain Inconel Sheet Tested in Argon at 1300, 1500, and 1650°F.

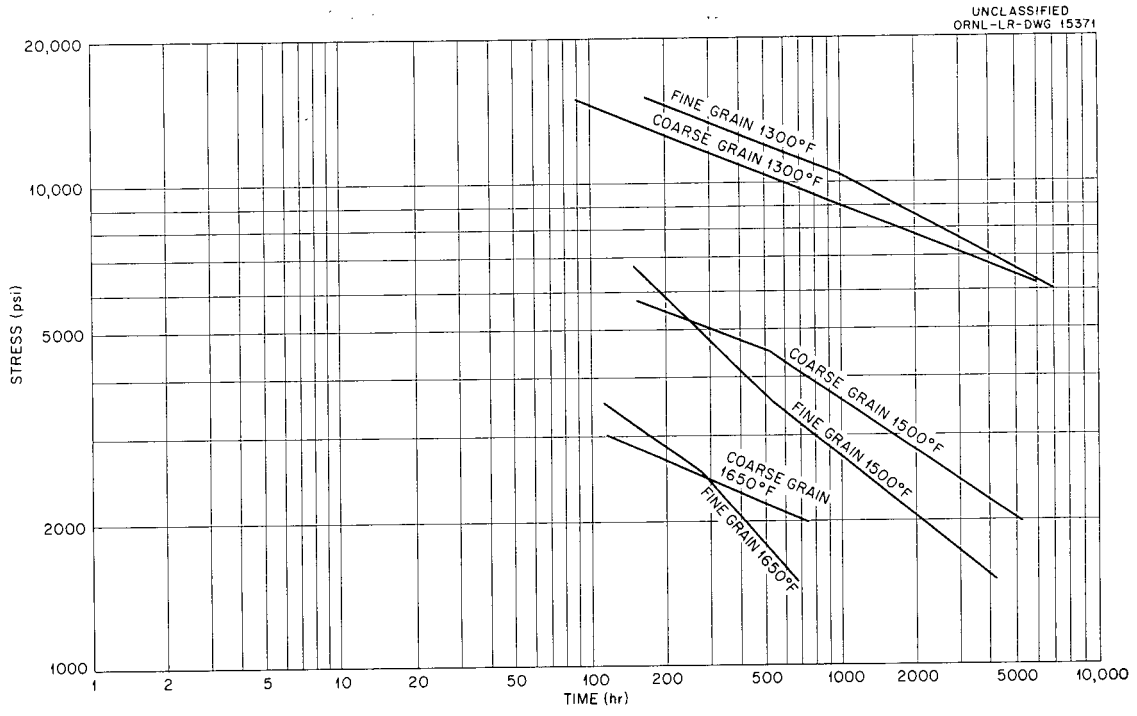

Fig. 83. Comparison of Stress-Rupture Properties of Fine-Grain and Coarse-Grain Inconel Sheet Tested in NaF-ZrF_4-UF_4 (50-46-4 mole %) at 1300, 1500, and 1650°F. (Secret with caption)

NONDESTRUCTIVE TESTING

R. B. Oliver

R. W. McClung J. W. Allen

J. K. White

The recently reported success in the inspection of small-diameter Inconel and Hastelloy B tubing with the Cyclograph[1] has prompted further study of the instrument. It is primarily a tuned oscillator in which the oscillator coil encircles the tubing. The instrument measures the amplitude of the oscillations, the amplitude being a measure of the resistive component of the coil's impedance. Theoretically, since only the resistive component is measured, all changes in the tubing will cause the same type of signal variation;[1] thus, good tubing could possibly be rejected because of an inconsequential variation. However, experience has proved that tubing wobble in the coil, which is the worst offender in producing spurious flaw indications, can be eliminated by a well-designed mechanical feed mechanism such as shown in Fig. 84. The instrument is sensitive to slight changes in the outside tubing diameter and in wall thickness, but these changes occur very slowly over the length of the tube and can be easily separated from flaws, which give abrupt signals.

The great advantage of the Cyclograph is that its operating frequency is determined by its sensing coil, and, hence, the frequency may be altered by merely changing this coil. The proper frequency for a particular tube is selected according to its outside diameter, wall thickness, permeability, and conductivity. Figure 85 is a graph of the Cyclograph reading vs tubing wall thickness expressed as percentage of the outside diameter. The parameter for the graph is frequency normalized to a value f_c, which is determined by the outside diameter, permeability, and conductivity, according to the relationship given on the graph. The operating frequency which gives the best results is the one which locates a point near a peak on the graph of Fig. 85. The dashed lines indicate the nonlinear characteristic of the instrument near the "quench" or zero-reading axis and indicate where extreme sensitivity to small flaws in the tubing is possible. Figure 86 is a plot such that each frequency will locate a peak on the graph of Fig. 85 appropriate to a particular wall thickness. By the consistent use of operating frequencies chosen from these plots, flaw types will always be detected in the same relative magnitudes. For instance, an inside-diameter crack extending through 10% of the wall thickness would cause the same indication from a $\frac{1}{4} \times 0.025$ in. tube as from a $\frac{1}{2} \times 0.049$-in. tube. Although it is not possible to obtain a calibration of flaw size vs instrument indication, it is possible to obtain an approximate determination of flaw size in terms of percentage reduction in wall thickness, averaged over the length of the coil. Figure 87 shows typical Cyclograph indications of outside-diameter cracking in Hastelloy B tubing and inside-diameter intergranular attack in Inconel tubing.

The eddy-current probe coil is currently being used in combination with the immersed ultrasonic transducer. The instrument and probe are shown in Fig. 88 in block-diagram form. The exciting coil is fed with a constant current from the crystal-controlled oscillator-amplifier, and the voltage from the pickup coil is balanced to zero by the balance circuitry. Thus, only the changes in pickup coil voltage resulting from variations in the tube wall are amplified and examined by the phase-sensitive detectors. The phase-sensitive detectors are necessary to separate the flaw signals from those resulting from probe liftoff and from vibration of the tubing. To accomplish this separation, the operating frequency must be selected (on the basis of tube wall thickness and conductivity) so as to allow approximately 90-deg phase difference in the flaw and liftoff signals. A frequency of 200 kc is utilized for the inspection of Inconel tubing having a wall thickness of 0.025 in. The readout is a "B" scan type presentation of flaw signal vs tubing rotation on a persistent-screen oscilloscope.

A variety of different probes and holders have been constructed and have been tested with varying degrees of success. The smallest and most sensitive probe made to date has an effective diameter of $\frac{1}{16}$ in. and was able to detect very

[1] R. B. Oliver *et al.*, *Met. Semiann. Prog. Rep. Oct. 10, 1955*, ORNL-1988, p 38.

UNCLASSIFIED
ORNL-LR-DWG 11015

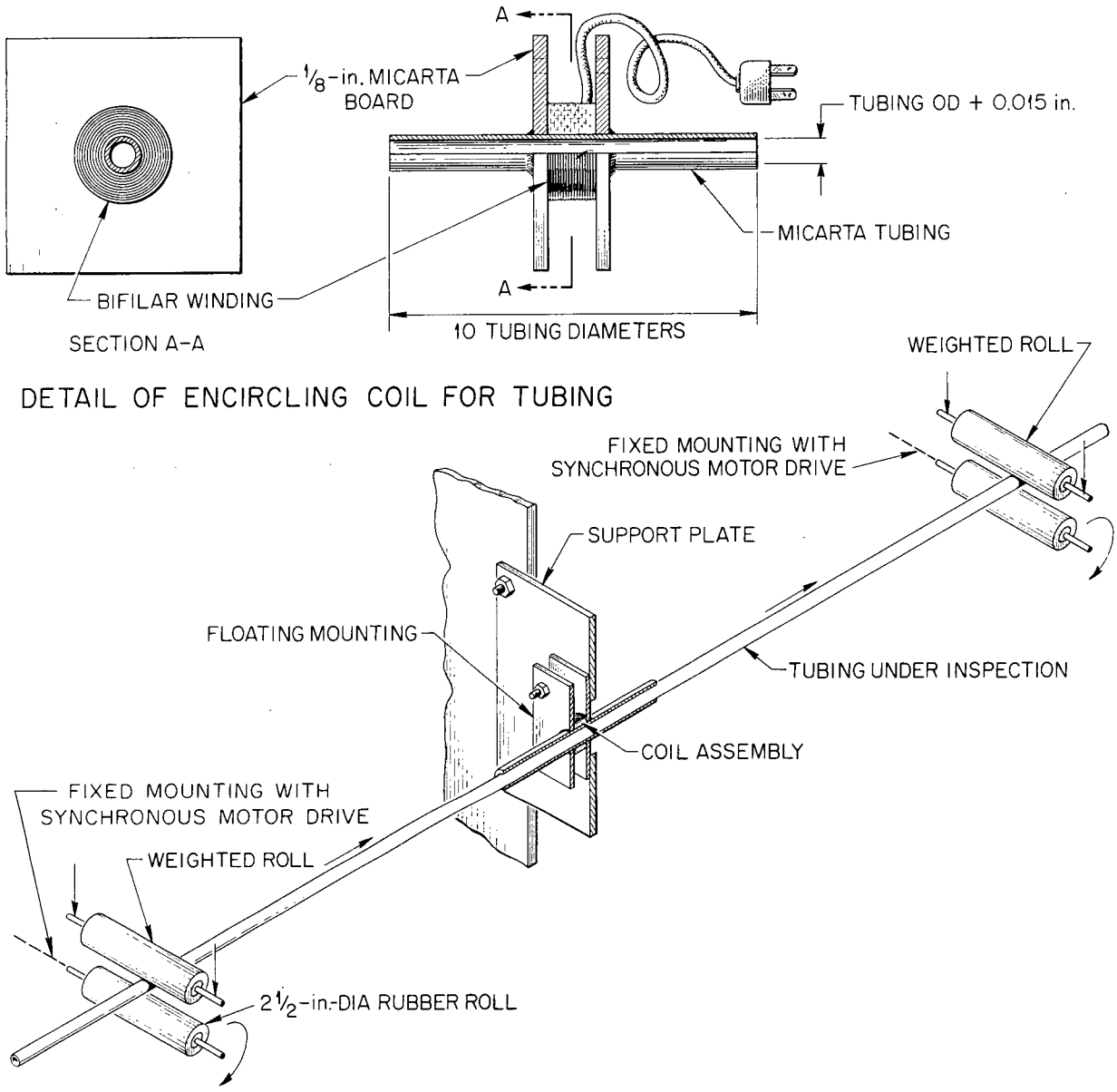

Fig. 84. Cyclograph Coil Assembly and Feed Mechanism for Tubing Inspection.

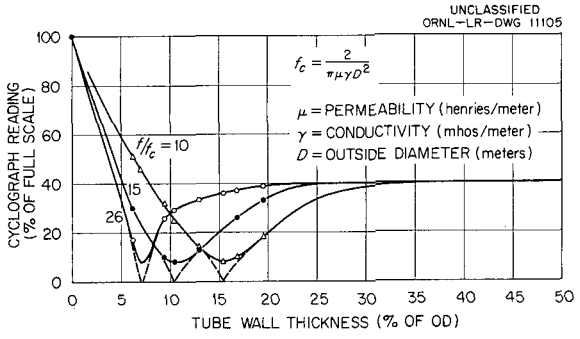

Fig. 85. Cyclograph Reading vs Tubing Wall Thickness with f/f_c as a Parameter.

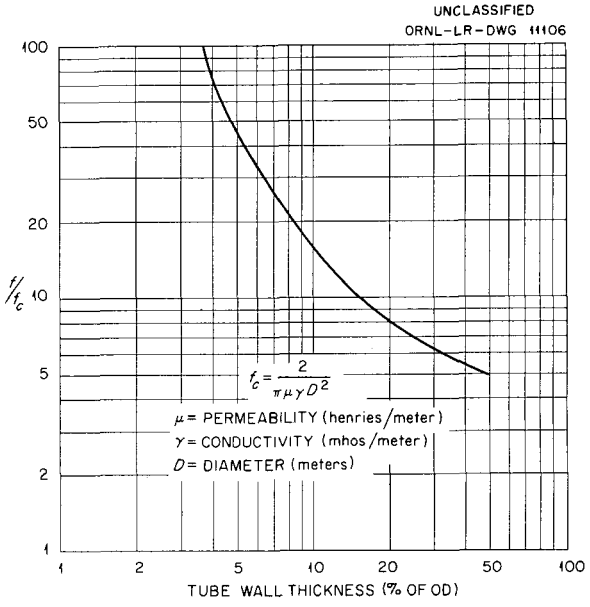

Fig. 86. Frequency vs Tubing Wall Thickness for Maximum Resistive Coil Impedance.

UNCLASSIFIED
ORNL-LR-DWG 11104

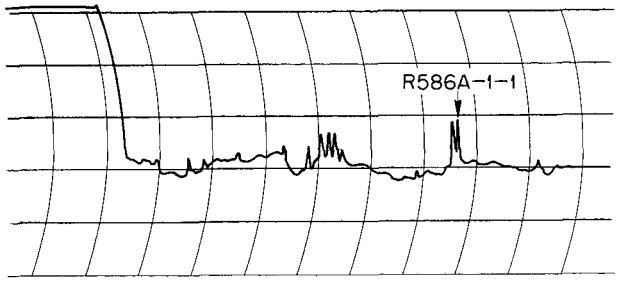

CYCLOGRAPH TRACE AT 160 kc OF REJECTED 0.25-in.-OD x 0.049-in.-WALL HASTELLOY B TUBING. OUTSIDE DIAMETER RADIAL CRACK 0.027 in. DEEP AT POSITION R586A-1-1 IS SHOWN IN FIG. 91.

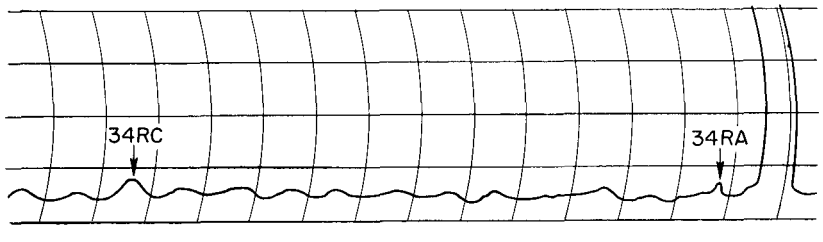

CYCLOGRAPH TRACE AT 200 kc OF REJECTED 0.25-in.-OD x 0.025-in.-WALL INCONEL TUBING. INSIDE DIAMETER INTERGRANULAR ATTACK AT POSITION 34RA TO A MAXIMUM PENETRATION OF 0.002 in. IS SHOWN IN FIG. 94.

Fig. 87. Cyclograph Traces of Defective Tubing.

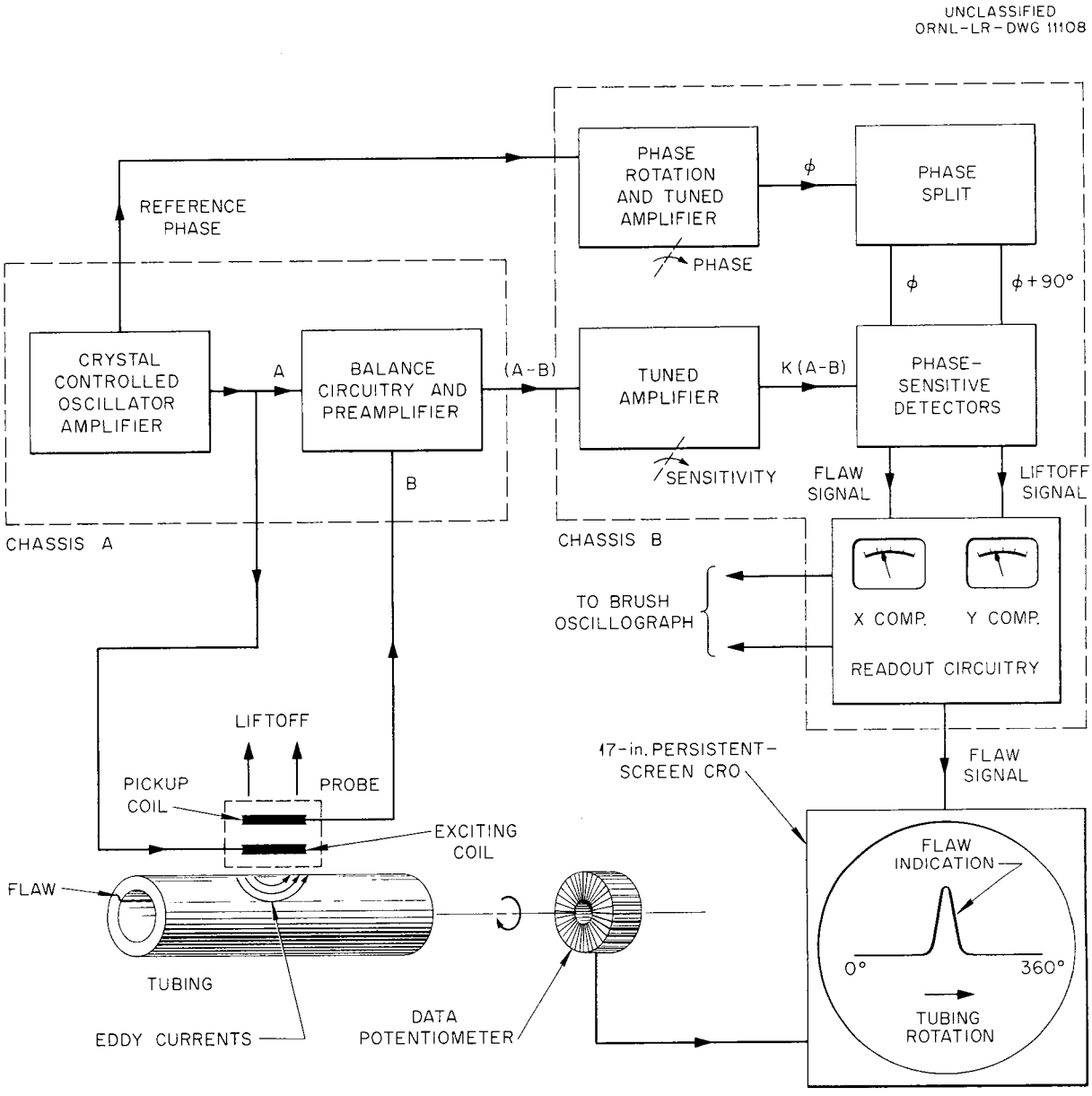

Fig. 88. Inspection of Tubing with an Eddy-Current Probe.

minute pin holes and cracks. It has been determined that the tubing can be rotated at 300 to 400 rpm without loss in definition of signals. Because of the small diameter, the longitudinal speed of the probe, even at these rotational speeds, is very slow for quantity inspection. For this reason, elongated probes, such as the one shown in Fig. 89, are being utilized, but with some loss in minute-flaw sensitivity and definition. Probe holders similar to the one shown have proved the most satisfactory.

Recent investigations have been conducted with a 5 mc, $\frac{3}{4}$-in.-dia high-resolution Li_2SO_4 transducer manufactured by Electro Circuits, Inc., Pasadena, California. This transducer, compared with the conventional 5 mc, $\frac{3}{8}$-in.-dia quartz-crystal transducer, produces a cleaner screen presentation on the cathode-ray tube by providing a greater signal-to-noise ratio, thus rendering detection of smaller defects possible. It is now planned to use this Li_2SO_4 high-resolution transducer for the inspection of tubing.

For high-speed production inspection, the speed with which the length of tubing can be scanned is limited by the length of tubing which can be inspected during one revolution of the tube. This limits the pitch ratio (longitudinal scan movement per tube revolution) which will ensure complete inspection coverage. To increase the pitch, the forementioned change was made, that is, from the $\frac{3}{8}$-in.-dia to the $\frac{3}{4}$-in.-dia transducer. However, the $\frac{3}{4}$-in.-dia transducer flooded the entire cross section of the $\frac{1}{4}$-in. tubing being inspected, producing a confused cathode-ray-tube pattern when the full $\frac{3}{4}$-in. diameter was used. In order to overcome this difficulty and still maintain the greater pitch ratio, a collimator was fabricated which effectively blocks out approximately one-third of the transducer energy pattern along a chord parallel to the tubing axis (see Fig. 90). With this collimation, a pitch of $\frac{1}{2}$ in. per revolution can be maintained.

Much effort has been expended toward the identification of the several characteristic defect types found in small-diameter tubing. This effort has included the preparation of photomicrographs of the appropriate tubing sections, as well as the recording of the indication of the defect as presented by each of several inspection methods. The indications from eddy-current probe-coil and

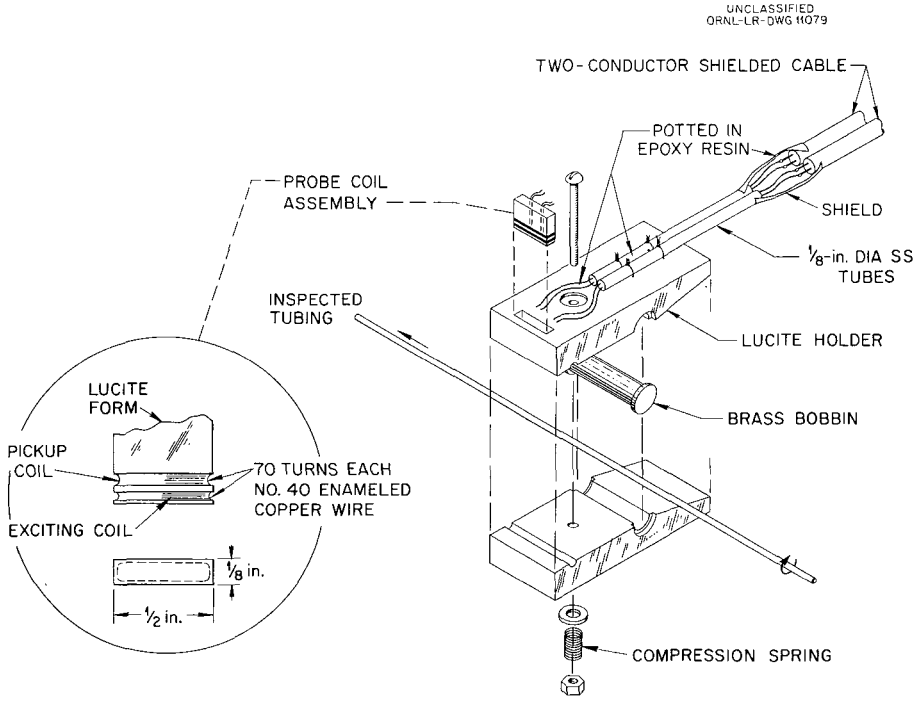

Fig. 89. Eddy-Current Probe Coil and Holder for Scanning Small-Diameter Tubing.

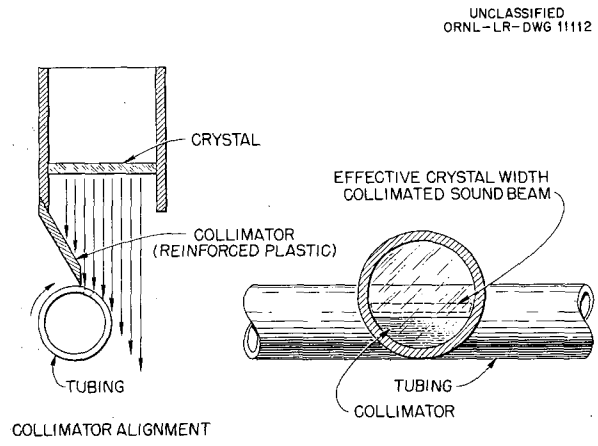

Fig. 90. Ultrasonic Collimation for Tubing Inspection.

immersed ultrasonic tests were recorded by photographing their respective "B" scan presentations. A certain amount of difficulty has been encountered in the preparation of representative metallographic sections because of the minute dimensions of the defects and because of inability to sufficiently pinpoint the defects for good metallographic presentation.

A defect type which has been prevalent in small-diameter Hastelloy tubing is a longitudinal crack which may penetrate as much as 80% of the tube wall from the outside surface. A typical example detected in ¼-in. Hastelloy B tubing is illustrated in Fig. 91. This crack penetrates approximately 0.027 in. in a 0.049-in. wall. The presence of this crack, as indicated by the Cyclograph, is shown in Fig. 87. The ultrasonic "B" scan for this

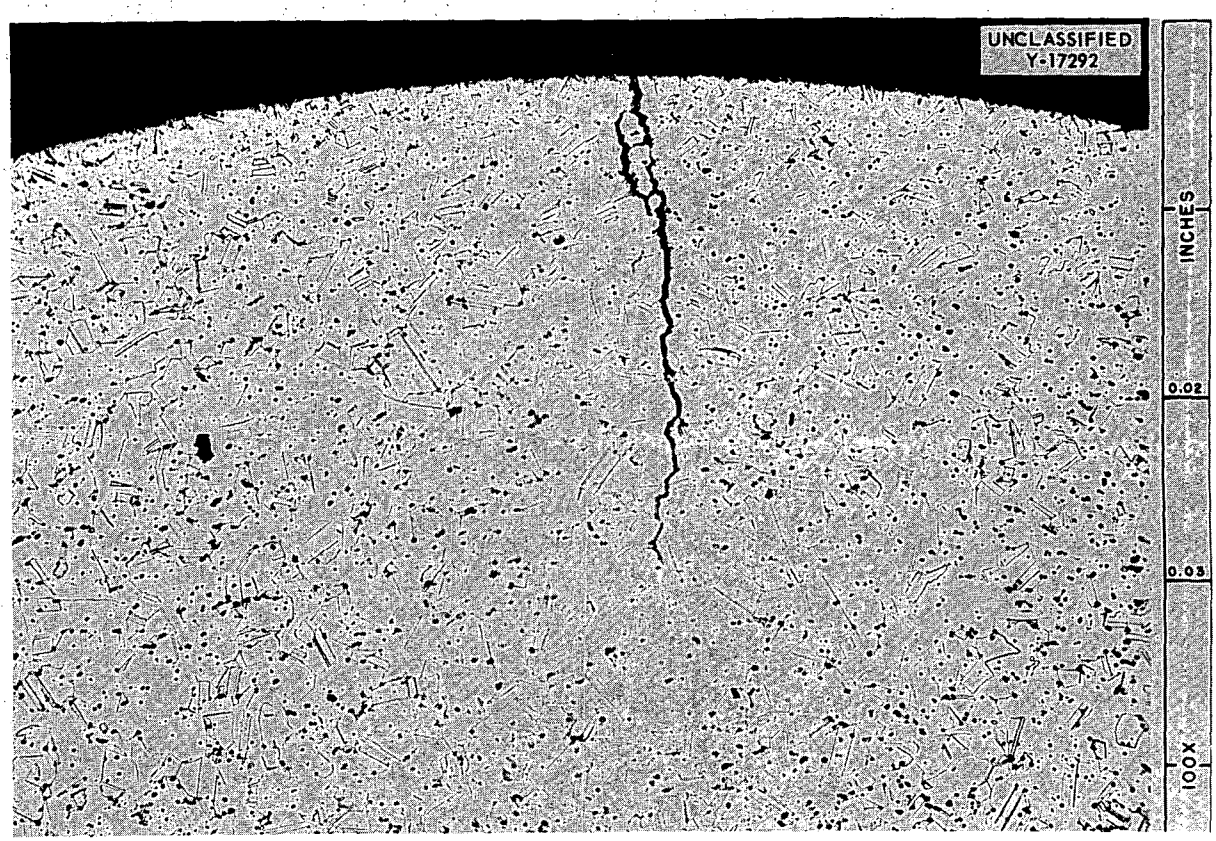

Fig. 91. Photomicrograph of Crack in ¼-in.-OD × 0.049-in.-Wall Hastelloy B Tubing. 100X. Reduced 2%.

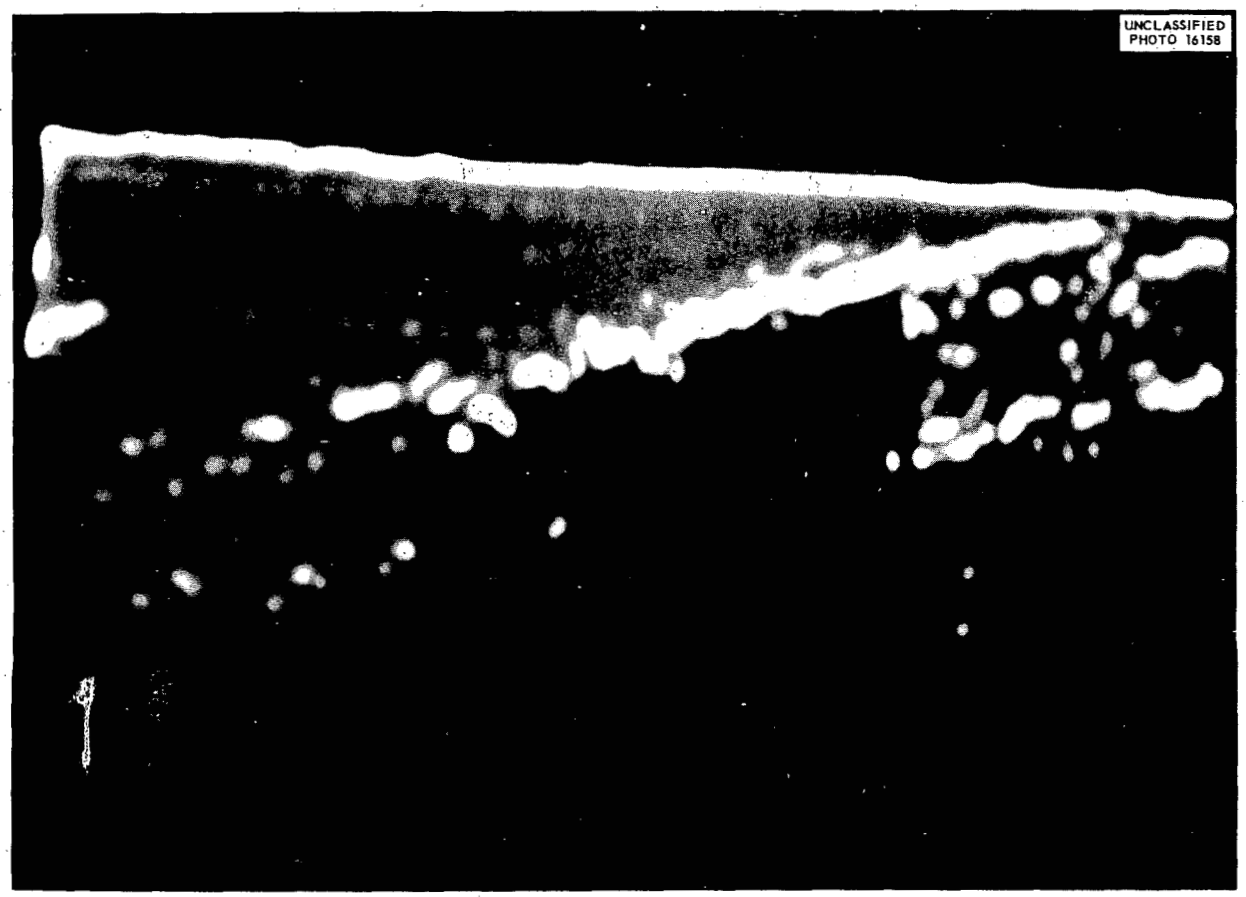

Fig. 92. Ultrasonic "B" Scan of Crack Shown in Fig. 91.

crack is seen in Fig. 92. The crack is of such a size that it can be detected by ultrasound through almost 300 deg of the tubing rotation, as is demonstrated by the diagonal indication extending almost completely across the screen. The eddy-current probe-coil "B" scan is presented in Fig. 93.

A characteristic defect in Inconel is intergranular attack, illustrated in Fig. 94. Attempts to ultrasonically detect this have been somewhat inconclusive, quite possibly, because of two factors: small penetration and orientation not parallel to the axis of the tubing. It is believed that these are cumulative factors which do not lend themselves to ultrasonic inspection. The Cyclograph detected this condition (Fig. 87, position 34RA).

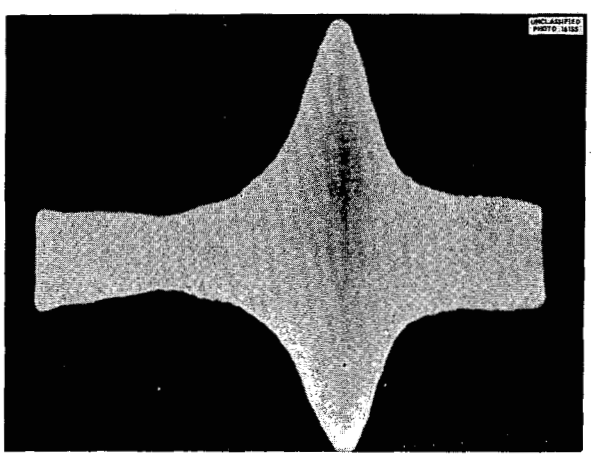

Fig. 93. Eddy-Current "B" Scan of Crack Shown in Fig. 91.

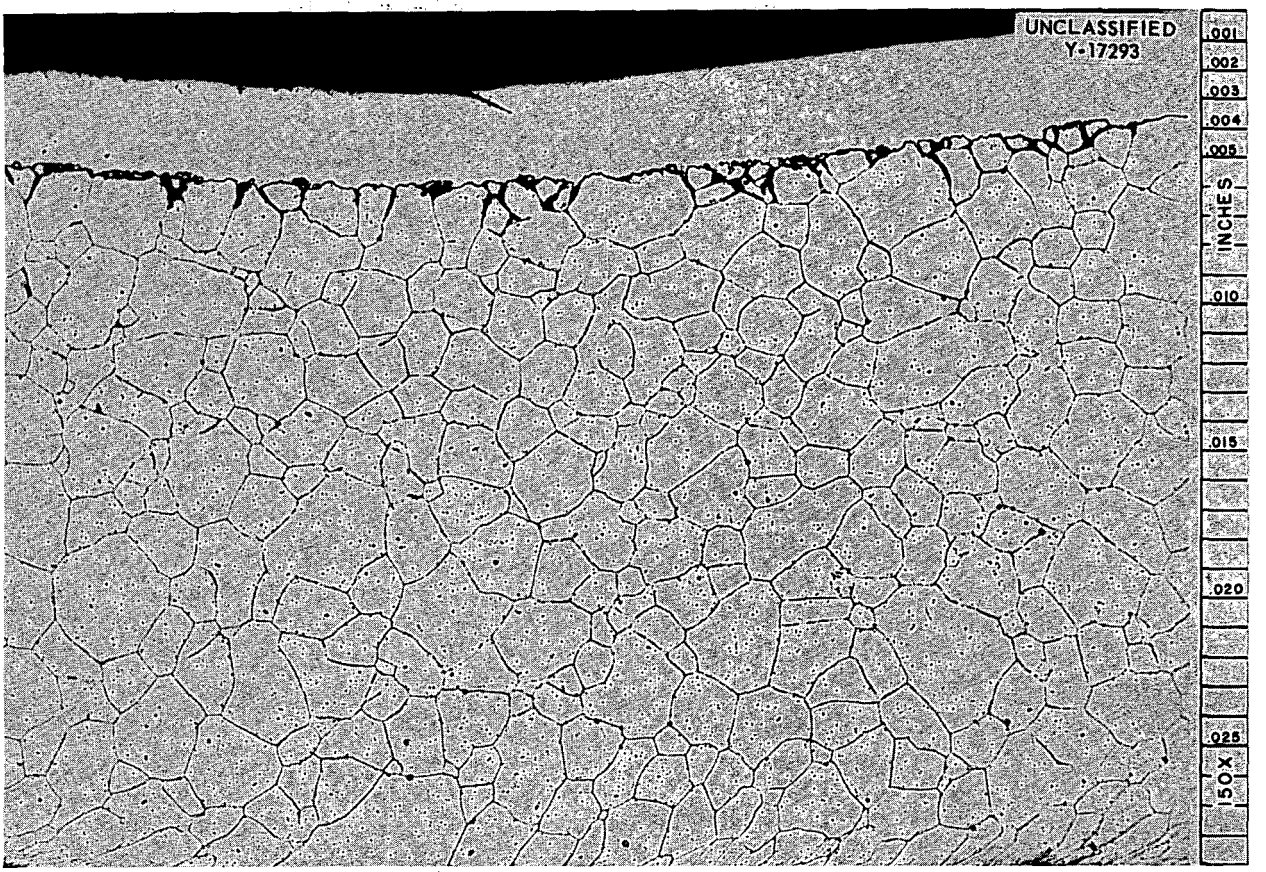

Fig. 94. Photomicrograph of Intergranular Attack in ¼-in.-OD × 0.025-in.-Wall Inconel Tubing.

Figure 95 is a photomicrograph of a section in which a small gouge, extending for about 1/16 in. along the tubing, was seen on the tubing surface. Figure 96 is a representative "B" scan picture for the ultrasonic detection of this defect.

Figure 97 is representative of defect types, as detected by ultrasound on the inside diameter of 3/16-in.-OD × 0.025-in.-wall Inconel tubing.

For comparison of inspection results as obtained by immersed ultrasound, radiography, and fluorescent penetrant, six pieces of Inconel tubing, 3/16 in. in outside diameter, 0.025-in. in wall thickness, and 7 ft in length, were inspected by the respective methods. Mere detection was considered sufficient to designate a defect, and no attempt was made to estimate the defect size. Table 39 presents the total number of such defect indications and the correlation obtained between the various methods. The sampling is insufficient to arrive at a final decision concerning the relative merits of the inspection methods, but the data indicate definite trends. It seems that any one of the methods alone would not be adequate; and if any one of them was eliminated, a few defects would be overlooked, as noted in Table 39.

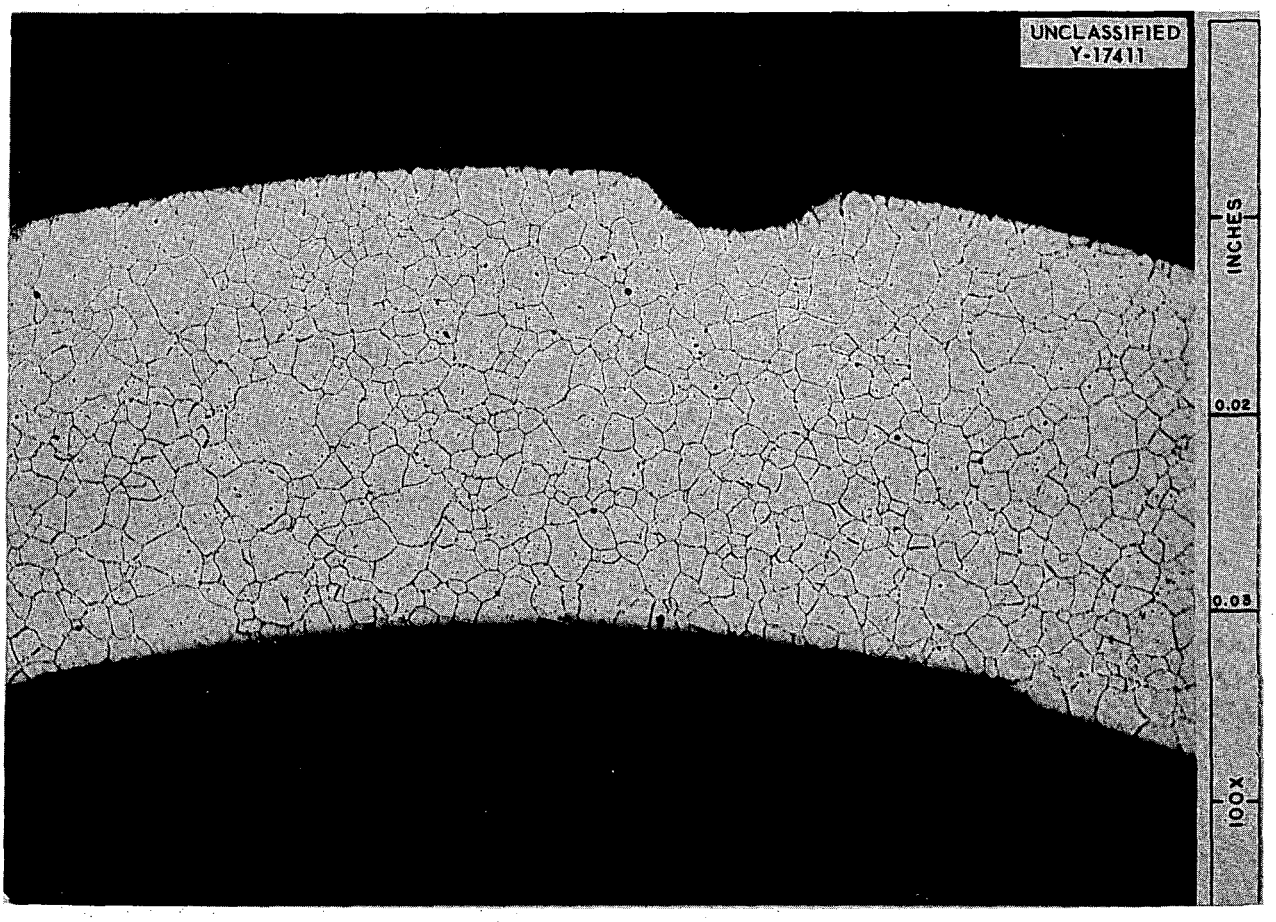

Fig. 95. Photomicrograph of Outside-Diameter Gouge on ¼-in.-OD × 0.025-in.-Wall Inconel Tubing.

TABLE 39. INSPECTION OF CX-900 INCONEL TUBING

Tube No.	Number of Defects Found by Each Method			Number of Defects Which Did Not Correlate with Other Methods			Number of Defects Correlated by Two Methods			Number of Defects Correlated by Three Methods
	X-ray	Ultrasound	Fluorescent Penetrant	X-ray	Ultrasound	Fluorescent Penetrant	X-ray and Penetrant	X-ray and Ultrasound	Ultrasound and Penetrant	
CX-1	7	13	14	2	5	6	3	3	6	1
CX-2	2	4	16	2	0	12	0	0	4	0
CX-3	1	25	13	0	13	1	1	1	12	1
CX-4	6	5	12	6	2	9	0	0	3	0
CX-5	3	4	14	1	1	11	1	1	2	0
CX-6	2	7	13	0	3	7	2	0	4	0
Total	21	58	82	11	24	48	7	5	30	2

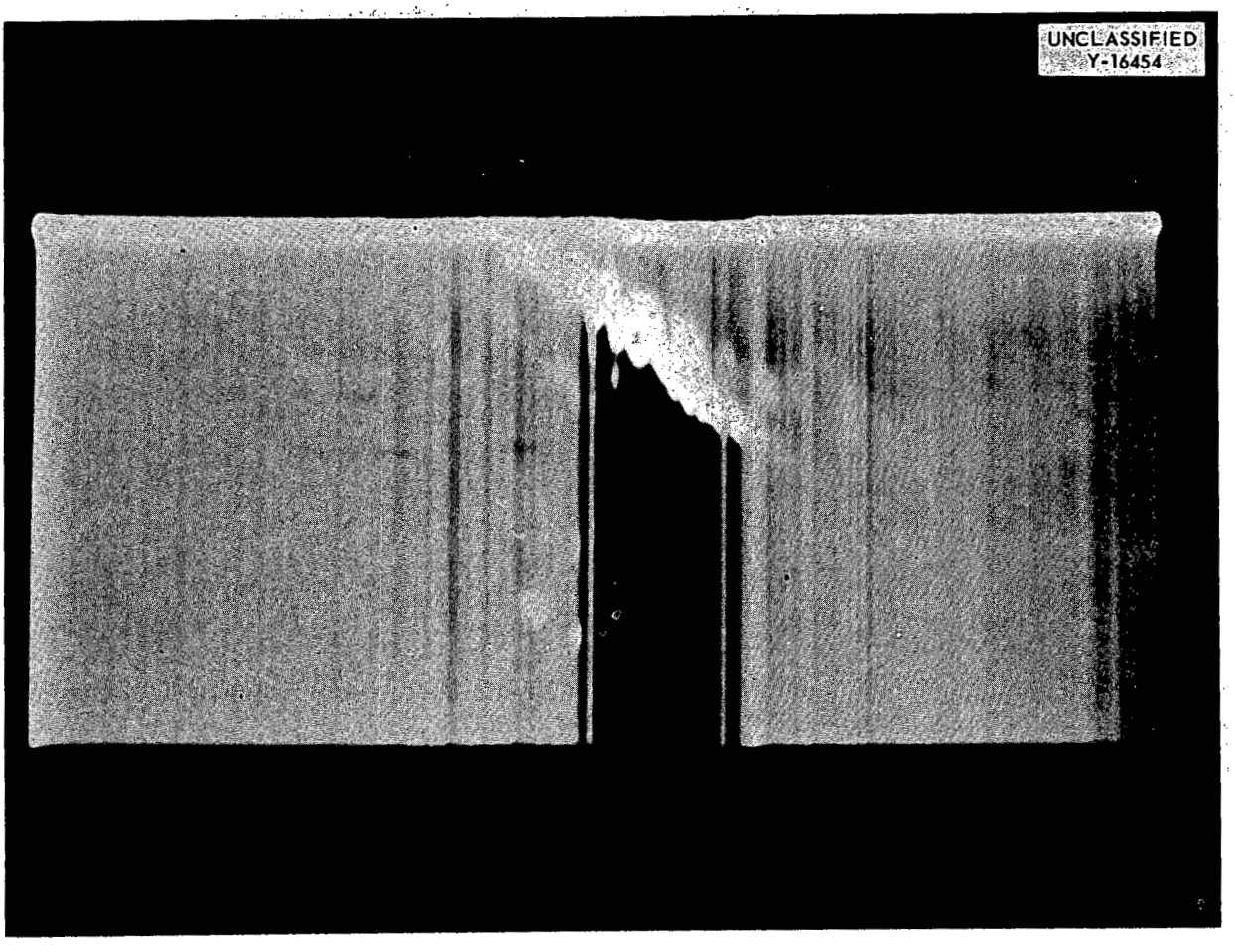

Fig. 96. Ultrasonic "B" Scan of Gouge Shown in Fig. 95.

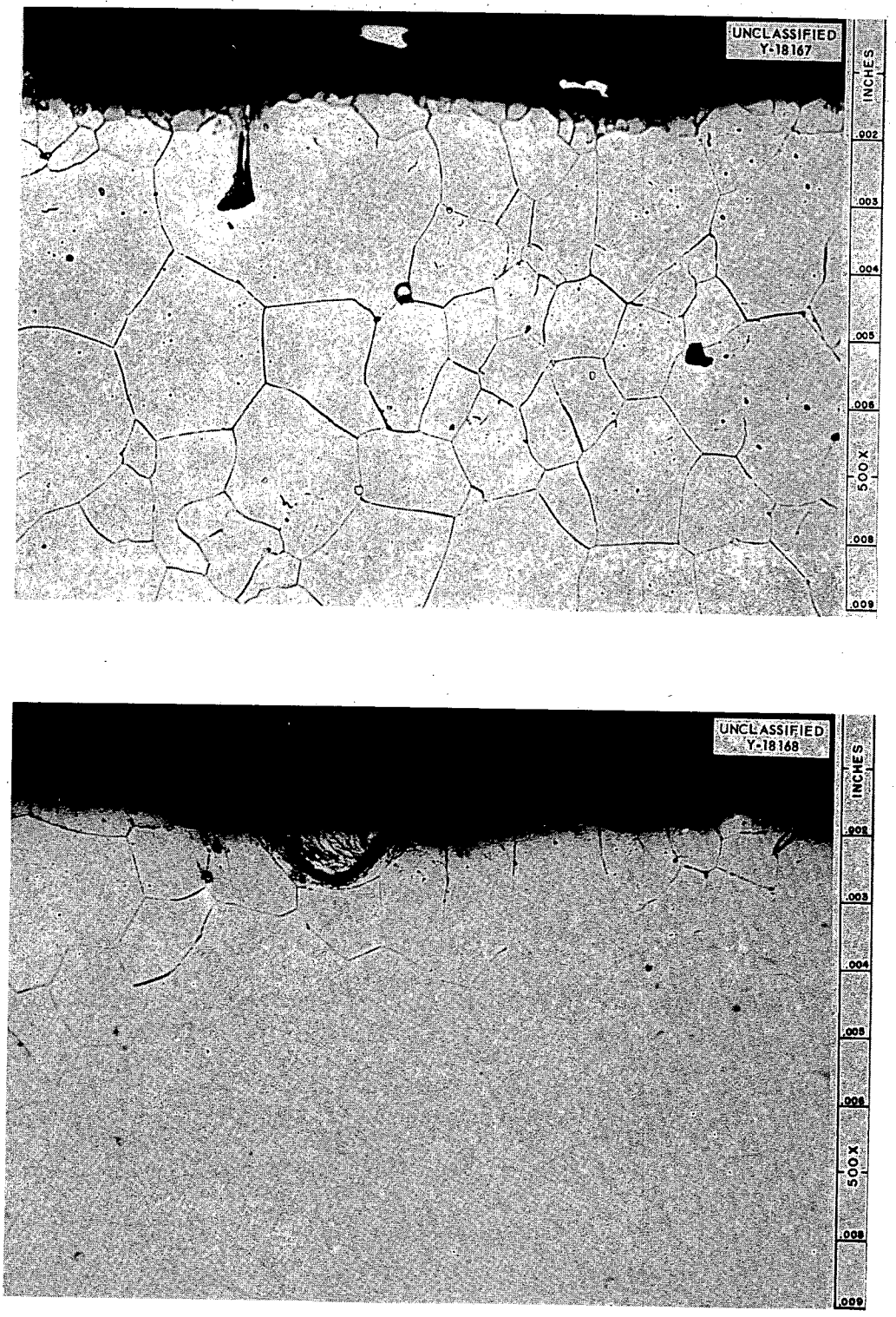

Fig. 97. Typical Defects on Inside Surface of Inconel Tubing. 500X. Reduced 18%.

WELDING AND BRAZING

P. Patriarca A. E. Goldman G. M. Slaughter

METALLOGRAPHIC EXAMINATION OF FAILURES OCCURRING IN NaK-TO-AIR RADIATORS

ORNL Radiator No. 1 and York Radiator No. 1

On July 24, 1955, a 500-kw high-conductivity fin radiator, fabricated by the Metallurgy Division and known as ORNL radiator No. 1, failed as a result of a leak after having been subjected to elevated-temperature service for approximately 600 hr. For the majority of this service time, the radiator was operated under isothermal conditions in the temperature range 1000 to 1600°F. For approximately 66 hr of the total time, the radiator was operated with the air blower on, thereby imposing a temperature difference of 50 to 300°F between the inlet and outlet NaK. Figure 98 is a photograph of the radiator as received from the test site.

On September 6, 1955, one of the first 500-kw high-conductivity-fin radiators fabricated according to ORNL specifications by the York Corporation, York, Pennsylvania, also failed as a result of a leak. This radiator survived approximately 150 hr of elevated-temperature service, 80 hr of which were isothermal and the remainder under conditions of a NaK temperature difference. Figure 99 is a photograph of the York radiator after failure. It may be noted that the extent of destruction caused by the fire following the failure was minimized by prompt detection and dumping of the NaK. The

UNCLASSIFIED
Y-16065

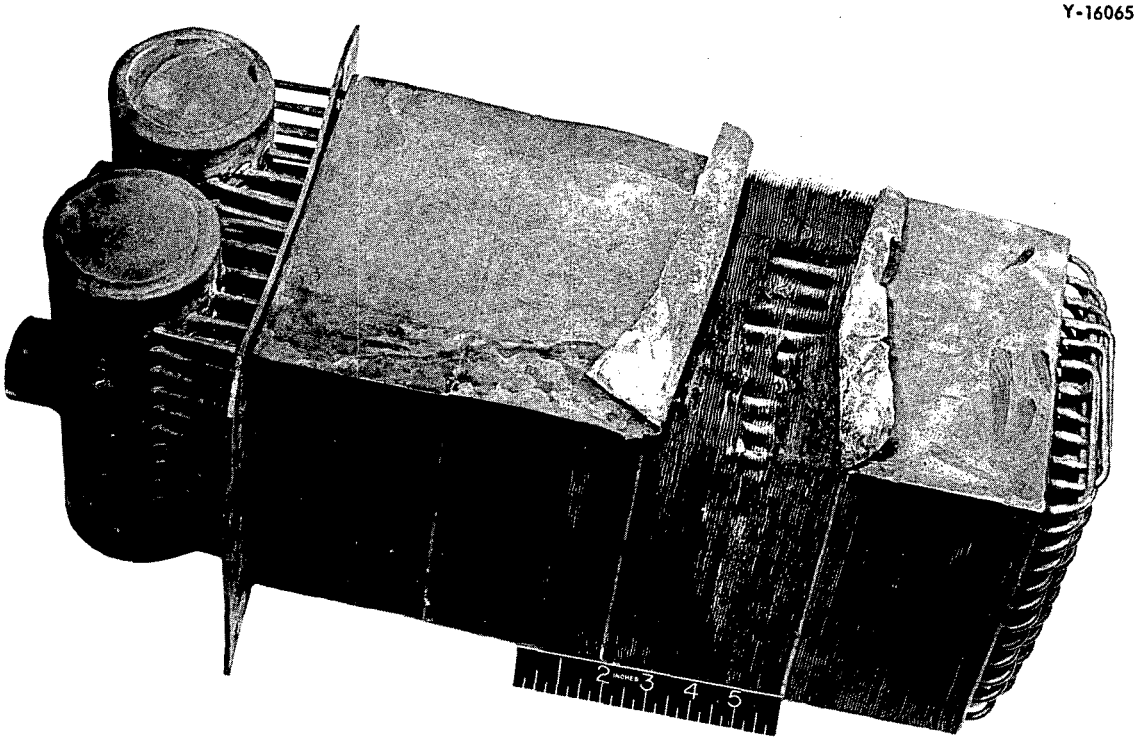

Fig. 98. ORNL Radiator No. 1 Which Failed After Approximately 600 hr of Elevated-Temperature Service in the Range 1000 to 1600°F.

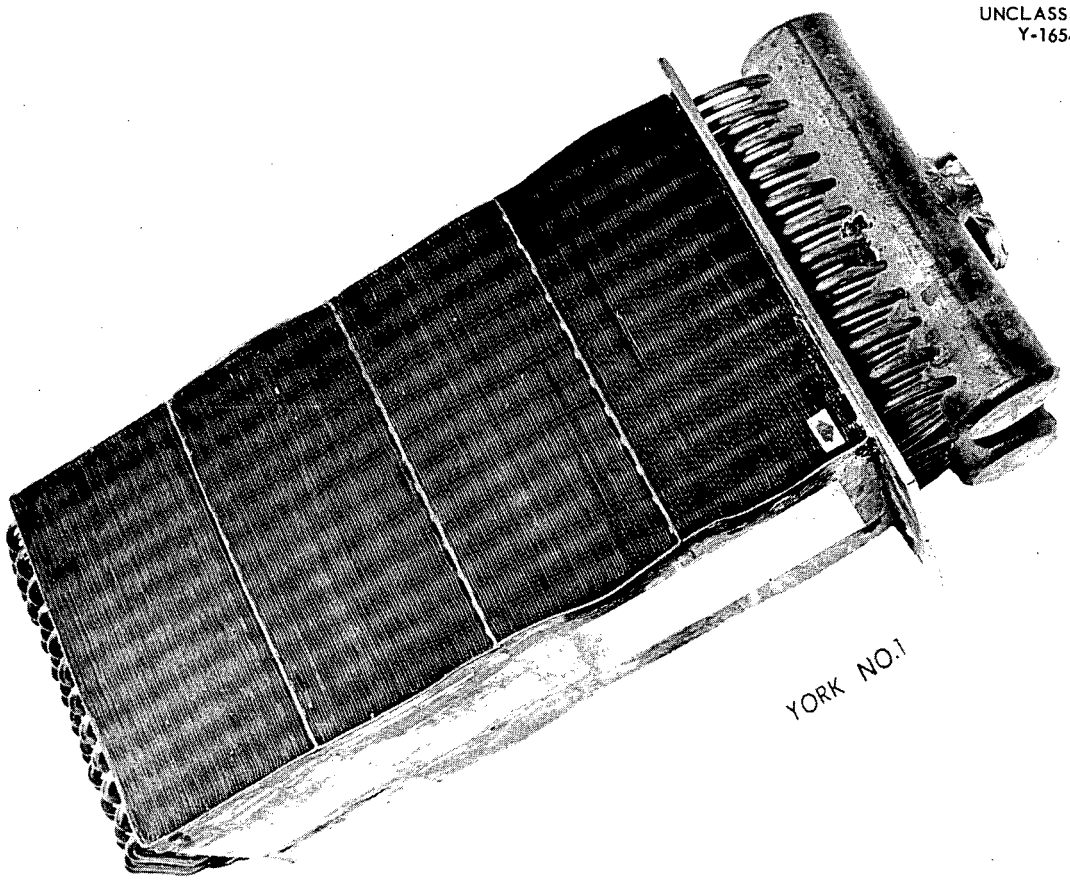

Fig. 99. York Radiator No. 1 Which Failed After Approximately 150 hr of Elevated-Temperature Service in the Range 1000 to 1600°F. Arrow indicates site of failure.

ORNL radiator, on the other hand, was ravaged by fire to such an extent that determination of the cause of the failure proved to be impossible.

From the foregoing, it appears that the service lives of the two radiators differed significantly only in the extent of isothermal service.

Examination Procedure and Results. – A sketch of a 500-kw air-cooled radiator is given in Fig. 100, wherein the regions that failed are denoted and the various parts are identified according to the nomenclature used throughout this report.

Figure 101 is a photograph of that section of the ORNL radiator which was destroyed by the failure wherein a total of 27 gross leaks were detected when pressure tested under water. Detection and examination of the original leak was impossible.

The York radiator after partial sectioning is illustrated in Fig. 102. Section 5 in this photograph is shown enlarged in Fig. 103. Each tube in this section was pressurized under water, and the leak was located by observing that bubbles emerged from the intersection of one of the tubes and the support member. The exact location of the leak is illustrated in Fig. 104. The arrow is pointed to the site where the air bubbles were evolved during the pressure test. This area was mounted intact for metallographic examination and was examined microscopically at frequent intervals as grinding and polishing down to the leak progressed. Although time consuming, this procedure was deemed necessary in order to ensure that metallographic evidence of the leak would not be destroyed.

UNCLASSIFIED
ORNL-LR-DWG 9806

PARTS LIST				
PART NO.	NO. REQ'D	NAME	SIZE	MATERIAL
1	960	RADIATOR FIN	2 1/4 X 8 1/4 in.	310 SS COPPERCLAD
2	1	TOP PLATE	0.062 X 8 1/4 X 8 1/4 in.	INCONEL ASTM-B-168-49T
3	4	SUPPORT MEMBER	0.062 X 8 1/4 X 16 3/4 in.	INCONEL ASTM-B-168-49T
4	1	BOTTOM FLANGED PLATE	0.125 X 9 3/4 X 11 1/4 in.	INCONEL ASTM-B-168-49T
5	24	RADIATOR TUBE	3/16 OD X 0.025 W X 42 in.	INCONEL ASTM-B-167-49T
6	24	RADIATOR TUBE	3/16 OD X 0.025 W X 42 in.	INCONEL ASTM-B-167-49T
7	24	RADIATOR TUBE	3/16 OD X 0.025 W X 42 1/4 in.	INCONEL ASTM-B-167-49T
8	4	HEADER END PLATE	3/16 X 2 1/4 X 2 1/4 in.	INCONEL ASTM-B-168-49T
9	2	LOWER HALF OF HEADER	2-in. SCH 40 PIPE X 8 in.	INCONEL ASTM-B-167-49T
10	2	HEADER INLET AND OUTLET CONNECTION	1-in. SCH 40 PIPE X 5 in.	INCONEL ASTM-B-167-49T
11	2	UPPER HALF OF HEADER	2-in. SCH 40 PIPE X 8 in.	INCONEL ASTM-B-167-49T

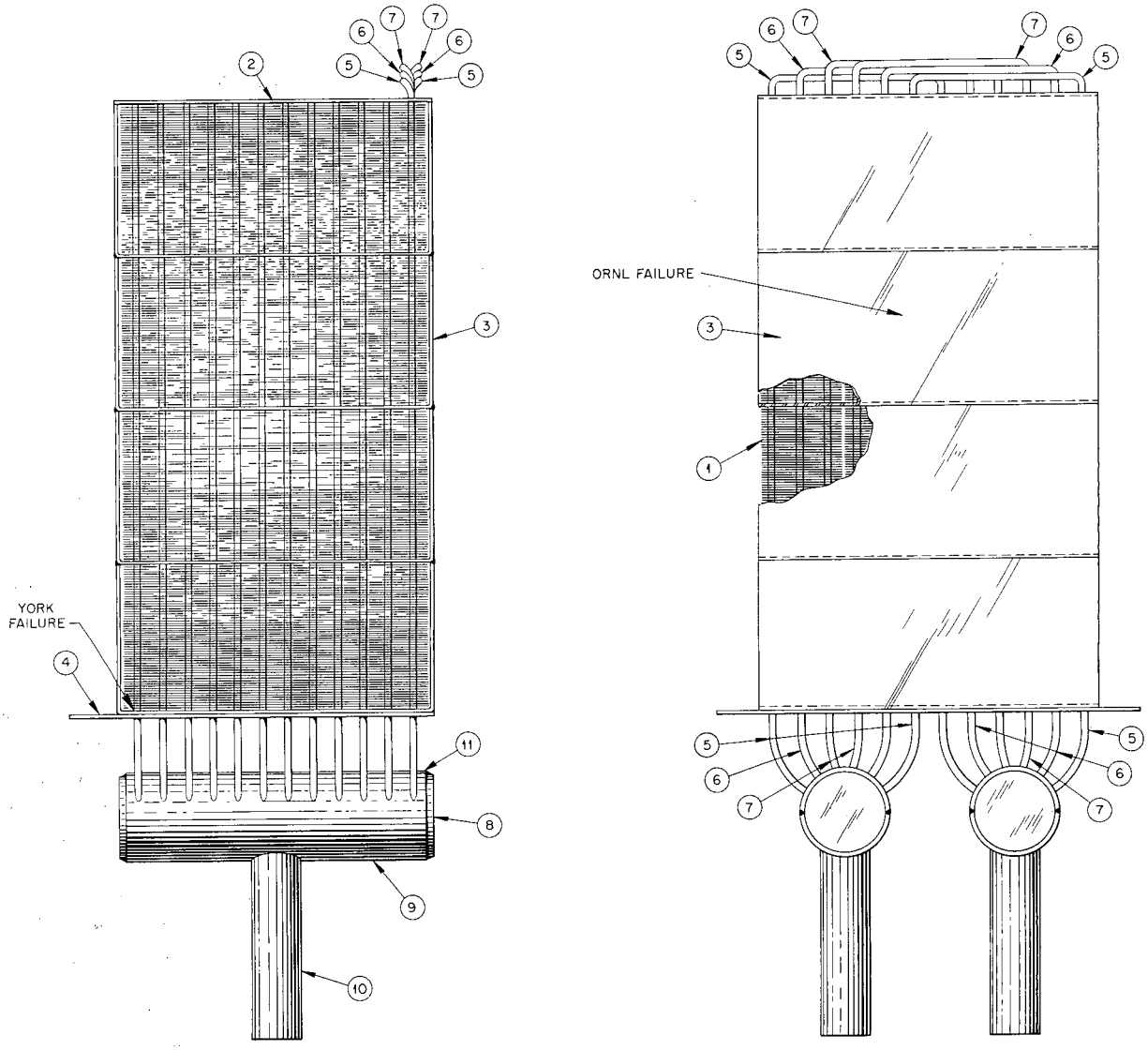

Fig. 100. Air-Cooled Radiator.

UNCLASSIFIED
Y-16246

Fig. 101. Failed Sections as Removed from ORNL Radiator No. 1, Illustrating the Extent of Destruction from Fire.

A photomicrograph of the failure is shown in Fig. 105 and magnified for clarity in Figs. 106 and 107. It is apparent that failure was due primarily to tensile forces, as evidenced by the ductile fracture and the reduction in tube-wall thickness of approximately 23%. A lateral shift of the tube is also evident, however, indicating that shear forces may have been instrumental in initiating a fracture in the braze metal, which was subsequently propagated by the tensile forces.

The tensile loading appears to have been the result of the restraining influence of the support members during cooling of the fin surfaces by forced air. Buckling of these components is clearly evident in the York radiator, as shown in Figs. 99, 102, and 103.

It may also be noted that the failed tube was securely brazed to the support member and the bottom flanged plate, which were brazed to each other. The shear loading may have resulted from the restraining influence of the bottom flanged plate during cooling of the fin surfaces by the forced air.

In view of these observations, a tube adjacent to the failure was microscopically examined. This tube had been found to be leak-tight in the pressure test. Figure 108 illustrates a fracture in this tube in the state of propagation. The reduction in tube-wall thickness and the lateral-motion characteristic of the failed tube may also be noted, indicating that the failure was not due to an isolated flaw.

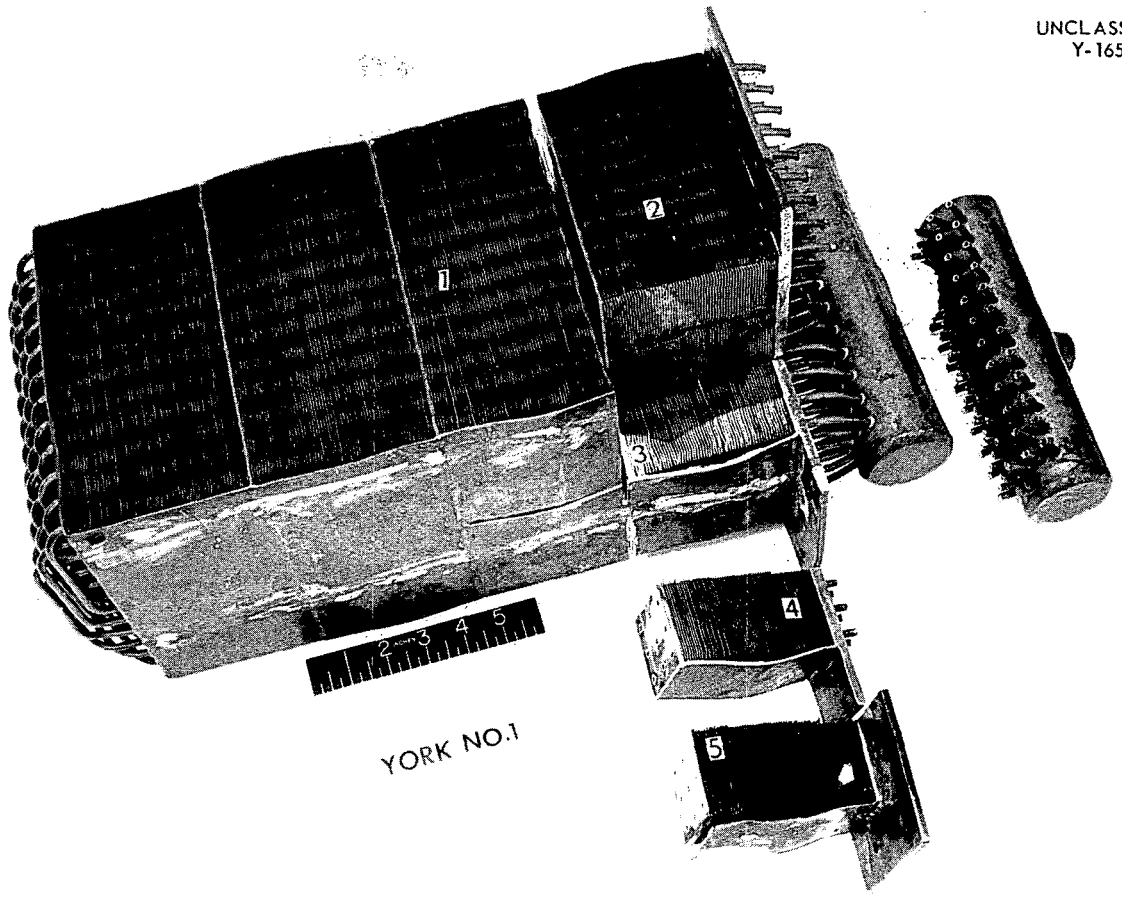

Fig. 102. York Radiator No. 1 After Having Been Sectioned for Examination. Arrow in section 5 points to failure site.

This was verified by extending the examination to two areas completely away from the failure. Samples were removed, as shown in Fig. 109, and metallographically examined. Figure 110 is a photomicrograph of a joint in area A of Fig. 109. It may be noted that a fracture has propagated through the braze fillet and partially into the tube wall. The lateral motion can also be noted, as can a small reduction in tube-wall thickness. Although the tube is not shown attached to the support member, except through the fractured fillet, the support member was securely brazed to the bottom flanged plate, fulfilling what appears to be the conditions necessary for the development of shear forces and lateral motion.

Conclusions. – 1. York radiator No. 1 failed as a result of the initiation of a fracture in a braze-alloy fillet by shear forces and as a result of the propagation of this fracture through the tube wall by tensile forces or combinations thereof.

2. The tensile loading was caused by differences in cooling rates between the support members and the finned tubes when cooling air was forced across the high-conductivity fin surfaces.

3. The shear forces were caused by a difference in cooling rate between the support member and bottom flanged plate and the finned tubes when cooling air was forced across the high-conductivity fins.

4. The ORNL radiator was ravaged by fire so extensively that metallographic evidence for the cause of failure has not been found.

Recommendations. – 1. The restraining influence of the support members, both parallel and

UNCLASSIFIED
Y-16573

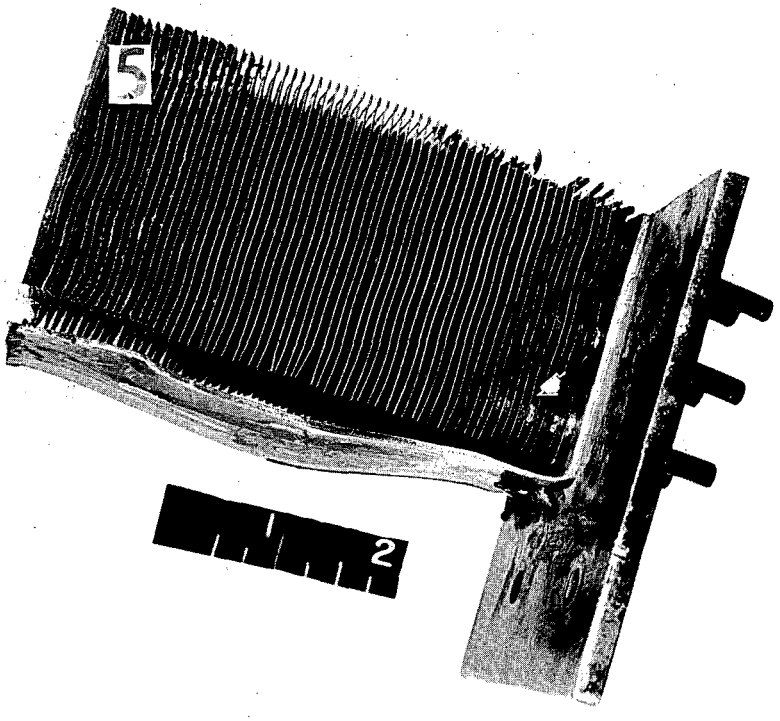

Fig. 103. Enlargement of Section 5 of Fig. 102 Showing Location of Tube That Failed.

transverse to the tubing, should be removed by redesign. It is suggested that the high-conductivity fin be used to provide transverse support at 2- or 4-in. intervals by assembling a layer of fins at right angles to the normal direction.

2. An enclosure for the radiators should be designed with freedom of motion, and preferably independent of the radiator, thereby eliminating the parallel support member.

3. The bottom flanged plate should be drilled with oversized holes and made of Inconel X, thereby providing assurance that the tubes will not be brazed to it.

4. Since sump plates constitute a transverse restraint, they should be made from 0.010-in. nickel sheet. They may be eliminated entirely by the use of accurately manufactured brazing-alloy rings and by better control of fin-to-tube fitup.

5. Another very promising means of removing the restraining members would be to do all brazing on the radiator while it is on its side and with its fins in the vertical position. No sump plates would then be required.

Other Radiators

Metallographic investigations of numerous segments of ORNL radiator No. 3, Pratt & Whitney radiator No. 2, and York radiator No. 3 are being conducted as a means of determining the possible reasons for failure of these components during service. Since the resultant fire completely gutted the areas near the leak in ORNL radiator No. 3, the analysis on this radiator must, of necessity,

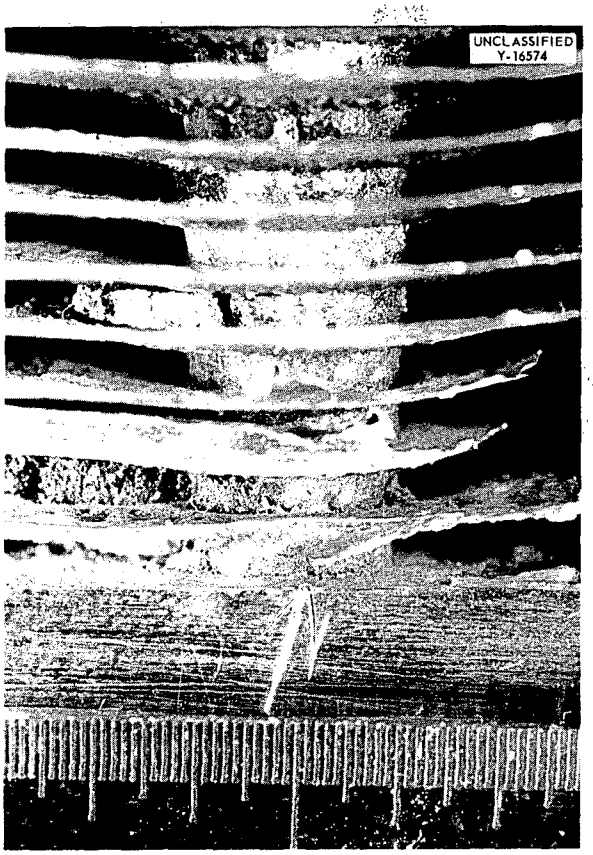

Fig. 104. Site of Failure, as Detected by Emergence of Air Bubbles with Tube Under Pressure.

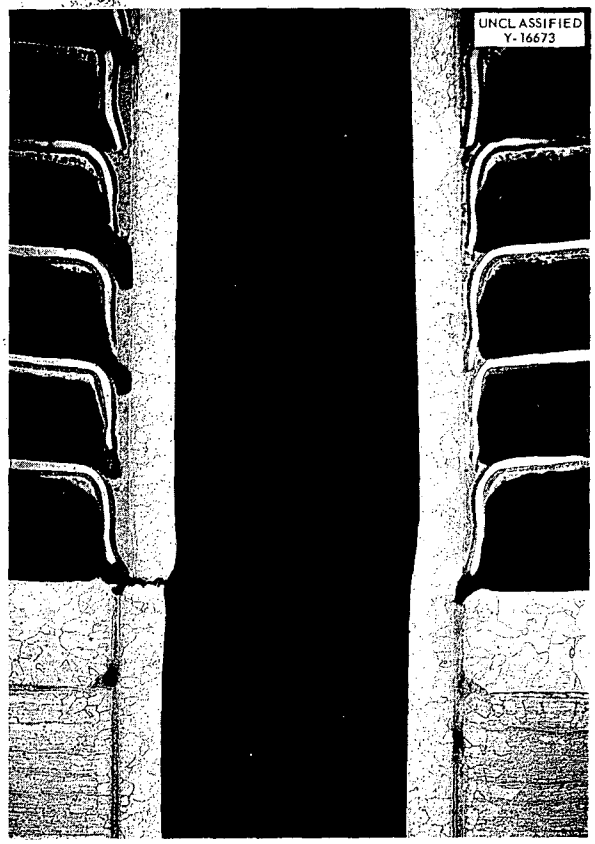

Fig. 105. Longitudinal Section Through Tube That Failed. Note that the tube was securely brazed to both the support member and the bottom flanged plate.

be centered on other segments of the radiator. The locations of 24 of these segments in the air-inlet and air-exit banks are shown in Figs. 111 and 112. The examination of these specimens is now underway. Examination of the other radiators is likewise only partially complete.

METALLOGRAPHIC EXAMINATION OF HIGH-CONDUCTIVITY-FIN RADIATOR TUBE-TO-FIN JOINTS

The degree of tube-to-fin braze-metal adherence and the degree of edge protection of exposed copper are important factors in the heat-transfer performance of NaK-to-air radiators. The disassembly of actual full-size radiators, after they have been subjected to high-temperature service, can furnish extremely large numbers of joints for metallographic examination. Investigations of adherence and of copper oxidation were therefore performed on the following radiators: ORNL No. 1, York No. 1, and ORNL No. 3.

ORNL radiator No. 1 failed as a result of a leak after approximately 600 hr of elevated-temperature service; the major portion of this service was isothermal in the temperature range 1000 to 1600°F. York radiator No. 1 failed as a result of a leak after it had been in elevated-temperature service in the range 1000 to 1600°F for approximately 150 hr. ORNL radiator No. 3 failed as a result of a leak after elevated-temperature service for 716 hr; the major portion of this service was isothermal in the temperature range 1000 to 1600°F.

Metallographic specimens were taken from each radiator, with each specimen containing a portion of three tubes joined to fifteen fins. These tubes

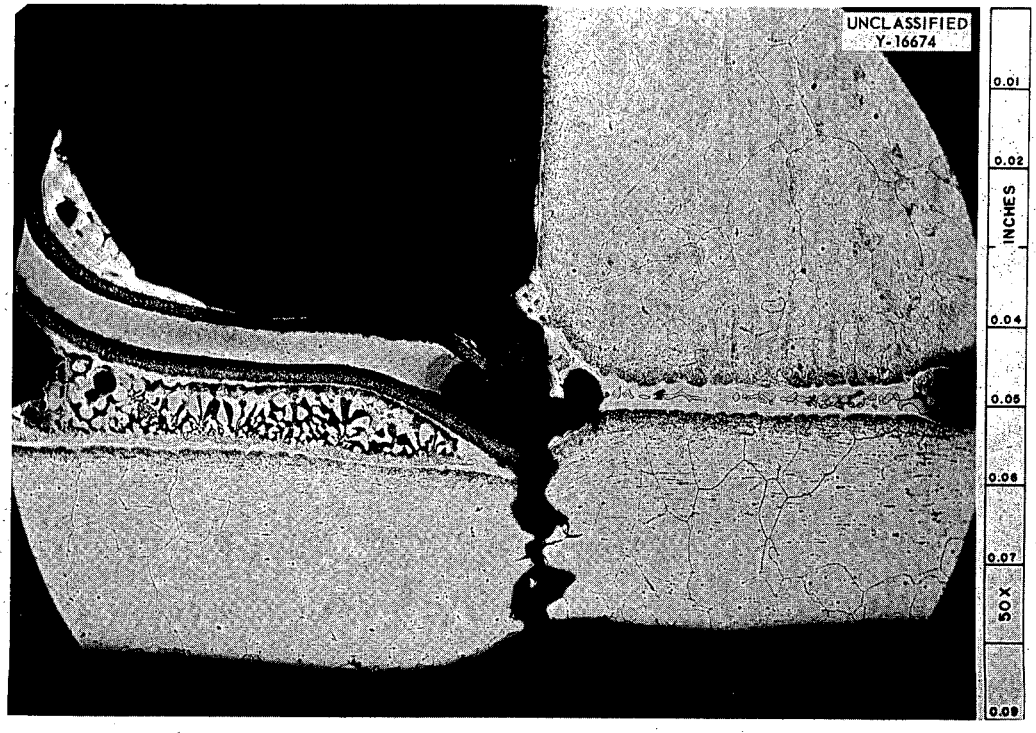

Fig. 106. Enlargement of Section of Fig. 105 Showing Tube Wall That Failed. Note the typical tensile failure of the necked-down area. 50X. Reduced 18%.

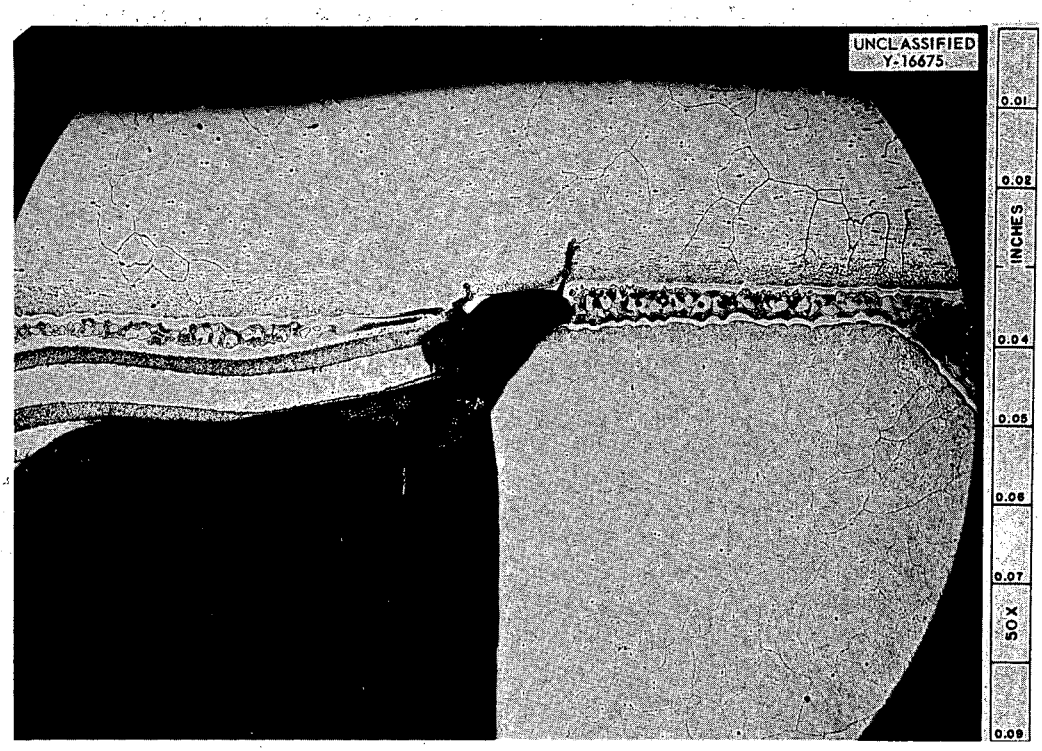

Fig. 107. Enlargement of Section of Fig. 105 Showing Tube Wall Opposite Wall That Failed. Note fissure partially propagated through the tube wall. 50X. Reduced 18%.

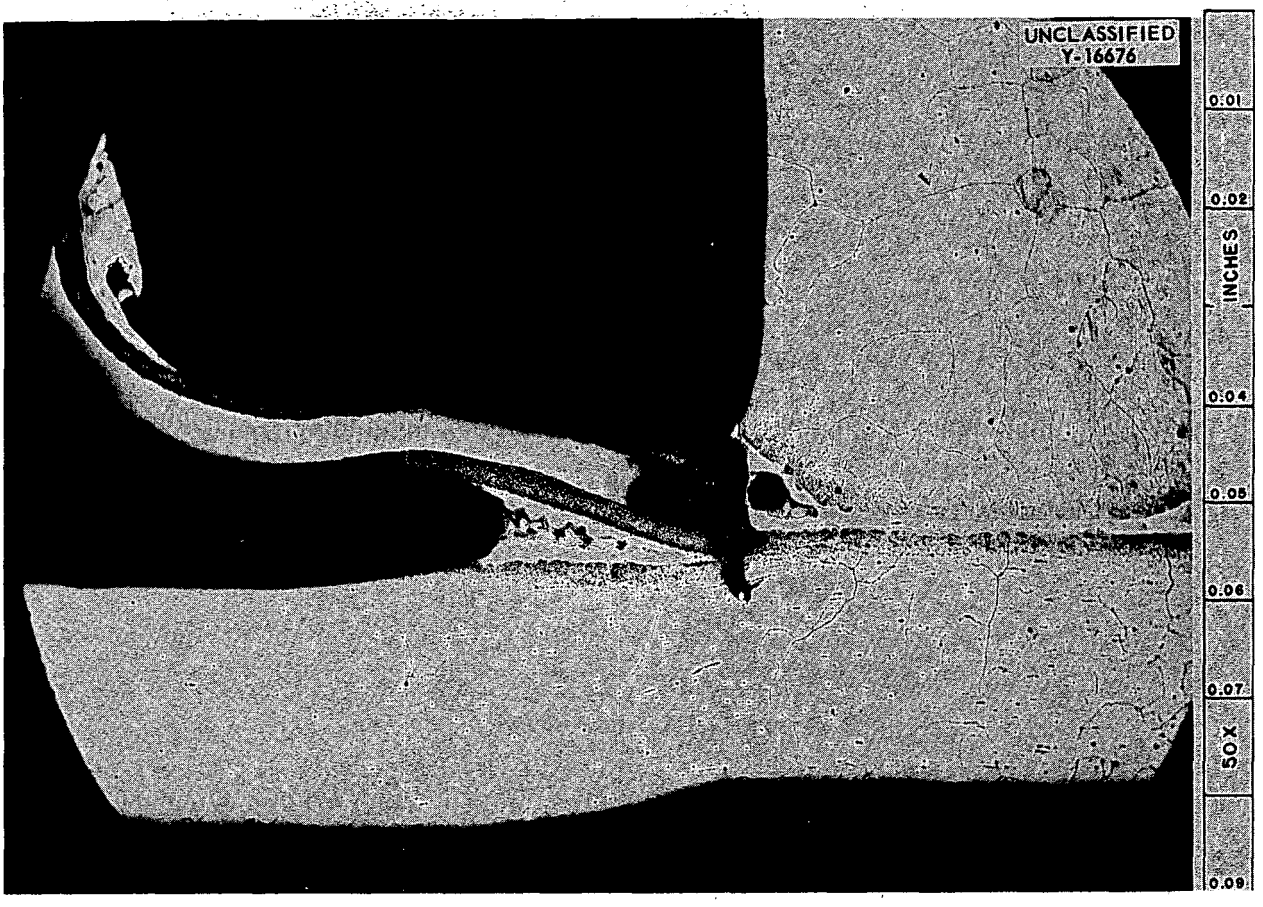

Fig. 108. Fracture in Tube Adjacent to Fractured Tube Shown in Figs. 105, 106, and 107.

were cross-sectioned in order to show two opposite areas of each joint. The tube-to-fin joint areas were counted and classified according to their degree of adherence, that is, 0–24, 25–49, 50–74, or 75–100%; and estimates were made of the degree of oxidation of the copper fins, and they were assigned to different categories according to whether they were nonoxidized, slightly oxidized, or heavily oxidized. The results of these investigations on the three radiators were recorded and tabulated and are presented in Table 40.

Similar investigations are now being performed on the tube-to-fin joints of other radiators, and the results will be presented in the next semiannual report.

FABRICATION OF AIR-COOLED RADIATOR 7503

One of the problems associated with the fabrication of the air-cooled radiator 7503, as described in Specification JS-P3-19, is the brazing of the core halves and the welding of these into a single unit. The specifications suggest an assembly procedure which permits the joining of two core halves into a single unit by welding after the brazing operation. An experiment was therefore conducted to determine how the stresses set up during welding influence the crack susceptibility of the back-brazed tube-to-header joints.

Two core halves of the type shown in Fig. 113 were assembled for brazing. One core half was brazed in the conventional upright position with

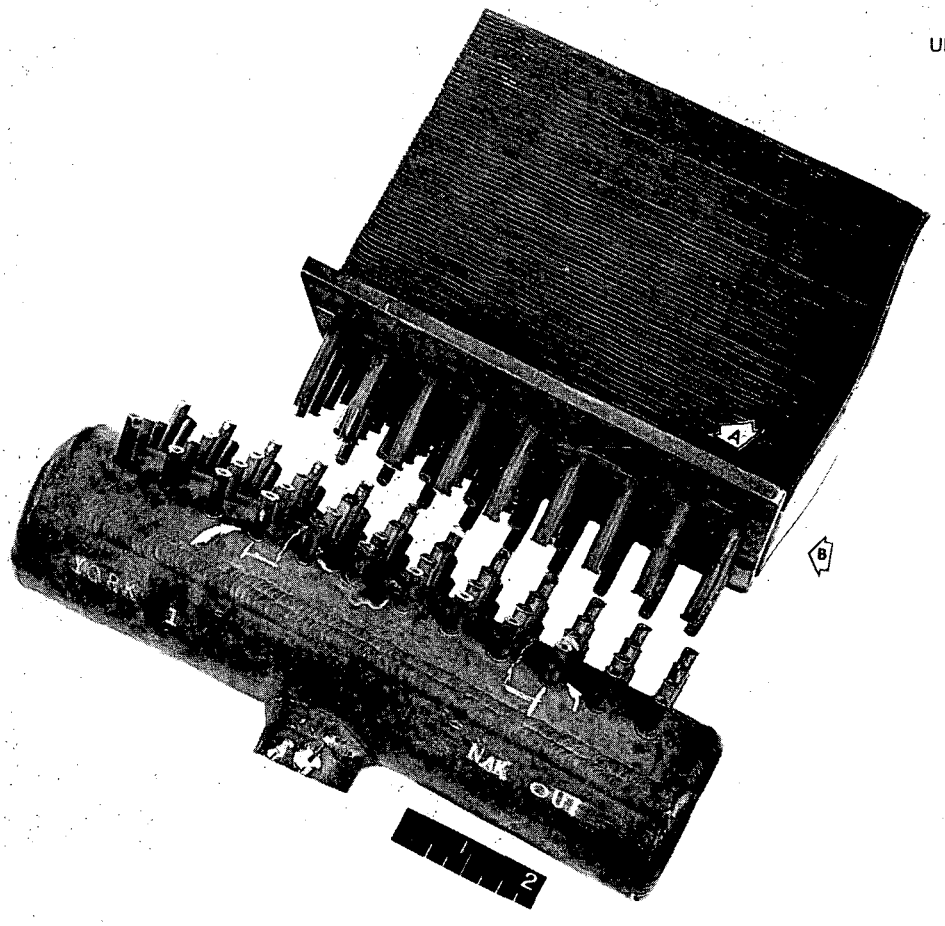

Fig. 109. Additional Areas, A and B, That Were Examined for Evidence of Fractures.

TABLE 40. EXTENT OF TUBE-TO-FIN ADHERENCE AND OF FIN OXIDATION EXHIBITED BY NaK-TO-AIR RADIATORS AFTER OPERATION AT ELEVATED TEMPERATURE

	Radiator		
	ORNL No. 3	ORNL No. 1	YORK No. 1
Number of joint areas examined	2282	4150	3847
Percentage of joint areas having 75–100% adherence	87.7	91.8	67.4
Percentage of joint areas having 50–74% adherence	3.5	4.2	13.0
Percentage of joint areas having 25–49% adherence	1.4	1.4	7.3
Percentage of joint areas having 0–24% adherence	7.4	2.6	12.3
Percentage of joint areas having nonoxidized copper fins	12.1	59.3	75.4
Percentage of joint areas having slightly oxidized copper fins	2.5	20.1	22.0
Percentage of joint areas having heavily oxidized copper fins	85.4	20.6	2.6
Number of hours of operation at elevated temperature, 1000–1600°F	716	608	152

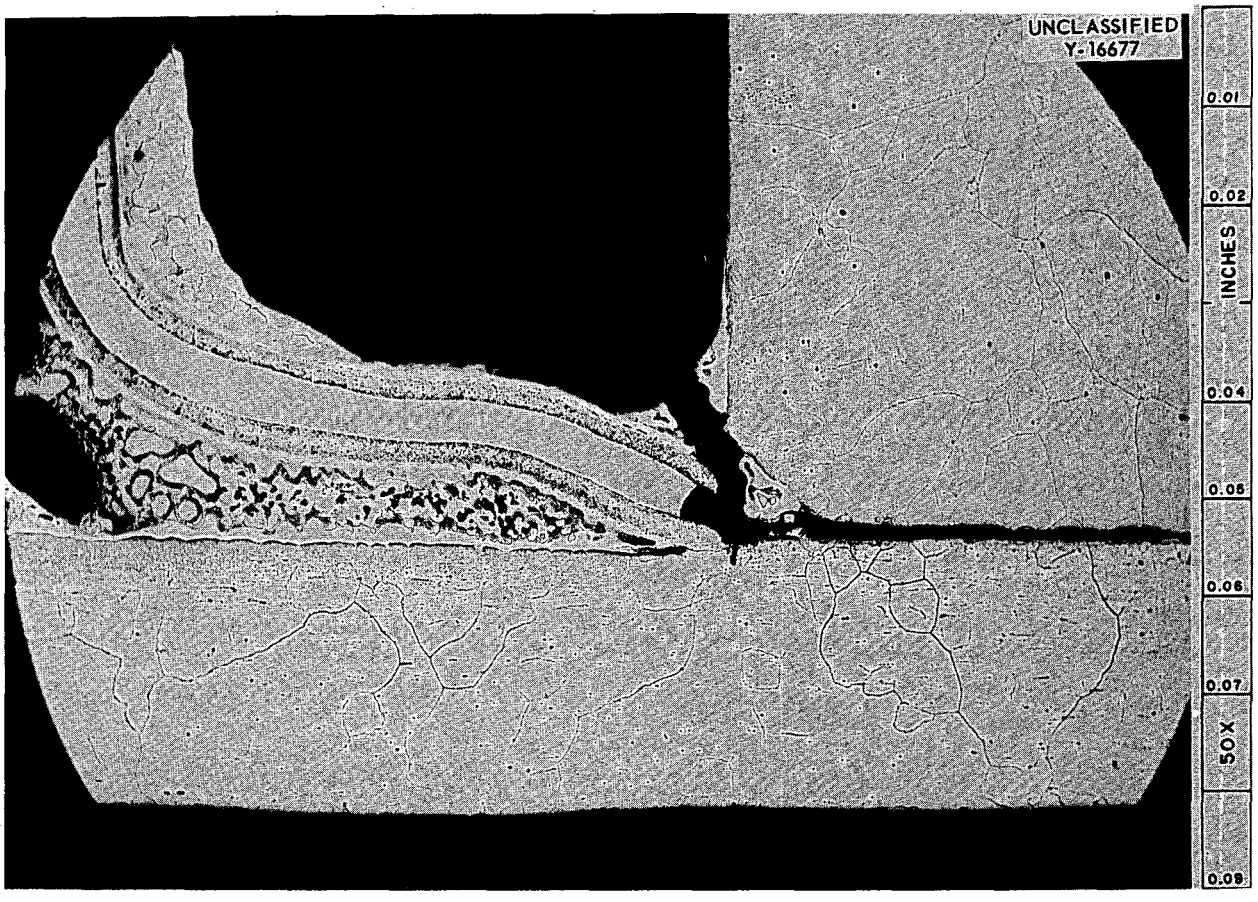

Fig. 110. Fracture in Process of Propagation Through a Tube Wall in Area A of Fig. 109.

the fin collars down; while the other was brazed in the horizontal position. Brazing in the horizontal position eliminates the need for sump plates to accommodate excess brazing alloy and, thereby, eliminates their consequent restraining effect upon the tubes during nonisothermal service.

The component parts of the crack-susceptibility test are shown in Fig. 114. The tube-to-header back brazes were dye-penetrant inspected before and after welding for evidence of cracking. All welding was done in the down-hand position according to PS-1 welding procedures. The completed assembly is shown in Fig. 115.

Dye-penetrant inspection of the tube-to-header back brazes indicated freedom from cracks, both before and after welding. Visual examination of the tube-to-fin joints indicated that good flow and fin-collar protection had been achieved in both the vertically and horizontally brazed core halves. However, the horizontal brazability of these radiator cores will be verified in experiments now underway utilizing $2\frac{3}{4} \times 8 \times 16$-in. fin banks and preplacing the brazing alloy as sintered rings or as dry powder.

MEASUREMENT OF WELD SHRINKAGE

In the construction of the Aircraft Reactor Test facility many instances occur where it is necessary to know the approximate values of the transverse shrinkage resulting from the various welding operations. Accordingly, an experimental research program has been set up for the purpose of obtaining information of interest to the designers and fabricators of this facility. Shrinkage was measured by use of micrometers and appropriate dial gages.

Butt welds have been made in Inconel plates $\frac{3}{16}$, $\frac{3}{8}$, $\frac{1}{2}$, and $\frac{3}{4}$ in. thick. Several joint designs were fabricated with both the Heliarc and metallic-arc processes. The summary of shrink data on

UNCLASSIFIED
Y-17425

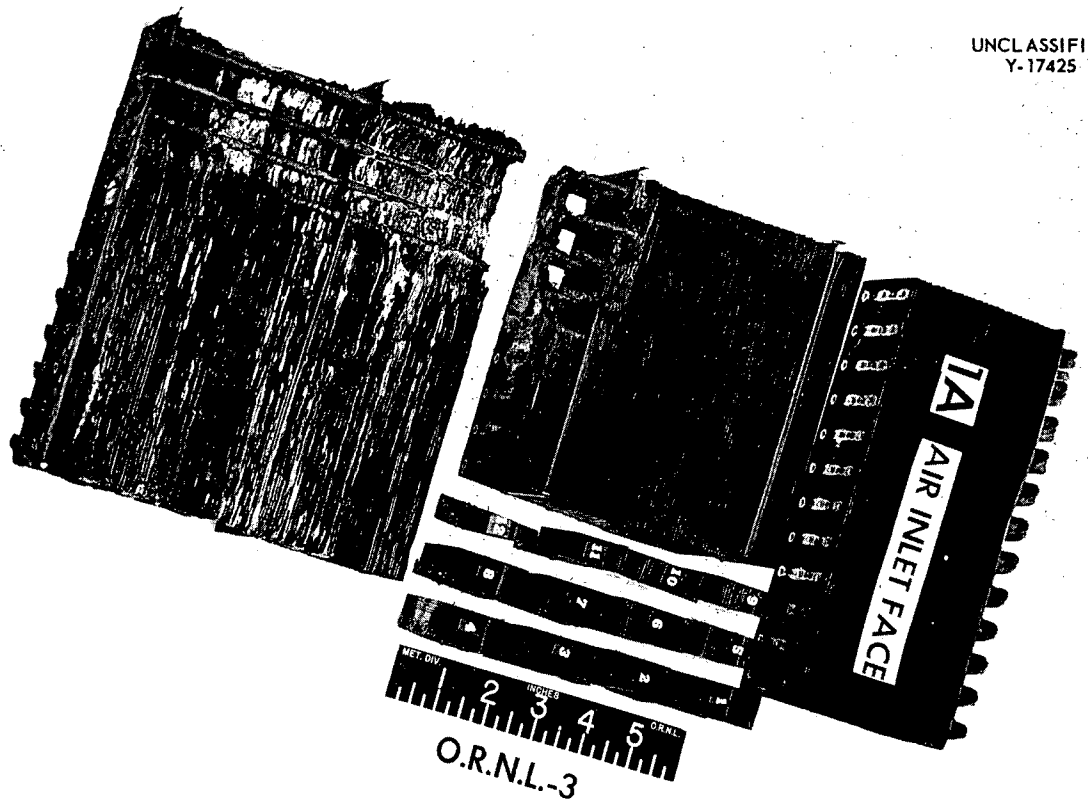

Fig. 111. Air-Inlet Bank of ORNL Radiator No. 3, Showing Sections Removed for Metallographic Examination.

UNCLASSIFIED
Y-17426

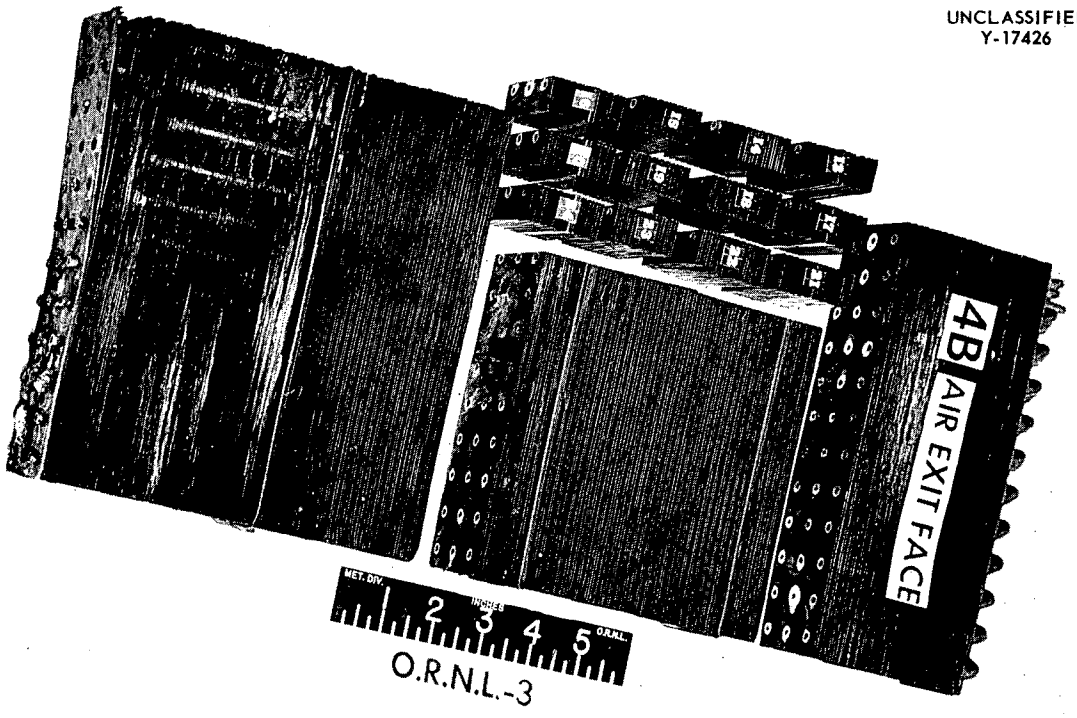

Fig. 112. Air-Exit Bank of ORNL Radiator No. 3, Showing Sections Removed for Metallographic Examination.

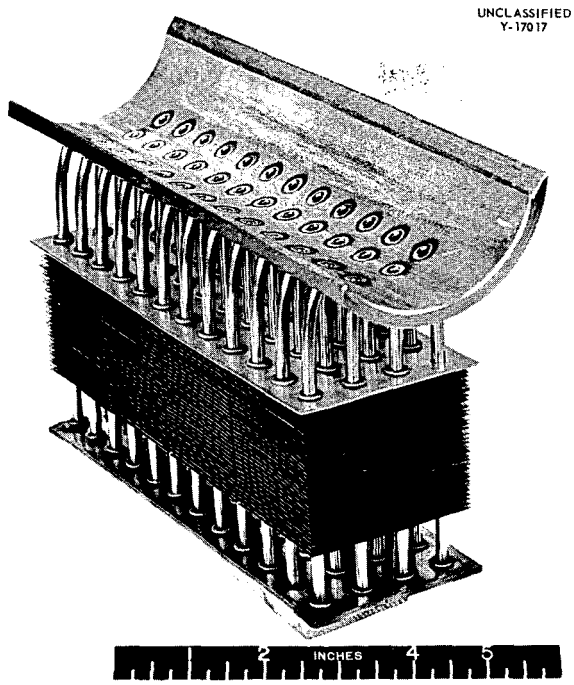

Fig. 113. Core Half for Crack-Susceptibility Test Unit.

these Inconel plates is presented in Table 41. It can be seen that the shrinkage to be expected increases with plate thickness and that the inert-arc welding process results in a larger shrinkage, for a given joint design in a given plate thickness, than does the metallic-arc welding process. An analysis of the cross-sectional areas for the different joint designs in ½-in. plate indicates that other parameters, such as the mean weld width, are also important. Experiments on butt-welded low-carbon-steel test plates indicate that the shrinkage for the steel can be expected to be slightly larger than that for Inconel, as would be expected from a comparison of their coefficients of thermal expansion (Inconel: 6.4×10^{-6} in./in./°F; carbon steel: 7.3×10^{-6} in./in./°F).

PK PUMP FABRICATION EXPERIMENTS

One of the problems associated with the fabrication of an Inconel pump of the PK type is the maintenance of dimensional tolerances. The space between the two volutes, which constitute the pump housing, is considered critical; and methods for the control of this dimension during fabrication are being investigated.

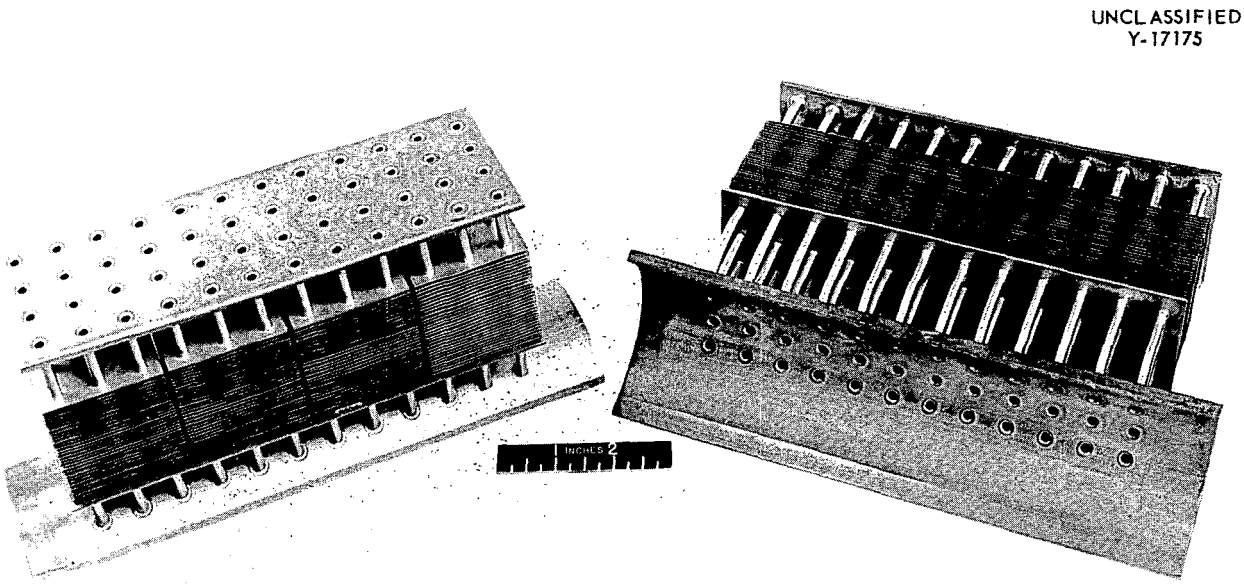

Fig. 114. Component Parts of Crack-Susceptibility Test Unit.

TABLE 41. EFFECT OF WELDING VARIABLES ON SHRINKAGE INCURRED BY INCONEL PLATES

Joint Design

1. J-type 60-deg bevel; joint geometry explicitly described in *Procedure Specification PS-12*
2. V-type 100-deg bevel; joint geometry explicitly described in *Procedure Specification PS-1*
3. V-type 75-deg bevel; joint geometry explicitly described in *Qualification Test Specification QTS-12*

Plate Thickness (in.)	Joint Design	Process	Shrinkage (in.)
		Effect of Plate Thickness	
3/8	1	Heliarc and metallic arc	0.091
1/2	1	Heliarc and metallic arc	0.95
3/4	1	Heliarc and metallic arc	0.129
		Effect of Plate Thickness	
3/16	2	Heliarc	0.113
3/8	2	Heliarc	0.140
1/2	2	Heliarc	0.192
		Effect of Process	
3/4	1	Heliarc and metallic arc	0.129
3/4	1	Metallic arc	0.119
3/4	1	Heliarc	0.189
		Effect of Process	
1/2	3	Metallic arc	0.090
1/2	3	Heliarc	0.129
		Effect of Welding Technique and Weld Volume	
1/2	3	Heliarc	0.129
1/2	2	Heliarc	0.192

Two test pieces, representative of the volutes to be incorporated in the pump, were machined from 2-in. Inconel plate. Four spacers were machined from Inconel plate; they act as rigid supports during the welding of the volutes and are shown in Fig. 116, along with the component parts of the test. These spacers were subjected to an aluminizing treatment prior to assembly of the components in order to prevent self-welding during the subsequent operations.

Micrometer measurements were made at four radial sections prior to and after each subsequent operation, and the two volutes were welded in accordance with Procedure Specification PS-12. After welding, the assembly was annealed in a helium atmosphere at 1850°F for a period of 2 hr. The heating and cooling rates were maintained at 600°F/hr. The completed pump casing – after welding, annealing, and removal of the spacers by machining – is shown in Fig. 117. An effort to remove the spacers intact, without exerting an excessive force, was unsuccessful, and the use of force was not attempted in view of the possibility of scoring the volute surfaces.

The results of micrometer measurements on the inside surfaces of the volutes indicate that the maximum change was 0.015 in. The maximum shrinkage observed on the diameter was 0.056 in. It was also noted that the dimensions after annealing and after removal of the spacers correspond

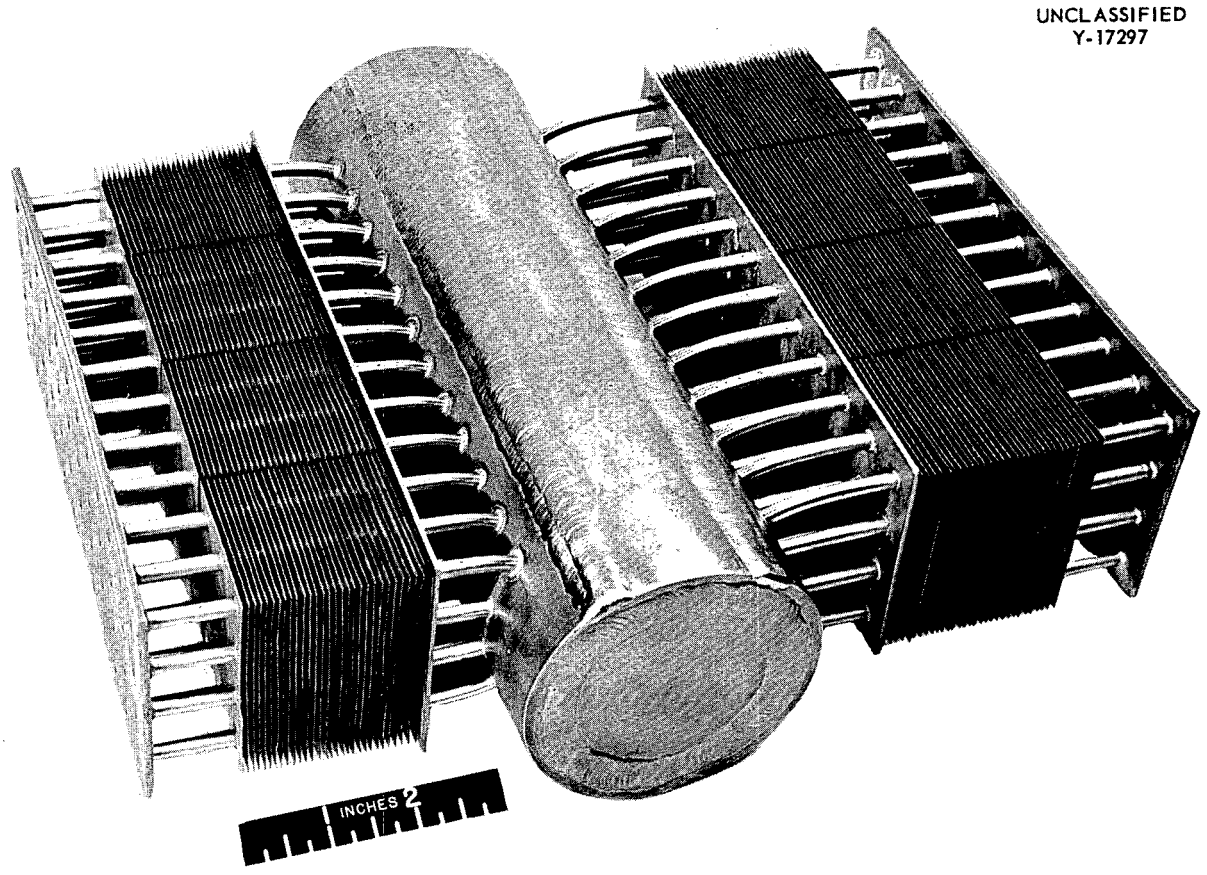

Fig. 115. Completed Crack-Susceptibility Test Unit.

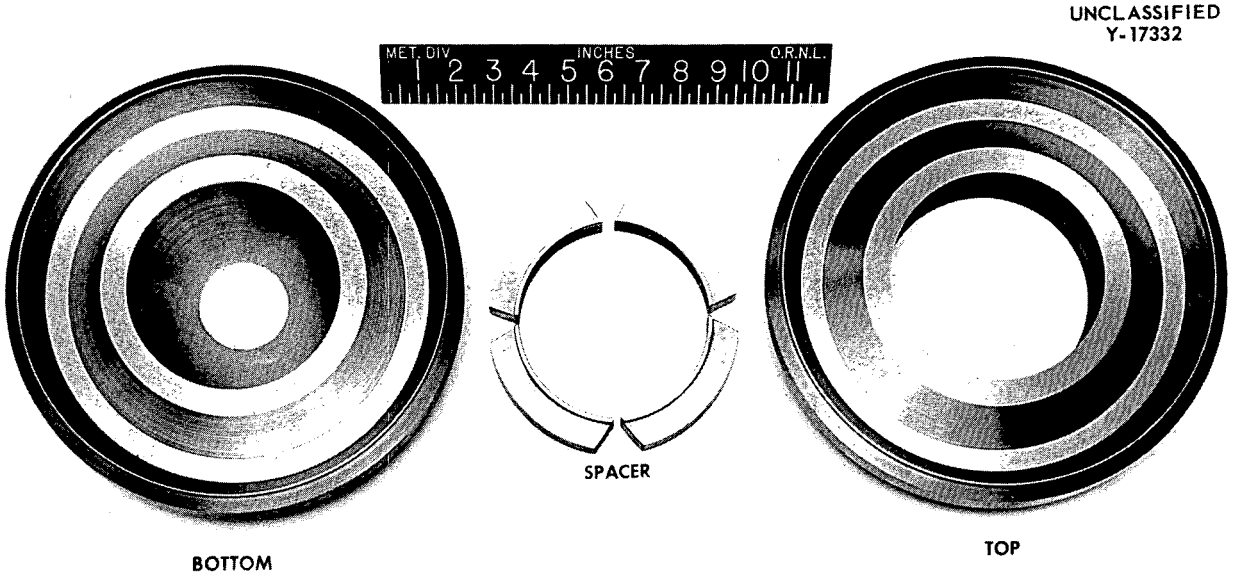

Fig. 116. Component Parts for PK Pump Fabrication Experiment.

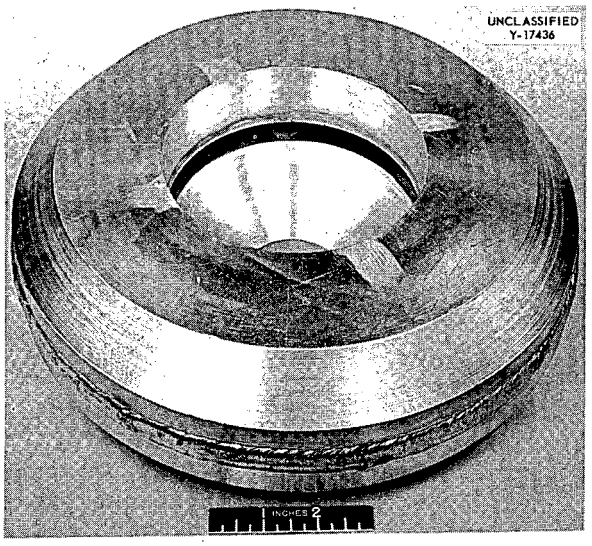

Fig. 117. Completed PK Pump Assembly.

exactly to those recorded after welding, indicating that the annealing cycle was successful in completely removing the residual stresses.

A similar experiment is now underway to determine the degree of dimensional control which can be obtained by using a brazing fabrication procedure.

CERMET-TO-METAL JOINING

The satisfactory use of cermet valve components for ANP valve applications depends to a large extent upon their being successfully joined to metallic structural materials such as Inconel. Several such components have been fabricated by the use of procedures previously determined and reported.[1] The success of these techniques, which utilized thin films of plated Electroless nickel-phosphorus brazing alloy, is predicated on the use of proper plating variables. Experiments are, therefore, now underway to develop a more reliable and consistent joining procedure.

Since high-temperature brazing alloys of the Ni-Si-B type (such as Coast Metals 50 – brazing temperature, 1120°C) will bond to cermets such as K-152B (complex carbides + 30% nickel binder), a series of tests was conducted with these materials. Since it is very difficult to obtain an even layer of brazing alloy over the entire faying surface of the hard-to-wet cermet, a nickel screen was placed in intimate contact with the cermet so as to facilitate wetting. The wetted surface was then ground flat and copper-brazed to the nickel transition layer and to the Inconel, as in the previously described procedure. A photomicrograph of a typical brazed joint is shown in Fig. 118. A valve disk has been fabricated by the use of these techniques, and dye-penetrant inspection of the component revealed no flaws.

Another procedure has been developed which eliminates the necessity for the nickel screen. By merely placing the cermet in intimate contact with the nickel at elevated temperatures (approximately 1350°C) a low-melting constituent is formed as a result of diffusion. Excellent bonding can be obtained at the cermet-to-metal interface, and the liquated constituent actually forms a fillet along the joint. A photomicrograph of a bond formed between K-151A and nickel is shown in Fig. 119. Slightly excessive temperatures promote extensive and nonuniform "settling", an example of which is illustrated in Fig. 120, a photograph of a small test sample heated at 1370°C for 10 min.

Two valve disks have been successfully bonded by this method, and an exploded view of the components of a typical assembly is given in Fig. 121. Two types of valve disks are shown and typify the two designs of interest. The ceramic supports were incorporated during bonding to permit controlled and uniform settling of the valve disk.

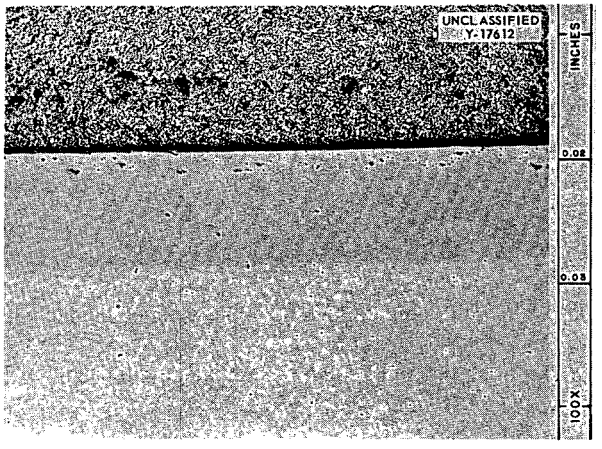

Fig. 118. Cermet-to-Nickel Joint Wetted with Coast Metals 50 Alloy and Brazed with Copper. 100X. Reduced 34%.

[1] P. Patriarca and R. E. Clausing, *ANP Quar. Prog. Rep. Sept. 10, 1955*, ORNL-1947, p 131.

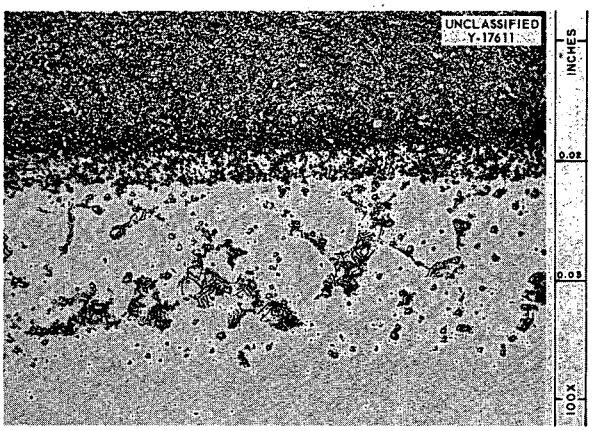

Fig. 119. Photomicrograph of the Bond Between Kentanium Cermet K-151A and Nickel. As polished. 100X. Reduced 36%.

An exploded view of the completed cermet-to-Inconel bonding procedure is shown in Fig. 122. The Inconel shank is attached to the nickel by copper brazing.

BRAZING-ALLOY DEVELOPMENT

Development of Low-Cross-Section Alloys for Fuel-to-NaK Service

The Ni-Ge-Cr-Si brazing-alloy system has been shown to be promising from a corrosion standpoint for fuel-to-NaK service. Several sample melts of alloys in the high-nickel range of this system were made and their flow points determined. The results are tabulated below.

Brazing-Alloy Constituents (wt %)	Flow Point (°C)
75 Ni–8 Ge–11 Cr–6 Si	1120
75 Ni–13 Ge–6 Cr–6 Si	1120
73 Ni–13 Ge–11 Cr–3 Si	>1160
70 Ni–13 Ge–11 Cr–6 Si	1100
68 Ni–13 Ge–13 Cr–6 Si	1100
68 Ni–10 Ge–16 Cr–6 Si	1100
67 Ni–13 Ge–11 Cr–9 Si	1120
65 Ni–13 Ge–11 Cr–11 Si	1140
65 Ni–13 Ge–16 Cr–6 Si	1080
62 Ni–13 Ge–19 Cr–6 Si	1080
62 Ni–16 Ge–16 Cr–6 Si	1100
62 Ni–13 Ge–16 Cr–9 Si	1100
59 Ni–16 Ge–19 Cr–6 Si	1080

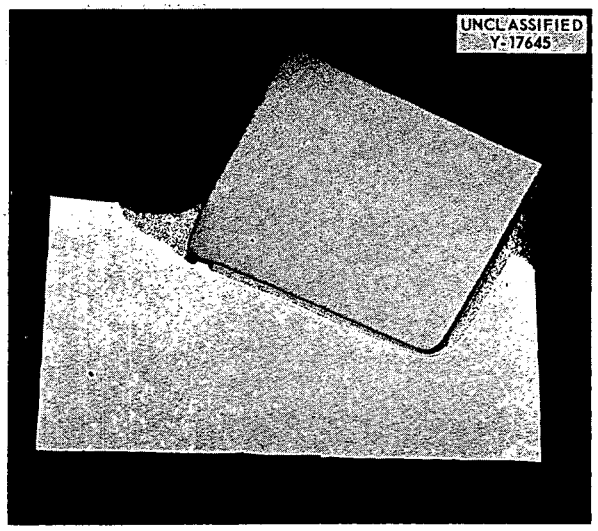

Fig. 120. Photograph of a Cermet-to-Nickel Joint Illustrating Extensive and Nonuniform "Settling" as a Result of Excessive Bonding Temperature.

The four alloys which possess the lowest flow points were submitted for corrosion testing in NaK and in fused fluorides, and the results have been reported in the General Corrosion section of this report.

Oxidation of Coast Metals 52 Alloy

Oxidation and corrosion tests on Coast Metals 52 alloy (Ni-Si-B) have indicated that one or more constituents are removed during the elevated-temperature test. Since this alloy has been used extensively in the fabrication of both NaK-to-air radiators and fuel-to-NaK heat exchangers, it is desirable to determine the type and extent of corrosion within the intended service times.

A program was therefore initiated which consisted of controlled experiments on cast-alloy buttons, and some results on the oxidation tests are available. Photomicrographs of the structure of as-cast Coast Metals 52 alloy after 100 hr and 500 hr at 1500°F are presented in Fig. 123. It can be seen that the depth of constituent removal increased with time and was approximately 0.006 in. after the 500-hr oxidation test. Microspark, spectrographic, and metallographic investigations on the sample indicated that removal of both boron

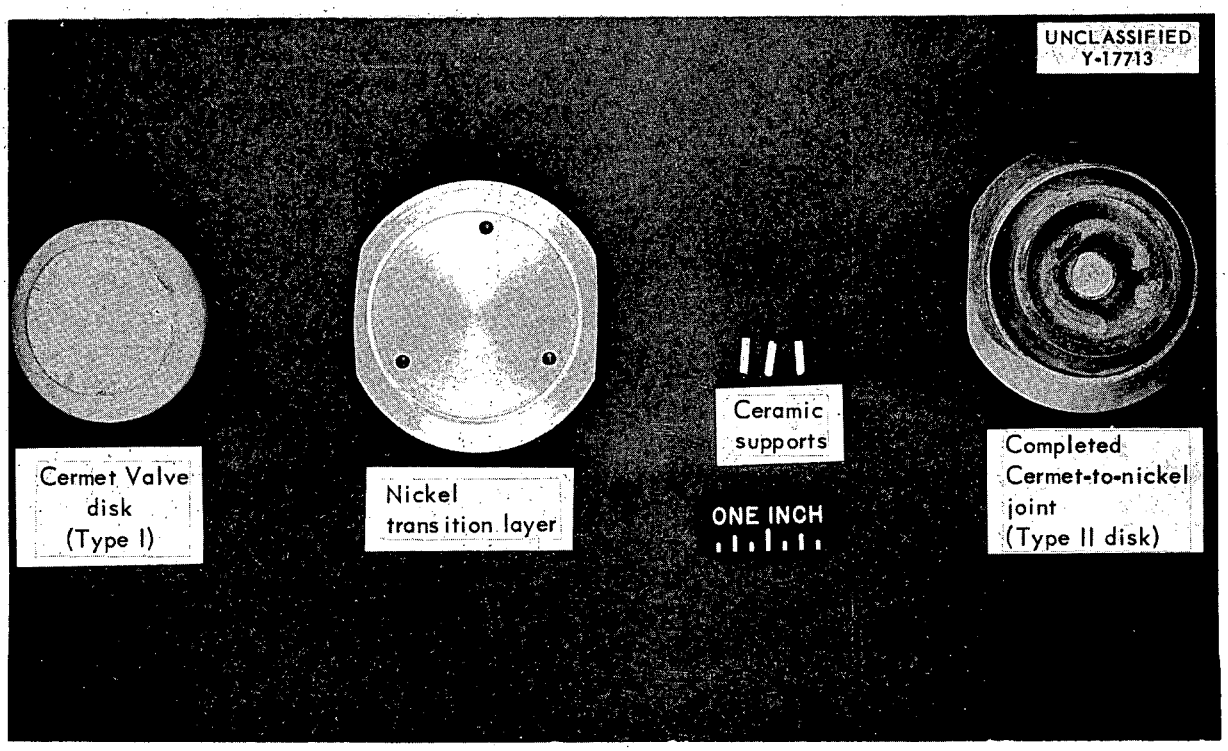

Fig. 121. Photograph of Completed Cermet-to-Nickel Joint and Components Used in Its Fabrication.

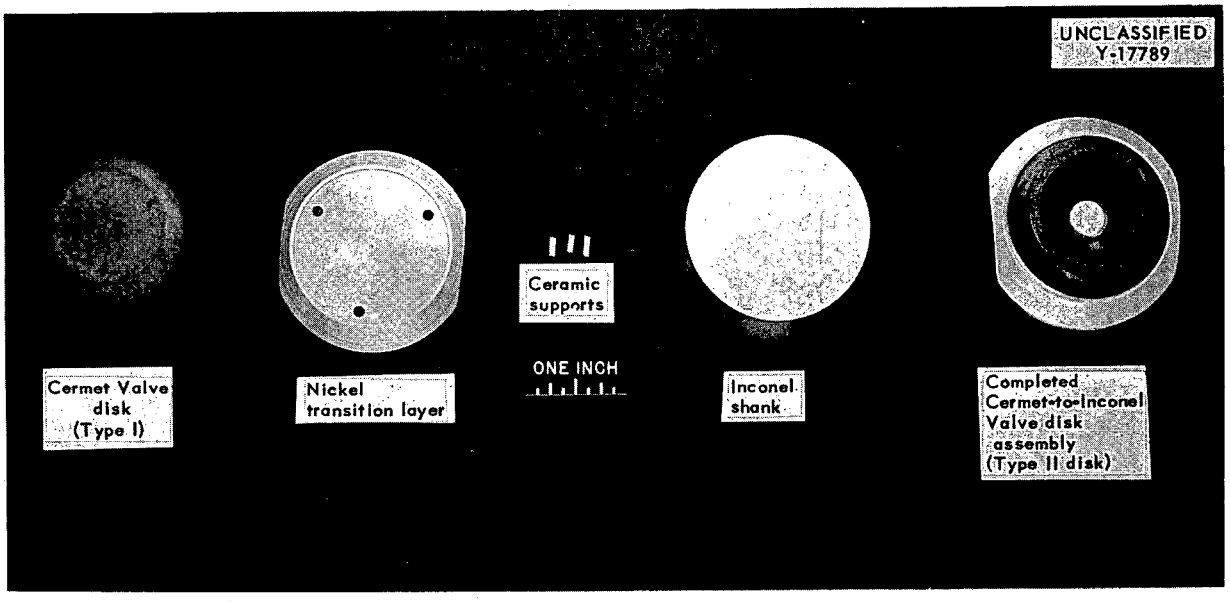

Fig. 122. Completed Cermet-to-Inconel Valve Disk and Components Used in Its Fabrication.

and silicon occurred. This seems highly probable, since microhardness measurements on the sample interior showed a hardness of 700 VHN as compared to a hardness of 140 VHN on the depleted surface.

Similar tests conducted in a vacuum and in helium showed no removal of the type mentioned above. Results of tests in NaK and in fused fluorides will be reported later by the General Corrosion Group.

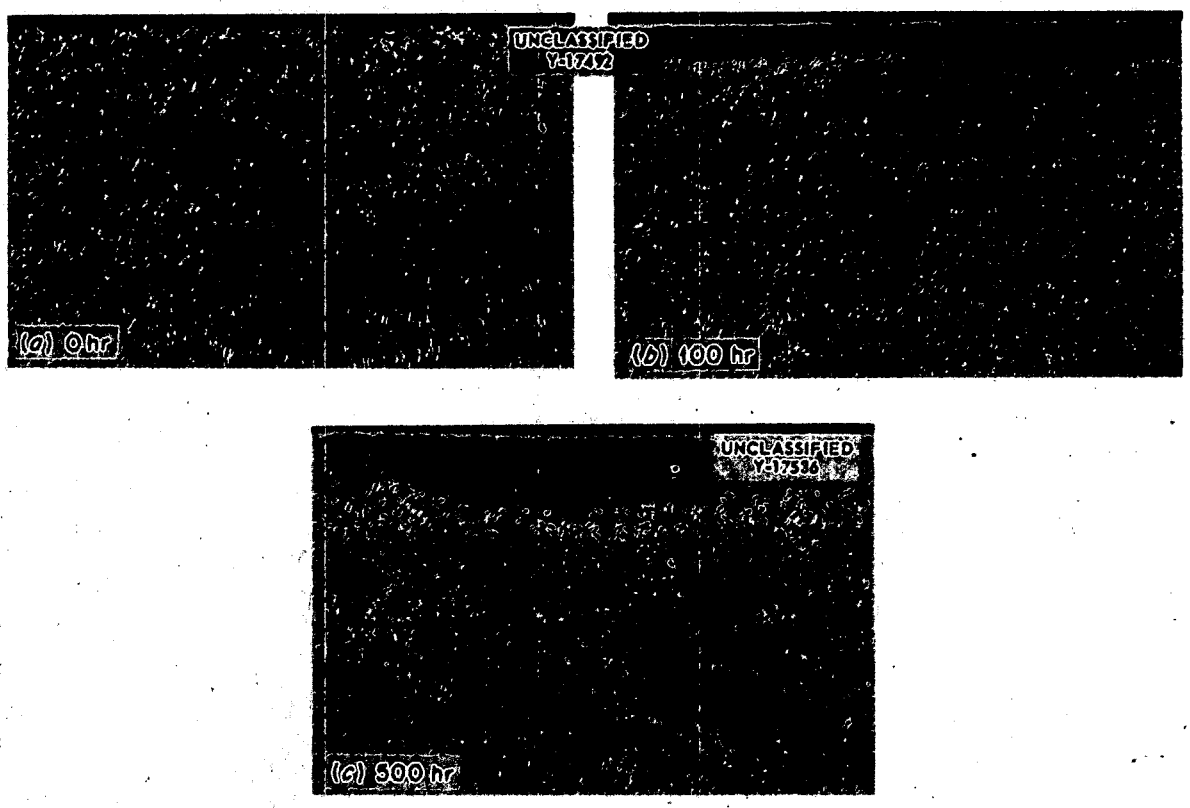

Fig. 123. Illustration of the Depth of Oxidation with Time at 1500°F. (*a*) 0 hr. (*b*) 100 hr. (*c*) 500 hr.

FABRICATION

J. H. Coobs H. Inouye
T. K. Roche J. P. Page
Metallurgy Division

M. R. D'Amore R. E. McDonald
Pratt & Whitney Aircraft

V. M. Kolba
Glenn L. Martin Co.

ALLOY DEVELOPMENT

T. K. Roche H. Inouye

Fabricability Studies on Nickel-Molybdenum-Base Alloys

As an approach to the problem concerning the poor fabricability of Hastelloy B, which is believed to be due to a stable high-temperature phase tentatively identified as $(Ni_4Mo_2)_6C$, the forgeability of the alloy 68% Ni–29% Mo–4% Fe (nominal composition of Hastelloy B) was studied as a function of carbon content. Arc melts of the alloy in amounts of 100 g were prepared under argon with nominal carbon contents of 0.01, 0.02, 0.04, 0.06, and 0.10%. The alloys were cast in the shape of a "finger" approximately 3 in. long by $\frac{3}{4}$ in. wide by $\frac{1}{2}$ in. thick. Hot-rolling experiments were carried out on these specimens at 1150°C. Reductions in thickness of 5% were used for the first few passes, followed by 10% reduction per pass to a final thickness of 0.160 in. Visual examination of the strips after hot rolling showed that slight edge cracking occurred in the specimens containing 0.01, 0.02, and 0.04% carbon and that the specimens containing 0.06 and 0.10% carbon were satisfactory. The alloys were then cold-reduced to 0.100 in. at a rate of 0.010 in. per pass without difficulty.

The most significant results from these experiments came from a correlation of the hot workability of these alloys with their microstructures. The amount of second-phase material, presumably a carbide, present in the alloy was found to increase with increasing carbon content. On the other hand, carbon additions were effective in reducing the fine oxide-type of impurity carried over from the melting stock and observed in the control alloy (0.01% carbon). Microstructures are illustrated in Figs. 126 and 127. In view of the hot-forgeability tests, it appears that the oxide type of precipitate is more detrimental to fabricability than is the carbide, up to 0.10% total carbon; it has become apparent that close control of the melting practice is quite important for improving the fabricability of nickel-molybdenum-base alloys.

Forged billets of Hastelloy W could not be extruded as tube blanks at 2000°F. Two Inconel-canned billets of this material shattered even at a moderate reduction ratio, and one uncanned billet

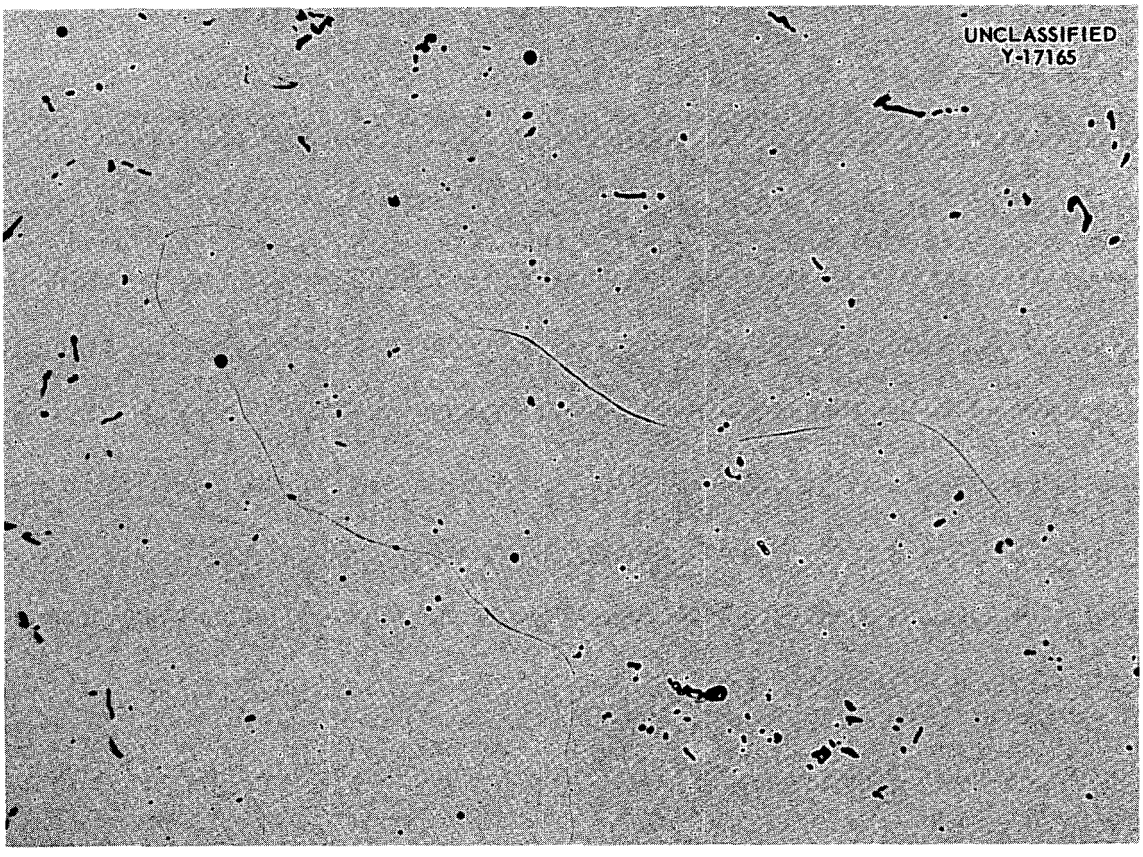

Fig. 126. Control Specimen of Hastelloy B Containing 0.01% Carbon, Homogeneized at 1150°C for 30 min and Water-Quenched. Oxide-type impurities precipitated in matrix. 500X.

stalled the press. It is felt that this latter extrusion failed because of excessive drop in billet temperature as a result of faulty preheat practice. A cut was made through a fractured area of one of the extruded billets and examined metallographically. Evidence of melting was found adjacent to some of the fractures, as shown by the presence of the eutectic seen in Fig. 128. X-ray analysis of the fractures did not reveal the nature of the eutectic, and, as a result, definite reasons for the hot shortness of the alloy are unknown. Lowering the billet preheat temperature from 2050 to 1950°F and modifying the present billet lubrication methods may improve the extrudability of these Hastelloy-type alloys.

Effect of Melting Practice on Nickel-Molybdenum-Base Alloys

Arrangements have been made with Battelle Memorial Institute to produce arc-melted ingots of nickel, Hastelloy B, Hastelloy W, 76% Ni–17% Mo–7% Cr, and 83% Ni–17% Mo. In an effort to improve the strength and fabricability of these alloys, the melts will be made by the consumable-electrode process whereby advantage is taken of the high arc temperatures for vaporizing "tramp" elements. Extrusion billets from these ingots will be prepared for the fabrication of suitable test specimens for strength evaluation.

Chromium-Molybdenum-Nickel Alloys

Past work has shown that chromium additions made to a base composition of 20% Mo–80% Ni result in an alloy with poor forgeability, which is generally attributed to the high oxygen content of of the chromium. In view of the general improvement in fabricability of Hastelloy B with carbon additions, 5-lb vacuum melts with the compositions 17% Mo, 7 and 10% Cr, balance nickel have been prepared with added carbon. If these alloys can be

Fig. 127. Hastelloy B Specimen with 0.1% Carbon, Homogeneized and Water-Quenched. Carbides precipitated, but matrix is free of oxide inclusions. 500X.

hot-rolled, larger heats containing 3, 5, 7, and 10% chromium will be prepared for the fabrication of seamless tubing which will be evaluated for corrosion resistance.

Special Alloys

Five special alloys in heats weighing 40 lb each, have been received from the International Nickel Company for corrosion and strength evaluation. The nominal composition of these alloys is as follows (nickel constitutes the remaining percentage):

Alloy No.	Amount (wt %)						
	Mo	Cr	W	Nb	Al	Ti	C
1	15	5	3	3	0.5		
2	17				0.5		
3	15		3	3	0.5		
4	15				1.0	1.5	
5	15		3	3	0.5		0.25

Extrusion billets are being machined from these ingots for subsequent fabrication of seamless tubing and test specimens.

Iron-Zirconium Alloys

Several compositions of iron-zirconium alloys containing between 1 and 16% zirconium were studied to determine their physical and fabrication properties. The alloys were studied in lieu of iron-hafnium alloys, since hafnium was not available and, moreover, is too expensive for experimentation.

The alloys were melted by induction heating in vacuum and were cast in a split cast-iron mold. The zirconium additions were contained in a drilled cavity in the iron melting stock.

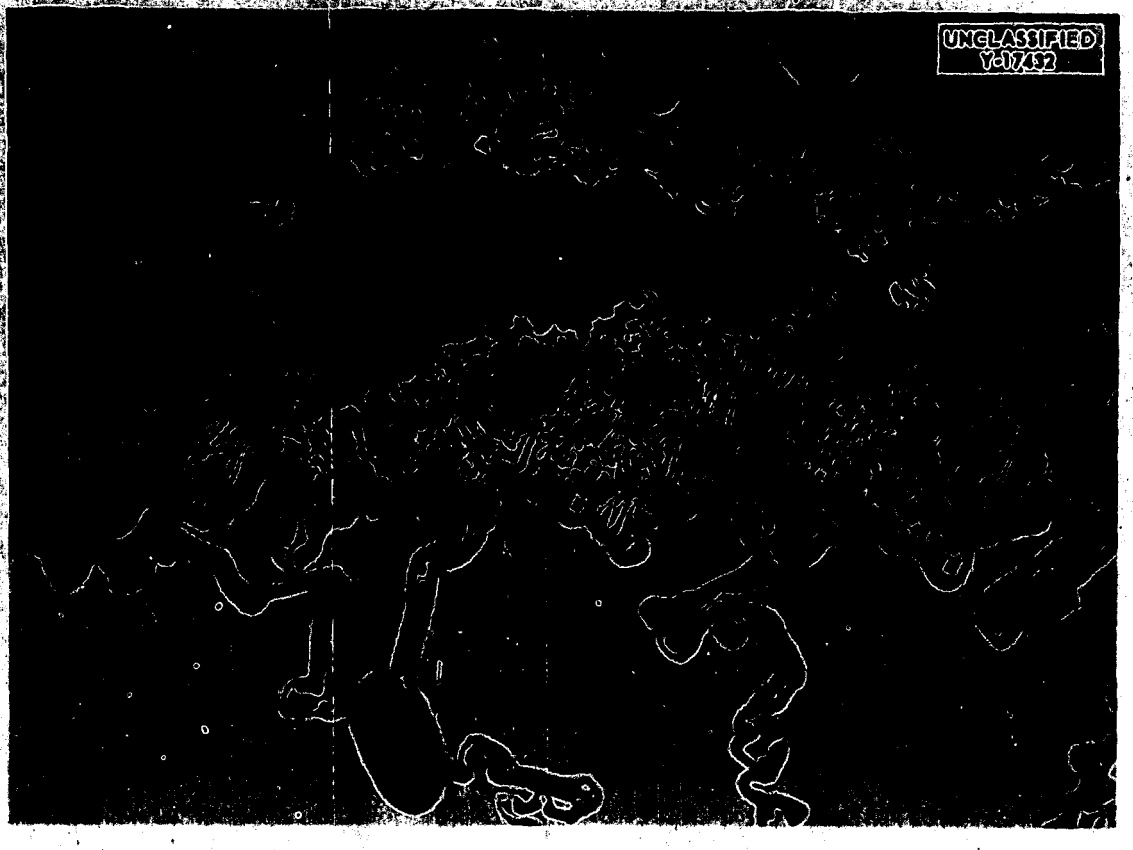

Fig. 128. Commercial Hastelloy W Extruded at 2000°F. Eutectic structure adjacent to fracture. 2000X.

The chemical analyses of the ingots are listed below:

Ingot No.	Zirconium (wt %)	
	Top of Ingot	Bottom of Ingot
527-1	1.02	1.07
527-3	3.51	3.30
527-5	4.95	5.70
527-8	8.36	8.93
527-12	11.60	13.18
527-16	14.40	14.50

All compositions, except 527-16, which was a poor ingot, were preheated at 2100°F and readily extruded from a 3-in.-dia ingot into 1-in. rod.

Standard 0.505-in.-dia bars of the various compositions were tensile-tested at room and elevated temperatures (see Table 45). At all temperatures these alloys show an increase in tensile strength with increasing amounts of zirconium. A corresponding decrease in the ductility accompanies the increase in strength. Data on ingot 527-12 were not obtained, since the extruded rod is too brittle to be machined. The data indicate that alloy compositions with up to 12% zirconium can be hot-formed. Fabrication of the alloys at room temperature seems to be limited to compositions of about 8% zirconium.

The higher zirconium-content alloys do not respond to an annealing heat treatment. This is as expected because the compound Fe_3Zr exists up to the melting point of the alloy.

EXTRUSION EXPERIMENTS

T. K. Roche H. Inouye

Preliminary work in developing seamless duplex tubing has been completed to the extent that several composite billets have been extruded into tube blanks. Little difficulty was experienced in extruding nickel-, Inconel-, and monel-clad type 316

TABLE 45. TENSILE TESTS AT 2100°F OF AS-EXTRUDED IRON-ZIRCONIUM ALLOYS*

Alloy No.	Testing Temperature (°F)	Tensile Strength (psi)	Elongation (%)
527-1	Room	57,300	32.5
	1300	10,500	80.0
	1500	5,100	93.7
	1650	5,800	13.8
527-3	Room	64,500	21.3
	1300	19,400	50.0
	1500	7,900	75.0
	1650	4,600	100.0
527-5	Room	66,500	18.8
	1300	24,900	55.0
	1500	70,000	100.0
	1650	5,100	102.0
527-8	Room	89,600	2.5
	1300	30,800	58.7
	1500	11,900	68.8
	1650	6,700	121.0

*Standard 0.505-in.-dia bars tested.

stainless steel billets; however, the extrusion of type 316 stainless steel clad with Hastelloy B remains problematical. Surface cracking of the Hastelloy B was indicative of the hot shortness which had previously been observed in the extrusion of this alloy. It has been concluded from past experiments that success in the extrusion of Hastelloy B is largely dependent on temperature. For the prevention of defects, the temperature had been determined to be optimum at approximately 2000°F. With the difficulties now encountered at this same temperature, it becomes apparent that melting practice and billet lubrication need to be given more careful consideration if Hastelloy B is to be successfully extruded.

Flame spraying of Hastelloy B with type 304 stainless steel for improved lubrication offered slight improvement with regard to its extrudeability. Two extruded tube blanks of this type had roughened surfaces, and, in addition, one showed signs of surface cracking. Table 46 gives pertinent information regarding the extrusion of the above-mentioned tube blanks from 3-in.-dia billets.

As a service to the Corrosion Group, six special alloys with the compositions shown below were successfully extruded into rod form. These 3-in.-dia cast billets were preheated at 2150°F and extruded with the reduction ratios given.

Composition (wt %)	Reduction Ratio
80 Fe–20 Cr	13:1
80 Fe–10 Cr–10 Ni	10:1
74 Fe–18 Cr–8 Ni	10:1
60 Fe–20 Cr–20 Ni	10:1
90 Ni–10 Mo	10:1
80 Ni–10 Mo–10 Fe	10:1

Future work will be directed toward improving melting practice in order to improve the hot forgeability of Hastelloy-type alloys. The fiber glass, which is introduced into the container of the press prior to the extrusion operation, sufficiently lubricates only one-fourth to one-third of an extruded piece. Therefore, it has become imperative to investigate methods and materials that will offer satisfactory lubrication of the billets during extrusion. Further evaluation of the duplex-type extrusions is in progress in order to determine the bond quality between the components and in order to determine if evacuation of the interface is necessary to achieve bonding.

TABLE 46. EXTRUSION DATA FOR DUPLEX TUBING

Number Extruded	Material	Clad	Condition	Soaking Temperature (°F)	Reduction Ratio	Remarks
3	316 stainless steel	Nickel	Duplex tubing	2100	9:1	Good
3	316 stainless steel	Inconel	Duplex tubing	2100	9:1	Good
3	316 stainless steel	Monel	Duplex tubing	2050	9:1	Good
3	316 stainless steel	Hastelloy B	Duplex tubing	2050	9:1	Surface of Hastelloy B was somewhat roughened in all extrusions; two extrusions showed evidence of cracking
2	Hastelloy B	304 stainless steel	Flame sprayed	2050	9:1	Surface of both extrusions was somewhat roughened; one extrusion cracked
2	Hastelloy W	Inconel	Canned	2050	7:1	Both extrusions shattered
1	Hastelloy W		Uncanned	2050	$5\frac{1}{2}$:1	Did not extrude.

TABLE 47. DESCRIPTION OF VARIOUS COMPOSITES PREPARED FOR TEST PURPOSES BY ROLLING AT 950°C

Barrier	Niobium Laminations (number per core)	As-Rolled Thickness (in.)	Test Purpose
Copper–stainless steel	1, 2, and 5	0.065	Pack rolling, creep bars, tensile specimens, cold rolling, thermal cycling
Tantalum	1, 2, and 5	0.065	
Copper–stainless steel	2	0.120	Thermal cycling, weld tests
Tantalum	2	0.120	

CONTROL-ROD FABRICATION

J. H. Coobs H. Inouye
M. R. D'Amore R. E. McDonald

Feasibility of $(Gd\text{-}Sm)_2O_3$ in Metal Matrices

Two core slugs of 35 vol % of $(Gd\text{-}Sm)_2O_3$ in copper and in iron were prepared by cold-pressing and sintering to densities of 79 and 82%, respectively. The iron mix was sintered at 1100°C and the copper mix at 980°C.

The core compacts were canned, evacuated, and hot-swaged to a total reduction of 75% in seven passes, reheating to 950°C between passes. The active sections of the finished rods were ½ in. in diameter by 7 in. in length.

The core was well compacted, with calculated densities of 97 and 98.5% for the copper and iron compositions, respectively. The core was thermally bonded to the stainless cladding but was slightly irregular in cross section. Metallographic examination showed the core components to be compatible under the sintering and hot-swaging conditions. No evidence was found of reaction between the iron or copper and the $(Gd\text{-}Sm)_2O_3$.

The method shows some promise. Further development of swaging techniques or an initial reduction by rod rolling should correct the irregularities in the core section. Longer sections, probably up to 30 in. in length, could be fabricated readily. The chief restriction of the method is that there is an optimum final diameter of the finished rods beyond which the method no longer is adequate. Control rods up to ⅝ or ¾ in. in diameter could be prepared in this way, but for finished rods, ¾ in. in diameter and larger, extrusion would be preferable.

A hot-pressed body of 30 wt % $(Gd\text{-}Sm)_2O_3$ plus 70 wt % iron was extruded in an Inconel can at 2100°F. The original compact, ¾ in. in diameter by 3 in. in length with 30% porosity, was extruded to a core 24 in. long with an average diameter of 0.230 in. Variations in core diameter were ±0.015 in. from the average.

Examination of the cross section and the longitudinal section indicated that metallurgical bonding had been attained. The density of the core after extrusion was 7.724 g/cm^3 or 98.7% of theoretical.

Tensile tests of the composite at room temperature indicate that the core elongated 3% before fracture. At 1650°F the composite elongated 17% before fracture. The tensile strengths of a 0.505-in.-dia rod of Inconel, containing a rare-earth-oxide core of 0.230-in. diameter, are as follows:

Test temperature	Room	1650°F
Tensile strength, psi	66,500	11,800
Elongation, %	42	17
Remarks	Core fractured at 3% elongation	Uniform elongation

Billets of the absorber composition could be extruded to form rods up to 1½ in. in diameter (including protective clad) with the present equipment and could be finished to size by swaging and/or machining.

Tubular Control Rods

A program has been initiated for the purpose of determining the feasibility of extruding tubular control rods to close dimensional tolerances. The control-rod material of interest is 30 wt % Lindsay oxide plus 70 wt % nickel fabricated into a 2.5-in.-OD × 2.0-in.-ID × 24-in.-long cylinder. The cylinder is to be clad externally and internally with 0.020-in.-thick Hastelloy X. Control materials containing iron as a substitute for nickel and Inconel as a substitute for Hastelloy X are also of interest. It is planned to conduct the initial extrusion studies on undersized control rods of these materials, since the extrusion press at ORNL does not have the capacity to extrude a full-sized rod.

Several methods have been investigated in an effort to determine the optimum means of fabricating cores for 3-in.-dia extrusion billets from the Lindsay oxide–metal mixtures. Small compacts containing 30 wt % Lindsay oxide–70 wt % nickel have been fabricated successfully both by hot pressing and by cold pressing plus sintering. Hot pressing of the powder mixtures at 1200°C produced a sound compact having a density of 86.4% of theoretical. Cold pressing plus sintering resulted in a compact having a density 83% of theoretical and involved the following procedure: (1) pressed at 30 tsi, (2) sintered at 1900°F for ½ hr, (3) coined at 50 tsi, (4) sintered at 2100°F, (5) coined at 50 tsi. The cold-pressed body cracked in one area during sintering at 2100°F. This method yields fair densities on small bodies but is not amenable to fabrication of cores for 3-in.-dia extrusion billets, since the pressure requirements would be beyond the capacity of the equipment at the Laboratory.

The Ceramics Laboratory has successfully prepared small tubes of 50 vol % iron–50 vol % Lindsay oxide by isostatic pressing, and the process is being scaled up to make cores for extrusion billets. The fabrication of cores containing 30 wt % Lindsay oxide–70 wt % nickel by isostatic pressing is also being studied.

[5] A. S. Kitzes and W. Q. Hullings, *Boral: A New Thermal Neutron Shield*, AECD-3625 (May 1954).

SHIELD PLUG FOR ART PUMP

J. P. Page J. H. Coobs

The shield plugs surrounding the impeller pump shafts on the ART must fulfill three primary functions: (1) act as a neutron shield, (2) act as a gamma shield, and (3) act as a thermal shield or heat dam so that fuel will not freeze on the lower surfaces during zero power, fouling the impeller blades.

As no known material will satisfy all these conditions adequately, it is proposed that the following layers be "stacked" in a vented Inconel can: (1) a ⅛-in. disk of B_4C-copper for neutron shielding, (2) a ⅝-in. disk of zirconia for thermal shielding, and (3) a 4- to 5-in. slug of high-density (>12 g/cc), low-conductivity (<0.12 cal/cm²/sec/°C) material for gamma shielding, the top surface of which must be brazed to an Inconel heat exchanger.

A study is being initiated to determine the effect of a helium atmosphere on the conductivity of porous zirconia. A thermal and stress analysis by the Reactor Experimental Engineering Division will determine the feasibility of this design.

Since the conductivity of the high-density material is an important factor, a fairly simple thermal-conductivity apparatus has been fabricated. Its design is basically that described by Hullings and Kitzes.[5] A test of an Inconel specimen used as a standard gave conductivities within 5% of literature values, which is considered quite adequate for present purposes. Thermal-conductivity specimens of tantalum-constantan and tungsten carbide–constantan have been pressed and will be tested in the immediate future.

A successful "diffusion bond" of tantalum-constantan to nickel was obtained by the Welding and Brazing Group by heating the parts to 1100°C in a hydrogen atmosphere for 20 min, then switching to helium before cooling. The specimen was cooled in helium in order to minimize the formation of tantalum hydride, to which was attributed the cracking of several earlier specimens during cooling.

PHYSICAL CHEMISTRY OF CORROSION

G. P. Smith

MASS TRANSFER IN LIQUID METALS

H. W. Leavenworth

Derivation of a mathematical expression to predict mass transfer is being attempted. In order for an atom to leave the surface of a solid, cross the solid-liquid interface, and become part of a liquid, it must surmount an energy barrier. The energy barrier to mass transfer is assumed to be the activation energy for diffusion of the container-metal atoms in the liquid plus the heat content of these atoms in the liquid minus the heat content of these atoms in the solid container material. This concept can be put into the form of an equation:

$$E = Q + H_l - H_s \quad . \tag{1}$$

Below a special temperature T_c, the sum of Q and H_l will be greater than H_s. In this range the energy barrier is positive, and the process is controlled by the rate at which atoms leave the surface of the solid metal. Above T_c the atoms should move into the liquid quite readily, and the process is controlled only by the rate at which atoms can diffuse away from the solid surface in a stationary, liquid-laminar layer.

Epstein[1] has written an equation for mass transfer,

$$R_t = 0.023\left(\frac{D}{\delta}\right)\left(\frac{V\delta}{\gamma}\right)^{0.8}\left(\frac{\gamma}{D}\right)^{0.4}\left(\frac{dC^\circ}{dT}\right)\Delta T \quad , \tag{2}$$

where

R_t = corrosion rate,

D = diffusion coefficient,

δ = diameter,

V = flow velocity,

γ = kinematic viscosity,

C° = equilibrium solubility,

ΔT = temperature differential.

If the form of this equation is changed by substituting the Arrhenius type of expression for D, γ, and C°, that is,

$$D = D_0 \exp(-Q_1/RT) \quad ,$$

$$\gamma = \gamma_0 \exp(-Q_2/RT) \quad ,$$

$$C^\circ = C_0^\circ \exp(-\Delta H/RT) \quad ,$$

where Q_1 and Q_2 are the activation energies for diffusion and viscosity, respectively, and ΔH is the heat of solution, the equation becomes

$$\text{Rate Constant} = \frac{R_t}{\Delta T} = \text{const} \cdot \frac{1}{T^2} \cdot \exp\left(-\frac{0.6Q_1 + 0.4Q_2 + \Delta H}{RT}\right) \quad . \tag{3}$$

The values for Q_1 and Q_2 are equal, according to either the Stokes-Einstein equation or the Eyring equation;[2] and, for dilute solutions, ΔH is equal to the difference in heat contents. The activation energy for mass transfer becomes $Q + H_l - H_s$, as postulated in Eq. 1.

Values for Q, H_l, and H_s have been approximated from data on pure metals, and the theory shows some promise. Experiments are being started in order to obtain the necessary data to test the validity of the diffusion-viscosity relationship.

HIGH-TEMPERATURE SPECTROPHOTOMETRY

C. R. Boston

Measurements of absorption spectra of fused electrolytes continue. A Cary recording spectrophotometer is now being modified for high-temperature research.

THE TRANSFORMATION OF $NaNiO_2$

J. J. McBride

The 220°C transformation of $NaNiO_2$, which was discussed in a previous progress report,[3] was studied further in order to establish whether

[1] L. F. Epstein, *International Conference on the Peaceful Uses of Atomic Energy*, A/conf. 8/P/119 (July 7, 1955).

[2] S. Glasstone, K. J. Laidler, and H. Eyring, *The Theory of Rate Processes*, McGraw-Hill, New York, 1941.

[3] C. R. Boston *et al.*, *Met. Semiann. Prog. Rep. Oct. 10, 1954*, ORNL-1875, p 156.

or not this is a martensitic-type transformation. Several new batches of $NaNiO_2$ were prepared by methods previously described.[3,4] This new material and $NaNiO_2$ samples preserved from previous preparations were both used in the experiments described herein. It was noted in preparing the new material according to the usual method of preparation that reproducible amounts of $NaNiO_2$ were not produced; however, the small amounts produced were sufficient for the experiments in this research. On the other hand, if a large batch (more than a few grams) is desired, further investigation of the experimental variables affecting the rate of formation of $NaNiO_2$ will be necessary before such a preparation can be attempted with a reasonable expectation of success.

The transformation from alpha to beta $NaNiO_2$ (and vice-versa) was observed by the use of reflected plane-polarized light, an electrically heated hot stage, and a Vickers projection microscope. The sample consisted of small, flat platelets of about 1 mm or less in diameter and was contained in a sealed, evacuated glass tube to prevent reaction with air. Generally, only one crystal was observed at a time.

Since the alpha form of $NaNiO_2$ is optically active and the beta form is not, the transformation could be followed by the appearance or disappearance of optical activity. However, the complete transformation front could not be seen (1) because in the alpha form the alternate bands, presumably of twin-related orientation, rotate plane-polarized light in opposite directions and (2) because for any given setting of the analyzer, which makes one-half of the bands a contrasting shade (lighter or darker) to that of the beta phase, the other half of the bands will be indistinguishable from the beta form. Thus, only part of the transformation front is visible.

Although no quantitative measurement of rate of transformation was made, the α/β interface always progressed across a crystal in a fast, jerky manner, even when there was only a small temperature gradient across the crystal. The total time to transform a crystal was in the range of tenths of a second to one second. Occasionally the entire crystal was transformed by the movement of one interface, but it was more common for several interfaces, usually starting from corners, to progress across the crystal simultaneously. As closely as it was possible to observe, bands appeared in the alpha form at the instant it formed. When alpha $NaNiO_2$ was transformed into the beta form, the bands completely disappeared; and they reappeared, although not necessarily with the same geometry as before, when the beta form was transformed back to the alpha. There appeared to be some hysteresis, in that supercooling was necessary to start the beta to alpha transformation; however, the extent of this hysteresis was not quantitatively measured. Once the interface motion had started, it was not possible to stop the motion by manipulation of the temperature control, probably because of the small size of the crystals.

It is concluded from the above that the mechanism of the $\alpha \rightleftharpoons \beta$ transformation is very probably a diffusionless (martensitic) one. No detailed description of the atom movements taking place during the transformation is attempted here because of the lack of complete data on "twin" orientations and interface planes. It is informative to note, however, that there is great similarity between the crystal lattices of the alpha and beta structures and that only small atom movements are necessary to transform one structure into the other. This structural similarity is brought out if a monoclinic coordinate system for the rhombohedral beta structure is defined by the transformation:

$$a = A_1 + A_2 - 2A_3 ,$$

$$b = A_1 - A_2 ,$$

$$c = A_3 ,$$

where A_1, A_2, and A_3 are the vectors defining the rhombohedral cell, and a, b, and c define a C-centered monoclinic cell. The unit cells for the two structures would then be defined as follows: for the α (monoclinic), a = 5.33 Å, b = 2.86 Å, c = 5.59 Å, and β = 110°31′; for the β (monoclinic), a = 5.13 Å, b = 2.96 Å, c = 5.53 Å, and β = 108°0′.

Also, from considerations of crystallographic symmetry, it is believed that the flat surface of the platelet crystals (the surface viewed during transformation observations) is a (100) plane of the monoclinic system. This surface is flat over the entire banded (presumably twinned) region of an alpha crystal; and, thus, during the transfor-

[4] L. D. Dyer, B. S. Borie, Jr., and G. P. Smith, *J. Am. Chem. Soc.* **76**, 1499 (1954).

mation there should be no rotation about an axis lying in this plane. It is notable, on the other hand, that the edges of the platelets are macroscopically distorted wherever a band intersects the edge.

FILM FORMATION ON METALS

J. V. Cathcart

Oxidation of the Alkali Metals

The previously reported investigation[5] of the oxidation characteristics of sodium has been continued, and the work has been extended to include potassium and rubidium. It has been found that all three of these metals oxidize much more slowly in dry oxygen than is predicted on the basis of theory. The results also emphasize the protective nature of the oxide films, at least at relatively low temperatures.

The oxidation rate measurements for the alkali metals were made manometrically; the same type of apparatus was used for the three metals. A film of the alkali metal was evaporated onto the walls of a small glass bulb attached to one arm of a sensitive differential manometer. The course of the reaction could then be followed by measuring the decrease in oxygen pressure in the bulb as a function of time. The details of the experimental apparatus have already been described.[5]

In the last semiannual progress report[5] it was stated that the oxidation rate of sodium, even at 48°C, continually decreased as a function of time and that, therefore, the oxide film could be considered to be completely protective. This conclusion was based on a series of experiments lasting approximately 20,000 min each. Subsequent oxidation rate determinations at 48°C, lasting in excess of 50,000 min, have been completed. A typical rate curve from these more recent experiments is shown in Fig. 129, along with rate curves obtained at 35, 25, −20, and −79°C. In Fig. 129, the number of moles of oxygen consumed per square centimeter of surface area is plotted against the time of oxidation. It will be noted that a slight increase in the oxidation rate occurred at 48°C after 25,000 to 30,000 min

[5] J. V. Cathcart, *Met. Semiann. Prog. Rep. Oct. 10, 1955*, ORNL-1988, p 73; *Met. Semiann. Prog. Rep. April 10, 1955*, ORNL-1911, p 97.

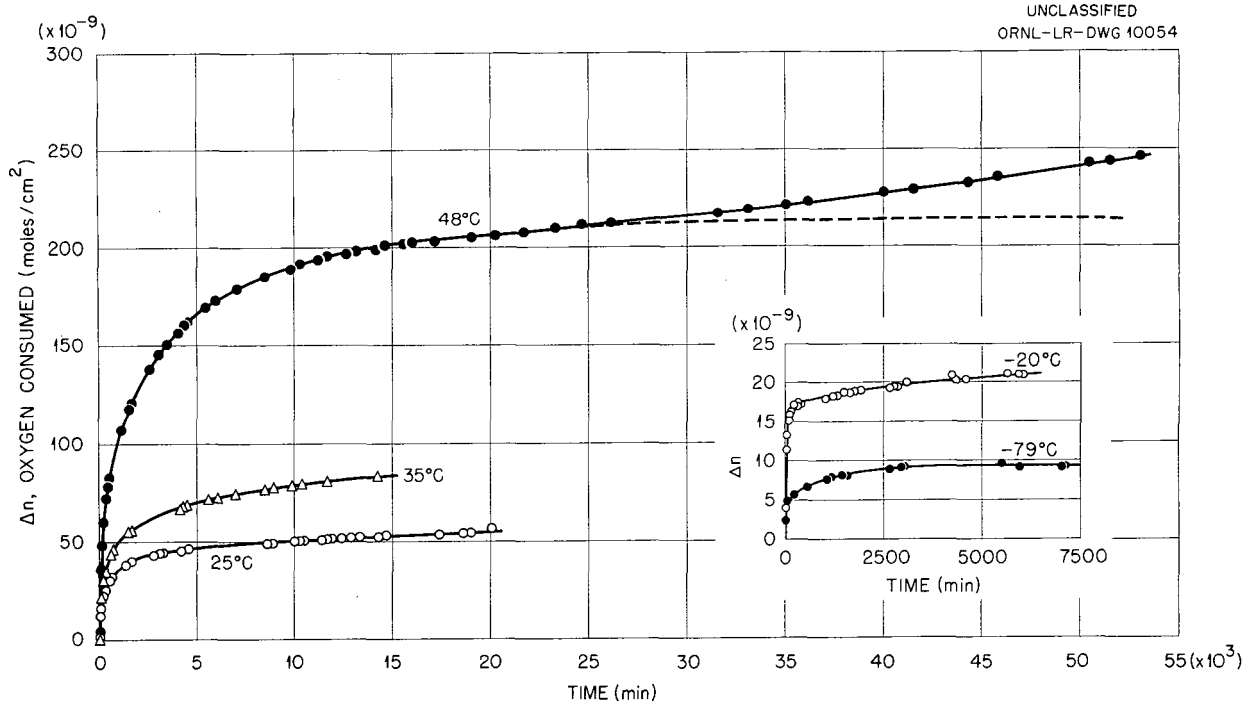

Fig. 129. Oxidation of Sodium at −79, −20, 25, 35, and 48°C.

of oxidation. The dotted line in the graph represents the rate curve which would have resulted if no rate increase occurred. The rate increase was small, but it was observed consistently. Furthermore, a similar, but much more pronounced, rate increase was observed at lower temperatures for potassium and rubidium. No evidence for a comparable increase for sodium was found at the lower temperatures investigated; however, these latter experiments were not carried out beyond a maximum of about 20,000 min. The possible significance of this behavior and its relation to the oxidation of potassium and rubidium are discussed below.

In previous reports,[5] it was shown that the oxidation data obtained for sodium did not conform to any of the rate equations formulated from conventional oxidation mechanisms[6] which have been proposed. An effort has also been made to find some purely empirical relationship which would express the data. It was hoped that an oxidation mechanism might be inferred from such an equation. A least-squares fit of the data was tried for a variety of relatively simple equations. Those investigated included:

$$\frac{1}{x} = \sum_{1}^{n} a_i t^{-1/i} + b \qquad (n = 1,2)$$

$$\frac{1}{x} = \sum_{1}^{n} a_i t^{-1/i} + b \log t \qquad (n = 1,2)$$

$$\log x = a_1 + a_2 \log (t + t^{1/2})$$

$$x = \sum_{1}^{n} a_i t^{1/i} \qquad (n = 3,4)$$

$$x = \sum_{1}^{4} a_i t^{i}$$

In these equations, x represents the quantity of oxide per square centimeter formed in time t, and a_i and b are constants. In no case was a really satisfactory fit obtained, although fairly good agreement between calculated and observed values occurred when the power series

$$x = \sum_{1}^{n} a_i t^{1/i}$$

was used. As might be expected, better agreement was obtained with a series containing four terms than with one containing only three.

It was impossible to attach any physical significance to these empirical equations, and it was finally concluded that the oxidation curves for sodium could not be expressed by any obvious, simple relationship. For this reason, it did not appear worth while to attempt to calculate an activation energy for this process.

The Oxidation of Potassium and Rubidium. – Typical oxidation rate curves obtained for potassium and rubidium at −79°C are shown in Fig. 130. Figure 131 shows a representative rate curve for rubidium at −50°C. In both graphs, a function of the quantity of oxygen consumed per square centimeter is plotted against the time of oxidation. Attempts to measure the oxidation rate for rubidium at −35°C and above and to measure the rate for potassium at 0°C failed because the reaction rate was very rapid. At 25°C, rubidium actually caught fire when oxygen was admitted to the system.

Measurements of the oxidation rate of potassium at −79°C were continued for more than 100,000 min, but no noticeable change in the degree of protectiveness of the oxide films was observed. The amount of new oxide formed after about 8,000–10,000 min was negligible. At −50 and −20°C, however, preliminary results indicate that the oxidation behavior of potassium is comparable to that of sodium at 48°C. The oxide films formed at these temperatures on potassium were initially protective, but an increase in the oxidation rate occurred shortly after the beginning of the reaction. Experiments at these two temperatures are still in progress.

This breakdown of the protective qualities of the oxide film was even more evident with rubidium. For about the first 3000 min of oxidation at −79°C, the reaction appeared to follow much the same course as those for sodium and potassium at the same temperature. At the end of this time, however, a pronounced increase in the rate occurred. The oxidation rate of rubidium at −50°C was considerably more rapid; the rate increase began about 50 min after the reaction started.

[6] O. Kubaschewski and B. E. Hopkins, *Oxidation of Metals and Alloys*, p 37–46, Academic Press, Inc., New York, 1953.

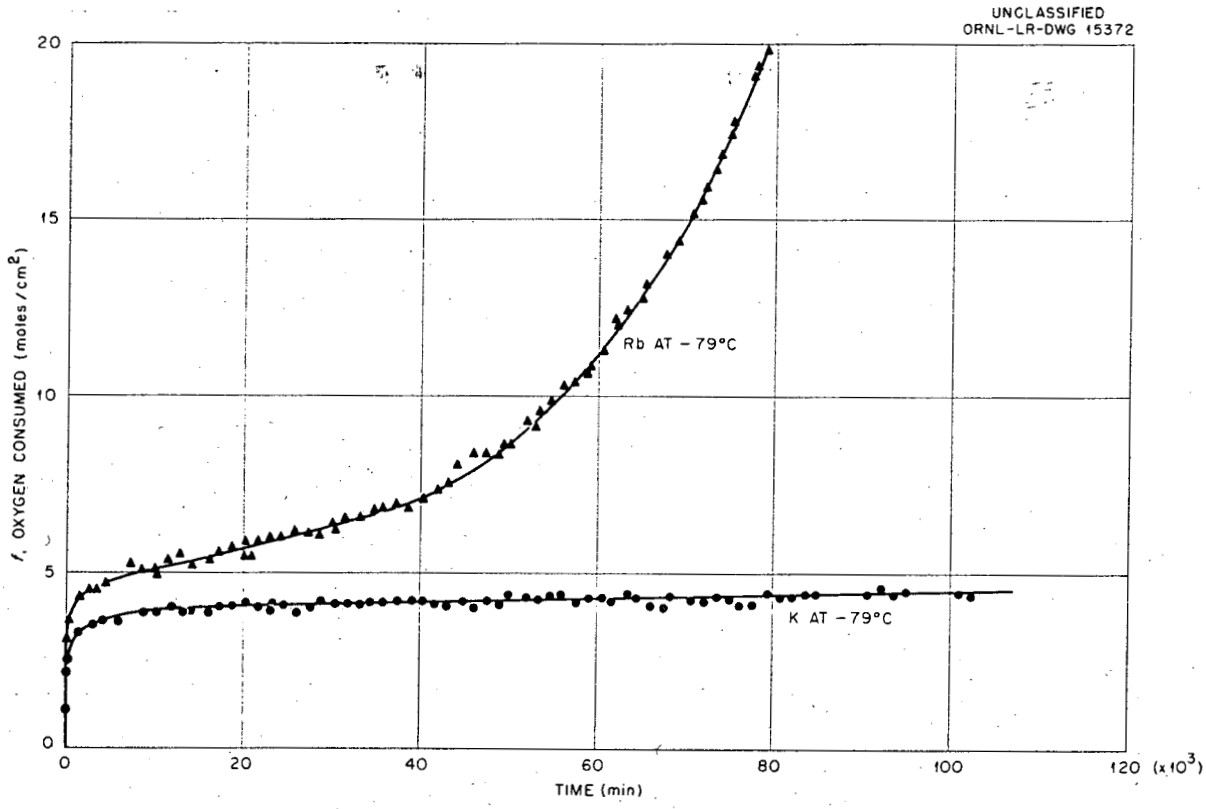

Fig. 130. Oxidation of Potassium and Rubidium at −79°C.

It should be emphasized that, as in the case of sodium, the rate of reaction of both potassium and rubidium with dry oxygen at −79°C was very slow. Even after the rate increase had set in, the oxide films were only a few hundred angstroms thick.

At the present time, it is possible to do no more than guess at the cause of the increase in oxidation rates described above. One explanation might be that cracking and/or composition changes occur in the covering oxide films and cause the films to become less protective. Any speculation as to the cause of these increases in rate can only be substantiated through a detailed study of the oxide films.

Summary of the Oxidation Characteristics of the Alkali Metals. – At sufficiently low temperatures and in dry oxygen, sodium and potassium formed highly protective oxide films. At −79°C, the oxide on rubidium was initially protective; but after a few thousand minutes, a slow increase in the oxidation began to occur. An apparently similar transition was observed for sodium and potassium in experiments at 48 and −50°C, respectively, although the rate increase was less marked. This phenomenon may be related to the production of cracks in the oxide films, or it may be caused by the formation of a second oxide phase; however, no proof exists for either point of view.

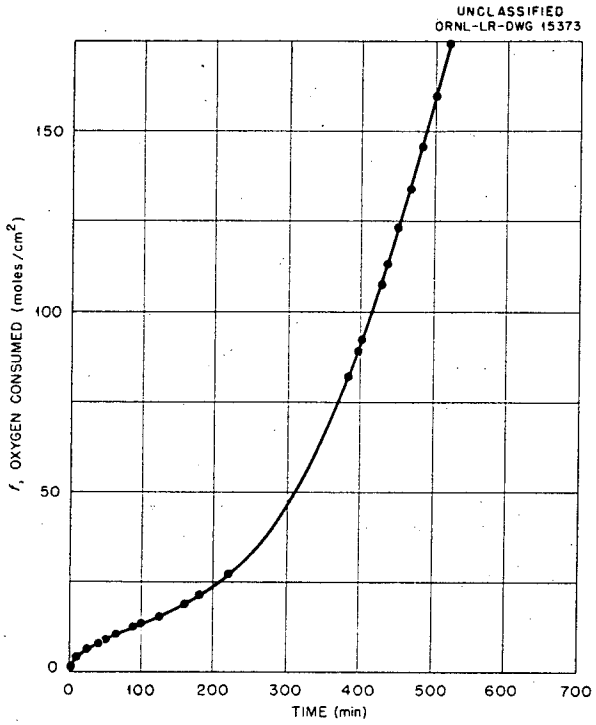

Fig. 131. Oxidation of Rubidium at −50°C.

HRP METALLURGY

G. M. Adamson, Jr.

HRP METALLURGY

G. M. Adamson

PHYSICAL METALLURGY

M. L. Picklesimer G. B. Wadsworth

Physical Metallurgy of Zircaloy-2, -2W, -3A, -3B, and -3C

The program that was initiated for the purpose of metallographically studying the heat-treated structures obtained in Zircaloy-2, -2W, -3A, -3B, and -3C (Table 52) is near completion. As soon as the photomicrographs are completed, a detailed topical report of the experimental data and the experimental techniques will be written.

TABLE 52. COMPOSITION OF ZIRCALOY ALLOYS

Alloy	Components* (wt %)			
	Tin	Iron	Nickel	Chromium
Zircaloy-2	1.5	0.1	0.05	0.1
Zircaloy-2W**	1.5	0.1	0.05	0.1
Zircaloy-3A	0.25	0.2		
Zircaloy-3B	0.5	0.4		
Zircaloy-3C	0.5	0.2	0.2	

*Sponge zirconium makes up balance of composition.

**Zircaloy-2W was a Zircaloy-2 melt made by WAPD from the same sponge and according to the same melting practice as the Zircaloy-3A, -B, and -C melts.

The study has resulted in the following conclusions which pertain primarily to Zircaloy-2 but which, in most cases, also apply to the Zircaloy-3 alloys:

1. The $\alpha/(\alpha + \beta)$ transition temperatures of the alloys ranged from 810 to 850°C and were in the following order: Zircaloy-2 (810°C) = 2W < 3C < 3B < 3A (850°C).

2. The $\beta/(\alpha + \beta)$ transition temperatures ranged from 925 to 970°C and were in the following order: Zircaloy-3A (925°C) < 3B < 3C < 2W = 2 (970°C).

3. The rate of grain growth at 785 and 805°C in annealed alpha specimens is very slow once equiaxed alpha grains, such as are obtained by cold working and recrystallization, are formed. After lineal analyses of the specimens are completed, rate measurements will be made.

4. From 980 to 1085°C, the rate of grain growth in the beta field is very slow after the beta grain size has been established by heating through the $(\alpha + \beta)$ field. The beta grain size (of the order of 1 mm in diameter) established in the upper portion of the $(\alpha + \beta)$ field is very large, is characteristic of the maximum temperature that is reached within the $(\alpha + \beta)$ field, and is established very rapidly during the heating to temperature. Specimens that were held for 10 min and for 2 hr at 950°C had the same grain size. Rate measurements are awaiting lineal analysis of the specimens.

5. Beta-quenched (30 min at 1000°C and water quenched) specimens annealed at 600, 700, and 800°C have shown the following characteristic transitions. The very fine alpha-prime or martensitic structure (acicular needles), formed on quenching, first anneals to coarser, acicular alpha needles with sharp boundaries, precipitating some compound. After 2 hr at 700°C, it undergoes what is believed to be secondary recrystallization to form very large, almost equiaxed, alpha grains (ASTM 1 to 0); and after 30 min at 800°C, smaller equiaxed alpha grains (ASTM 2 to 3) are formed. In both cases a mixed grain size occurs. Figure 135 shows an as-received Zircaloy-2 sample; and on comparison with the photomicrographs in Fig. 136, this change in grain size is apparent. Cold working the beta-quenched specimens 20% and annealing at 800°C for 30 min resulted in a very fine equiaxed alpha grain structure (ASTM 8 or smaller) with considerable randomization of the highly oriented texture[1] of the hot-rolled material (Fig. 137). Specimens cold-worked 10 and 15% and annealed at 800°C showed a progressively larger grain size with decrease in reduction, the grain size for 10% reduction being ASTM 1 or larger. Annealing of the beta-quenched material in the $(\alpha + \beta)$ field for times up to 2 hr and at temperatures up to 900°C resulted in a retention of the acicular needle structure for considerably longer times, presumably, because formation of the

[1]C. J. McHargue and L. K. Jetter, "Preferred Orientation in Zircaloy-2 Plate" (this report).

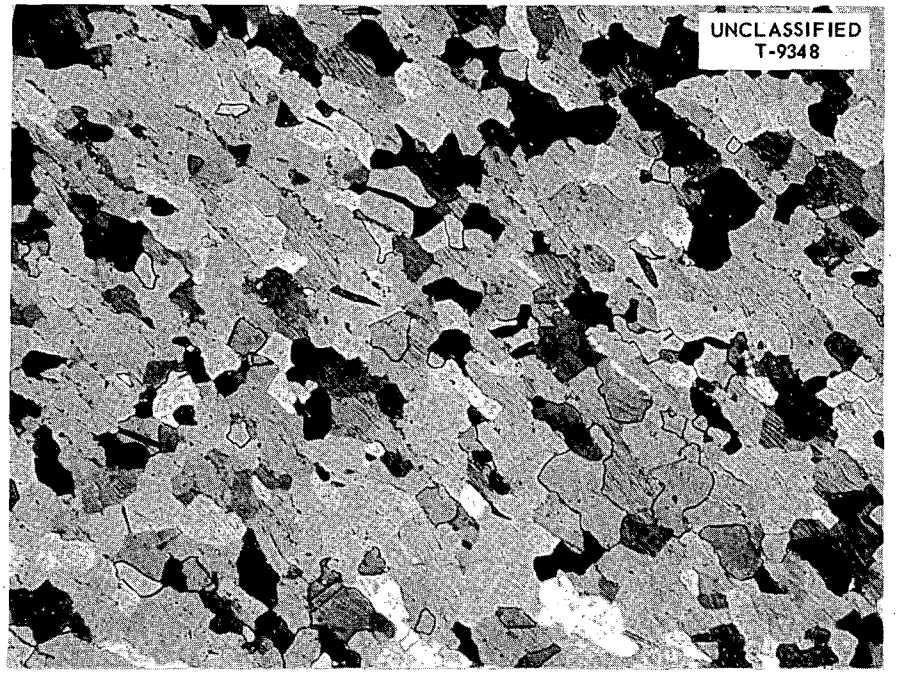

Fig. 135. Photomicrograph of As-Received Commercial Zircaloy-2 Showing Preferred Orientation with Small Grains and the Presence of Stringers. Polarized light. 200X.

beta phase in the grain boundaries resulted in tying-down the grain boundaries and, thus, caused any grain growth to be extremely slow.

6. The structure obtained in the transformation from beta phase to alpha phase in the alloys is essentially the same regardless of cooling rate, except that the structure is coarsened by a decrease in the cooling rate. Apparently there are only a few certain orientations that the alpha needles may take in their formation from the beta structure. This has been found by several investigators to be true in the formation of beta from alpha and alpha from beta in crystal-bar zirconium and would, presumably, also hold in the alpha alloys (Fig. 138).

7. The stringers observed in the hot-rolled plate (Fig. 135), as received from the fabricators, are intermetallic compounds apparently formed from beta phase which was present when the material was hot-rolled. The rolling schedule stipulated that the metal be heated to 840°C and then rolled. In this particular alloy, approximately 15% beta material is formed at 840°C (Fig. 139). The beta constituent present at this temperature would tend to pull iron, nickel, and chromium (eutectoid formers) from the neighboring alpha grains, forming a more stable beta, which when cooled below the decomposition temperature would form the iron, nickel, and chromium intermetallic compounds plus alpha. The beta material present during the hot rolling would, since it is the minor constituent and is in the grain boundaries and grain corners, string out into sheets and stringers. The intermetallics formed from the beta would occur in the same stringer and/or sheet fashion, with the alpha that is formed being deposited on the neighboring alpha grains. These conclusions have been verified by cathodic etching, which shows the stringers to be a metallic phase continuous with the matrix (Figs. 135 and 140), and by the fact that at 1000°C the stringers are dissolved in 30 min (Figs. 136, 137, and 138).

Zirconium-Hydrogen and Zircaloy-Hydrogen Alloys

A study of the mechanism and kinetics of hydride formation in zirconium and zirconium-base alloys has been initiated; the metallography, heat treatment, and properties of these materials are also

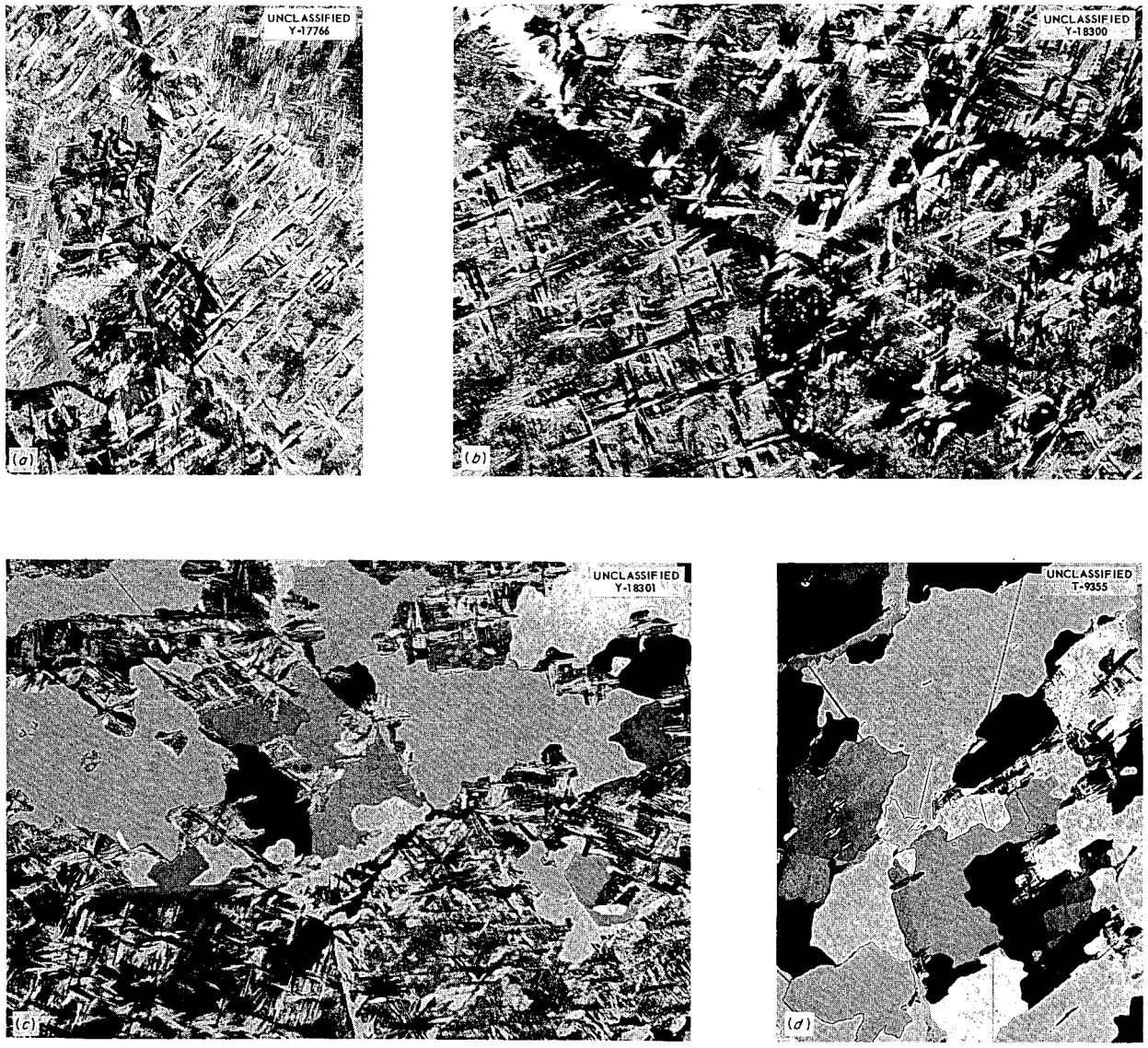

Fig. 136. Photomicrographs Showing the Formation of Equiaxed Alpha Grains Obtained by Aging Beta-Quenched Zircaloy-2. (*a*) As quenched, showing fine acicular alpha-prime needles. (*b*) Annealed at 600°C for 2 hr, showing sharpening of alpha-prime needles. (*c*) Annealed at 700°C for 2 hr, showing large equiaxed grains from a secondary recrystallization. (*d*) Annealed at 800°C for 15 min, showing smaller equiaxed alpha grains. Polarized light. 100X. Reduced 37.5%.

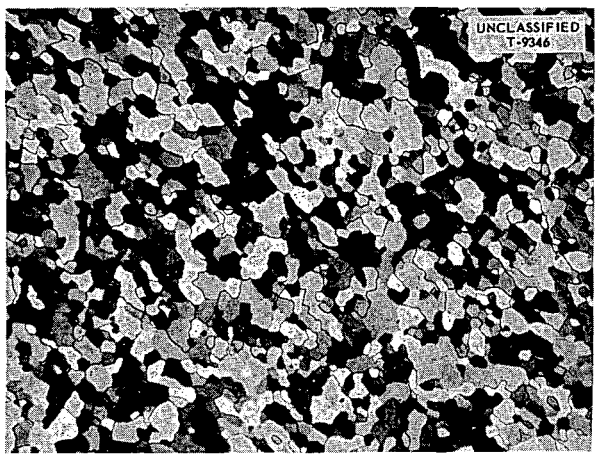

Fig. 137. Desired Small-Grain, Randomly Oriented Zircaloy-2 Structure Obtained by Heat-Treating Highly Oriented Commercial Material. Polarized light. 400X. Reduced 30.5%.

being investigated. Specimens of crystal-bar zirconium, Zircaloy-2, -3A, -3B, and -3C were vacuum-annealed at 900°C so as to contain less than 5 ppm H_2; hydrogen was added at 900°C so that they contained <5, 10, 25, 50, 100, 250, 500, and 1000 ppm hydrogen; they were cooled to 300°C in increments of 100°C at 30-min intervals and were finally furnace-cooled to room temperature. The purpose of this procedure was to reveal the "near equilibrium" structure and the appearance of the hydrides in the microstructure. The metallographic techniques which resulted in the successful delineation of the microstructures consisted of alternately mechanically polishing with fine diamond paste, electropolishing in a perchloric acid–acetic acid bath, and anodizing[2] the specimen to reveal the various microconstituents by color difference. Anodization at 20 v colors the hydrides golden yellow and the matrix purple, thereby providing positive identification of the hydrides in the microstructure.

The procedure reported in the last report[3] for the addition of hydrogen to the alloy specimens at 450°C resulted in the formation of a hydride layer

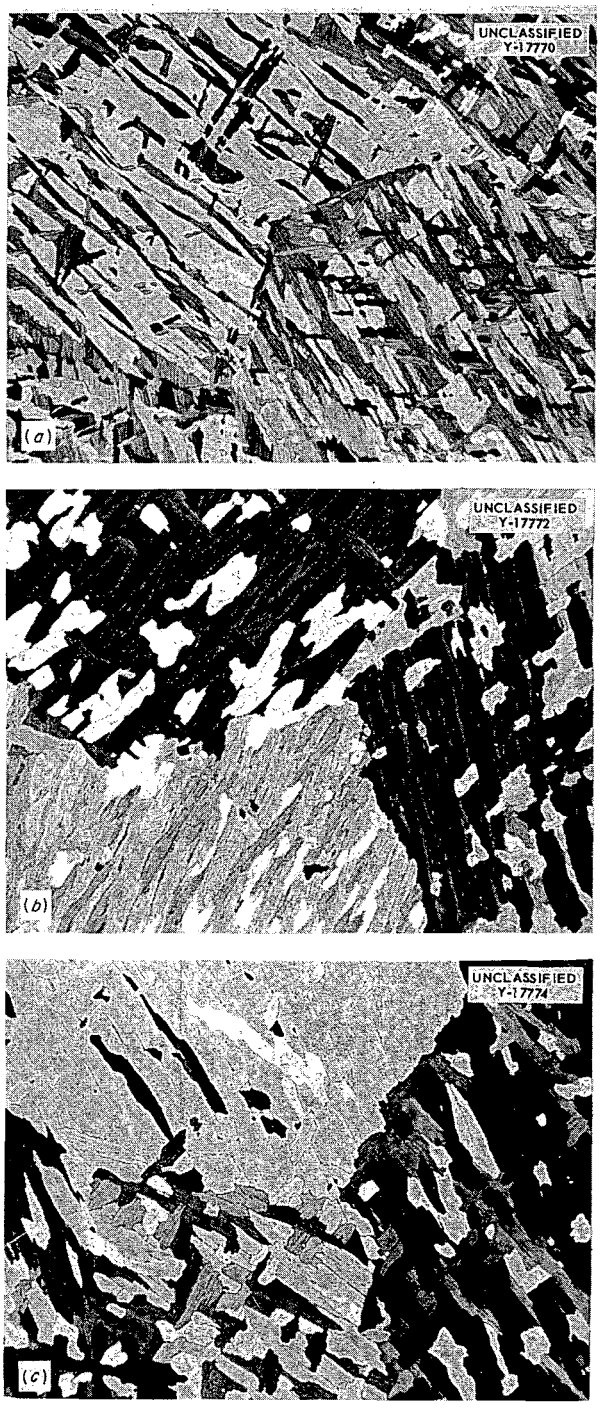

Fig. 138. Photomicrographs Showing the Similarity in Alpha Structures of Zircaloy-2 on Cooling from 1050°C Under Different Conditions. (*a*) Air cooled. (*b*) Furnace cooled. (*c*) Furnace cooled to 800°C; held 30 min; furnace cooled. Polarized light. 100X. Reduced 30.5%.

[2]M. L. Picklesimer and E. E. Stansbury, *Met. Semiann. Prog. Rep. Oct. 10, 1954*, ORNL-1875, p 19–20.

[3]W. O. Harms *et al.*, *Met. Semiann. Prog. Rep. Oct. 10, 1955*, ORNL-1988, p 107.

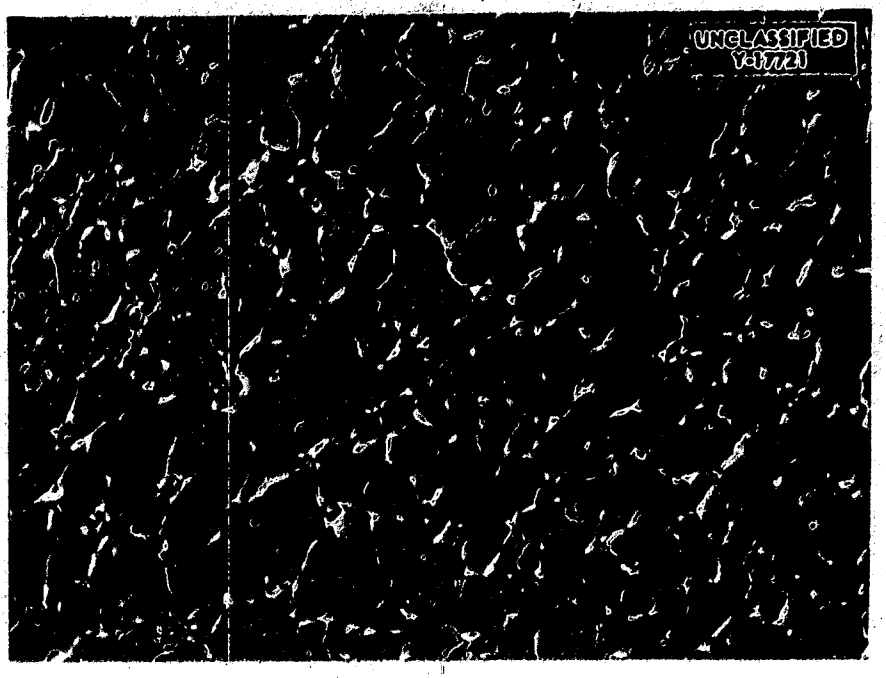

Fig. 139. Beta Phase Formed at 840°C in Grain Boundaries of Zircaloy-2. Water quenched. Bright-field illumination. 200X.

on the surface of the specimen, but without the necessary random distribution of hydride. Homogeneization of the specimens at 900°C caused the random distribution of the hydride, but a distorted and porous surface remained when the hydride layer was dissolved. The procedure for hydrogen addition has been modified; the hydrogen is added to the specimen at 900°C and is followed by homogeneization at 900°C for 1 hr.

To the extent that this study has been carried out, it has been possible to arrive at the following conclusions.

1. The hydride particles in crystal-bar zirconium range in size from massive needles to chunks in a Widmanstätten pattern in the grains and have no decided preference for the grain boundaries until quite high hydrogen contents are reached (Fig. 141).

2. The hydrides in the zirconium-tin alloys definitely prefer the grain boundaries and are only rarely seen penetrating the alpha grains (Fig. 141). The hydrides, ranging in form from needles to plates, tend to occur in the grain boundaries, sometimes being continuous along the boundaries of two to four successive grains. Occasionally, very thin films occur in the grain boundaries and are difficult to resolve at 2000X; these are colored yellow by anodization and are thought to be hydrides, although it has not been conclusively proved that they are not etching effects. As a conclusive test, cathodic etching will be performed on these specimens.

Specimens have been hydrided for heat treatment and kinetic studies, but none, as yet, have been used. Lineal analysis of the "equilibrium" and heat-treated specimens will be performed to determine the effects of alloying elements.

Mechanical-property tests of the hydrided, heat-treated specimens will be conducted after the metallography and heat-treatment studies are completed.

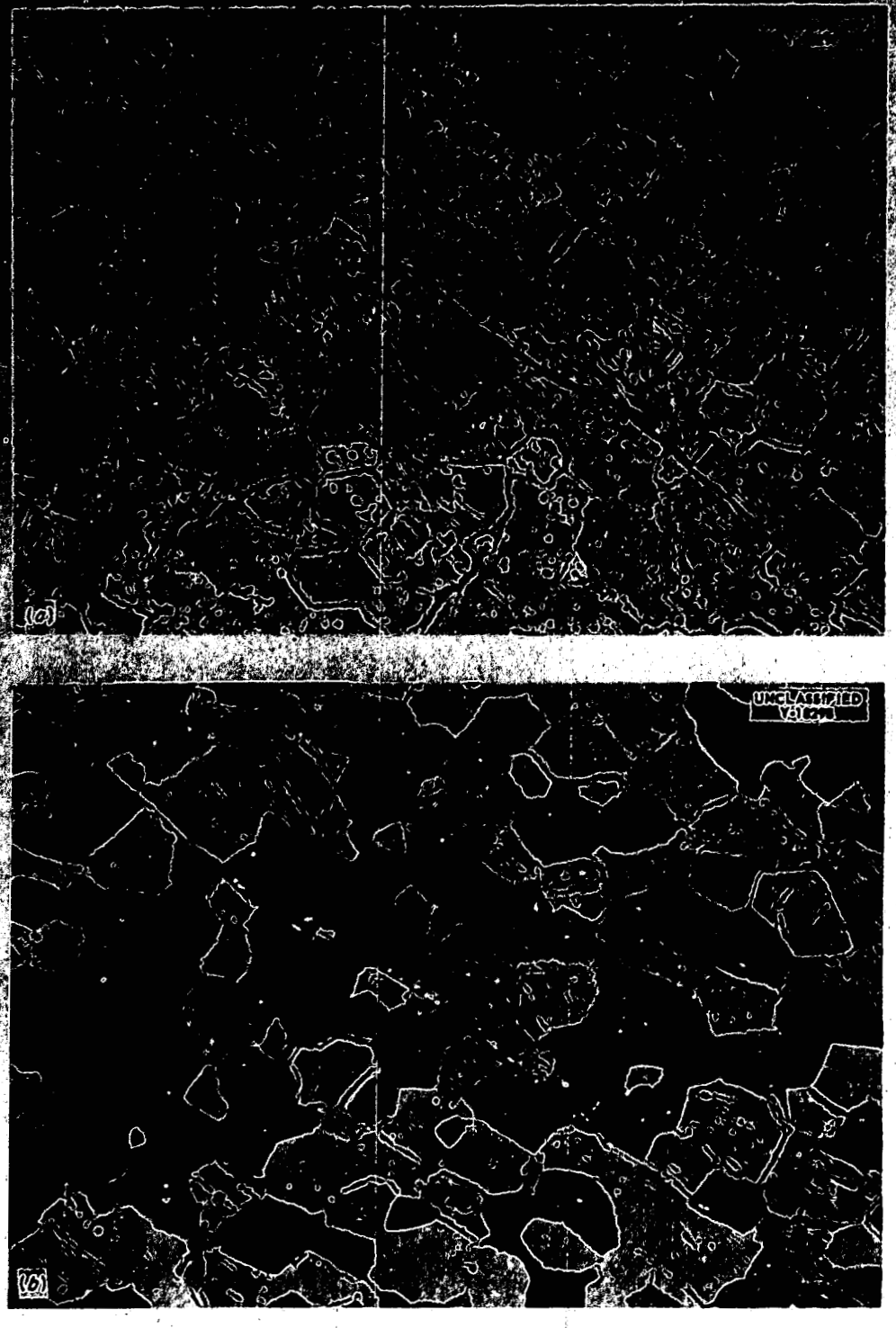

Fig. 140. Stringers Present as a Metallic Phase in As-Received Zircaloy-2. (*a*) Photographed under bright-field illumination. (*b*) Photographed with polarized light. Cathodic etch. 500X. Reduced 18%.

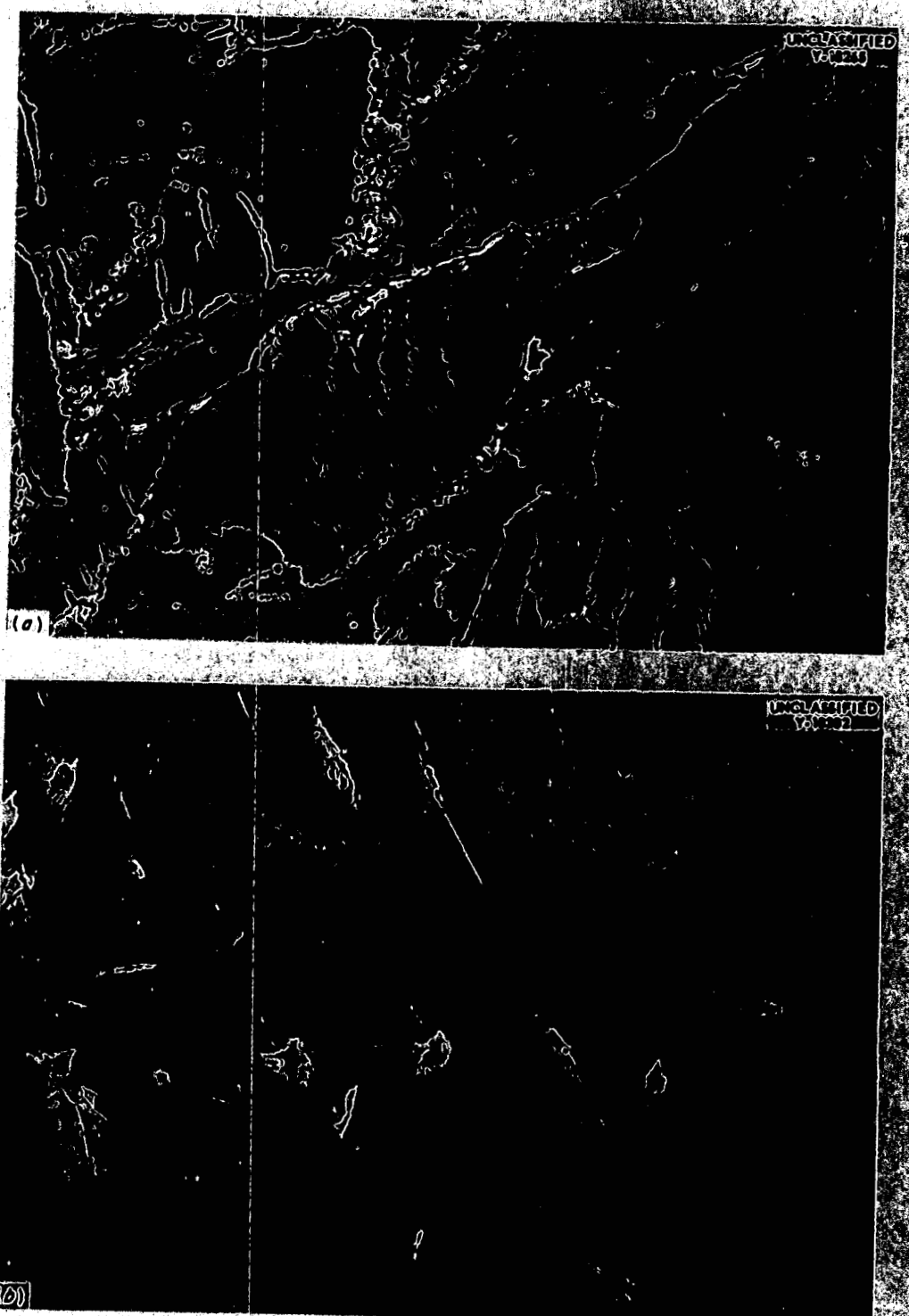

Fig. 141. Comparison of Distribution of Hydrides in (a) Zircaloy-2 Containing 100 ppm Hydrogen and in (b) Crystal-Bar Zirconium Containing 160 ppm Hydrogen. Bright-field illumination. 500X. Reduced 17%.

Stress Corrosion of Stainless Steels

Stress-corrosion testing of several stainless steels has continued.[4] Additional data on types 304L and 347 stainless steels have been obtained in an attempt to determine the threshold stress of these steels in boiling 42% $MgCl_2$. Stresses from 5,000 to 15,000 psi have been used, but the results are too scattered and nonreproducible to report. Various surface and annealing treatments, including electrolytic polishing, vacuum annealing, and annealing in air, have been tried but with no improvement in reproducibility. Rupture times for specimens prepared as identically as possible have varied from 6 to 60 hr for the same stress level. Further testing has been stopped for the present because of the lack of manpower and time.

Cell measurements against a calomel electrode have been made in an etching solution of HCl, picric acid, and alcohol on annealed and cold-worked type 304 stainless steel specimens. The cold-worked (partly martensite) specimen was more negative to the calomel electrode than the annealed specimen. The measurements were reproducible on freshly prepared surfaces but not on specimens that had been in the etching solution for several hours. Measurements made in the etching solution on cold-worked vs annealed specimens were not reproducible, although the emf's were of the correct sign and magnitude; this was probably because the surfaces were not freshly prepared.

Inconel X specimens, heat-treated to spring temper (solution-treated at 2150°F and aged at 1500°F), were held for 194 hr at 70,000 psi (suspension wire broke) and for 320 hr at 70,000 psi, followed by 196.5 hr at 90,000 psi in boiling 42 wt % $MgCl_2$. Both tests were stopped by equipment failure, and neither specimen showed any evidence of stress corrosion.

[4] *Ibid.*, p 99.

MECHANICAL METALLURGY

W. J. Fretague

Zirconium Alloys

In order to determine whether the embrittlement found in Zircaloy-2 impact samples irradiated in the corrosion loops[5] could be due simply to aging, a series of subsize tensile and impact specimens are being aged for various times at a variety of temperatures. Data are now available only on specimens aged at 250°C, which was the temperature encountered in the corrosion loop.

Tensile specimens of 0.180-in. diameter and 1¼-in. gage length were pulled at strain rates of 0.01 and 0.1 in./in./min at 250°C and at room temperature. As shown by the data in Table 53, there was no systematic variation in the yield strength, tensile strength, or elongation of the samples, which were aged for times ranging from 0 to 1585 hr.

The data from the subsize, round impact specimens, 0.204-in. in diameter with a 0.164-in. diameter at the root of the notch, are tabulated in Table 54 and plotted in Fig. 142. These data, also, do not indicate any embrittlement as a result of aging the Zircaloy-2 at 250°C. The curve is similar to the curves presented previously[4] that were obtained with control specimens and specimens irradiated in loops for a short time.

WELDING DEVELOPMENT

W. J. Leonard

Titanium Alloys

Due to its great chemical affinity for other elements and its extremely great alloying tendencies, titanium is difficult to weld or maintain at elevated temperature, except in inert-gas atmospheres. Moreover, because it is not practical to construct a complicated titanium reactor system by the use of dry-box welding techniques, a program has been initiated for the development of alternate titanium welding procedures.

In the development of this technique, welds were made in two dry boxes and in air. One dry box was a compressible type in which the atmosphere is purified by successive cycles of collapsing the box to exhaust the atmosphere and then

[5] W. J. Fretague, *Met. Semiann. Prog. Rep. Oct. 10, 1955*, ORNL-1988, p 93.

TABLE 53. MECHANICAL PROPERTIES OF ZIRCALOY-2* AFTER AGING FOR INCREASING LENGTHS OF TIME AT 250°C

Specimen No.	Aging Time (hr)	Strain Rate (in./in./min)	Testing Temperature (°C)	Yield Strength, 0.2% Offset (psi)	Tensile Strength (psi)	Elongation (%)
242	0	0.01	Room temperature	53,700	80,700	25.0
244	0	0.1	Room temperature	60,230	86,300	22.5
246	0	0.01	250	29,330	44,120	25.5
248	0	0.1	250	33,860	49,600	22.0
241	500	0.01	Room temperature	57,680	81,180	25.5
243	500	0.1	Room temperature	57,970	82,950	26.2
245	500	0.01	250	29,600	48,000	25.0
247	500	0.1	250	26,380	46,450	25.5
258	1085	0.01	Room temperature	55,250	82,490	22.0
260	1085	0.1	Room temperature	58,660	84,170	22.0
262	1085	0.01	250	24,210	43,300	23.0
264	1085	0.1	250	32,290	49,100	27.5
257	1585	0.01	Room temperature	57,280	84,800	25.0
259	1585	0.1	Room temperature	63,190	85,980	22.5
261	1585	0.01	250	25,900	46,200	27.0
263	1585	0.1	250	24,600	49,600	26.5

*The material for these tensile specimens was prepared by cold swaging $\frac{3}{8}$-in.-dia Zircaloy-2 rod to 0.253-in.-dia rod. The swaged rod was sandblasted, pickled, vacuum-annealed at 750°C for 2 hr, and furnace-cooled, prior to machining to final specimen size. The indicated aging treatments were performed in vacuum after the final machining operation.

TABLE 54. IMPACT ENERGY vs TESTING TEMPERATURE FOR ZIRCALOY-2 AGED AT 250°C

Impact Temperature (°F)	Impact Energy (in.-lb)			
	Aged 0 hr	Aged 500 hr	Aged 1085 hr	Aged 1585 hr
−100	8	10	9	8
15	15	13	12	14
90	16	22	20	20
150	27	24	27	28
200	32	38	34	36
254	~60*	~60*	~60	50

*Incomplete fracture, broke on rebound.

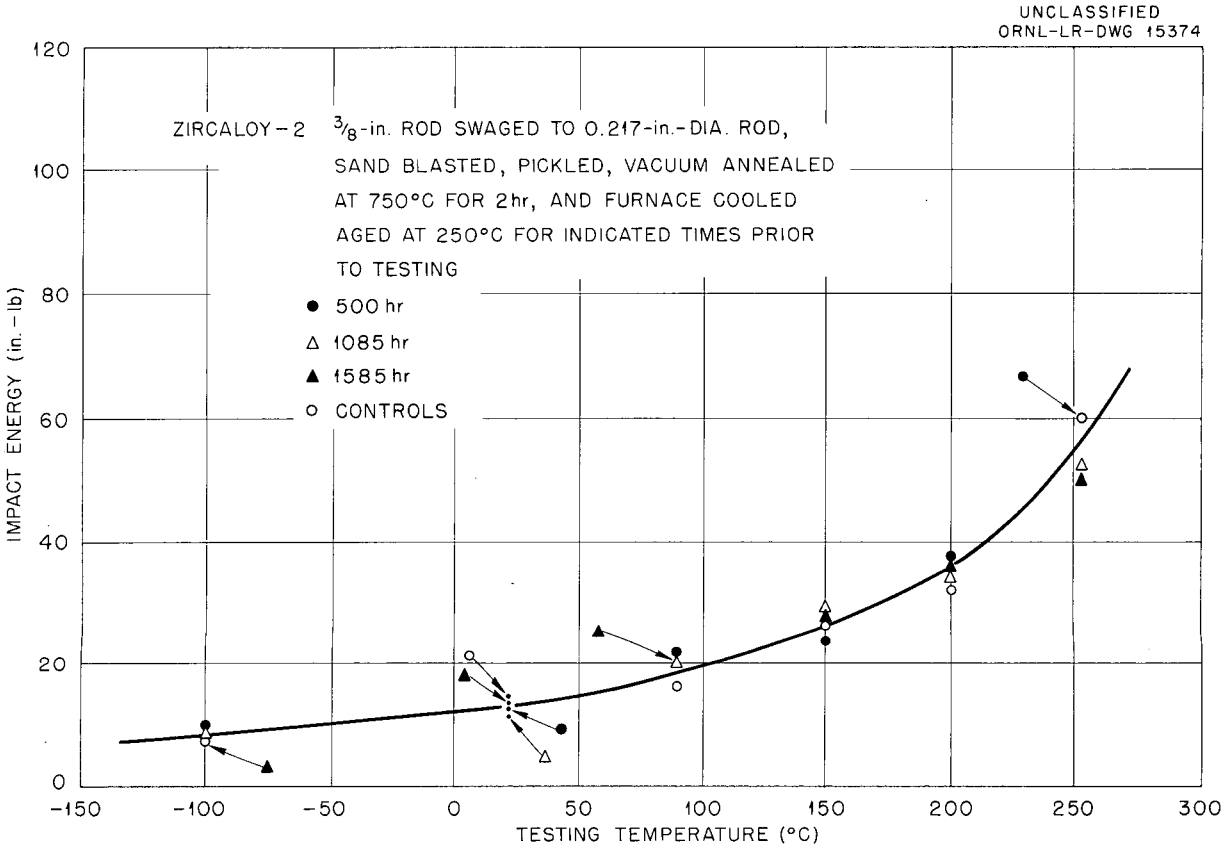

Fig. 142. Impact Energy vs Testing Temperature for Zircaloy-2.

re-extending the box and introducing inert gas. The other box was the usual rigid type in which the atmosphere was removed by evacuation. The inert-gas-shielded tungsten-arc welding process was used for all this work. In order to provide increased protection for the welds made in air, the torch used was modified to permit an increase in gas flow. Extreme care was also used to provide complete coverage and purging by the inert gas used for backup. A high-purity-titanium weld wire Ti-A40 (55,000 psi tensile strength) was used as the filler metal. The mechanical properties of the welds were compared by means of bend tests and microhardness traverses and by spot checking the tensile and impact properties. The soundness of the welds was checked by liquid penetrants and by radiography.

By keeping the size of the liquid pool to a minimum and by carefull purging, it was found that welds approximately equal in quality to those made in a dry box could be made in air. Comparative mechanical-property data for welds made in ¼-in. plate are tabulated in Table 55. Hardness comparisons on welds made on two types of pipe and on a plate are shown in Table 56. The hardnesses of the wrought pipe and plate used for this work averaged 150 DPH; vacuum-cast metal would average about 160 DPH. The increase in weld hardness above this was caused by contamination from nitrogen and oxygen.

Because of the higher-purity gas atmospheres, the welds made in a vacuum-type permanent-volume dry box and with inert-gas coverage generally resulted in a weld-metal hardness that was approximately 20 points lower than that obtained on welds made in a compressible-type dry box. Welds made in the open atmosphere averaged approximately 15 points higher in hardness than did those made in the compressible-type dry box. A variation in hardness from 165 to 210 VPN had very little effect on the resultant mechanical properties of

TABLE 55. COMPARATIVE MECHANICAL PROPERTIES OF TITANIUM WELDS MADE IN AIR AND IN A DRY BOX

Welding Conditions	Hardness (VPN)		Tensile Strength (psi)	Yield Strength (psi)	Elongation (%)	Impact* Strength (in.-lb)	Maximum Bend Angle, 2T Bend Radius (deg)
	Weld Metal	Base Plate					
Dry box	188 (av)	136	52,500	40,200	21	33	180
Atmosphere	199 (av)	136	51,300	40,200	20	38	180

*The impact tests were made on subsize V-notch Charpy specimens with the notch cut into the weld metal.

TABLE 56. COMPARISON OF HARDNESSES OF TITANIUM WELDS MADE IN A DRY BOX AND IN AIR

Material	Hardness (VPN)	
	Dry-Box Welds	Atmosphere Welds
½-in. pipe, sched 80	171, 185, 181, 176, 175, 163 (av 175)	204, 219, 201 (av 208)
3-in. pipe, 9/16-in. wall	182, 174	183, 185
3/32-in. plate	173	179, 181

the weld metal. The base metal in the heat-affected zone exhibited a coarsened microstructure but very little increase in hardness.

Two titanium loops have been fabricated by using the air welding technique. One loop has been used for testing by the Chemical Technology Division, while the Reactor Experimental Engineering Division has operated the other as an in-pile loop at 300°C and 2000 psi.

Corrosion Tests of Simulated Weld Metal

W. J. Leonard

Alloys of zirconium and commercial titanium were vacuum-melted in water-cooled copper-hearth molds. The melting chamber was evacuated to a few microns, and then a high-purity argon atmosphere was maintained during the melting and solidification. The size of the buttons and cooling rates were such that the cast structures approximated ¼-in.- to ½-in.-plate weldment. They were then used as simulated weld-metal corrosion-test specimens.

The specimens were static-corrosion-tested for a total of 1000 hr with interruptions at 50, 150, and 430 hr. Over-all corrosion rates are given in Table 57; since descaling methods are not available for these alloys, the corrosion rates are approximate, being based on weight loss or weight gain. All the alloys completed the total 1000 hr in solution, except specimen 5; this sample was withdrawn after 430 hr because of its rapid corrosion rate. The corrosion rate reported is the average for 430 hr.

Listed below are some of the more important phenomena that were observed:

1. Specimen 1 built up a heavy, black, imperious scale which withstood brushing.
2. Specimen 5 formed a white, friable scale which easily flaked off.
3. The other specimens had very thin, practically transparent, scales.
4. The corrosion rates on all specimens were extremely low, except those of samples 1 and 5.
5. The addition of up to 3.5% chromium to the zirconium had no significant effect.

TABLE 57. CORROSION RATES FOR SIMULATED WELD MATERIAL AFTER 1000-hr EXPOSURE IN STATIC AQUEOUS UO_2SO_4 SOLUTION AT 300°C

Sample	Alloy	Weight Change (mg/cm^2)	Corrosion Rate (mpy)
1	Zr-Cr (53% Cr)*	+8.7	~21
2	Zr-Cr (3.5% Cr)	−2.2	1.1
3	Zr-Cr (1.4% Cr)	−0.2	~0.1
4	Zr-Cr (0.7% Cr)	+0.06	Negligible
5*	Zircaloy-2 +1.9% Al	−100	121
6	Zircaloy-2	Negligible	Negligible
7	Zr, crystal bar	−0.1	0.05
8	Ti-75A	Negligible	Negligible

*Composition corresponds to the intermetallic $ZrCr_2$ occurring in the binary phase diagram.

APPLIED METALLURGY

J. E. Cunningham

PACKAGE POWER REACTOR PROGRAM

R. J. Beaver R. C. Waugh C. F. Leitten, Jr.
Metallurgy Division
E. C. Edgar
Alco Products, Inc.

IRRADIATION TEST OF MINIATURE APPR FUEL PLATES IN THE MTR

R. C. Waugh

Twelve miniature fuel plates were prepared for irradiation, as a phase of the APPR fuel element development program. The purpose of this phase of the program is to determine the effect of different amounts of cold reduction and of different types of uranium dioxide on the radiation damage imparted to the prealloyed stainless steel matrix. The uranium dioxide was prepared by (1) steam oxidation of uranium, (2) reduction of burned oxide chips, (3) reduction of uranium trioxide monohydrate, and (4) hydrogen peroxide precipitation from ammonium diuranate.

Plates containing each type of oxide were prepared in the as-hot-rolled condition and with 10 and 30% reductions by cold rolling.

FABRICATION OF COMPOSITE STAINLESS STEEL APPR FUEL PLATES

R. C. Waugh

Fuel-Melting Experiment

Fifty-three enriched miniature plates of APPR composition were fabricated for use in the APPR fuel-melting experiment. Each core, containing a nominal 0.100 g U^{235}, was oblong in shape and had maximum dimensions of 0.203 × 1.375 in.

Metal-Water-Reaction Experiment

Two enriched miniature plates were fabricated for use at the MRT in an experiment to determine the extent of reaction between the alloy and water. One contained a prealloyed stainless steel–uranium dioxide core and had a U^{235} loading of 0.98 g/in.^{2}. The second contained an aluminum–UO_2 core and had a U^{235} loading of 3.84 g/in.^{2}. This corresponded to 70.6 wt % UO_2 in the core.

Application of Roller Leveler to the Flattening of Fuel Plates

The use of roller leveling in the flattening of APPR fuel plates appears to be promising. After cold rolling, 20 fabricated plates were free-annealed for 5 min at 1150°C; this resulted in severe buckling. By subsequent use of the roller-leveling technique, a fair degree of flatness was attained. Brazing these plates into a standard APPR assembly will be the final criterion used in evaluation of this technique.

Powder-Metallurgy Blending Studies

Work has continued toward the attainment of a homogeneous distribution of the core components in the fabricated plate. Emphasis was shifted from the batch blending of several cores to individual blending of each core. The particle sizes of each constituent were:

Uranium dioxide: 20.25 wt %, 44–48 μ
Boron carbide: 0.20 wt %, –325 mesh
Prealloyed stainless steel: 79.55 wt %, –100 mesh

The powder for each core was weighed into a 4-oz bottle and blended in an oblique blender. Lauryl alcohol was added by means of an atomizer. The blending parameters are outlined in Table 63. Each core was subsequently fabricated into a fuel plate and radiographed after cold rolling. Four specimens were cut from along the core length of each plate and analyzed for boron and uranium. These results are also given in Table 63.

Excellent distribution of uranium can be obtained by proper blending. Although deviations in the boron concentration are apparently appreciable, it should be borne in mind that there is an inherent inaccuracy in the analysis of boron in the range of 0.1% because of the presence of stainless steel.

APPR ABSORBER

C. F. Leitten, Jr.

The poison specified for the APPR control rod is boron. Originally, specifications stipulated that 75 g of natural boron in the form of B_4C be incorporated in a copper matrix by powder-metallurgy

TABLE 63. POWDER-METALLURGY BLENDING STUDIES

Sample No.	Dry Blending (hr)	Squirts of Alcohol	Reblending (hr)	Radiographic Evaluation	Boron Deviation*	Uranium Deviation*
769-1	2	2	1	Slight streaking	0.00	−1.39
769-2					+5.50	−1.39
769-3					+0.79	+0.49
769-4					−5.50	+2.29
771-1	2	4	1	Homogeneous	−1.00	−1.24
771-2					+23.5	0.00
771-3					−5.10	+0.50
771-4					−17.3	+0.83
773-1	4	1	1	Homogeneous	+19.7	+0.83
773-2					+9.8	+0.50
773-3					+0.93	−2.16
773-4					−29.5	+0.92
775-1	4	2	1	Homogeneous	−22.7	−1.28
775-2					+26.7	+0.72
775-3					−28.0	−0.88
775-4					+21.4	+1.43
777-1	4	4	1	Homogeneous	−29.1	+1.80
777-2					+8.1	−1.80
777-3					−5.8	0.00
777-4					+26.8	0.00

*Percentage from the average.

techniques and that this core mixture be roll-clad with type 304 stainless steel. Billets fabricated by the use of a picture-frame technique were unsatisfactory. The plates exhibited clad ruptures at both core ends and very poor over-all bonding. It was found that rupturing of the clad could be prevented by inserting powder-metallurgy stainless steel cores at both ends of the copper-B_4C cores and using light total reductions. The core-clad bonding was improved by inserting a 0.005-in. strip of electrolytic copper between the core and clad. In a similar manner, the stainless-stainless bonding was improved by electroplating a thin layer of nickel onto the stainless steel frame. Both the copper and nickel were found to act as bond aides during hot rolling at 1000°C. Control-rod plates fabricated in this manner were acceptable for the critical experiment; however, they were not satisfactory for reactor service.

Several techniques were employed in an effort to fabricate a copper-B_4C control rod that would meet specifications. Billets were fabricated at greater total reductions in thickness in an attempt to improve the bonding. It was found, however, that increasing the total reduction resulted in clad rupture. This rupturing of the clad is attributed to the difference in plasticity between the copper-B_4C core and the type 304 stainless steel. At 1000°C, the copper-B_4C core is apparently more plastic than the stainless steel. Since the degree of plasticity decreases with temperature, it was felt that by reducing the rolling temperature clad rupturing could be prevented. Billets fabricated at 800°C were found to exhibit no evidence of clad rupture; however, there was a decrease in bond strength. In order to fabricate at 1000°C without rupturing the clad at heavy reductions, it was found necessary to machine V-notches into the frame ends. These V-notches absorbed the excess core extension during rolling and thereby prevented the clad from rupturing. Satisfactory end effects were obtained by using a single rolling direction and a combination of V-notches, which consisted of a $\frac{1}{16}$-in. notch at the trailing end and a 0.4-in. notch at the leading end of the billet. Such a combination essentially confined the core extension to one

end of the plate. The stainless-stainless bonding along the edges, however, was unsatisfactory, since specifications stipulated a $\frac{1}{8}$-in. maximum edge width of stainless steel. Metallographic examination revealed that the bonding was satisfactory $\frac{1}{4}$ in. from the core edge. Since such a plate did not meet the required specifications, this combination of materials was abandoned.

Several other boron compounds were considered along with other matrix materials. The feasibility of MoB_2, CaB_6, AlB_{12}, ZrB_2, BN, and elemental boron and of iron and stainless steel as matrix materials was considered. The compounds MoB_2, ZrB_2, and BN were eliminated from further consideration because of the excessive volume of compound required. The CaB_6 and AlB_{12} reacted with iron and with stainless steel at 1000°C and, likewise, were dropped from further consideration. Elemental boron in amounts of 1.5 to 3.6 wt % was found compatible with iron when sintered at 2050°F.

Billets containing 3.43 wt % B^{10} in iron were fabricated at 1000°C and with a total reduction in core thickness of 10 to 1. There was no evidence of clad rupturing; however, the core exhibited extreme stringering at both ends. This stringering was prevented by using a single rolling direction, which produced a plate with essentially a blunt core end at the trailing end of the billet and a fishtail at the leading end. Such ends are acceptable for the APPR control rod. The core-clad bonding and the side stainless-stainless bonding were metallurgically sound.

The rolling temperature was increased in an attempt to improve bonding further. Billets fabricated at 1100 and 1150°C showed satisfactory metallurgical bonding and no evidence of reaction. Figures 154 and 155 are photomicrographs showing the side stainless-stainless bonding in plates fabricated at 1100 and 1150°C, respectively. Interfacial grain growth is present in each. Figure 155 shows the greater degree of boron diffusion that occurred.

EXAMINATION OF 18-PLATE APPR ELEMENT IRRADIATED IN THE MTR

R. J. Beaver

Further postirradiation examination of this fuel element was made in the MTR hot cells subsequent to 1431 Mwd irradiation in the MTR and two months cooling time in the MTR canal. Four plates were machined from this unit. Three of these plates contained, respectively, 16.5, 19.5, and 23.7 wt % uranium and were examined carefully for imperfections which may have been caused by irradiation. No evidence of blistering, corrosion, or warpage was observed. Sections from the plates have been delivered to the ORNL Solid State Division for microscopic examination of damage.

EXAMINATION OF MINIATURE APPR PLATES IRRADIATED IN THE MTR

R. J. Beaver

Several of the miniature APPR plate sections, after an estimated 30% burnup of U^{235} atoms, were delivered to the ORNL Solid State Division and were microscopically examined for irradiation damage.

The results available at the present time are listed in Tables 64 and 65. Based on this information and the microscopic results obtained from the full scale MTR irradiation test, a UO_2 particle size ranging from 44 to 88 μ has been selected for the APPR-1.

COMPONENT ASSEMBLY BY BRAZING

R. J. Beaver E. C. Edgar

A stainless steel brazing jig, illustrated in Fig. 156, has been designed and will be substituted for the graphite self-locking-type jig. Experimental results obtained by brazing APPR assemblies with this stainless steel jig have revealed improved plate spacings and the elimination of bowing in the top and bottom plates which occurred during brazing in a graphite jig. Use of the stainless steel jig also has the advantage that the units can be assembled and brazed in the same fixture. Slight distortion of the base plate of the jig occurs during the brazing cycle; however, it appears that the jig will withstand 10 to 20 cycles before redressing is required. This distortion has not affected the fuel-element dimensions. The brazing cycle previously established remains unchanged and will be used during production brazing. Engineering drawings have been completed, and brazing of the first reactor loading is scheduled to begin shortly.

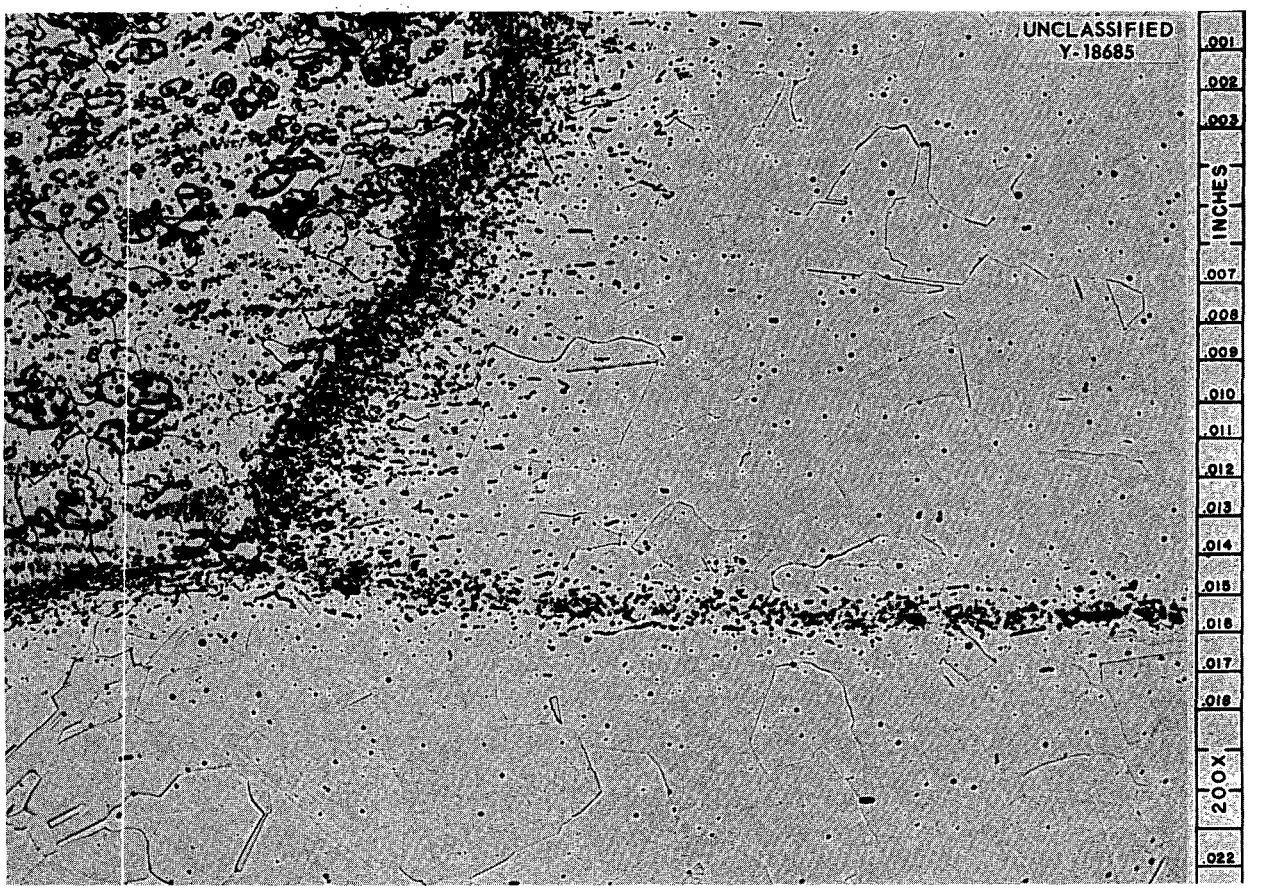

Fig. 154. Photomicrograph of a Section of a Control Rod Fabricated at 1100°C Showing Side Bonding Between Core and Frame and Between Clad and Frame. Note interfacial grain growth and boron diffusion into both frame and clad. (Confidential with caption)

TABLE 64. HARDNESS DATA FOR PREIRRADIATED AND POSTIRRADIATED STAINLESS-STEEL-CLAD FUEL SECTIONS CONTAINING DIFFERENT PARTICLE SIZES OF UO_2

Sample	Original Particle Size (μ)	Hardness (DPH)								Normalized Value
		Before Irradiation				After Irradiation				
		Clad		Core		Clad		Core		
		Range	Average	Range	Average	Range	Average	Range	Average	
12	7–11	141–145	144	198–210	204	202–211	206	422–484	475	500
14	16–22	136–141	138	192–208	198	203–213	209	445–501	465	482
16	22–31	134–139	136	178–193	189	207–231	222	417–463	437	427
18	31–44	133–134	134	173–193	184	209–236	223	389–463	420	410
20	53–62	129	129	175–184	179	204–223	214	350–468	393	399
22	74–88	129–141	136	180–197	184	206–215	210	350–439	390	403
24	88–105	139–147	144	173–186	178	223–246	234	351–396	371	344

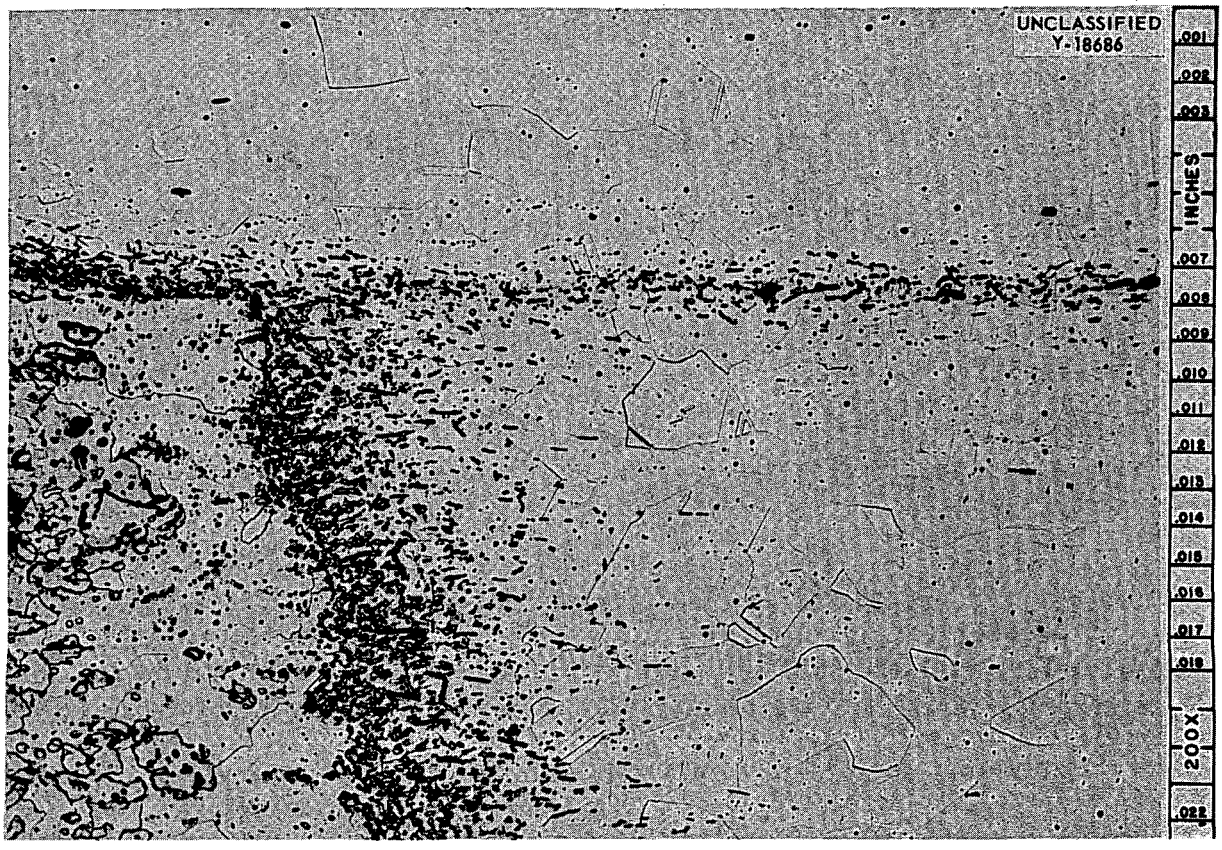

Fig. 155. Photomicrograph of a Section of a Control Rod Fabricated at 1150°C Showing Side Bonding Between Core and Frame and Between Clad and Frame. Note interfacial grain growth and boron diffusion into both frame and clad. 200X. Reduced 2%. (Confidential with caption)

TABLE 65. EFFECT OF IRRADIATION AND HEAT ON HARDNESS OF CORES CONTAINING DIFFERENT PARTICLE SIZES OF UO_2 IN STAINLESS-STEEL-CLAD FUEL SECTIONS

Sample	Original Particle Size (μ)	Hardness (DPH)					
		Before Irradiation	After Irradiation	Anneal			
				400°C	600°C	800°C	1000°C
12	7–11	204	475	586	500	364	115
14	16–22	198	465	579	512	349	97
16	22–31	189	437	509	446	338	141
18	31–44	184	470	462	425	325	168
20	53–62	179	393	397	393	392	135
22	74–88	184	390	406	333	276	173
24	88–105	178	371	389	346	278	144

UNCLASSIFIED
Y-18743

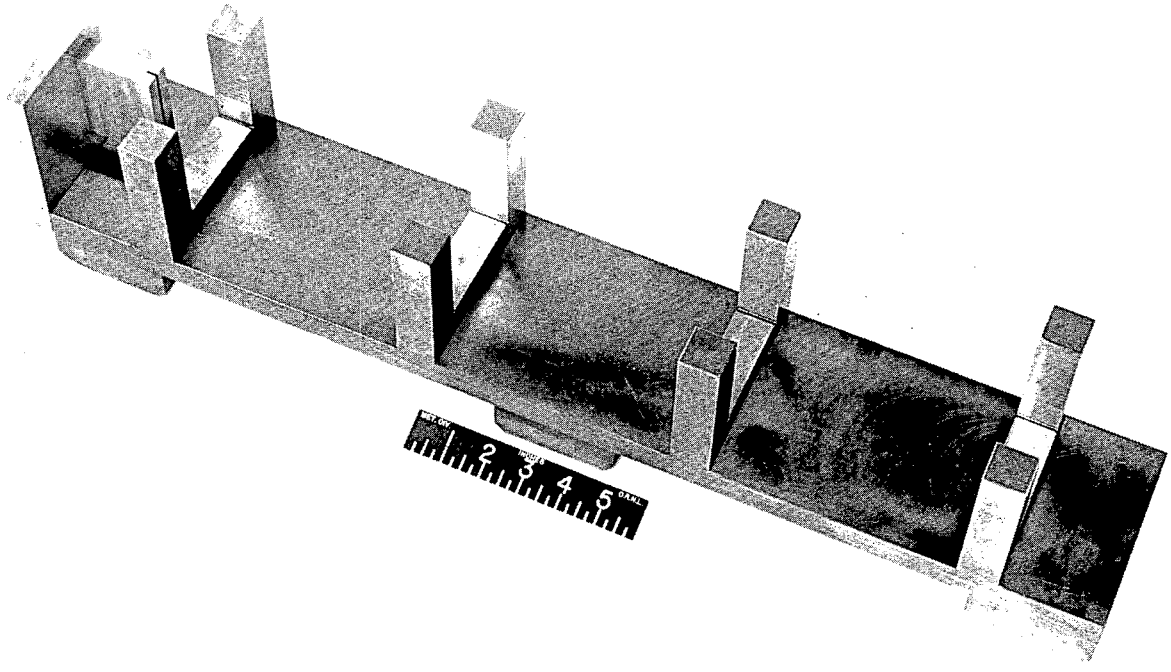

Fig. 156. Stainless Steel Jig for Use in the Brazing of Stainless Steel APPR Fuel Elements. (Confidential with caption)

METALLURGICAL MATERIALS AND PROCESSING

R. E. Adams E. S. Bomar J. I. Federer

THORIUM – METALLEX PROCESS

E. S. Bomar

Differential Thermometry

In the previous semiannual progress report,[1] it was stated that differential thermometry experiments were being considered as a means of obtaining additional information on the nature of the decomposition of thorium amalgam. It was hoped that the heat effects associated with the phase changes would be large enough to be detectable, even in a simple piece of equipment. To this end, thermocouples and the necessary wiring and switching equipment were assembled. Tungsten was selected as the reference sample material because of its relative inertness to mercury vapor. The thermocouples, sheathed in thin-wall quartz tubes, were placed in holes drilled to the center of each of the samples. The absolute temperature of the thorium sample and the difference in temperature between the thorium and tungsten were recorded simultaneously. The thermal decomposition of two samples of thorium amalgam at pressures less than 1 μ were monitored and the results plotted in Fig. 157. Although the two plots are not identical, there is considerable similarity between them. The initial lead in temperature established by the thorium sample is interpreted as an emissivity effect. The sharp decrease in temperature of the thorium below that of the tungsten at about 300°C is thought to have been caused by the heat effect associated with the boiling away of uncombined mercury. (In view of the fact that uncombined mercury is evolved with no increase in volume of the compact,[1] apparently no damage has been done to the compact.) On continued heating,

[1] E. S. Bomar, *Met. Semiann. Prog. Rep. Oct. 10, 1955*, ORNL-1988, p 129.

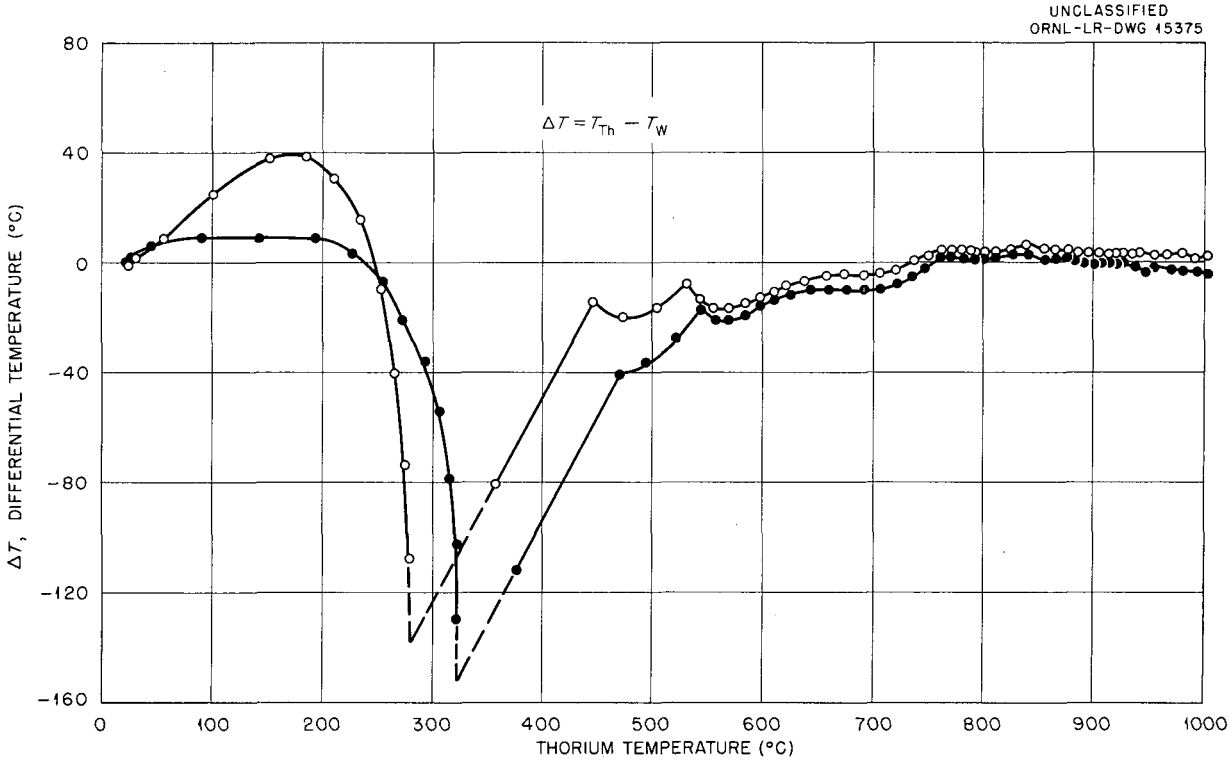

Fig. 157. Results from Differential-Thermometry Experiments with Thorium Amalgam. Thorium-amalgam samples pressed cold at 10 tsi. (Confidential with caption)

during the period in which the thorium sample is attempting to re-establish equilibrium with the tungsten sample, three arrests occur at 445–470°C, 530–545°C, and 610–625°C. If these points of inflection denote compound-decomposition temperatures, then in the establishment of a retorting cycle, the possibility of large quantities of mercury being evolved during these periods should be taken into account.

Consolidation Experiments

E. S. Bomar

Sufficient material for two additional consolidation experiments was accumulated in the period since the last progress report. All of this metal was produced from thorium amalgam by retorting in a manner similar to that described earlier.[1] Both batches of metal (a total of approximately 20 lb) were prepared for consolidation by loading them into mild steel cans and outgassing them at an elevated temperature. A maximum pressure of 2 μ existed during the outgassing of the first batch, and the final pressure was 0.3 μ at 350°C. Even better conditions were obtained for the second charge; the maximum pressure rose to 1 μ, and at 350°C the pressure was 0.03 μ. Both of these charges were pressed at 800°C into 4-in.-dia billets and then machined to 3 in. in diameter in order to remove the canning material. Prior to extrusion, the second billet was given a surface treatment, which consisted of superficial melting with an inert arc. The purpose of this operation was to heal any defects which might have given access to the interior portions of the billet. A network of cracks developed at what seemed to be the interfaces between the original compacts of the charge (see Fig. 158). Both the surface-treated and the as-machined billets were preheated in a liquid-salt bath[2] prior to extrusion to $\frac{7}{8}$-in.-dia rod. The billet which did not have the surface treatment was extruded and yielded a rod which had a good surface appearance (Fig. 159). (The ragged end is characteristic of extrusions in which a graphite "dummy block" is used to push the last portion of the billet from the container of the press.) The treated billet, on the other hand, developed slivers which peeled from its surface

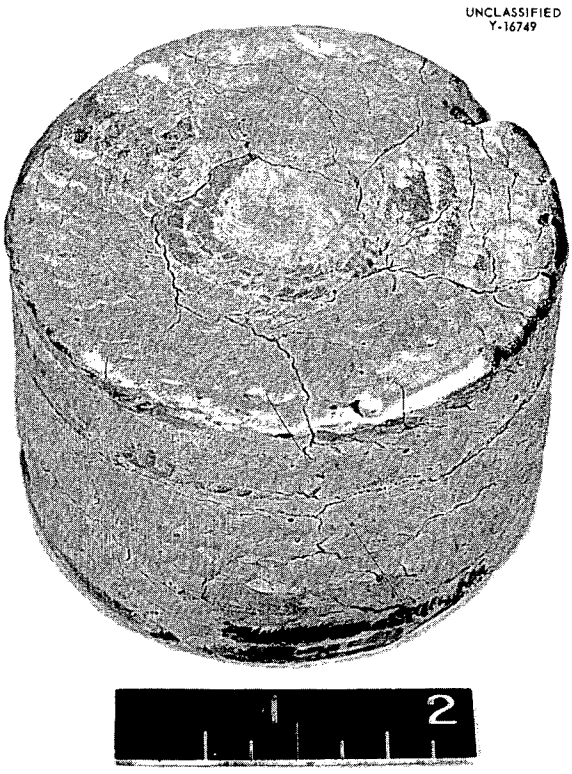

Fig. 158. Surface Appearance of Hot-Pressed Thorium Billet After Superficial Melting with Inert Arc. (Confidential with caption)

during the extrusion step, and, in general, the resultant rod had a poor appearance. A metallographic section through the rod, resulting from extrusion of the as-machined billet, gave no evidence of salt penetration into the billet.

Two $\frac{1}{4}$-in.-dia tensile specimens were prepared from stock taken from the front and rear of the extruded rod and gave the following results:

	Front	Rear
Tensile strength, psi	38,200	20,300
Yield point, 0.2% offset, psi	25,000	12,200
Elongation, %	28	20
Reduction in area, %	37	76
Hardness, BHN	74	71
Density, g/cc	11.66	11.51

Even though greater care was taken in outgassing the billets prior to extrusion than was taken with previous charges, the tensile specimens still developed longitudinal cracks on breaking. These cracks are interpreted as a sign of

[2] Liquid Heat N.D., E. F. Houghton & Co., Philadelphia, Pa.

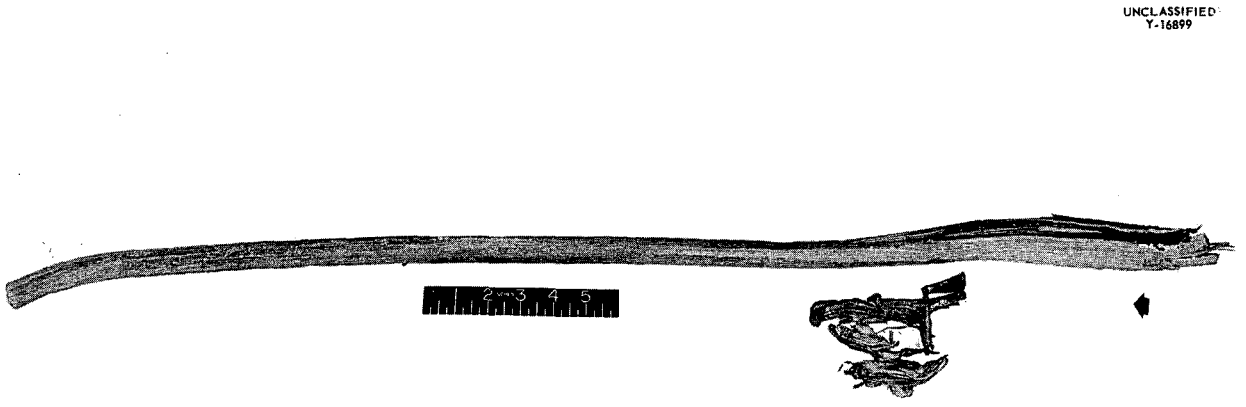

Fig. 159. Thorium Rod, $\frac{3}{4}$ in. in Diameter, Resulting from Extrusion of Billet Prepared by Hot-Pressing Retorted Thorium Amalgam. (Confidential with caption)

poor bonding in some regions of the extruded rod and point to the probable need for incorporating a melting step into the consolidation sequence in order to obtain a sound extrusion.

Future Work

E. S. Bomar

A budget reduction in the Metallex program has materially curtailed the work previously planned. Nevertheless, it is still planned to determine the behavior of compacts measuring about 5 in. in diameter. An effort will also be made to evaluate the product resulting from the extrusion of billets prepared by arc melting the retorted product.

GROWTH OF ORNL GRAPHITE-REACTOR SLUGS

R. E. Adams

A continuing program is being carried on for the purpose of studying the service performance of the aluminum-clad, silicon-bonded uranium slugs used in the ORNL Graphite Reactor. This work is described in detail in earlier reports.[3,4]

Additional measurements have been made on the length of the slugs discharged from rows in which ruptures occurred. The data have confirmed earlier results wherein it was shown that slugs which had been completely beta-transformed grew very slowly, whereas slugs which had not been transformed grew at a constant rapid rate. Figure 160 shows the effect of operating time on the average growth of the different types of slugs.

In slugs which have not been completely beta-transformed, considerable differences are found in

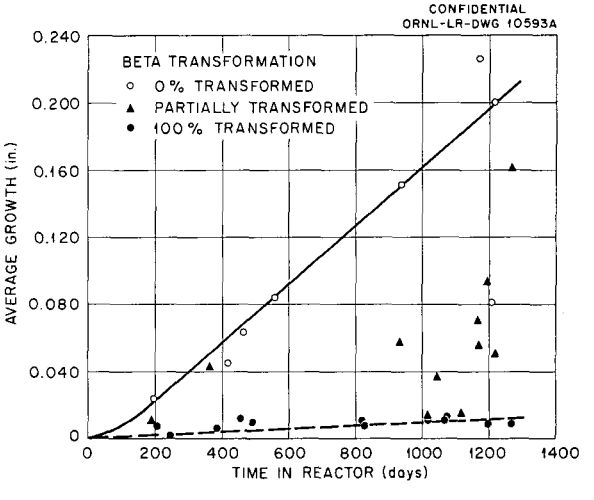

Fig. 160. Average Growth of Slugs in ORNL Graphite Reactor.

[3]R. E. Adams, *Met. Semiann. Prog. Rep. April 10, 1955*, ORNL-1911, p 5.

[4]R. E. Adams, *Behavior of Silicon-Bonded Slugs in the X-10 Graphite Reactor*, ORNL CF-55-12-8 (Dec. 2, 1955).

the growth of individual slugs. This is shown in Table 66, in which the growth data have been grouped for approximate times of exposure and in which the total number of slugs which grew to within certain specified ranges are shown.

These data indicate that growth of incompletely beta-transformed slugs is likely to cause rupture at increasing rates, whereas growth of completely beta-transformed slugs will not cause rupture.

Examination of ruptured slugs has not indicated any definite causes of rupture. In some batches of slugs, frequency of rupture is high; on the other hand, many batches of slugs have been operating for four years without any ruptures. This may indicate that slugs from batches which show high rupture rates may contain defects caused by imperfect techniques which could be prevented during manufacture.

Thus far, this study has shown that completely beta-transformed slugs are quite satisfactory. The study will be continued in order to provide data on the behavior of slugs exposed for longer times. In future work the slugs from batches which show high rupture frequency will be examined in greater detail in an attempt to identify defects which may be contributing to rupture.

METALLURGICAL PROCESSING OF SPENT FUEL ELEMENTS

R. E. Adams

Metallurgical treatments are being examined which may assist in the processing of spent power-reactor fuel elements for the recovery of unburned uranium.

Previous research on this problem demonstrated that carburization allowed easy dissolution of the type 304 stainless steel APPR fuel-element material. The carbon combined with the chromium and precipitated the chromium from the matrix phase, thereby allowing the matrix phase and the unburned uranium to be dissolved in dilute nitric acid. The feasibility of carburizing full-size fuel elements so as to contain approximately 2.5% carbon was demonstrated. However, interest in this method of processing has declined, since preliminary studies by the Chemical Technology Division have indicated that the combined carburizing and dissolution treatments may be less economical than direct dissolution in mixed nitric and hydrochloric acids. Dissolution of fuel elements in aqua regia will require titanium equipment and will also require decomposition of the chlorides before the uranium can be extracted and the waste products stored. Until the economics of the two processes are more thoroughly evaluated, further research on carburization has been deferred.

Some further effort is being directed toward the investigation of metallurgical treatments which might allow a reduction in processing cost by retaining appreciable fractions of the waste materials as solids. The objective is to devise a treatment process whereby the fuel material is broken down into individual grains and the unburned uranium recovered by leaching from the solid residue. Intergranular corrosion affords a

TABLE 66. RANGE OF GROWTH OF DISCHARGED SLUGS

Extent of Beta-Transformation (%)	Approximate Exposure (days)	Number of Slugs Measured	Growth (in.)						
			>0.400	0.400 to 0.300	0.300 to 0.200	0.200 to 0.100	0.100 to 0.050	0.050 to 0.025	<0.025
100	200–250	68	0	0	0	0	0	0	68
100	385–500	70	0	0	0	0	0	1	69
100	800–850	70	0	0	0	0	0	3	67
100	1000–1267	100	0	0	0	0	0	3	97
Partial	900–1287	157	0	1	3	32	40	20	61
0	400–600	77	0	0	0	10	38	19	10
0	935	40	1	2	10	8	11	6	2
0	1175–1215	56	3	5	7	19	16	4	2

method of accomplishing this objective with the type 304 stainless steel APPR fuel elements. Experiments have shown that by adding only small amount of carbon and precipitating chromium carbides only at the grain boundaries, the steel crumbles into individual grains on being subjected to the corrosive action of appropriate solutions. The following series of treatments was used to disintegrate a 0.031-in.-thick specimen of type 304 stainless steel:

1. carburized at 1000°C for 20 min so as to contain 0.3% carbon,
2. homogenized at 1150°C for 2 hr, thereby dissolving the carbon and allowing it to diffuse uniformly through the steel,
3. sensitized at 650°C for 2 hr, which precipitated the chromium carbides at the grain boundaries,
4. boiled for 4 hr in a corrosive solution consisting of 88 cc H_2SO_4 and 112 g $CuSO_4 \cdot 5H_2O$ per liter.

The corroded piece could be crumbled with the fingers into individual stainless steel grains. It was estimated that less than 1% of the stainless steel material was dissolved.

Further tests are planned which will investigate under similar conditions the behavior of samples of fuel-element material containing UO_2. Tests will also be made for the purpose of determining whether nitric acid will be a suitable corrosive solution.

An iron-base alloy containing 25% chromium and 5% aluminum is also being considered as a possible fuel-element material. This material is not readily carburized, but it readily absorbs nitrogen when heated in an ammonia atmosphere. Specimens of this material, 0.017 in. thick, disintegrated into a granular powder during a 4-hr nitriding test in gaseous ammonia at 700°C. Based on weight gain, the nitrided material contained 11.5% nitrogen. Furture work will be concerned with investigating the utility of such nitriding treatments in the processing of this fuel material.

METALLOGRAPHY

R. J. Gray

W. H. Bridges
R. S. Crouse
T. M. Kegley, Jr.
E. L. Long, Jr.
J. R. Riddle
D. F. Stoneburner
J. E. Van Cleve, Jr.

NICKEL-MOLYBDENUM SYSTEM

J. R. Riddle

The Metallography Group is presently working on two projects dealing with the nickel-molybdenum system.

The purpose of one project is to identify the phases in the binary nickel-molybdenum system. The experiment was started by hot rolling buttons of molybdenum surrounded by sheets of nickel. These couples were encased in stainless steel and allowed to diffuse for 500 and 1000 hr at temperatures of 800, 860, and 1150°C. Phases stable at 800°C are alpha, beta, gamma, delta, and epsilon. Phases stable at 860°C are alpha, gamma, delta, and epsilon. Phases stable at 1150°C are alpha, delta, and epsilon. Two methods of identification will be attempted: the samples will be chemically etched and examined for precipitates in the region of diffusion, and the samples will be heat-tinted. It is hoped that the variation in color of the oxide produced by the latter method will aid in identifying the compounds. Identification will be based on phases stable at time of diffusion, on their position relative to original nickel-molybdenum areas, and on evidence of a precipitate.

The other program is the construction of a chart to show the structure of Hastelloy B after various heat treatments. Structures will be plotted for temperatures of 1100, 1200, 1300, 1400, 1500, 1650, and 1800°F and for times of 100, 200, 400, 800, 1200, and 1600 hr. All specimens are from the same heat and have been solution-annealed for two hr at 2100°F prior to the isothermal treatment. Samples are $\frac{1}{16}$-in. plate sealed in quartz under a partial pressure of argon. Specimens to be used in obtaining data for the chart will be air-cooled, while other specimens will be water-quenched. The effects of quenching from high temperatures will be observed, and a more extensive study of the 1300°F treatment will be made in an attempt to clarify the controversial structure which occurs when the alloy is held for 1000 hr at that temperature.

CERAMICS RESEARCH

J. M. Warde

L. M. Doney

CERAMICS

L. M. Doney

UO_3 CRYSTAL PRODUCTION

A. J. Taylor

At present the investigation concerning the production of hydrothermally grown UO_3 crystals has three objectives:

1. to increase the batch size to a maximum consistent with the autoclaves which will be put into production,
2. to increase the uranium yield to a maximum,
3. to obtain the maximum yield of crystals in a particular size range.

This work is being rather heavily emphasized. The oxide that will go into the APPR fuel plates has been ordered. The production equipment is being changed so as to conform with that used in the Ceramics Laboratory. The latter equipment is presently being used to determine the conditions which will attain the three objectives stated above. This investigation is on a pilot-plant scale inasmuch as a production order for depleted oxide is being filled. Moreover, this appeared to be the most appropriate method for obtaining, and then disposing of, the large amounts of material involved in the investigation.

The uranium yield and the UO_3 particle size are affected by several variables; the variable having the most effect is the concentration of uranyl ion in the solution from which the crystals are grown. The other variables, which have less effect on the process, are time and the temperature of the autoclave. In the present experiments, all variables are being held constant, with the exception of factors affecting the uranyl ion concentration. These factors are the source and amount of uranyl ion added and the amount of free water entering the autoclave. The uranyl ion is supplied by the addition of uranyl nitrate hexahydrate (UNH); and the free water entering the autoclave consists of free H_2O from the peroxide cake, water of crystallization from the UNH, and any water added to the batch. In the change from hydrated UO_4 to hydrated UO_3, water of crystallization is released; but since at present there is no way to predict the amount accurately, it is not included as part of the free water. The above factors are regulated by two ratios as follows:

$$R_1 = \frac{\text{Uranium from UNH}}{\text{Free } H_2O}$$

$$R_2 = \frac{\text{Uranium from UNH}}{\text{Uranium from } UO_4 \text{ hydrate}}$$

Time and temperature were held constant at 10 hr and 250°C, respectively, while R_1 and R_2 were varied in an attempt to achieve the necessary process control. The UNH was used so as to eliminate variations in uranyl ion concentration which would result from excess acid if uranyl nitrate solutions were used. Uranyl nitrate solution and even nitric acid alone were used successfully, but until process-control conditions are established, the acid solutions will not be further investigated.

Of the crystals grown by this process, those that are 50 mesh and larger are unstable. Rough handling will cause them to break into platelets; even without rough handling they will break down if allowed to remain at room temperature for moderately long periods of time. The platelets have one very small dimension, which makes them useless for matrix fuel elements; and a fairly small percentage of platelets in a batch of crystals will ruin the entire batch. In such an event, it may be possible to make a separation between the flat and the bulky particles and, thereby, save an entire batch of crystals. For this purpose, two pieces of equipment are being designed. In one, separation of the particles in a flowing stream of water will be attempted; whereas with the other, separation by means of a tilted, horizontally vibrated, felt-covered plane surface will be tried.

Si-SiC DEVELOPMENT

A. J. Taylor

The development work on the Si-SiC element is now directed toward the problem of incorporating larger amounts of UO_2 into the plates. As the amount of UO_2 is increased, the tendency for the plates to be disrupted during fabrication also increases. Two bodies, one containing SiC and the other containing graphite as base materials, are still being considered; and development work is being done on both types.

The SiC body is more resistant to thermal shock than is the graphite body. Thus, some plates containing the SiC body were fabricated for testing in the LITR. However, some test plates will also be made from the graphite body, since the thermal stresses encountered in the LITR will at no time approach the stresses encountered in the present test procedure. Thermal testing currently amounts to no more than a crude survival test wherein the pieces are cycled between room temperature and 1000°C until failure occurs. The SiC body has never failed under the thermal cycling. The graphite body has been inconsistent; some pieces have failed immediately, whereas others have never failed.

The reason or reasons for the failures are not well understood at present. There are several possibilities, other than thermal shock, although these have not yet been investigated. One of the possibilities is the existence of extremely fine cracks or pinholes which allow the fuel to oxidize, thereby causing a volume change which cracks the piece. Another is the possibility that the skin over the fuel is too thin to withstand the stresses set up by the differential expansion between the Si-SiC and the UO_2.

The SiC body has a tendency to develop a single crack beginning on the edge at which the impregnation starts. This crack was filled with silicon either during impregnation or immediately afterwards. Ordinarily the crack heals completely, except possibly for a few pinholes. The strength of the piece and its thermal properties all seem unaffected by the presence of this healed crack, but the fact that an occasional pinhole remains unfilled will certainly have an effect on the ability of this material to retain gaseous fission products.

The healed crack has never occurred in the graphite body. Plates made from the graphite body may have internal flaws, such as unimpregnated areas; but ordinarily the skin has been flawless, as nearly as the eye can detect. Any failures which occurred during the impregnation were complete failures, and the damage was too extensive for any amount of healing to have taken place.

A radiation-damage study on ceramics in general has been going on for some time in a cooperative effort with the Solid State Division. As part of that program, test plates of Si-SiC containing enriched UO_2 have been placed in the LITR for study. These plates are made from the SiC body, are $1\frac{1}{2} \times \frac{1}{2} \times \frac{1}{8}$ in., and contain 0.2 g of product-level UO_2. This is sufficient fuel to bring the plates to a temperature of 1000°C when they are properly placed in the LITR. The plates are canned with thermocouples in place and left uncooled. The following table summarizes the tests which will be run on the specimens:

Before Irradiation

Density
Porosity
Young's modulus
Internal friction
Breaking strength
Spectrographic analysis
X-ray diffraction
Microscopic examination

During Irradiation

Thermal measurement

After Irradiation

Density
Dimensional stability
Young's modulus
Internal friction
X-ray diffraction
Microscopic examination
Breaking strength
Fission-product analysis
Neutron dosage

In fabricating these plates some difficulty has been experienced in properly placing the fuel in order to obtain the desired even distribution. This is one of the fabrication details which remains to be worked out.

As mentioned above, the graphite body, also, will be made into test plates for the radiation studies.

YTTRIUM OXIDE

C. E. Curtis

In continuation of the study of rare-earth oxides as ceramics, 99.9% pure Y_2O_3 is under investigation. The absence of sharp breaks in the differential thermal analysis and weight-loss curves, as well as evidence from x-ray spectrometry, indicate that there are no radical structure changes that result when Y_2O_3 is heated to 1200°C.

Yttrium oxide ceramics heated at 1800°C had 0.3% porosity remaining and, therefore, were more refractory than the Gd_2O_3 and Sm_2O_3 ceramics previously studied; the latter were vitrified at only 1500°C. The Y_2O_3 lattice was only slightly smaller at 1600°C (10.597 Å) than at room temperature (10.604 Å); the crystallite size had increased from 350 ± 5 Å to greater than 10,000 Å over the same temperature range.

Thermal expansion of a specimen fired at 1800°C was determined to be 9.3×10^{-6} in./in./°C between room temperature and 1400°C.

Yttrium oxide blended with an equimolar amount of Al_2O_3, BaO, Fe_2O_3, SiO_2, or TiO_2 and heated at 1500°C for 1 hr reacted, presumably in the solid state, to form binary compounds. The compound with Al_2O_3 had the perovskite structure; the iron compound was magnetic, and TiO_2 formed an isotropic face-centered cubic compound. The ZrO_2 and HfO_2 compositions contained solid solutions. No reactions at 1500°C between Y_2O_3 and CaO, MgO, or ThO_2 were apparent by x-ray or microscopic examination.

THORIUM OXIDE SUSPENSIONS IN WATER

C. E. Curtis

In an investigation of the nature of suspensions of Thorex thoria in water (used for the slip casting of ceramic ware), some electrical properties were noted. Use of a small electrophoretic cell with platinum electrodes 5 in. apart resulted in the following observations:

1. Thoria particles in suspension in still water are discharged in the neighborhood of a positive electrode, but they do not migrate more than a centimeter through the suspension toward the electrode under an emf of 140 v dc (0.2 ma). Apparently the electrophoretic separation of the finer particles requires a special cell, perhaps a revolving-anode type, with means for circulating the suspension.

2. Thoria particles in still water owe their suspendibility to negative electric charges. They give up these charges to a positive electrode and settle rapidly in the form of soft, coarse agglomerates or flocs that are easily resuspended. At the same time, precipitation of the suspension occurs throughout the cell; near the negative electrode sedimentation is slow and the cake formed is dense and not easily resuspended.

In Fig. 161 the progress of precipitation under an emf of 140 v is shown. Picture 1 shows the start of the test; the control material is in the graduated glass tube at the left. Pictures 2 through 7 were taken at 10-min intervals; picture 8 shows the condition after 2 hr and picture 9 after 3 hr, at which time the suspension has completely precipitated.

The rate of sedimentation increased with increase in emf; at 400 v, precipitation was complete in 10 min; whereas at 1½ v it was only slightly faster than settling by gravity.

3. Apparently the conductivity of the suspension in this cell was not due to thorium ion, since no thorium could be detected spectroscopically in the solutions surrounding either electrode after electrodialysis through an organic membrane. With the ThO_2 suspension surrounding the positive electrode and distilled water around the negative electrode, the principal ions migrating through the diaphragm to the negative electrode were Ca^{++}, Mg^{++}, and traces of the alkali metals. With the positive electrode in water and the negative in the suspension, only traces of calcium and magnesium were detected at the positive electrode.

4. It was observed also that there was a sufficient number of ions present in the ThO_2 suspension to produce a voltaic action, an emf of 5 to 10 mv, when strips of unlike metals were immersed in the suspension and connected through a millivolt meter. Two strips of zirconium metal, one of which was freshly polished, formed a voltaic cell also; in this case the voltage fell off to nearly zero in approximately ten min; it was restored to its original value by scratching or polishing off the oxide film.

5. The source of the electrical charges is being sought by means of electrodialysis.

URANIUM ORE SAMPLES

G. D. White

Six samples of uranium ore and the slimes that result from chemical treatment of these ores were studied by x-ray and petrographic examination and by differential thermal analysis for the Materials Chemistry Division. The mineral constituents, except for the microcrystalline material in four samples, were identified. There was a correlation between the recovery of uranium and the values obtained by differential thermal analysis. Those samples which showed an exothermic reaction at

UNCLASSIFIED
PHOTO 25373

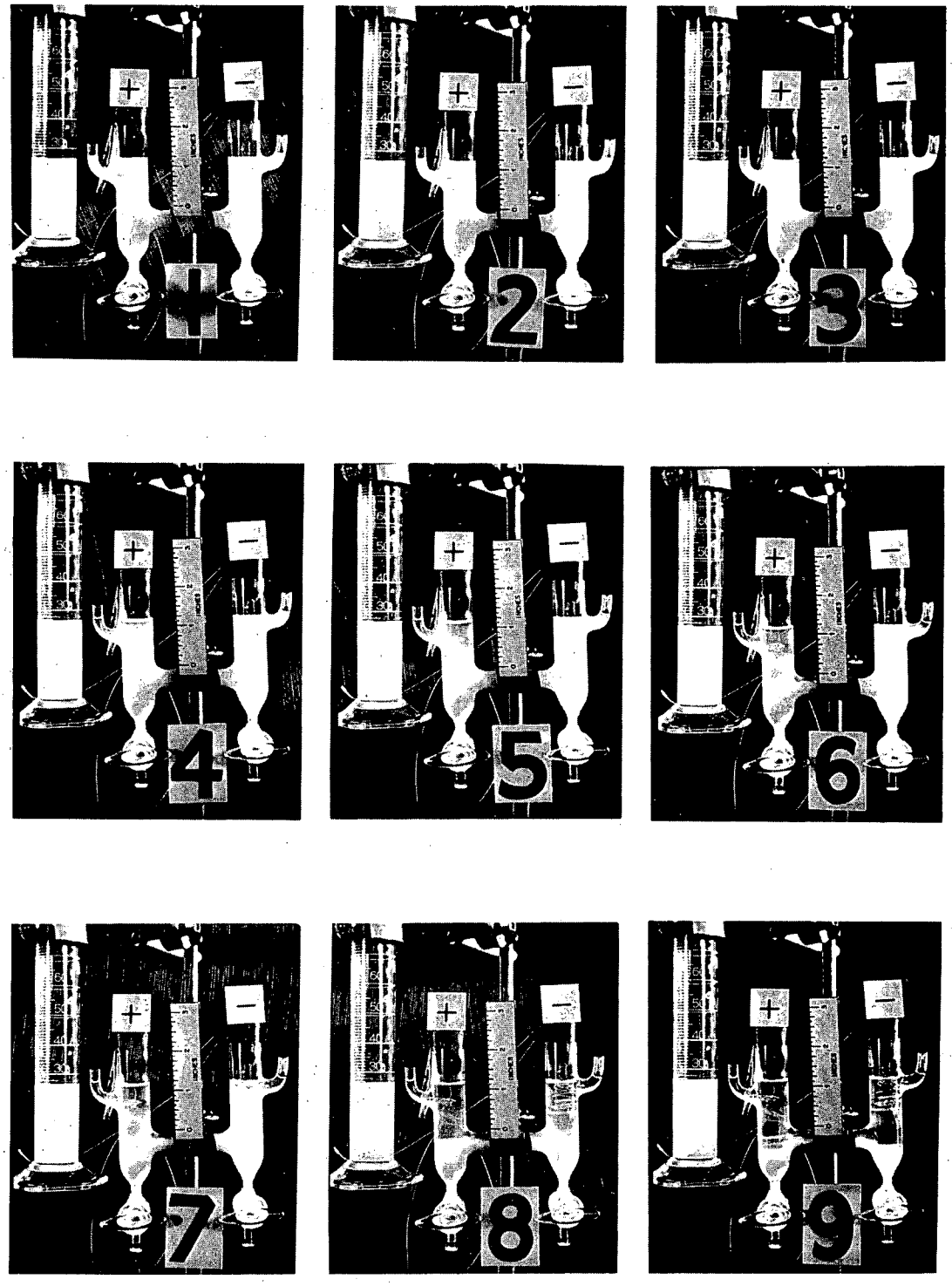

Fig. 161. Settling of Thoria Suspension Under the Influence of an Electrolytic Current.

about 500°C (indicating the presence of carbon) did not leach as well as those which did not exhibit such a reaction; this indicates that part of the uranium is associated with organic material.

PETROGRAPHIC EXAMINATION OF FLUORIDES

G. D. White

This work is primarily service work for the Materials Chemistry Division. On the average, about 100 samples are examined each week.

SPODUMENE

G. D. White

Spodumene is the principal source of lithium compounds. A study has been made of six samples of spodumene: five were obtained from domestic sources, and the other was the Quebec mineral.

The ores were crushed to pass 70 mesh, and the −70, +325 mesh fraction was separated by the sink-and-float method in heavy liquids. The spodumene, being heavier than the quartz and feldspar, was in the sink fraction. This process was repeated until only a trace of impurities remained in the spodumene.

It has been determined by means of chemical analyses, x-ray and petrographic examination, and differential thermal analysis that there are no significant differences among the spodumene samples studied and that all approach the theoretical formula $Li_2O{\cdot}Al_2O_3{\cdot}4SiO_2$.

Spodumene inverts at about 1000°C from the alpha to the beta form with a large increase in volume. In the Lithium Corporation of America process, the crude ore containing feldspar and quartz is fed into a rotary kiln and decrepitated at about 2500°F. It is then roasted with sulfuric acid; and the lithium sulfate, thus produced, is leached and subsequently converted into other lithium compounds.

It has been found that the fusion point of spodumene is lowered by feldspar. It is also known that any glasses formed in the rotary kiln tend to decrease the amount of reaction between sulfuric acid and the inverted spodumene.

In the Foote process, froth-flotation concentrates are sintered with limestone, and the lithium compounds are subsequently leached. It has been determined that high sintering temperatures reduce the amount of leaching of the lithium compound. Sinters formed at high temperature contain a large amount of tricalcium silicate.

Tests were run in cooperation with the Y-12 Research and Development Group to determine the effects of heat and pH on the leaching operation. Two samples of β-spodumene from which 98% of the lithium had been leached were heated in solutions of Li_2SO_4 and LiOH, respectively. From differential thermal analysis and x-ray diffraction data, it was concluded that the leached β-spodumene contained molecular water, which it began losing at 480°C; and with further heating, the residue reacted to form mullite at 980–1000°C. The leached samples which were heated in solutions containing lithium were partially converted back into the original β-spodumene lithium structure, as was evidenced by much less intense thermal effects during differential thermal analysis and by the x-ray patterns obtained before and after the differential-thermal-analysis runs. Chemical analyses indicated that the leached spodumene treated with Li_2SO_4 solution recombined with 37% of the lithium necessary to fill all the original lithium positions of the β-spodumene structure, and the sample treated with LiOH solution recombined with 55% of this amount. This difference in recombination was also indicated by the DTA and x-ray results.

WASTE DISPOSAL

Fixation of Radioisotopes in Ceramic Bodies

R. L. Hamner M. P. Hayden

In order to determine whether radioisotopes that are present in a simulated aluminum nitrate waste solution can be permanently fixed in fired ceramic masses, several process conditions, believed to be of primary importance, must be considered.

1. Radioactive chemical wastes are to be treated as received from the fuel-reprocessing plants. If sufficient activity is present the wastes will be mixed with other materials and sintered by the heat released from radioactive decay. Otherwise, an outside source of heat will be utilized.

2. Materials added to the process solution should be cheap and readily available; consequently, the choice of materials will probably be limited to naturally occurring clays, shale, silica, limestone, dolomite, fly ash, phosphate tailings, and soda ash.

3. For economic reasons, the temperature of firing should be low; however, the possibility of leaching of the radioisotopes must not be ignored. In addition to the fact that low-temperature firing

may minimize volatilization of isotopes having high vapor pressures, the self-sintering caused by radioactive decay would be assisted.

4. The amount of clay or other diluents should be kept as low as possible in order to minimize the weight and volume of the final atomic garbage; moreover, a minimum of adulterants will make self-fusion more feasible.

5. The materials added should be capable of forming a slurry so as to minimize zone settling of additives.

Promising results have been obtained by the addition of shale, soda ash, and limestone. Satisfactory fixation has been obtained with such materials at temperatures as low as 1050°F.

Work during the past few months has been concerned primarily with the continued testing of all compositions, the screening of new materials, and the development of techniques to determine what constituents in the clay-flux mixtures are "tying up" the radioisotopes.

Experiments:

1. *Removal of Radioactive Materials by Treated Clay Materials.* – The following clay materials, received from the University of Illinois, were tested for possible use in fission-product-waste disposal:

Designation	Description
CP-F-7A	Kaolin; acid treated to develop a surface area of 443 sq m/g
CP-F-18	Kaolin; treated to develop a surface area of 294 sq m/g
CP-F-28	Kaolin; acid treated to develop a surface area of 209 sq m/g
E-197-55X	Attapulgite clay
E-197-55V	Fibrous silicate; produced by acid treatment of attapulgite
E-197-55W	Bauxite; heat activated

For comparative purposes these materials were tested by the "jar stirring" method of Brockett and Placak[1] for the removal of radioactive materials by various clays. This involved shaking 1 g of material in 500 cc of contaminated tap water for 2 hr. After stirring, a portion of the contaminated water was centrifuged, and a 1-ml sample of the clear liquid was dried and counted. The difference between the number of counts in the latter and in an equal aliquot of the original contaminated tap water was a measure of the effectiveness of the material in removing the radioactive contaminant.

Table 67 gives the results of this experiment for Sr^{90}, $(Cs, Ba)^{137}$, Ce^{144}, $(Ru, Rh)^{106}$, and mixed fission products.

Generally speaking, all the materials were effective in removing a high percentage of the contaminants, except Sr^{90} which was not removed as effectively. In a study of the effect of surface area on removal, no significant difference was noted in the case of the acid-treated kaolins, where one sample had twice the surface area of another.

[1] T. W. Brockett, Jr., and O. R. Placak, *Removal of Radioisotopes from Waste Solution by Soils – Soil Studies with Conasauga Shale*, Eighth Industrial Waste Conference, Purdue, Indiana, 1953.

TABLE 67. REMOVAL OF RADIOACTIVE ISOTOPES FROM SOLUTIONS BY TREATED CLAY MATERIALS

Composition	Removal After 2 hr Contact (%)				
	Sr^{90}, 3.5×10^{-2} μc/ml	$(Cs, Ba)^{137}$, 0.53×10^{-2} μc/ml	Ce^{144}, 0.31×10^{-2} μc/ml	$(Ru, Rh)^{106}$, 1.03×10^{-2} μc/ml	Mixed Fission Products, 2.12×10^{-2} μc/ml
CP-F-7A	32	75	83	89	93
CP-F-18	69	96	93	90	94
CP-F-28	27	81	93	98	94
E-197-55X	37	97	60	89	86
E-197-55V	22	95	96	88	91
E-197-55W	29	57	94	98	94

2. *Old Compositions.* – Composition 15,[2] tagged with various radioactive materials, had been soaked for several months, and samples of the leach solutions were counted; the results are presented in Table 68.

Because of its satisfactory behavior, as shown by the data in Table 68, and because of its very low clay content, composition 15 was selected for the proposed large-scale hot-pot experiments.

3. *New Compositions.* – A Florida kaolin and a shale obtained from the General Shale Products Corp. were tested as possible substitutes for the Volunteer Portland Cement Co. shale in compositions 5 and 15. After having been tagged with mixed fission products, these mixtures were fired at 850°C for 1 hr and then placed in water for leaching. A heavy gelatinous substance precipitated from the sintered mass which, based on spectrographic analysis, was assumed to be $Al(OH)_3$; this undesirable behavior was not observed with Volunteer shale.

After leaching both compositions for one week, the leach solutions from each were counted, and the results are presented in Table 69.

The results are inconsistent with respect to composition and particle size, and no conclusions may be drawn, except that neither the General shale nor the Florida kaolin are as effective in the fixation of radioisotopes as is Volunteer shale.

As reported before, compositions 5 and 15 have been the most satisfactory mixes for the fixation of radioisotopes. However, neither of these contains sufficient limestone to neutralize the Hope solution, and therefore some attack can be expected on any concrete liner used in a disposal pit. Both have 30 g of limestone to 250 ml of Hope solution; 47 g would be required to neutralize the

[2] J. M. Warde *et al.*, *Met. Semiann. Prog. Rep. April 10, 1955*, ORNL-1911, p 122.

TABLE 68. RESULTS OF LEACHING RADIOACTIVELY TAGGED COMPOSITION 15 FIRED AT A VARIETY OF TEMPERATURES

Radioactive Material	Firing Temperature (°F)	Leaching Time (months)	Leach Solution (counts/min/ml)
$(Ru, Rh)^{106}$	1750	6	0
Sr^{90}	1050	6	0
Sr^{90}	1750	7	0
Mixed fission products	1050	5	0
Mixed fission products	1350	5	0

TABLE 69. FISSION-PRODUCT RETENTION BY COMPOSITIONS 5 AND 15 PREPARED WITH GENERAL SHALE AND FLORIDA KAOLIN

Description of Clay Used	Leach-Water Activity (counts/min/ml)	
	Composition 5	Composition 15
General shale; as received	0	17
General shale; –16 mesh, +100 mesh	11	5
General shale; –16 mesh	13	0
General shale; –100 mesh	2	43
General shale; calcined at 600°C		0
Florida kaolin	0	29

mass. Experiments using increasing amounts of limestone show that a ratio of more than 35 g/250 ml will make the mass develop quickly into a crumbly, porous structure, rather than a thick, smooth slurry, which fires to a very weak, powdery mass easily slaked down by water. Therefore, since the amount of limestone in the clay-flux mixture must be limited, any concrete pit liner used must be tested for excessive attack before it is contacted with the strongly acid mixture.

4. *Pit Liner Material.* – Concrete compositions 5 and 6, either of which might be used in lining disposal pits, were tested as containers for composition 15 plus Hope solution at 180°C. Upon removal of the dried cake, little, if any, corrosion of the concrete wall was observed.

Other concrete compositions containing either Mascot aggregate or Knox sand and gravel aggregate are now undergoing test.

5. *Monitoring of Radioactive Gases.* – Furnace equipment and counting equipment are now being set up in order to determine the temperature and the rate at which radioactive gases are evolved upon heating clay-flux mixes up to 900°C.

6. *Autoradiographic Study of Clay Minerals.* – In the evaluation of clays for use in sintered masses that will retain radioactive waste material, it was deemed desirable to know something about the adsorption or absorption capacities of the individual clay minerals and to determine if possible which mechanism is responsible for the retention of the radioactivity.

A feasibility study was made of a technique involving the sedimentation of the clay from a suspension onto a nuclear photographic plate for radiation detection. After an appropriate exposure time, the photographic plate was processed, and after drying, the plate was examined microscopically. After processing, most of the clay-mineral grains were still embedded in the surface of the photographic emulsion. The nuclear particles emanating from the clay grains formed tracks whose direction, length, and other characteristics were determined microscopically. In the case of a naturally radioactive material, if the nuclear particle can be identified and its energy deduced from its path length in the emulsion, an important adjunct has been made to the identification of the mineral grain. If the material has been "tagged" with a known isotope, the location and identification of the captor mineral can be determined by hunting the origin of the tracks found in the photographic emulsion and by making a petrographic analysis of the optical properties of the mineral grain from which the tracks originated.

The first step in the feasibility study was a preliminary sedimentation of a clay from Africa that was known to contain some naturally radioactive minerals, possibly as monazites. The Ilford C-2 (50 μ thick) photographic emulsion was used; the exposure was for 19 days in a light-tight lead box. Microscopic examination of the plate revealed a number of alpha tracks. Some of these were single tracks that seemed to emanate from a crystal located on the emulsion surface. About 30% of the events involved two or more tracks emanating from a single grain. Positive identification of these grains is not practicable at the present time because the microscope accessories, that enable a petrographic study to be made of the same slide where the nuclear tracks were analyzed, are not yet available. Figures 162 and 163 are photomicrographs showing two mineral grains and their associated alpha tracks. Photographs of this type are especially difficult because, at the high magnification necessary to distinguish the nuclear tracks, the depth of focus is too shallow to include a clear image of both the mineral grain and the tracks.

Autoradiographs of the beta tracks from a Sr^{90}-tagged sintered gel comprised the second step in the feasibility study. Two different beta-particle-sensitive photographic emulsions were used: Eastman Kodak NTB and Ilford G-5, 25 μ thick. Composition 15 sintered gel, made from Conasauga shale, Chicamauga limestone, and soda ash, was tagged with Sr^{90} carrier in Hope solution and was deposited by sedimentation from a water suspension onto the photographic plates. The plates were exposed in light-tight stainless steel boxes for different periods of time ranging from 80 min to 23 hr. After regular processing, the plates were examined microscopically. The NTB plates were from an old batch of plates and showed signs of photographic deterioration. The G-5 plates were fresh emulsions, and a representative number of beta tracks were located in a brief examination period. Beta tracks are quite difficult to orientate with respect to their origin since their ionization is not dense during the initial, or fast, part of their travel. As they slow down and their ionization increases, definite, although tenuous, tracks may

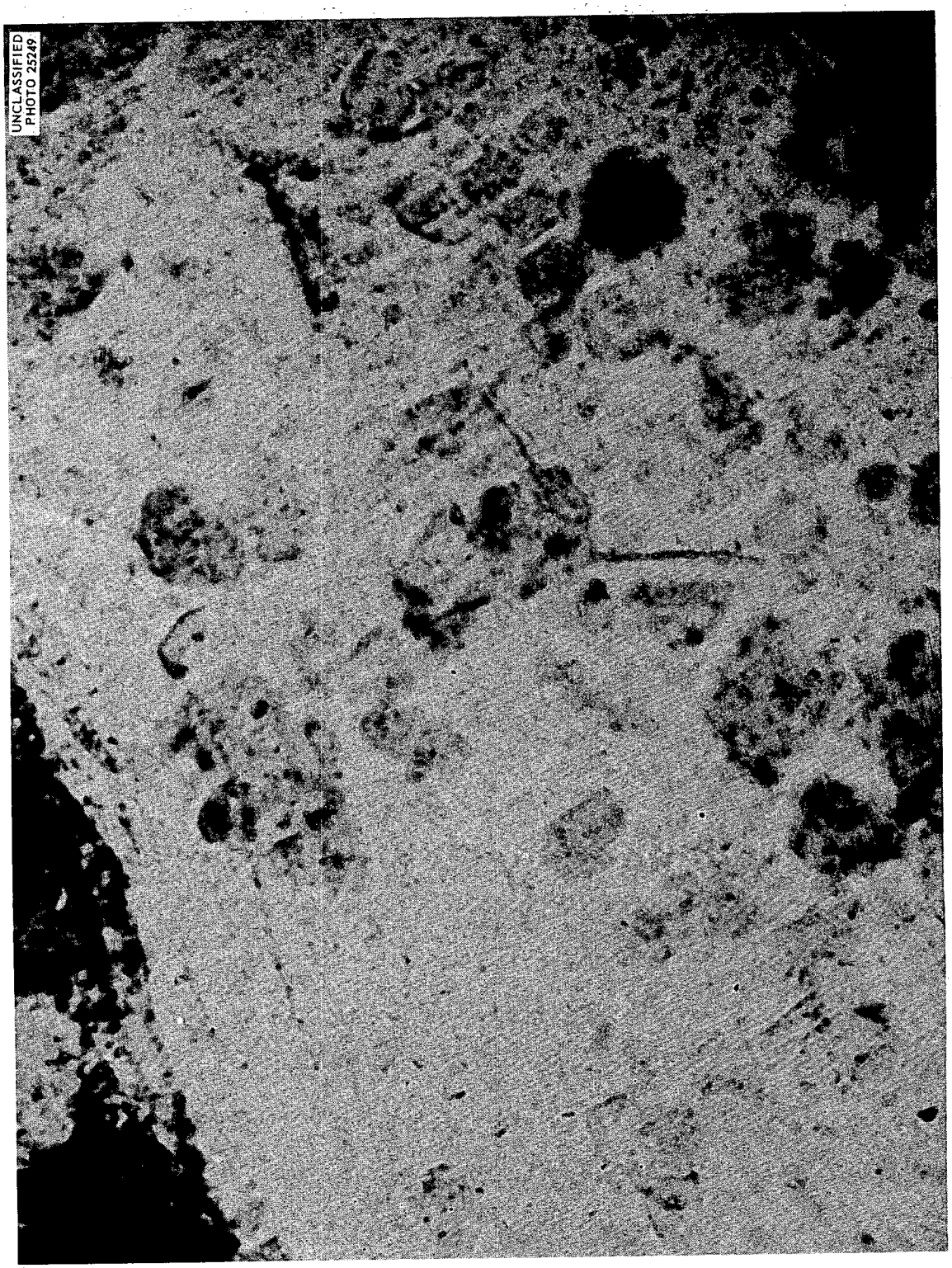

Fig. 162. Alpha-Track Autoradiogram of a Clay Sediment on a Nuclear Photographic Plate. 1080X. Reduced 19.5%.

Fig. 163. Radioactive-Mineral Grain in a Clay Deposited by Sedimentation onto a Nuclear Photographic Plate. 1080X. Reduced 20%.

be observed. These will be much more difficult to photograph than the alpha tracks; but with an oil-immersion low-power objective, it is hoped that photographs will be possible.

The mineral-grain density on the emulsions was so high that the beta tracks could not be traced back to the radioactive grain from which they originated. A sedimentation from a more disperse suspension will be advantageous in that the mineral-grain density will be less.

One of the clay materials from the University of Illinois was used for the third step of the feasibility study. The CP-F-18 kaolin had been treated with acid to develop a surface area of 294 m^2/g and was chosen for this study because of its high performance in removing radioactive materials from the leach water in the "jar-stirring" method. An uncontaminated sample of this clay was used as a control in the following experiment. Fresh NTB and NTB-3 emulsions from Eastman Kodak, as well as the Ilford G-5 plates, were employed. After the sedimentation, the plates were washed in methyl alcohol and then dried further in a vacuum desiccator. The total exposure time was 105 min. The fragile latent images of the beta tracks are subject to fading if there is moisture present. Of the three emulsions used, the G-5 seemed to have the most positive autoradiograph, which indicates that this emulsion requires less exposure than the NTB or NTB-3 to register a good beta-track count.

The grains of the CP-F-18 kaolin material were uniformly spherical pellets ranging in diameter from about 10 to 100 μ, the major portion being in the 30- to 50-μ size. The larger grains made the study of these plates difficult at high magnification because of the small working space required by oil-immersion techniques. However, at low power there was a marked autoradiographic effect, which could be detected even macroscopically. The G-5 plate from the control sample showed an even coloration which was made up of the background gamma and beta radiation. The plate with the tagged sediment was darker than the control; and under the microscope, round dark spots were visible around each grain of the kaolin material. In areas where the grains had been brushed off the small craters of emulsion which held them and where the high-power objective could be used, it was possible to see that the dark spots were made up of a tangle of beta tracks, which formed semi-spherical halos in the emulsion surrounding each clay grain. Every grain of this uniformly pelletized kaolin material also appeared to be uniformly beta radioactive after the "jar-stirring" treatment with Sr^{90}-tagged water and subsequently leaching the material repeatedly with water.

Photomicrographs of these phenomena cannot be obtained until a low-power oil-immersion objective and a photo tube attachment are available for the microscope, but a schematic drawing of the results is shown in Fig. 164.

From these preliminary studies, it seems certain that a study of the retention of radioactive waste by a combination of autoradiographic and petrographic techniques is feasible, and further work toward identification of radioactive mineral grains will be undertaken.

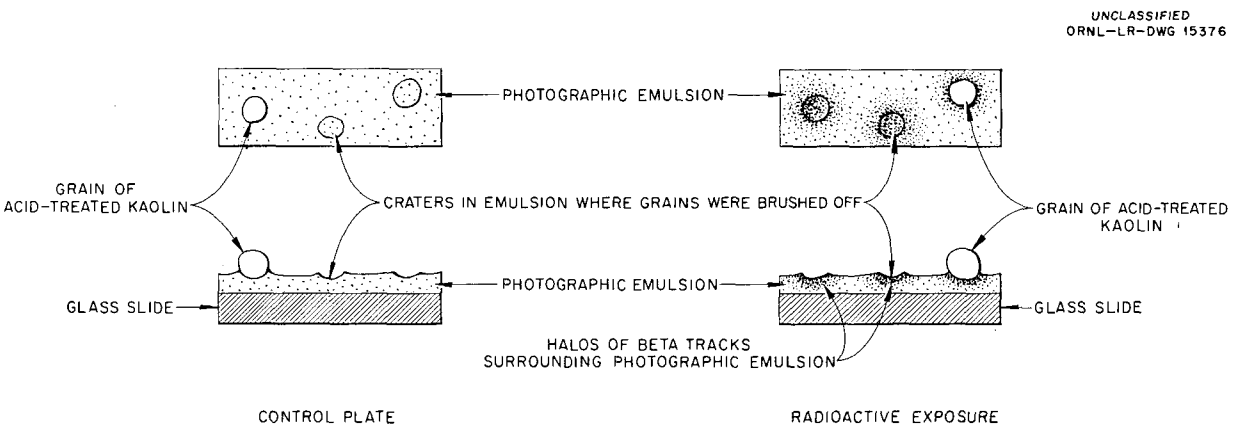

Fig. 164. Diagram of Autoradiogram of CP-F-18 Kaolin.

7. *Viscosity Studies of Selected Clays for Use in Lining Waste Disposal Pits.* – The study of various clays suspended in distilled water, in acid Hope solution, and in alkaline W-8 solution, simulating three types of waste carriers, was completed. The apparent viscosities of different solid-to-liquid concentrations of these clays were measured with the MacMichael viscosimeter, a rotating-cup-type viscometer, calibrated with graded sucrose solutions. Table 70 shows the results of the measurements. Some of the values are unreasonably high; these are the result of extrapolating the curves beyond the experimental region and beyond the scope of this instrument and are reported only for intercomparison of the clays in this group. Most of the readings were made with the disk bob or spindle with the No. 26 wire, except where the stiffness of the mixture required the use of the cylinder, as noted. Consistency curves were made within the limits of the viscometer, 14 to 45 rpm, and notations are placed with the tabulated viscosities so as to designate the type of consistency curve that was obtained.

The drastic changes in the viscosity characteristics shown by these selected clays as their concentrations and pH environments are changed indicate that any clay material being considered for waste-disposal uses should be rigorously tested over as wide a range of conditions as it might encounter in service.

Heat Experiments

S. D. Fulkerson R. L. Hamner

Heat Experiment No. 6. – A second liquid-type heat experiment, using composition 15 clay-flux mix, was made. This mix contained less clay than composition 5, the mix used in the first liquid-type heat experiment. In addition, more energy was supplied – approximately that required to reach 900°C in an enclosed system such as the one investigated in the dry-heat experiments.

The apparatus used was the same as that used in the first liquid experiment, with a slight modification; a spiral Calrod heater was substituted for the silica-glass-enclosed wire heater. The stainless steel container, 12 in. in diameter by 24 in. deep, was filled with the liquid-clay-flux mix. The mix became a gel within a few minutes after filling. In order to avoid possible boiling over, only 20 w were applied for the first few hours, and 100 w was applied until the end of the second day. This apparently was an unnecessary precaution. Although a slight frothing occurred, the gel became a frothy liquid after 24 hr and settled to about half its original volume. Full power, 200 w, was applied after 48 hr, and evaporation was continued until the end of the fifth day. No violent bubbling or "burping" occurred; the level of the mass simply dropped to its final 6-in. height. It ceased to appear "liquid" after 64 hr. A small fan was placed nearby to simulate a mild breeze over an outdoor waste pit. At the end of the fifth day, vermiculite was added to cover the heated mass. Fumes of NO_2 were observed for the next 3 days, indicating breakdown of the nitrates in the mix. Readings of the thermocouple at the center of the mass indicated that equilibrium temperature (850°C) was reached at about 14 days. The average temperature of the mass was about 780°C. Figure 165 shows the temperature of the mass as a function of time. The mass was observed after cooling and was found to be well sintered. It was quite hard; and whereas cracks appeared on the surface of the mass in the first liquid experiment, there were none in this experiment. Figure 166 shows the structure of pieces of the sintered cake which were removed from the "hot pot."

Pilot-Pit Experiment. – A pilot radioactive-waste-disposal unit has been built. In Fig. 167, this pit and its auxiliary equipment are shown schematically.

The pit is located on a knoll so as to minimize the possibility of water seepage. It consists of an outer concrete liner 6 in. thick, 12½ ft deep, with an outside diameter of 11 ft; this liner is sunk 11½ ft below ground level. Insulating material is inserted between this outer liner and the primary pit liner. The insulating material consists of 18 in. of vermiculite around the walls, with 18 in. of Foamglass blocks at the bottom which serve as support and insulation for the primary liner. The inner concrete liner, which serves as the container for the clay-flux mix, is 6 in. thick and 10 ft deep, with an inside diameter of 6 ft. Two banks of Calrod heaters are located near the bottom of the pit so that when the clay-flux mix is heated to dryness, the heaters will be appropriately located within the mass so as to produce efficient sintering. The pit is protected from rain by a shed. The power supply and recording instruments are located in an adjoining shed and are, thereby, shielded from the corrosive NO_2 fumes that will be

TABLE 70. VISCOSITY MEASUREMENTS OF VARIOUS CLAYS

Material	Concentration of Solids (%)	Distilled Water		Hope Solution		W-8 Solution	
		Average Viscosity (centipoises)	Type[a] of Consistency Curve	Average Viscosity (centipoises)	Type[a] of Consistency Curve	Average Viscosity (centipoises)	Type[a] of Consistency Curve
Gleason Ball Clay	9.1	5.38×10^{2}	T	2.16×10^{8}	T	1.40×10^{14}	T
						4.07×10^{26}[b]	
	20.0	2.45×10^{18}	T				
		4.94×10^{32}[b]	T				
	23.0	1.56×10^{30}	T				
		6.97×10^{46}[b]	D				
Wyoming Bentonite	9.1	1.45×10^{99}[b]	T	1.27×10^{4}	D	3.82×10	D
	16.6			5.40×10^{11}	D	5.18×10^{9}	D
Panther Creek Bentonite	9.1	8.12×10^{2}	D	23.59×10^{4}	D	2.80×10^{2}	D
	16.6	1.21×10^{18}	T	1.34×10^{24}	D, T	1.03×10^{10}	T
	16.6[c]	1.24×10^{19}	T	4.07×10^{24}	D, T	4.99×10^{9}	T
Filtrol (Montmorillonite)	9.1	1.52×10^{2}	T	2.48×10^{4}	T	9.12×10^{3}	T
	16.6	3.43×10^{24}		3.92×10^{15}	T	6.68×10^{11}	T, D
Florex, calcined	9.1	9.17×10^{4}	T	5.25×10^{4}	T		
	16.6	1.57×10^{44}	T, D	2.77×10^{25}	T, D	6.7×10^{41}	T
		1.27×10^{87}[b]	T, D				
Baroid "B"	9.1	2.13×10^{11}	T, D	7.69×10^{3}	T	9.90×10^{8}	T, D
	16.6	1.06×10^{732}[b]	T	1.45×10^{26}	D	3.88×10^{23}	T, D
				4.60×10^{31}[b]	D, T	1.02×10^{69}[b]	T, D
Baroid "A"	9.1	5.52×10^{379}[b]	T, D	5.96×10^{3}	T	8.76×10^{3}	T
	16.6			1.02×10^{15}	T, D	1.02×10^{16}	T, D

[a] T, thixotropic; D, dilatant.
[b] Cylinder bob.
[c] Second run.

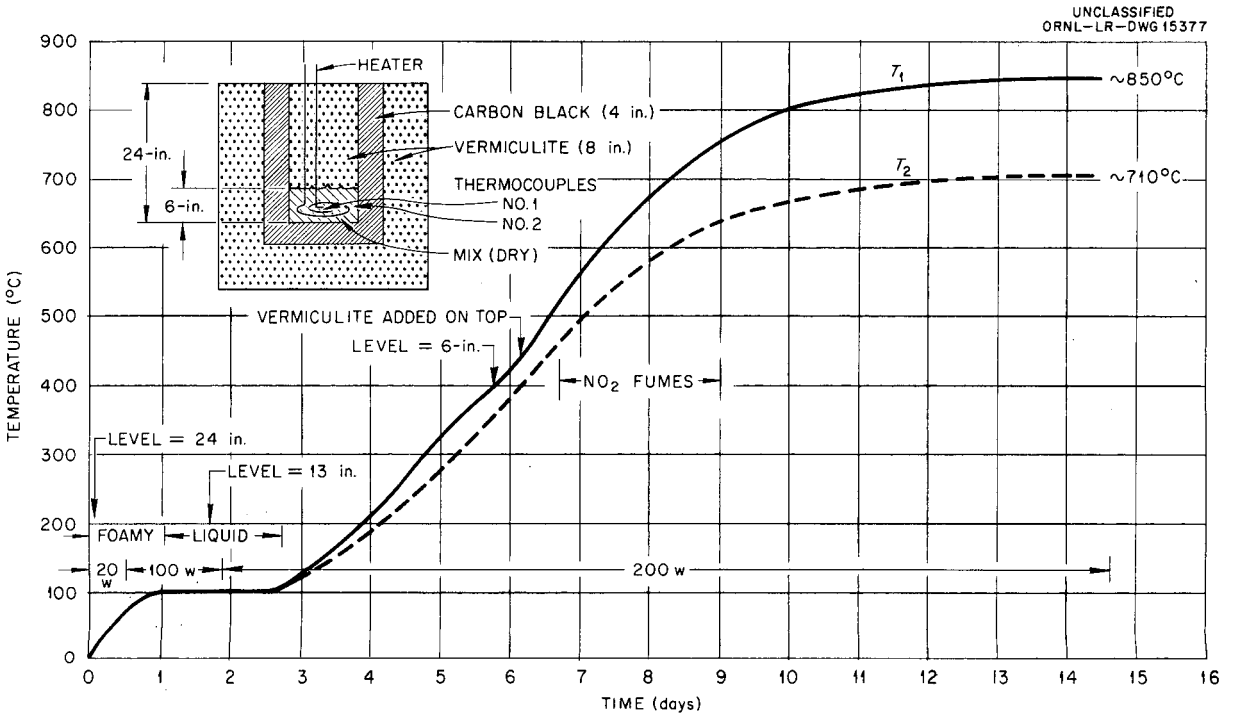

Fig. 165. Time-Temperature Plot of Fusion Experiment No. 6.

evolved. Heat-transfer data is to be obtained by means of 24 dual thermocouples located as shown in Fig. 167.

Considerable difficulty was encountered in getting the pit into operation due to excessive rainfall. There was considerable leakage of water into the pit, presumably as the result of a perched water table. It was necessary to sink four 20-ft wells near the pit for drainage.

The pit was charged in February. This charge consisted of 2400 lb shale, 720 lb limestone, 720 lb soda ash, and 720 gal Hope solution. For unknown reasons, the mixture did not gel and had to be poured as a thin slurry, and, thus, settling occurred. The composition of the Hope solution is believed to be at fault; it is now being analyzed. Even though settling occurred, it may be that the end result will be the same, although this can be determined only after the sintered cake has been examined.

ENTHALPY DATA FROM 0 TO 1200°C FOR PHYSICAL-PROPERTY STUDIES OF CERAMIC MATERIALS

M. P. Haydon

The heat contents and the derived specific heats of ceramic materials, especially the rare-earth oxides and those cermet types of material that have not been investigated before, are among the physical properties which are deemed important to know before these materials can be successfully utilized.

For obtaining the enthalpies of these materials an isothermal Bunsen-type ice calorimeter was used. This consisted of a glass enclosed air envelope of about an inch average thickness surrounding a deaired system of water, ice, and mercury, about 6 in. high and 3 in. in diameter. The mercury at the bottom of the system was connected to the outside through the glass enclosed

UNCLASSIFIED
PHOTO 25833

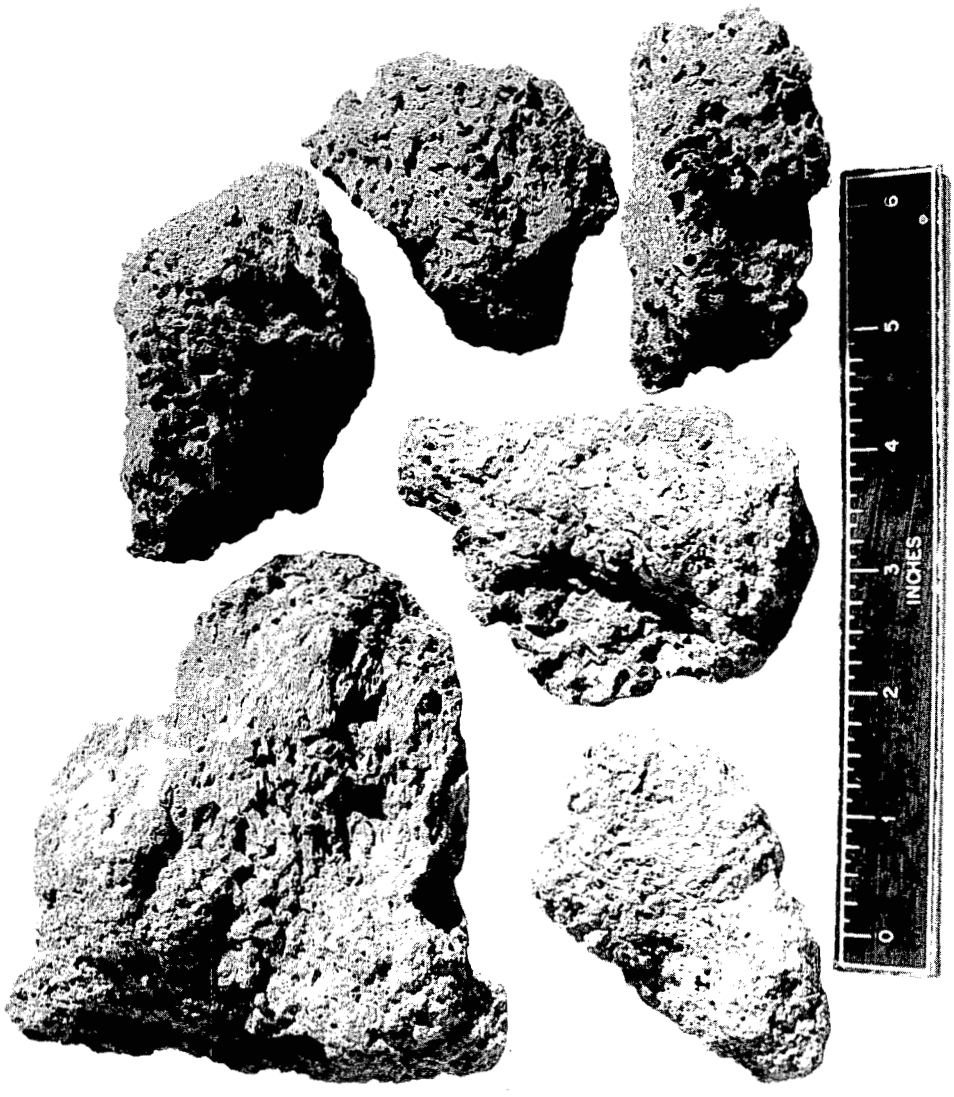

Fig. 166. Photograph of Sintered-Cake Samples from Waste Disposal–Heat Experiment No. 6.

UNCLASSIFIED
ORNL-LR-DWG 15378

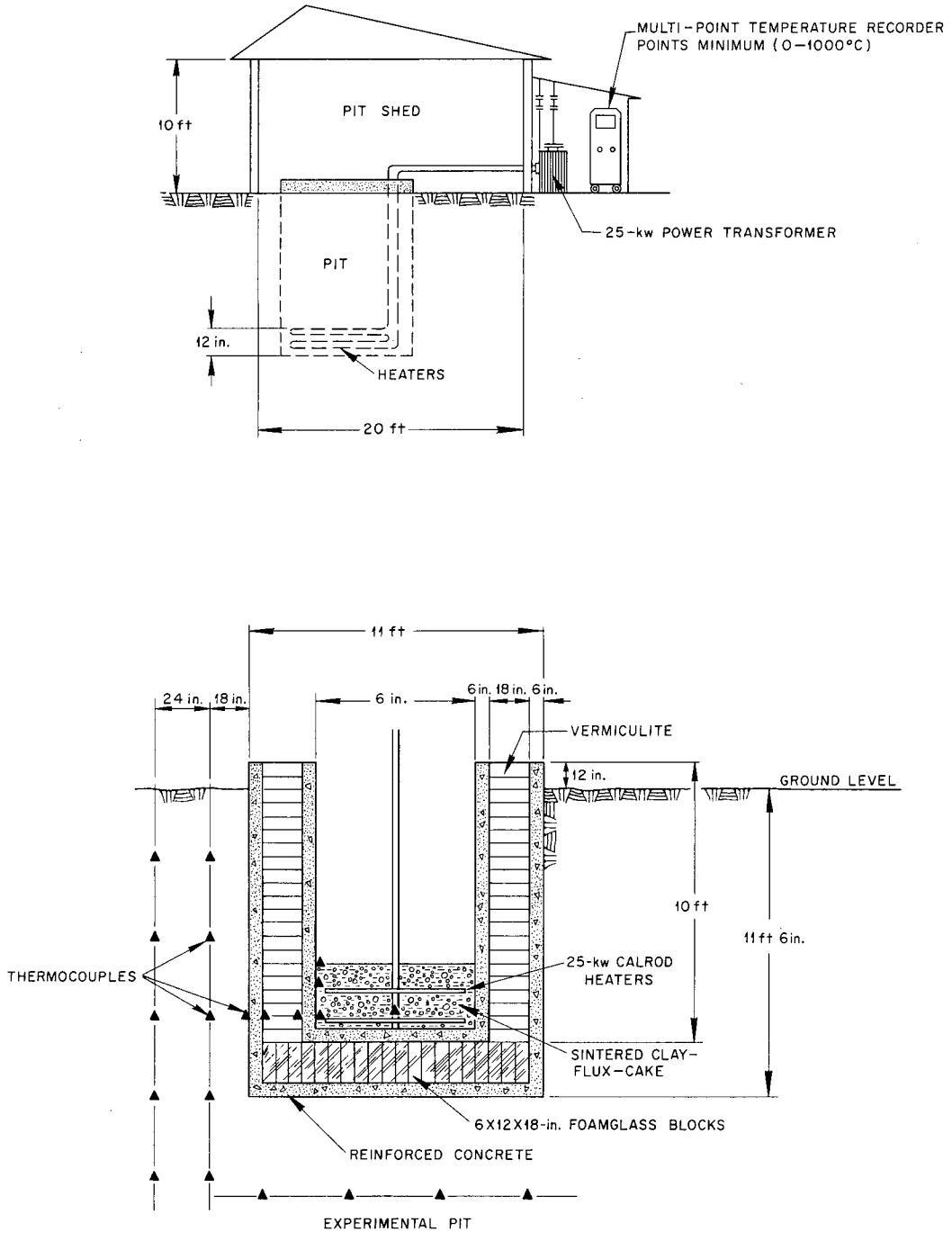

Fig. 167. Schematic Diagram of Waste-Disposal Pilot Pit No. 1.

air envelope by a glass capillary tube. Extending into the water, ice, and mercury system from the top through the glass enclosed air envelope was a quartz glass tube or central well about which the ice was frozen into a mantle by inserting dry ice into the central well. When an equilibrium at 0°C was established in the system, a heated specimen was dropped into the central well. The volume change in the ice melting, from the introduced heat, produced an intake of mercury through a calibrated capillary. The amount of mercury was proportional to the amount of heat put into the system and thus was a measure of the heat content or enthalpy of the specimen.

The calorimeter was kept in a water-ice mixture in a Dewar flask which, in turn, was packed in crushed ice in a steel-lined wooden cask. On the wooden cover were mounted a telescope and alidade for measuring the travel of the mercury meniscus. These parts are illustrated in Fig. 168.

The cask and calorimeter assembly was rolled under a platinum-wound furnace so as to receive the heated specimen as it was dropped from its position in the furnace. The suspending wire was 3 mil platinum and the drop was accomplished by burning the wire electrically. Two platinum – platinum + 10% rhodium thermocouples were located in the sample area of the furnace; one was connected with an L&N Speedomax recorder and controller, the other with an L&N precision potentiometer. The calorimeter cask, furnace, and controller are shown in Fig. 169.

A reduction of all the heat content or enthalpy data which has accumulated over the past two years from "drop" determinations with the ice calorimeter has resulted in a compilation of data from 233 runs involving seven different ceramic materials and one metal, the platinum sample container. A rigorous comparison of these data with those gleaned from other investigations[3–6] and from handbooks shows that the present data is generally in line with the published literature. The variations noted are at present unresolved and afford a challenge that further detailed investigation be made in these areas to corroborate the implications.

In these enthalpy determinations, it was intended that the Bureau of Standards corundum data[3] be used as a standard of calibration against which the errors involved in the particular setup and procedure used here could be resolved. It became apparent that this action was not justified since the samples of corundum were not the same and had different thermal histories. Also, the platinum wire from which the spiral basket container was made had a different thermal history from those reported in handbooks and in the literature.

Thus, it was decided that the simple formula of Ginnings[2] and other investigators be used, that is, sample-plus-basket value minus basket-alone value.

The combined enthalpy values for the corundum sample plus the platinum basket over a range of temperatures were plotted. The enthalpy values for the platinum basket were also plotted. Smooth curves through these points were used to obtain the values at regular intervals, and then the enthalpy of the sample alone was computed from the following equations:

$$(1) \qquad W_1H_1 + W_2H_2 = A$$

$$(2) \qquad W_2H_2 = B$$

$$(1\text{-}2) \qquad W_1H_1 = A - B$$

or

$$H_1 = \frac{A - B}{W_1}$$

where

W_1 and W_2 = weights in grams of the corundum and platinum basket, respectively

H_1 and H_2 = enthalpies in calories per gram of the corundum and platinum basket, respectively, between temperatures T and zero,

A = total heat in calories from "drop" of sample and basket,

B = total heat in calories from "drop" of basket.

Enthalpy values for HfO_2, Sm_2O_3, Gd_2O_3, Si-SiC, and SiO_2 glass were obtained in the same manner. A slight variation was necessary in the case of UO_2, however, because the UO_2 samples were

[3] D. C. Ginnings and R. J. Corruccini, *J. Research Nat. Bur. Standards* **38**, 593 (1947).

[4] J. C. Southard, *J. Am. Chem. Soc.* **63**, 3142 (1941).

[5] G. E. Moore and K. K. Kelley, *J. Am. Chem. Soc.* **69**, 2105 (1947).

[6] K. K. Kelley, "Contributions to the Data on Theoretical Metallurgy. X. High-Temperature Heat-Content, Heat-Capacity, and Entropy Data for Inorganic Compounds," *U. S. Dept. of the Interior, Bureau of Mines, Bulletin 476*, Washington, D. C., 1949.

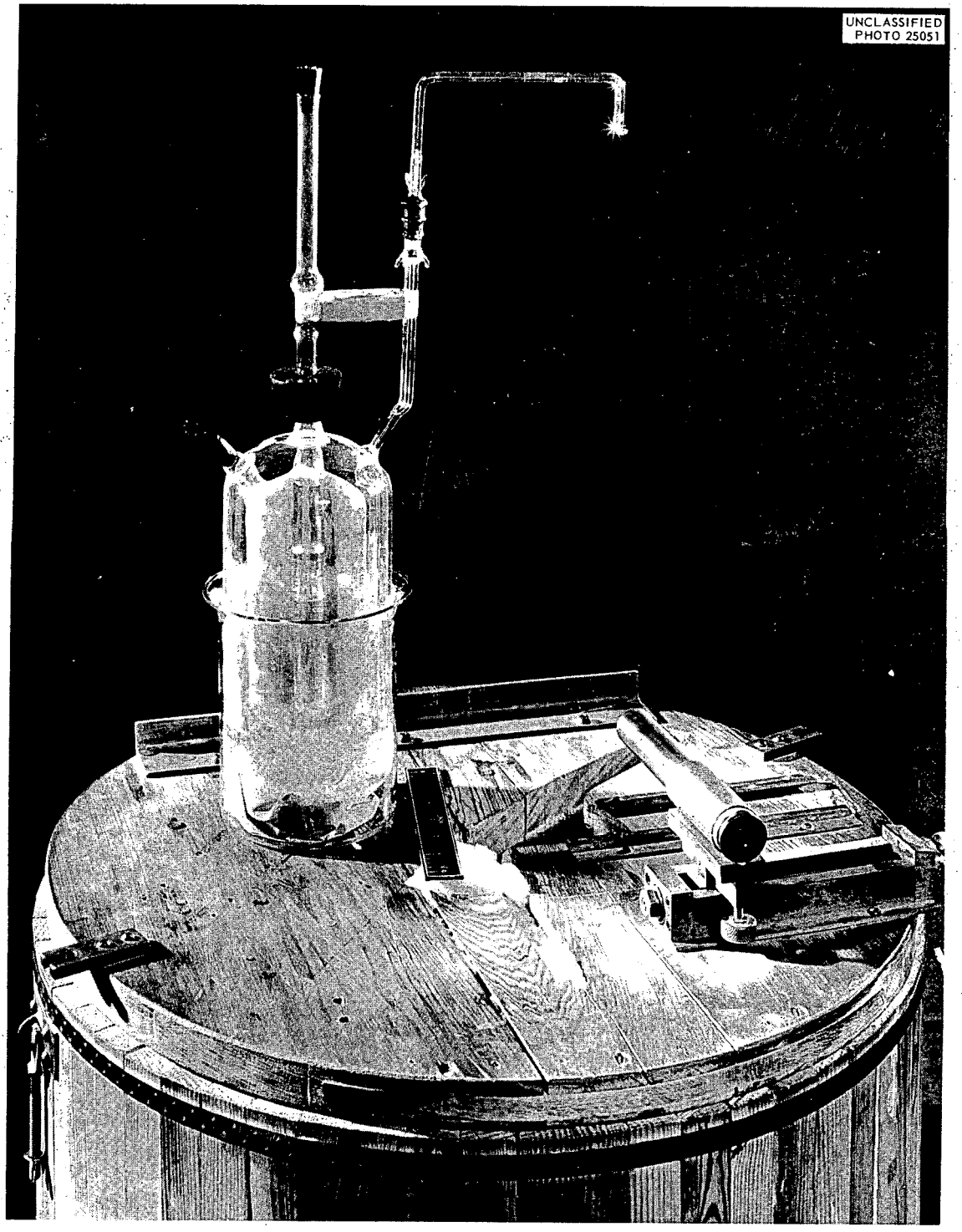

Fig. 168. Bunsen-Type Ice Calorimeter Used for Enthalpy Determinations from 0 to 1200°C.

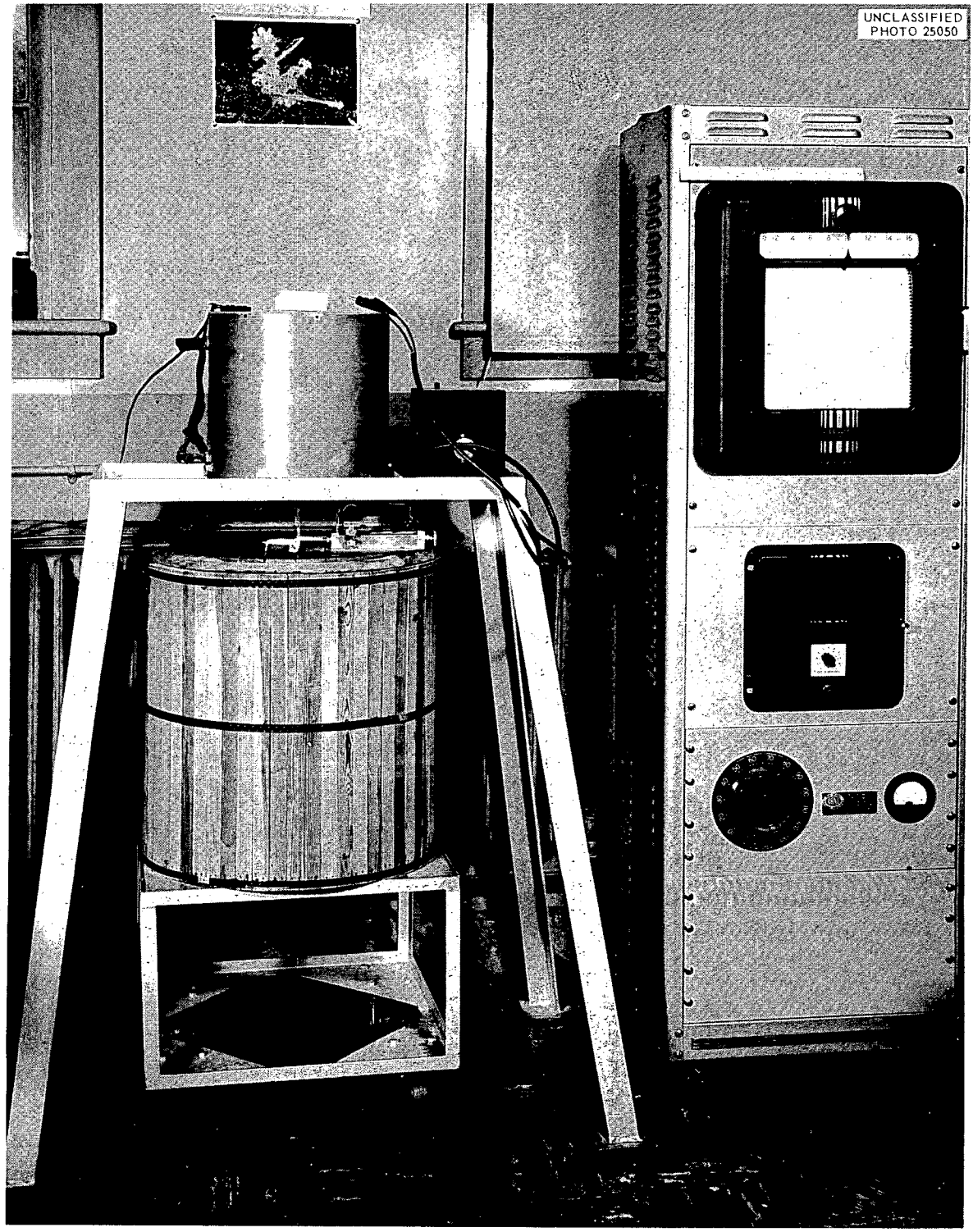

Fig. 169. Bunsen-Type Ice Calorimeter, Furnace, and Controller Used for Enthalpy Determinations from 0 to 1200°C.

sealed in SiO_2 glass capsules in a vacuum. Here, the SiO_2 enthalpy and the weight of the capsule had to be considered.

Table 71 is a compilation of enthalpy values obtained from smoothed-curve plots as described. These values are plotted in Figs. 170 and 171. The alumina enthalpy values in the 400 to 450°C range are in close agreement with the values reported by Ginnings and Corruccini; however, at temperatures below this range, the values are as much as 5 cal/g lower, and at temperatures above this range, the values are as much as 7 cal/g higher.

The present data for SiO_2 show a discontinuity between 500 and 600°C. This is not apparent in the values given by Southard,[4] which are a compilation of his values and those of several other investigators. However, Sosman has noted[7] "a slight irregularity in the curve [heat capacity] for vitreous silica at about 500 to 700°C" and later states "there are suggestions here and there of a

[7]R. B. Sosman, *The Properties of Silica*, The Chemical Catalog Company, Inc., New York, 1927.

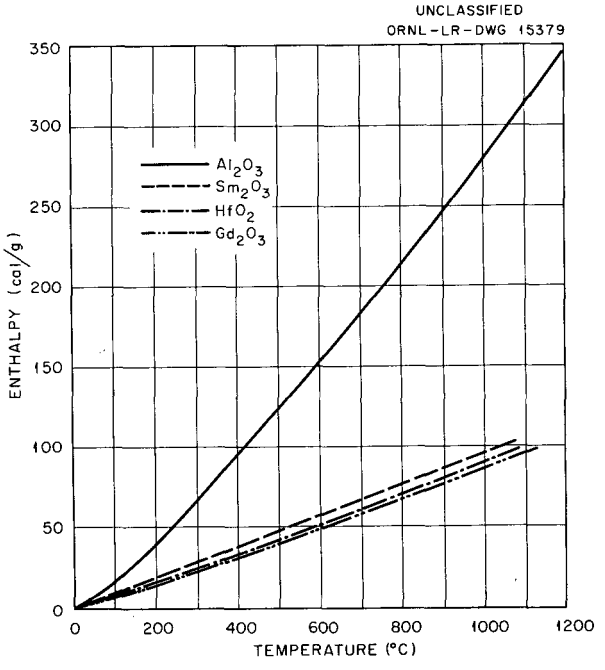

Fig. 170. Enthalpy Values for Alumina, Samaria, Hafnia, and Gadolinia.

TABLE 71. DERIVED ENTHALPY VALUES FOR SEVEN CERAMIC MATERIALS IN THE TEMPERATURE RANGE 0 TO 1200°C

Temperature (°C)	Enthalpy (cal/g)						
	Al_2O_3	HfO_2	Gd_2O_3	Sm_2O_3	Si-SiC	Silica Glass	UO_2
200	38.13	15.56	15.38	19.08	45.83	34.81[a]	12.91[b]
300	66.19						
400	94.54	32.72	31.14	37.84	89.80	75.91[a]	36.20[b]
							37.13[c]
500	122.55					95.60[a]	32.81[c]
600	152.35	49.72	48.04	56.49	130.37	151.55[a]	
						146.91[d]	34.48[c]
700	182.48						
800	213.23	68.15	65.35	76.95	181.74	199.71[d]	49.79[c]
900	245.05						
1000	277.94	88.35	84.17	94.40	239.66	263.29[d]	64.42[c]
1100	311.45						
1200	346.62					338.37[d]	70.49[c]

[a]First sample fused-quartz tubing.
[b]Norton fused oxide.
[c]Precipitated from ammonium diuranate.
[d]Second sample fused-quartz tubing.

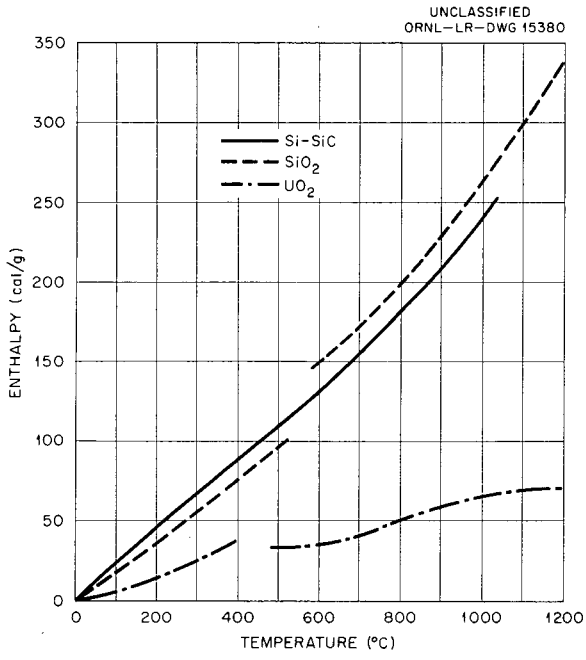

Fig. 171. Enthalpy Values for Silica Glass, Uranium Dioxide, and Siliconized Silicon Carbide.

TABLE 72. COMPARISON OF ENTHALPY DATA FOR UO_2 FROM 0 TO 1200°C

Temperature (°C)	Enthalpy (cal/g)	
	ORNL Data	Moore and Kelley Data
127		6.22
200	12.91*	
227		12.84
327		19.77
400	36.20*	
	37.13**	
427		26.96
500	32.81**	
527		34.25
600	34.48**	
627		41.66
727		49.17
800	49.79**	
827		56.80
927		64.50
1000	64.42**	
1027		72.24
1127		80.05
1200	70.49**	

*Norton fused oxide.

**Precipitated from ammonium diuranate.

genuine irregularity in vitreous silica near 600°C." He also mentions that the true heat capacity of vitreous silica probably varies, depending on its previous history. Two of the quartz capsules used in the UO_2 determinations failed because of devitrification and progressive evidence of this was noted in the samples of quartz tubing used for the separate enthalpy runs.

Another discontinuity has been noted in the UO_2 curve between 400 and 500°C. This is not evident in the data of Moore and Kelley,[5] as shown in Table 72, a comparison of ORNL data with that of the Bureau of Mines.

None of the ORNL data has been corrected for errors that are not systematic (the heat losses by radiation as the sample is dropped from the furnace into the calorimeter). Some of these errors would be furnace-thermocouple deviation from a standard, thermal "drift" of the calorimeter and its surroundings; difference in equilibrium times for the different materials; measuring errors in the potentiometer slides, the alidade, and the telescope; day-to-day effect of changes in barometric pressure on the ice-water-mercury system; and the effect, on the mercury in the capillary, of variations in the head of mercury in the weighing vials, which are used in conjunction with the measured capillary contents.

The effect of several of these corrections, the thermocouple calibration, the thermal drift, and the change in equilibrium points, have been spot-checked and found to be quite insignificant as individual contributions. However, the combined effects might be more noticeable, and a more careful study will be made of them.

It seems rather imperative in view of the apparent anomalies in the quartz and uranium dioxide values that more determinations or "drops" will have to be made in the ranges where the discontinuities occur.

Specific-heat, or heat-capacity, values may be derived from the enthalpy curves by graphic differentiation, since equations have not been fitted to the curves at the present time.

FABRICATION OF CERMETS COMPOSED OF A METAL AND A RARE-EARTH OXIDE FOR EXTRUDED CONTROL RODS

L. M. Doney J. A. Griffen

A cermet compact of rare-earth oxide plus nickel or iron is required for the impact extrusion of a clad control rod for the ART. These compacts were in the form of short, hollow cylinders.

A mixture of 70% nickel and 30% samarium and gadolinium oxides (Lindsay mix, code 920) or of 25% iron, 25% Fe_2O_3, and 50% Lindsay mix, code 920, was dry-pressed with a light pressure in a steel die and then isostatically pressed to 40 tsi. This compact was then sintered in hydrogen at the appropriate temperature (~1400°C).

The sintered density of these compacts was low but was sufficiently high (~75% of theoretical) for the extrusion process.

FABRICATION OF RARE-EARTH-OXIDE COMPACTS FOR CONTROL RODS

L. M. Doney J. A. Griffen

Porous low-density compacts of rare-earth oxide (Lindsay mix, code 920), which have high absorption for sodium, are required for the ART control-rod assembly.

It was shown that the measured sodium absorption of these compacts when immersed in the metal at 1200°F was very nearly equal to the water absorption of the same compact, measured in the usual manner.

In order to achieve the required low density (3.95 to 4.45 g/cc), the as-received oxide was calcined, crushed, and screened. A mixture of 75% calcined oxide and 25% raw oxide was made and was pressed with a low pressure in a steel die. When sintered at about 1400°C, a porous compact of good mechanical strength resulted.

These compacts are then ground to the required inside diameter, outside diameter, and length and are assembled into the control-rod container.

FUNDAMENTAL METALLURGY

FUNDAMENTAL PHYSICO-METALLURGICAL RESEARCH

J. K. Jetter

C. J. McHargue J. O. Betterton, Jr. G. D. Kneip, Jr.

PREFERRED ORIENTATION IN EXTRUDED THORIUM ROD

C. J. McHargue L. K. Jetter

The deformation fiber textures of face-centered cubic metals have been reported to be <111> or varying ratios of <111> and <001>; the relative amount of each component is considered to be characteristic of the individual metal and the fabricating procedure.[1] Despite considerable literature on the subject of annealing textures, there appears to be some uncertainty as to which components are to be expected for any given thermal treatment.[1] Theories of both deformation- and annealing-texture formation are in an incomplete state at the present time. In order to obtain experimental data to serve as a base for the development of theories, a quantitative study of the textures of face-centered metals and alloys has been undertaken. As a part of this program, the fiber-axis distributions of four specimens of thorium rod having different past histories were determined.

Billets of Ames thorium (0.04% carbon) were extruded at 850°C to form rods 0.875 in. in diameter (a reduction in area of 92.2%). Extrusion speeds of 2.3 and 588 fpm were used, and the rods were die-quenched in order to retain, insofar as possible, the as-extruded structure. A portion of each rod was vacuum-annealed for 1 hr at 750°C.

From a 0.19-in. spherical x-ray diffraction specimen, pole-distribution data were obtained by the spectrometric method described previously.[2,3] The axis-distribution charts (T vs ϕ, β), deduced from the pole distributions, are shown in Figs. 172–175. On these latter charts, the contours indicate angular positions of equal normalized fiber-axis density; and a value of unity corresponds to a random distribution.

The axis-distribution chart for the specimen taken from the rod extruded at 2.3 fpm shows that

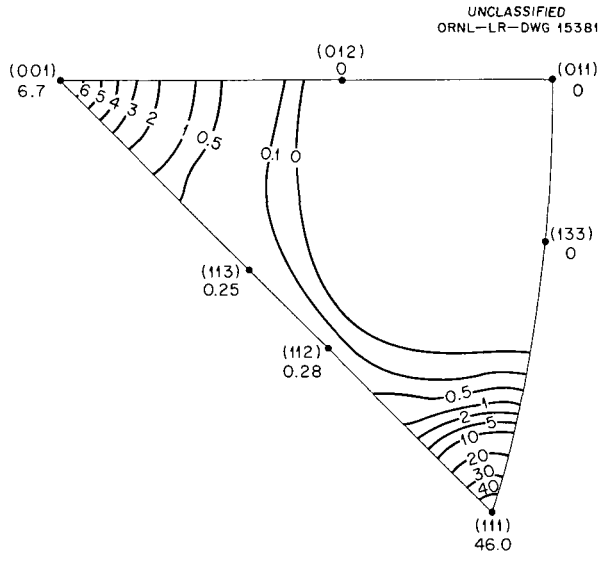

Fig. 172. Fiber-Axis Distribution Chart for Thorium Rod Extruded at 2.3 fpm at 850°C.

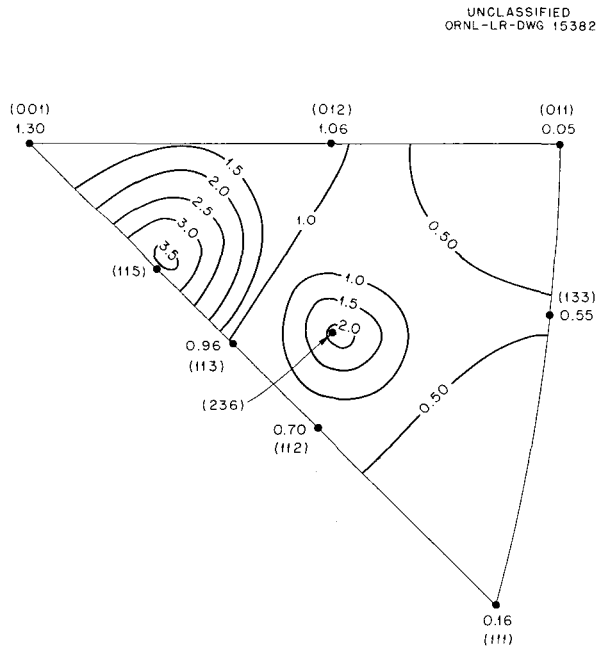

Fig. 173. Fiber-Axis Distribution Chart for Specimen in Fig. 172 Annealed 1 hr at 750°C.

[1] C. S. Barrett, *Structure of Metals*, 2d ed., McGraw-Hill, New York, 1952.

[2] L. K. Jetter and B. S. Borie, Jr., *Proceedings of the Spring Metallurgical Conference March 24–26, 1952*, vol 2, p 529, TID-5084 (June 1952).

[3] L. K. Jetter and C. J. McHargue, *Met. Semiann. Prog. Rep. April 10, 1954*, ORNL-1727, p 97.

the texture is duplex, the <111> and the <001> being the more preferred crystallographic directions of the fiber axis (Fig. 172). Initially the axis density falls off symmetrically from both peaks, but later it becomes asymmetric and forms a low "saddle" along the <110> zone. The <111> component was found to be associated with 75% of the volume and the <001> component with 25%.

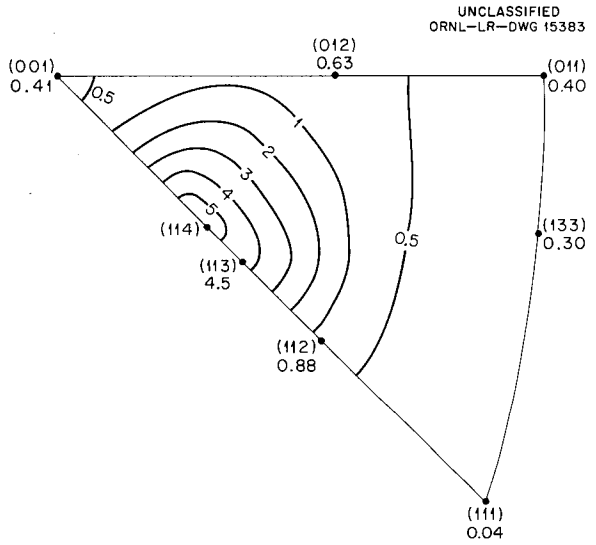

Fig. 174. Fiber-Axis Distribution Chart for Thorium Rod Extruded at 588 fpm at 850°C.

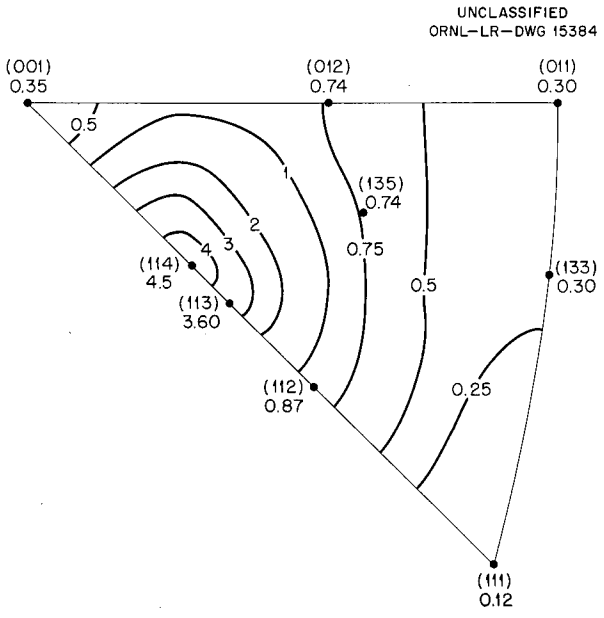

Fig. 175. Fiber-Axis Distribution Chart for Specimen in Fig. 174 Annealed 1 hr at 750°C.

An earlier study of thorium rod extruded at 850°C and 1 fpm, but with a reduction in area of 89.8%, showed a duplex texture consisting of 93% <111> and 7% <001>.[4] The photomicrograph of this earlier specimen[4] showed a small number of recrystallized grains in a deformed matrix; whereas, that of the present specimen showed a number of recrystallized grains. In aluminum rods which exhibited the duplex <111> – <001> texture, it has been shown that the <111> component was associated with the deformed regions and that the <001> component was associated with recrystallized grains.[5] A similar relationship between texture and microstructure is indicated for thorium rod. The increase in amount of reduction, the faster extrusion speed, and the higher purity of the thorium used in the present study, contrasted with that of the specimens used previously, tend to favor the increased amount of recrystallization observed.

The axis-distribution chart for the specimen taken from the rod extruded at 2.3 fpm and annealed 1 hr at 750°C is given in Fig. 173. The more preferred crystallographic directions of the fiber axis are <236> and a direction 2 deg from <115>. The microstructure of this specimen was that of a completely recrystallized state but with no exceptionally large grains.

The <236> fiber texture has never been reported for any face-centered cubic metal, and a <115> has been reported only for one specimen of extruded aluminum rod.[5]

Figure 174 shows that extruding at a speed of 588 fpm at 850°C produced a single <114> fiber texture in thorium rod. The rod was completely recrystallized in the as-extruded condition. Annealing a specimen of this rod at 750°C produced little change in either the axis distribution (Fig. 175) or the microstructure.

The fiber-axis-distribution chart is particularly well suited for studying the symmetry of the fiber axes about the more preferred crystallographic directions. From Fig. 172 it can be seen that the distributions about <111> and <001> are symmetrical for all contours having a value of unity or higher.

[4]L. K. Jetter and C. J. McHargue, *Met. Semiann. Prog. Rep. April 10, 1955*, ORNL-1911, p 11.

[5]F. T. Howard, *Oak Ridge National Laboratory Status and Progress Report June 1955*, ORNL-1920.

Calnan[6] has postulated that differences in textures of face-centered cubic metals arise from differences in strain-hardening rates. Metals exhibiting equal strain-hardening on all slip planes (active and latent) should develop duplex <111> – <001> drawing (fiber) textures for intermediate amounts of reduction. After severe deformation, these intermediate textures should decrease in intensity, and a shift from <111> toward <112> should take place. The ultimate texture is predicted to be an axis between <111> and <112>, the <001> component having disappeared.

Since Smallman[7] has concluded that the slip systems of thorium harden equally during deformation, the shift from <111> toward <112> might be expected in the thorium rod studied; but, on the contrary, the distribution remains symmetrical about <111>. It would be desirable to determine the fiber texture in a thorium rod given a greater reduction; however, it appears from the present and previously reported studies[4] on thorium that Calnan's theory does not completely explain the experimental data.

The present study shows four texture components which result from thermal processes rather than from deformation processes. These are <001>, <115>, <236>, and <114>. As in the case of extruded aluminum rod, the <001> component in the recrystallized grains of rods appeared partially recrystallized in the as-extruded condition. The <115> and <236> components appeared upon annealing at 750°C, and <114> was the fiber axis of the rod completely recrystallized during fabrication.

It has been found informative by many investigators to relate deformation-texture and recrystallization-texture components in terms of a rotation about some axis which moves one orientation into the orientation of the other. The most commonly reported relationship for face-centered cubic metals has been rotations of 25 to 40 deg about <111> axes, although there have been a few reports of rotations about <001> and <011> axes.[1,8,9] It has also been reported, in a number of instances, that grains which are related to a matrix by such relationships grow at higher rates than when associated with other orientations.[1] The physical basis for a relationship of this sort is not known at the present time, but such observations have been taken as evidence for both the "oriented-nucleation" and "oriented-growth" theories of recrystallization-texture formation.

Some possible rotational relationships for the texture components observed in the present study are illustrated in Fig. 176. The great circle angularly bisecting the small circle connecting two points on a Wulff net is the locus of axes that would rotate one point onto the other. Because of the lack of information about the meaning of such relationships, directions with low indices have been chosen to represent the axes of rotation.

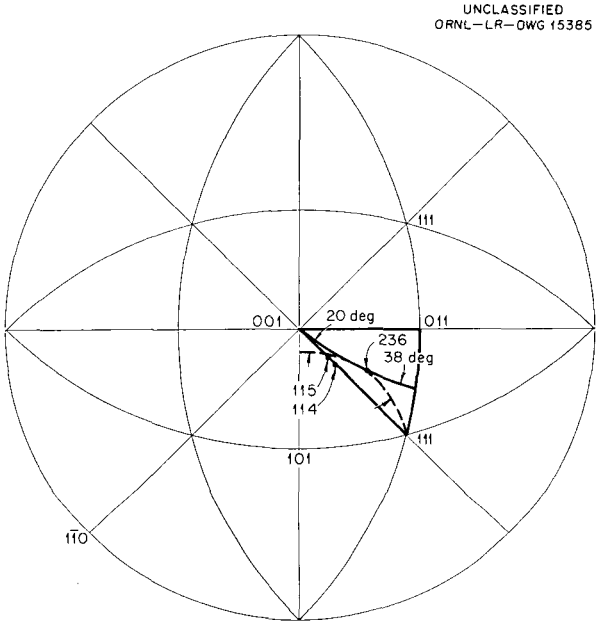

Fig. 176. Some Rotational Relationships Between Deformation and Recrystallization Components of the Textures of Thorium Rod.

A rotation of 19.5 deg about a <111> axis brings the <001> component to a position 1.5 deg from the <115>, and a rotation of 38 deg about the same axis brings the <001> component to the position of <236>. Kronberg and Wilson[8] found that the "secondary recrystallization" texture components of copper could be related to those in copper containing the "cube" texture by rotations of 22 and

[6] E. A. Calnan, *Acta Met.* **2**, 865 (1954).

[7] R. E. Smallman, *Deformation and Annealing Textures in Thorium*, AERE M/R 1529 (Oct. 18, 1954).

[8] M. L. Kronberg and F. H. Wilson, *Trans. Am. Inst. Mining Met. Engrs.* **185**, 501 (1949).

[9] Y. C. Liu and W. R. Hibbard, Jr., *Trans. Am. Inst. Mining Met. Engrs.* **203**, 1249 (1955).

38 deg about <111> axes. These authors discussed the observed relationships in terms of the positions of atoms before and after the recrystallization process. From their coincidence plots, it was seen that rotations of 22 and 38 deg about <111> axes would have one-seventh of the atoms on {111} planes in the same lattice sites in the two phases, and the remaining atoms could be brought onto the sites of the new lattice by simple movements of the order of one-third an interatomic distance.

The observation of Kronberg and Wilson that a 38-deg rotation about <111> axis brings the "secondary recrystallization" texture into the "cube" texture in copper suggests that the <236> component in thorium may result from a "secondary recrystallization" which originates in grains having a <001> texture. The <001> fiber texture is analogous to the "cube" texture in sheet. The plot of atom positions for a 19.5-deg rotation about <111> shows a relatively low density of coincidence sites.

The question arises as to the origin of the <001> component. There seems to be justification for suggesting that this component is the result of a recrystallization process which occurred during or just after fabrication procedure. Figure 176 shows that the <111> and <001> components are related by a 54°44′ rotation about the <$\bar{1}$10> axis, which is perpendicular to the fiber axis, but that no rotation about the <111> axis will bring the components into coincidence. Liu and Hibbard[9] observed that some of the components obtained by annealing a cold-rolled single crystal of aluminum could be obtained from certain of the rolled components by <011> rotation of 30 deg. The data of Graham and Cahn[10] can be interpreted as showing a high rate of growth for one grain growing into another, where the relative orientation was that of a <011> rotation of approximately 55 deg.

A coincidence plot was constructed showing the atom positions in {110} planes that are related by a 55-deg rotation. It was found that this rotation brought only a few sites into coincidence and that relatively large atom movements were required to bring the other sites into coincidence. Thus, it is concluded that the proposed relationships of Kronberg and Wilson are not the only ones applying to the orgin of the <001> texture.

Also illustrated in Fig. 176 are relationships between the <111>, the <115>, and the <236> components. These consist of rotations of 38.5 and 43.5 deg about <110> directions perpendicular to and at an angle of 35°16′, respectively, to the rod axis.

In Fig. 177 is shown a coincidence plot of a rotation of 38.5 deg about a <$\bar{1}$10> axis. Approximately 12% of the atom positions coincide, and the remaining positions are related by simple atom movements. The movements required for coincidence are of the order of $0.25a_0$ and $0.5a_0$. This formal construction is not intended to imply that the orientation change actually occurs by means of the indicated rotational shear operation. Rather, it serves only to illustrate the relative positions of the atoms in a {011} plane before and after the annealing process. The plot in Fig. 177 appears to be as reasonable, with respect to density of coincident sites and to atom rearrangements, as the data of Kronberg and Wilson. A coincidence plot of a 43.5-deg rotation about a <011> axis was constructed. Only approximately 3.5% of the atom sites were in coincidence; however, another 10% were approximately $\frac{1}{7}$ of an interatomic distance distance ($0.1a_0$) from corresponding sites. For density of coincidence sites, this 13.5% is rather high. On the other hand, 20% of the atoms must move $\frac{5}{7}$ to $\frac{6}{7}$ of an interatomic distance. Moreover, it seems probable that 20% of the atoms would make movements of this magnitude.

In their discussion, Kronberg and Wilson regarded the coincidence plots as giving evidence for the "oriented nucleation" theory of texture formation. However, this kind of a chart can reasonably be interpreted as showing the relative atom positions on each side of a moving interface. For example, in Fig. 177, atoms in positions x must move only 0.35 of the interatomic spacing d in order to get to the corresponding site x' but must move at least $2d$ to reach any other site in the growing phase. It might be expected that atoms moving across an interface from one phase to another would take the path of minimum movements. Hence, the coincident atoms would prefer to remain on their former sites, and the movement x to x' would be more favorable than x to any other position. The other movements are those necessary to fill in the new lattice and are approximately equal. When more information is

[10]C. D. Graham, Jr., and R. W. Cahn, "Grain Growth Rates and Orientation Relationships in the Recrystallization of Aluminum Single Crystal" (to be published in *Trans. Am. Inst. Mining Met. Engrs.*).

available concerning annealing processes, models such as these may be helpful in understanding the the nature of the thermally activated atom rearrangements.

Thus, consideration of possible likely rotational relationships indicates that the <115> and <236> components could have developed either from <111> or <001> components. A study of coincidence plots, however, suggests that the <115> component originates in the <111> regions and that the <236> component arises from the <001> texture. The <001> component is considered to result from a thermal process rather than from a deformation process. The orientation relationship between <111> and <001> is believed to be favorable for rapid growth rates, but the coincidence plot for such a relationship does not appear to be satisfactory. It may be that the recrystallization

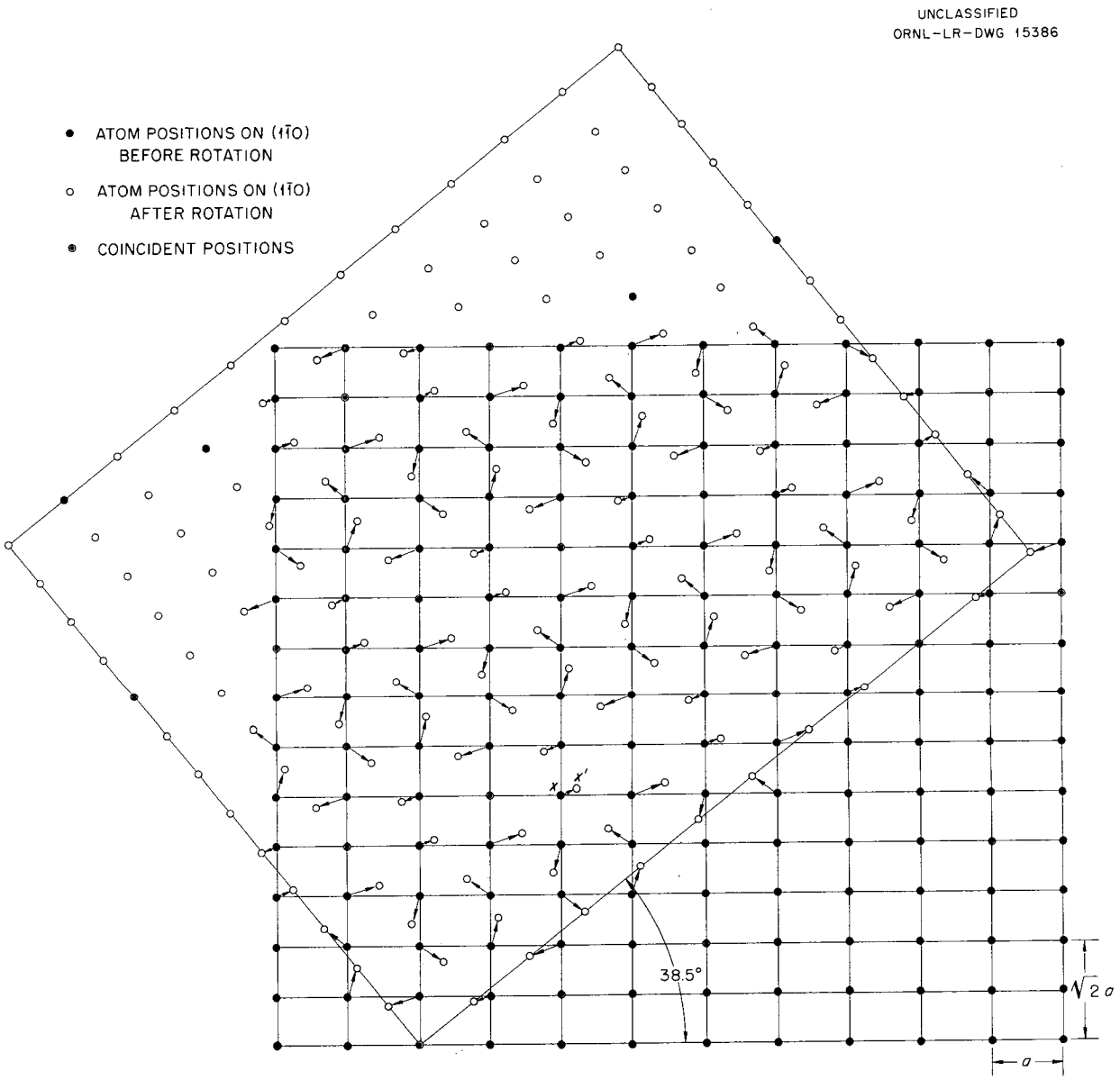

Fig. 177. Coincidence Plot for (1$\bar{1}$0) Showing Atom Positions for a Rotation of 38.5 deg About <1$\bar{1}$0>.

process producing the <001> component occurred during the late stages of fabrication; and, therefore, this component was formed in a stress field, which might affect the texture.

Because of the speed with which the deformation was done, the temperature in the rod extruded at 588 fpm was somewhat higher than the billet temperature of 850°C. The <114> position is 3°41′ from <115> and can be obtained from <001> by a 23.5-deg rotation about <111>, compared with 19.5-deg for <115>, or from <111> by a 35.3-deg rotation about <$\bar{1}$10>. It is desirable to know if the rod containing the duplex <111> – <001> texture would develop the <114> component upon annealing at 850°C or higher. It would also be interesting to observe the effect of further annealing the rod containing the duplex <115> – <236> texture. These further experiments would give information regarding possible temperature dependence of the factors determining annealing textures.

In recapitulation, the following information has been derived. The fiber-axis distribution for thorium rod fabricated at 850°C, such that the as-extruded rod showed partial recrystallization, revealed a duplex <111> – <001> texture, whereas that for a rod completely recrystallized in the as-extruded condition showed a single <114> texture. Annealing the rods at 750°C produced a duplex <115> – <236> texture in the former rod but no significant change in the <114> texture of the latter. The textures obtained were discussed in terms of present theories, and the need for additional experimental data and for further development of the theories was pointed out.

PREFERRED ORIENTATION IN ZIRCALOY-2 PLATE

C. J. McHargue L. K. Jetter

In cooperation with the HRP metallurgy section, a study was made of the preferred orientation in a specimen taken from Zircaloy-2 plate.

The $\frac{5}{16}$-in. plate was obtained from ingot number 710D546P70BK, which was furnished by the Crucible Steel Company of America and was forged and rolled according to the following schedule: (1) reductions in thickness, totaling 69%, by cross rolling at 1440°F and (2) reductions, totaling 72%, by straight passes at approximately 1400°F. The plate was given a heat treatment which simulated the heat treatment necessary for certain hot-forming operations; this consisted of heating the plate to 1200-1225°F four times for a total time at temperature of 20 to 30 min.

Pole-distribution data were obtained by the usual ORNL method on a 0.200-in. spherical x-ray diffraction specimen that was machined from the plate. According to this method, each of the principal reference directions (rolling, normal, and transverse) is treated as a "fiber axis". The distributions of each of the reference directions, with respect to the crystallographic axes of the grains, were deduced and are presented in Figs. 178-180.

The more preferred crystallographic direction aligned with the rolling direction is 14 deg from

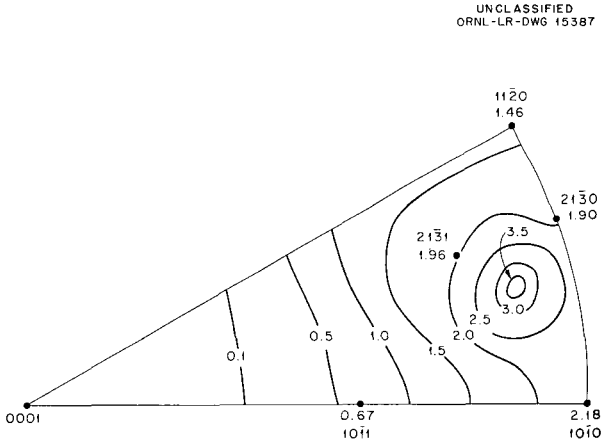

Fig. 178. Axis-Distribution Chart for the Rolling Direction of Zircaloy-2 Plate.

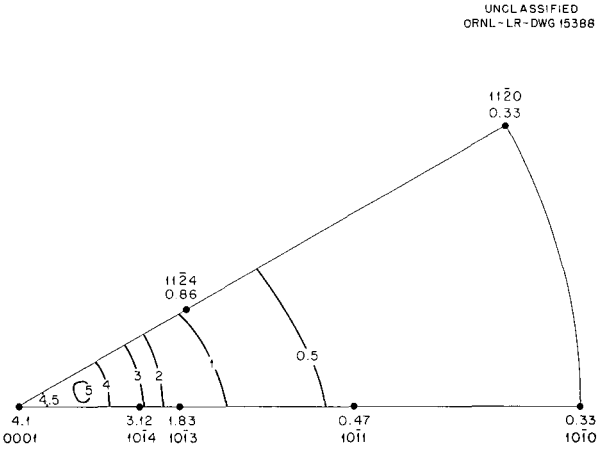

Fig. 179. Axis-Distribution Chart for the Normal Direction of Zircaloy-2 Plate.

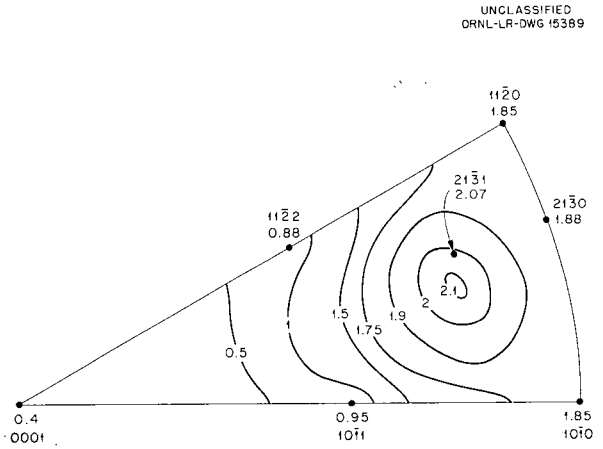

Fig. 180. Axis-Distribution Chart for the Transverse Direction of Zircaloy-2 Plate.

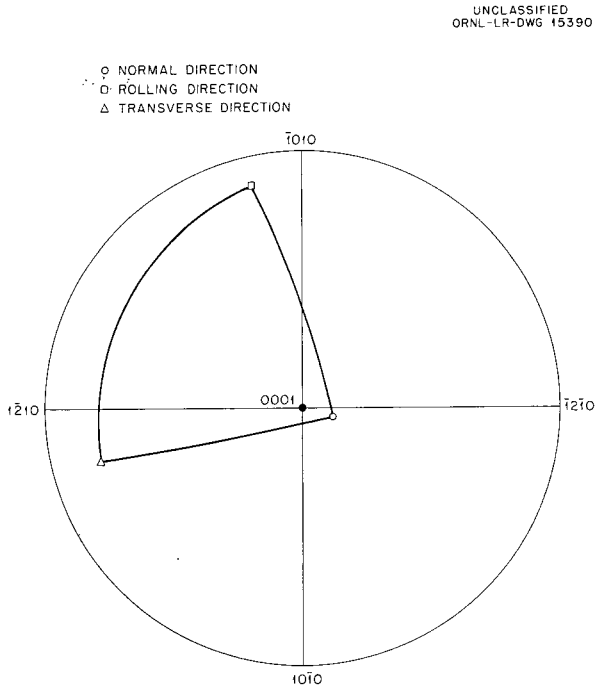

Fig. 181. Standard Stereographic Projection Showing the Texture of Zircaloy-2 Plate.

<$10\bar{1}0$> and 18 deg from <$11\bar{2}0$>, and there is a symmetrical distribution about the peak position (Fig. 178). The normal directions are symmetrically arranged about a position 14 deg from <0001> and 80 deg from <$11\bar{2}0$> (see Fig. 179). The transverse directions are symmetrically distributed about a peak which lies 90 deg from each of the above peaks, as shown in Fig. 180.

The texture is illustrated on a standard stereographic projection in Fig. 181. The normal directions are in a position intermediate to those reported for straight-rolled and cross-rolled zirconium sheet. Straight-rolled sheet was found to have the normal directions approximately 30 deg to {0001} poles, and cross-rolled sheet was found to have the normal directions parallel to {0001} poles.[11] In the present case, it appears that the intermediate position is the one which might be expected for the combination of rolling procedures used in fabricating the plate.

The rolling direction is in a position which might be expected from the standpoint of the thermal history of the sheet. It is interesting that neither {$10\bar{1}0$} nor <$11\bar{2}0$> is in the normal plane of the plate. This agrees with the recent observations of Geisler and Keeler on zirconium and titanium sheet.[12,13]

An analysis was made of the anistropy of mechanical properties which might be expected in this Zircaloy-2 plate. Because of the lack of data on the modes of deformation operative in zirconium and zirconium alloys, it was necessary to assume that the behavior would be similar to that of titanium. Preliminary work on zirconium indicates that this is probably true, at least for the pure metal.[14] The relative resolved shear stresses were calculated for the {$10\bar{1}0$} <$11\bar{2}0$> and {$10\bar{1}1$} <$11\bar{2}0$> slip systems, assuming the centers of the axis-distribution peaks as the "ideal" texture. The former system is probably much more active, although there is some evidence that interstitial atoms such as carbon, nitrogen, and oxygen cause the latter system to become relatively more active. Considerations was also taken into account for twinning on {$10\bar{1}2$} and {$11\bar{2}1$} planes.

It is to be expected, on the above basis, that the mechanical properties in the rolling and transverse directions would be similar. Figure 182 shows the variation of the resolved shear stress in the plane

[11] R. K. McGeary and B. Lustman, *Trans. Am. Inst. Mining Met. Engrs.* **191**, 994 (1951).

[12] J. H. Keeler and A. H. Geisler, *Trans. Am. Inst. Mining Met. Engrs.* **203**, 395 (1955).

[13] J. H. Keeler and A. H. Geisler, *Trans. Am. Inst. Mining Met. Engrs.* **206**, 80 (1956).

[14] E. J. Rapperport, *Acta Met.* **3**, 208 (1955).

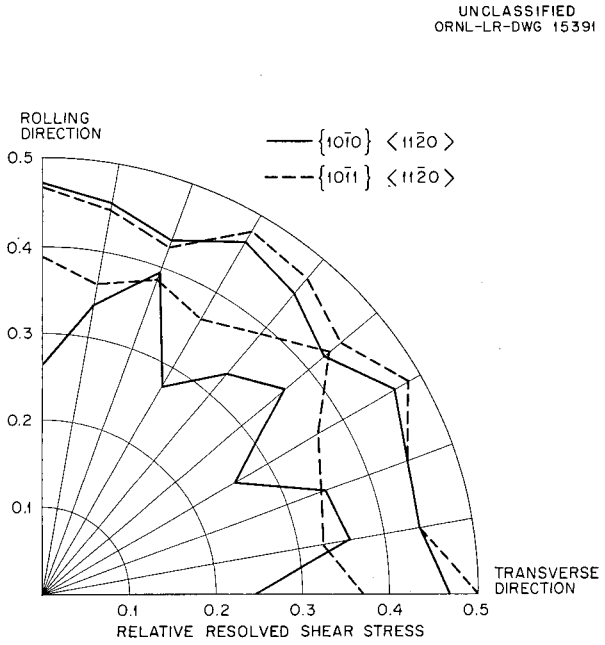

Fig. 182. Variation of Resolved Shear Stress in the Rolling Plane of Zircaloy-2 Plate.

of the plate, from the rolling direction to the transverse direction, for the more favorable slip systems. At all positions, twinning on {11$\bar{2}$1} planes will result from a tensile stress applied in that direction. There is the possibility that specimens taken at 20, 50, and 80 deg from the rolling direction may show slightly lower yield strengths and greater elongation than those taken from other positions.

Brittle behavior is to be expected for this material which has been subjected to a tensile stress in the normal direction. Since the resolved shear stress is less than 0.15 for all possible slip systems, little slip can occur. Some {10$\bar{1}$2} twinning is to be expected, but it cannot produce extensive deformation.

THE CONSTITUTION OF ZIRCONIUM-RICH ALLOYS OF THE SILVER-ZIRCONIUM SYSTEM

D. S. Easton J. O. Betterton, Jr.

A comparison of the phase diagrams of zirconium with various solutes from the B-subgroups of the Periodic Table has shown[15] that zirconium is effectively divalent in these alloys, providing that the conventional 1, 2, 3, and 4 valencies are assumed for Groups IB, IIB, IIIB, and IVB solutes, respectively, and that an electron-concentration law is valid for the α/β boundaries. Thus, adding univalent silver to divalent zirconium would be expected to have the effect of reducing the mean number of valency electrons. The zirconium-silver phase diagram[16] is characterized by a depression of the α/β phase boundaries: by a eutectoid reaction $\beta \rightleftharpoons \alpha + Zr_2Ag$; and by two intermediate phases, Zr_2Ag and ZrAg. Measurements have now been made of the lattice spacings of the alpha phase. The alpha-phase boundaries have also been reinvestigated in greater detail by the quenching method, and a new determination of the temperature of the peritectic formation of the Zr_2Ag phase has been started.

Lattice Spacings of the Alpha-Phase Region

The lattice spacings of the alpha phase of silver-zirconium are significant because they show the effect of changing the number of valency electrons in zirconium and because from them the solid-solubility limit can be determined and can be compared with that found by the microscopical technique. Since the amount of silver which can be dissolved is relatively small, the accuracy of measurement of these spacings is especially important.

The investigation of zirconium lattice spacings by the Debye-Sherrer method was discussed previously. Almost the same spacings were obtained with a powder specimen which was filed in vacuum and with a second specimen which was filed in air and vacuum-annealed at 550°C. These spacings, however, differed by 1 part in 6000 from spacings obtained on a wire specimen of the same material. Recent experiments were done on a second wire specimen of the same material enclosed in a protective annealing foil with a hydrogen content of 1 to 7 ppm. The result is shown in Table 73 along with the results from the earlier wire and powder experiments for comparison.

As noted in the table, both the a and the c spacings are slightly expanded in the earlier wire experiment, an effect which is thought to be due to the greater hydrogen content of the latter. Like results were also obtained in a similar experiment

[15] J. H. Frye, Jr., and J. O. Betterton, Jr., *Met. Semiann. Prog. Rep. April 10, 1954*, ORNL-1727, p 104.

[16] D. S. Easton and J. O. Betterton, Jr., *Met. Semiann. Prog. Rep. April 10, 1955*, ORNL-1911, p 16.

TABLE 73. EFFECT OF PRELIMINARY TREATMENT ON LATTICE SPACINGS OF PURE ZIRCONIUM

Type of Specimen	Spacing (Å)	
	a	*c*
Pure zirconium wire annealed in foil containing 1 to 7 ppm hydrogen	3.2327	5.1469
Pure zirconium wire annealed in foil containing 30 to 40 ppm hydrogen	3.2328	5.1473
Pure zirconium filings prepared in vacuum	3.2323	5.1482

with a wire of silver-zirconium alloy. The difference between the wire and powder specimens, on the other hand, cannot be explained on the basis of hydrogen in the wire alone. The powder specimen with a much larger surface-to-volume ratio may have been contaminated with some combination of hydrogen, oxygen, iron, nitrogen, or carbon. Since the *c* spacings in particular are likely to be expanded when interstitial-element contamination has occurred, the result for the wire specimen annealed in the low-hydrogen foil is tentatively accepted as the most reliable; and the matter of attempting to answer questions concerning the influence of impurities in zirconium wire and powder specimens will be deferred to a future time when they can be resolved by means of data from additional experiments.

In order to determine the lattice spacings of silver-zirconium alloys, wire specimens were used; and the results are plotted against silver content in Fig. 183. Small cylinders of the alloys containing silver in the range 0 to 1.2 at. % were annealed for 40 days at 775°C, were fabricated into wire, and reannealed for 30 min at 775 ± 0.5°C. A cylinder of alloy containing 1.63% silver was annealed at 790°C and reannealed as wire at 790 ± 0.4°C.

If the addition of silver to zirconium produces a random substitutional solid solution, the simplest behavior of the lattice spacings would consist of symmetrical effects with respect to the crystal directions, and the axial ratio would remain constant with increasing amounts of silver. Since silver has a smaller atomic volume than zirconium, however, both the *a* and *c* spacings might be expected to decrease in the manner shown by the dotted lines (Fig. 183), which represent a linear variation of mean atomic volume between the zirconium and the silver. The experimental specimens deviate from this behavior, a fact which is significant mainly because the deviations of the *a* and *c* spacings are in opposite directions. This deviation results in an expansion of the axial ratio with increasing silver content in the same manner as has been observed upon adding silver to titanium. The effect may be related, as discussed later, to a critical situation in zirconium where the (10.0) faces of the Brillouin zone have been overlapped and where the (00.1) faces either have been or are about to be overlapped. Consequently, the number of data points which are shown on Fig. 183 are not really sufficient to plot the behavior of the lattice spacings; however, straight lines have been drawn in order to show that the lattice spacings are consistent with the phase boundaries determined by the microscopical method; the crosses in Fig. 183 indicate the results obtained by this latter method. The *a* spacing decreases in a regular manner until the two-phase region is reached, indicated by the square symbols on this figure. In a similar manner, the *c* spacing decreases until the limit of solid solubility is reached. Several other alloys in the alpha-phase region are now being prepared in order to complete the investigation.

Annealing Experiments on Zirconium Alloys Containing 0 to 28 at. % Silver

A new set of zirconium alloys with silver compositions in the range 0 to 2.2 at. % silver have been investigated by long-time annealing at temperatures near 800°C. The microscopical results and the chemical analyses of the individual specimens are now complete; and, thus, a more accurate equilibrium diagram for this region can be plotted. The new data are shown in Fig. 184, together with results obtained previously with iodide-zirconium alloys of low-iron content.

Neutron-activation and vacuum-fusion analyses for minor impurities in the alloys are summarized, according to the order in which they were prepared, in Tables 74 and 75. The results indicate that progressive reduction in iron content has occurred during the course of the study and that the iron content varies from 24 to 88 ppm. in the alloy series (GWC, E2, E3, and E4) which were used in plotting Fig. 184. The analyses also indicate that other impurities – copper, hydrogen,

molybdenum, nickel, and silicon – have varied in the range of less than 100 ppm. On the basis of the consistency of the constitutional data, the effects of variations in the small amounts of these latter impurities are less significant than the effect of variation in iron content. For example, in Fig. 184, the data include results from alloys that contain hydrogen in the range 10 to 17 ppm and in the range 2.5 to 6 ppm; however, no differences are apparent that are any larger than the usual experimental errors. The effects of other impurities are therefore neglected in plotting Fig. 184. The effect of iron on the constitution of this region is shown to this same degree of approximation by plotting Fig. 185. This figure gives the constitution determined with two other earlier batches of zirconium

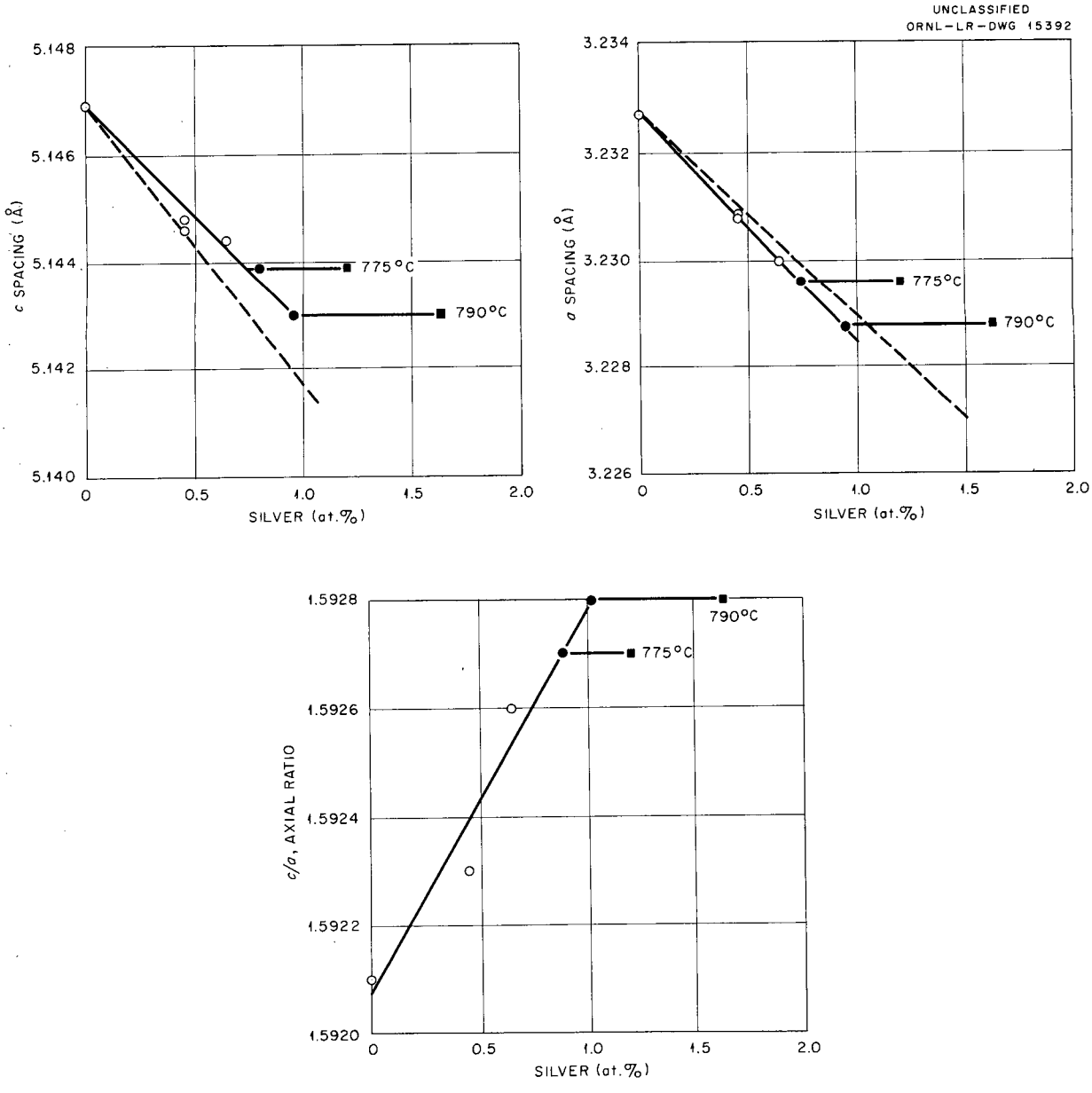

Fig. 183. Lattice Spacings of the Alpha-Phase Region of the Silver-Zirconium System.

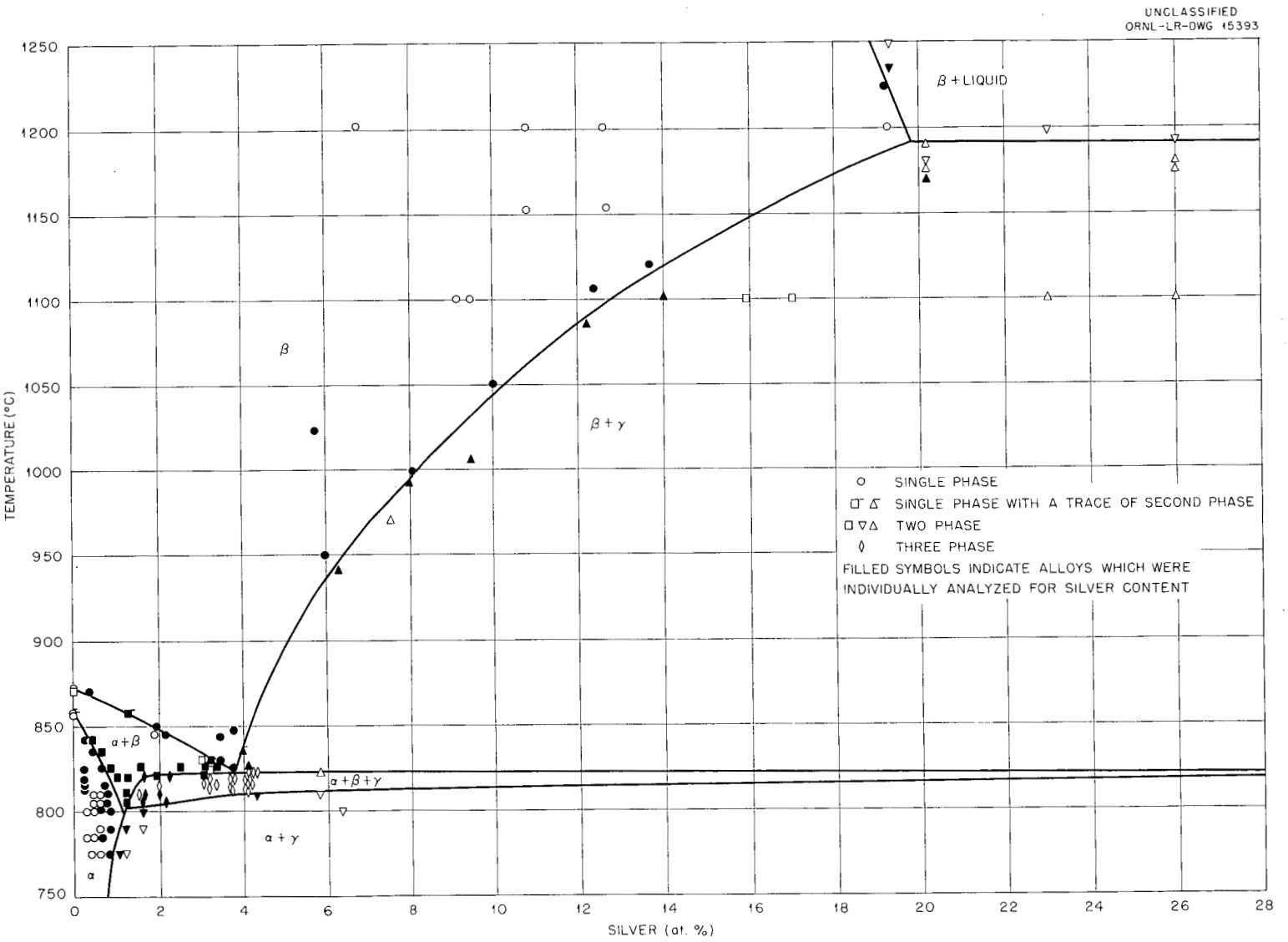

Fig. 184. The Zirconium-Rich Part of the Silver-Zirconium System – Alloys Contain 21 to 86 ppm Iron.

TABLE 74. NEUTRON-ACTIVATION ANALYSIS FOR IMPURITIES IN ZIRCONIUM-SILVER ALLOYS

Series	Period of Preparation	Analysis No.	Amount (ppm)					
			Cu	Fe	Mo	Ni	Si	W
S	1953	318–319	20	233	10	11	31	
E1	1953	211–251	38	430	17			
		406	30	280	<0.5	<1.5	10	42
GWC	1953	315	<1	55	14	<10	63	
E2	1954	405	10	54	34	<1.5	17	1.3
E3	1954	404	6	88	<0.5	<1.5	38	2.2
E4	1955	396	2.3	86	<0.2		2.2	15
		581–582	<3	24–31	<1	11–20		≦2
		548–551	<3	21–55	<1			≦2

TABLE 75. VACUUM-FUSION ANALYSIS FOR HYDROGEN IN ZIRCONIUM-SILVER ALLOYS

Series	Period of Preparation	Analysis No.	Amount (ppm)
S, E, E1	1953	210	28
		403	15
E2, E3	1954	402	17
		401	10
E4	1955	579–580	6
		397–398	2.5

(E1 and S series) which had iron contents in the range 280 to 430 ppm.

A comparison of Fig. 185 with Fig. 184 shows that the phase boundaries of the alpha phase occur at lower silver compositions in the alloys containing higher amounts of iron. This important effect of iron upon the alpha phase of zirconium is supported by zone-refining experiments, in which the removal of iron is closely related to the variation of the $\alpha/(\alpha + \beta)$ boundary of nearly pure zirconium, and by the zirconium-iron phase diagram where the maximum solid solubility of the alpha phase is approximately 200 ppm iron. A comparison of the phase boundaries of the beta phase in Figs. 184 and 185 shows that this region is not appreciably affected by the variation in iron content and that the $\beta/(\alpha + \beta)$ and $\beta/(\beta + \gamma)$ boundaries can be plotted as the same curves in both figures.

Both Fig. 184 and Fig. 185 are characterized by the presence of an $(\alpha + \beta + \gamma)$ region in place of the eutectoid horizontal which would be expected in binary equilibrium.

The $(\alpha + \beta + \gamma)$ region may be examined by considering the proportion of the alpha, beta, and gamma phases in an alloy of constant silver content as the temperature is varied throughout this region. This is shown by the microstructures of an alloy containing 2.1 at. % silver (Fig. 186). The proportion of beta phase increases very slowly as the temperature increases in the lower-temperature portion of the $(\alpha + \beta + \gamma)$ region and then rapidly increases near the upper-temperature portion. If the three-phase effect is a result simply of ternary Zr-Ag-Fe equilibrium, this behavior implies that the boundary of the $(\alpha + \gamma)$ region in a ternary section of this diagram at 2.1% Ag is nearly parallel to the temperature axis. Thus, further reductions in the iron content of the alloys of Fig. 184 would raise the lower boundary of the region rapidly, and the present upper boundary of this region would give the closest approximation to the binary eutectoid temperature.

The above interpretation of the $(\alpha + \beta + \gamma)$ region simply in terms of iron content is not entirely reasonable for the lower iron-content alloys. In these alloys, the carbon, oxygen, silicon, and hydrogen impurities should be of almost equal importance as a source of deviation from the true binary diagram. It is intended to determine the effects of these other impurities by investigating other zirconium-alloy systems. Zone-refined zirconium with a low content of eutectoid-type impurities and with less

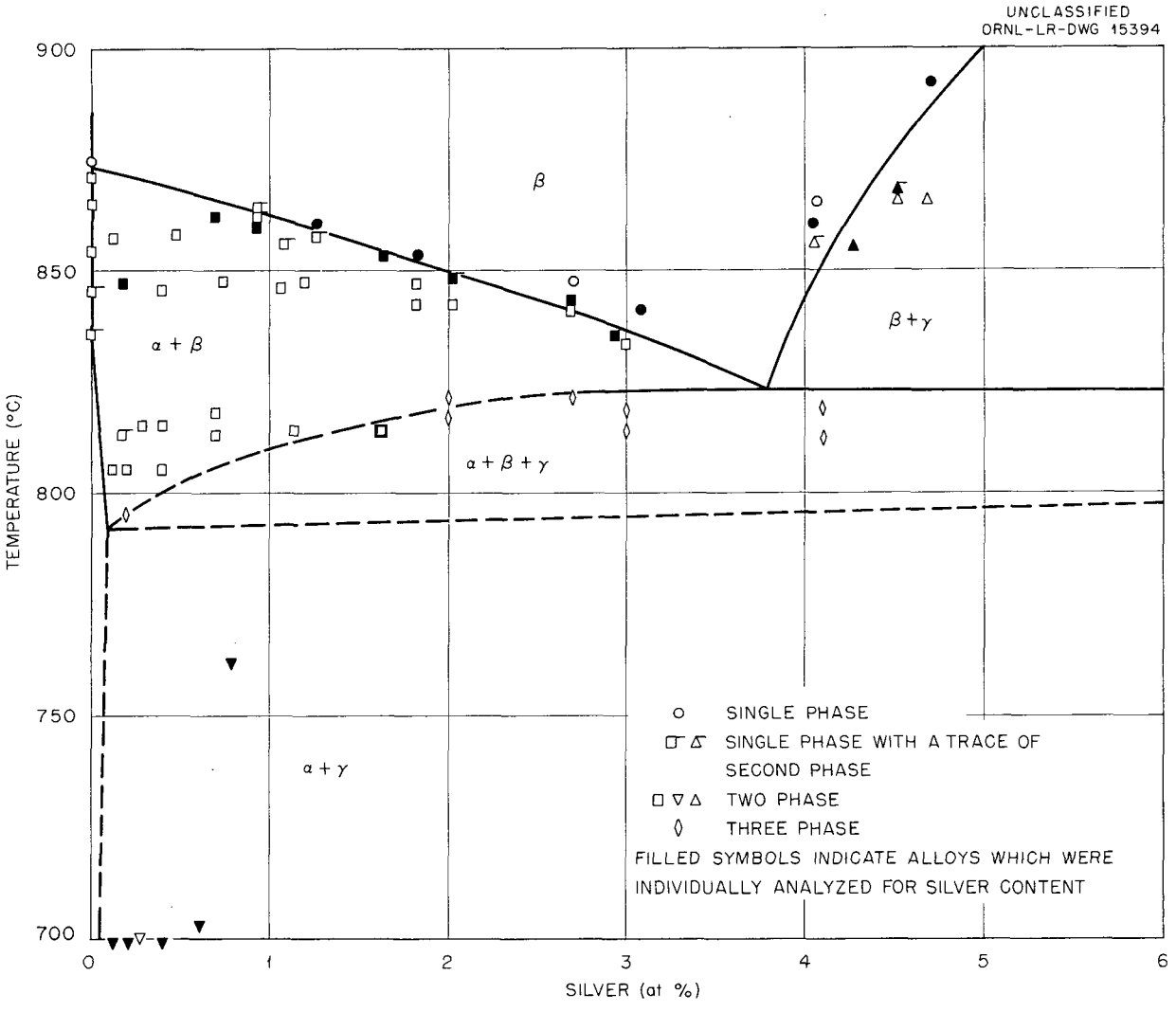

Fig. 185. The Eutectoid Region of the Silver-Zirconium System – Alloys Contain 230 to 430 ppm Iron.

than 3 ppm hydrogen will be used, and it should be possible to determine how the impurities which remain after this purification affect the phase diagram.

The $\beta/(\beta + \gamma)$ boundary was one of the first features of the silver-zirconium system to be investigated, and there is some question as to the accuracy of this boundary in view of the significant effects of minor impurities in the alpha region. A new temperature bracket across the phase boundary at 6 at. % silver was determined with a new alloy containing less iron (20–30 ppm, as contrasted to 50–90 ppm), less hydrogen (6 ppm, in contrast to 30 ppm), and of lower hardness (235 VPN, compared with 263 VPN) than the earlier alloys. This result, as shown by the microstructures of Fig. 187 and by the phase diagram of Fig. 184, is in good agreement with the earlier results and supports the viewpoint that the beta phase is much less sensitive to impurities than the alpha phase. The investigation of the $\beta/(\beta + \gamma)$ boundary, with the use of improved alloys, will be continued in the composition range 13 to 20 at. % silver.

The temperature and nature of formation of the gamma (Zr_2AG) phase has been investigated by incipient-melting experiments with alloys containing 23 and 26 at. % Ag in the $(\beta + \gamma)$ region. Earlier work had shown that the combination of an inner zirconium protective foil and an outer molybdenum protective foil did not give satisfactory protection

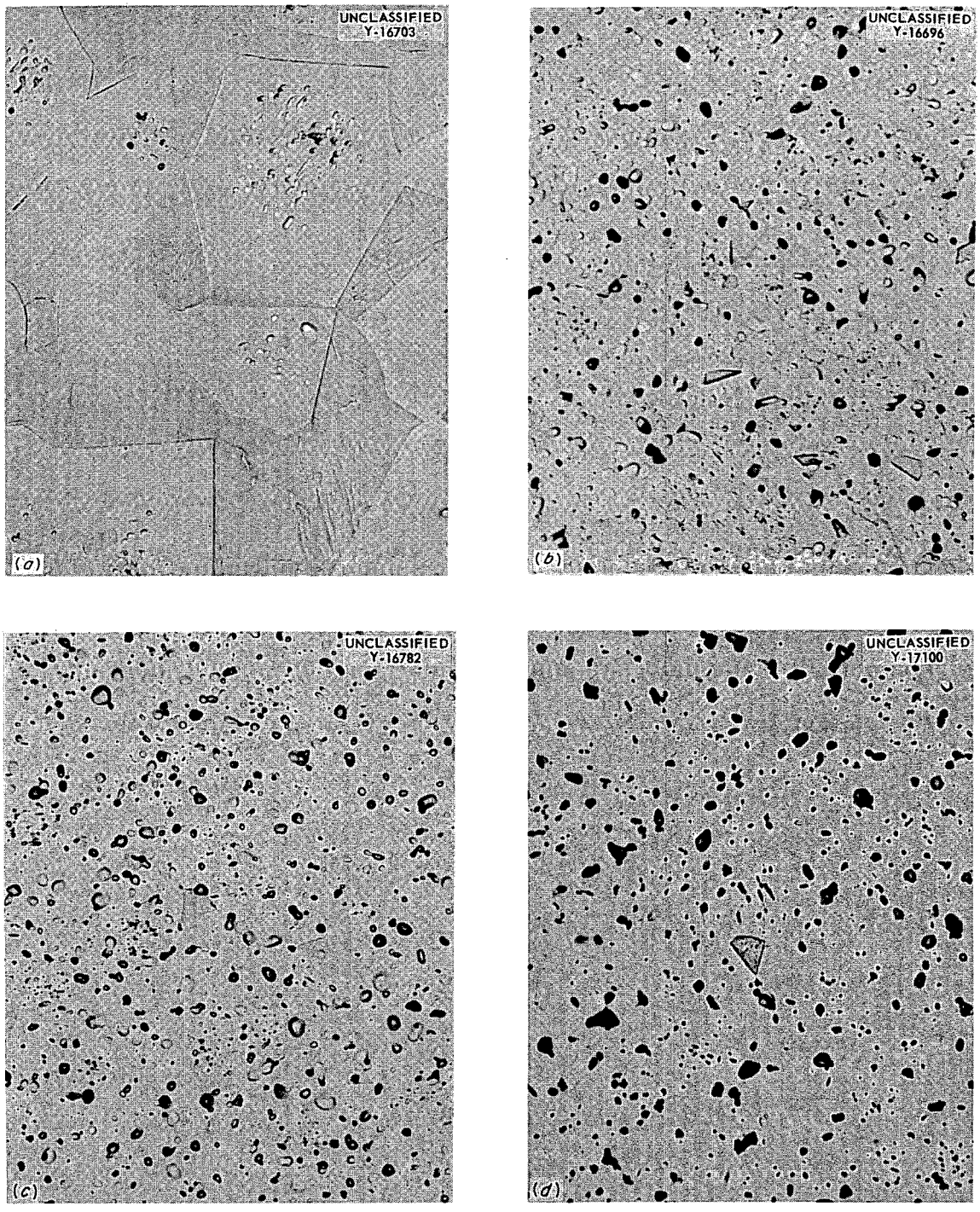

Fig. 186. Three-Phase Microstructures of Alloy Containing 2.1 at.% Silver. (*a*) Annealed 25 days at 820.1°C. Etchant: 30 parts HNO_3, 50 parts H_2O, 10 parts HCl, and 5 parts HF. 750X. (*b*) Annealed 24 days at 815.0°C. Etchant: 30 parts HNO_3, 50 parts H_2O, 10 parts HCl, and 5 parts HF. 500X. (*c*) Annealed 25 days at 809.8°C. Etchant: 30 parts HNO_3, 50 parts H_2O, 10 parts HCl, and 5 parts HF. 500X. (*d*) Annealed 29 days at 805.3°C. Etchant: 50 parts H_2O, 50 parts HNO_3, and 3 parts HF. 750X. The gradual change with temperature in the amount of beta phase in the lower portion of the ($\alpha + \beta + \gamma$) region is illustrated. Reduced 19.5%.

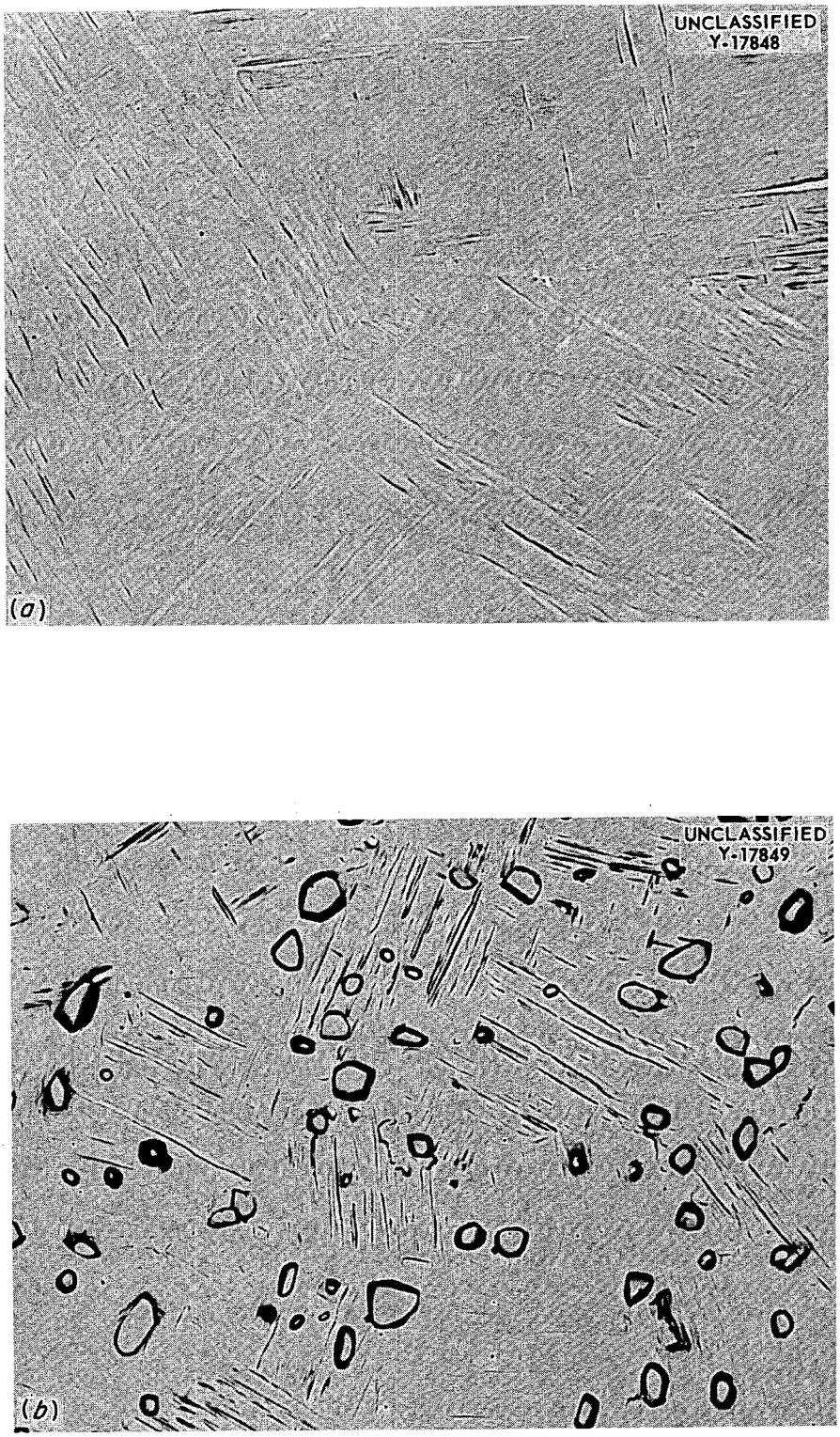

Fig. 187. A Recent $\beta/(\beta + \gamma)$ Phase-Boundary Bracket at 6 at.% Ag. (*a*) Transformed beta phase of zirconium alloy containing 5.9 at.% silver annealed for 15 days at 950 ± 0.6°C. 500X. (*b*) Zr_2Ag grains in a matrix of transformed beta phase of a zirconium alloy containing 6.3 at.% silver annealed for 9 days at 839 ± 4°C. 500X.

to the surface of the specimen. The use of an inner zirconium foil and an outer tantalum foil was more satisfactory, but the surface of the specimen still melted before the remainder of the alloy. The temperature at which incipient melting of the surface gamma phase took place in the 29.5 to 30.5 at. % silver alloys was 1175 ± 5°C. The technique next adopted consisted of reducing the silver content of the surface of the specimen by prolonged high-temperature evacuation so that the melting could be observed in the interior of the sample, well away from the zirconium-rich surface layer. This method worked satisfactorily for the determination of the melting temperature of the 19.3 at. % silver alloy; but with the 20.3 at. % silver alloy, a discrepancy occurred in that the gamma phase of the 1180°C specimen melted, whereas no melting was observed in the 1190°C specimen. Close examination of the 1180°C specimen showed that most of the melting occurred along an edge where the depleted surface layer was absent, although several other small interior areas also melted. Since experimental errors due to contamination appear to depress the melting temperatures, the 1190° specimen was accepted as the more reliable, and the peritectic temperature was placed above 1190°C.

Results from the recent investigation of the alloys containing 23 and 26 at. % silver agree with this interpretation, since the gamma phase of the 23 at. % silver alloy was completely molten at 1198°C and since the gamma phase of the 26 at. % silver alloy showed incipient melting at 1193°C, but no melting whatsoever occurred at 1180°C. The microstructure of a chilled-liquid region of the 23 at. % silver is shown in Fig. 188. The complicattng feature of this microstructure is the fine structure, which resembles a eutectoid or eutectic structure, on the edges of the large beta-phase grains. Kemper[17] may have adopted this type of structure in his interpretation, since his diagram shows a eutectic between the beta and Zr_2Ag phases. The interpretation taken here is that this fine structure is a precipitation phenomenon which occurs during cooling of the beta phase and which is similar to the precipitation occurring in commercial Mg-Al-Zr casting alloys.

This precipitation hypothesis is needed in order to reconcile the observed microstructure with the peritectic formation of Zr_2Ag. Several facts point to evidence for the peritectic formation of Zr_2Ag. Thus, alloys containing between 25 and 36 at. % silver are always of three-phase structure ($\beta + \gamma + \delta$) which is arranged in such a manner that the beta appears as primary crystals and is separated from the ($\gamma + \delta$) eutectic (more commonly a divorced eutectic) by a wall of gamma phase. Furthermore, incipient melting of alloys from 18.5 to 30.5 at. % silver has always produced chilled liquid of ($\gamma + \delta$) eutectic. This eutectic is shown between the beta grains in Fig. 188. Finally, when a ($\beta + \gamma$) specimen is only partly melted, the melting occurs in the gamma grains, and occasionally this melted gamma phase may be seen to penetrate the grain boundaries of the beta phase in a typical liquid

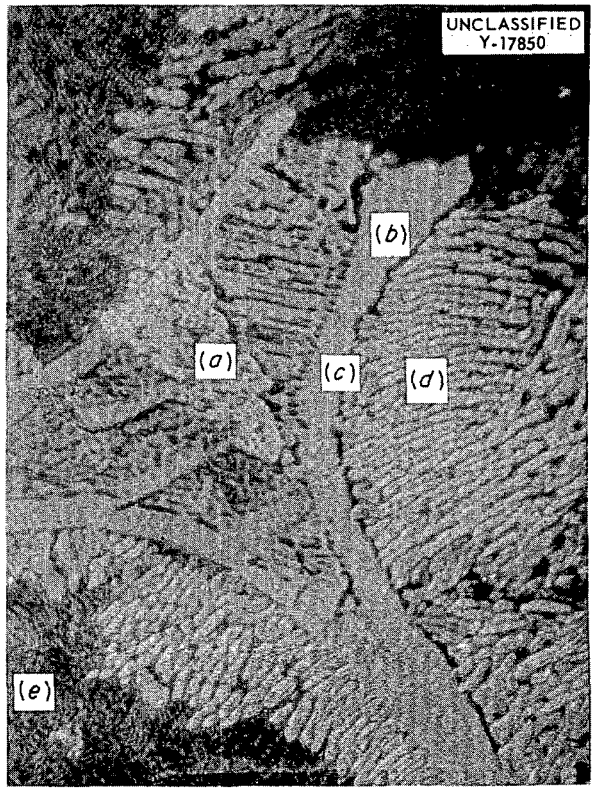

Fig. 188. Zirconium Alloy Containing 23 at.% Silver, Annealed in the (β + Liquid) Region for 30 min at 1198°C. (*a*) Eutectic, ($\gamma + \delta$). (*b*) Peritectically formed gamma. (*c*) Interface between chilled liquid and beta. (*d*) Precipitation structure in beta. (*e*) Transformed beta. Unetched. Polarized light. 2000X. Reduced 10%.

[17] R. S. Kemper, *The Zirconium-Silver System*, M.S. Thesis, Oregon State College, 1952.

manner. Further clarification of this question would be possible if a homogeneous gamma alloy could be prepared and melted, but problems connected with the narrow region in which the Zr_2Ag exists and with the difficulty of homogeneizing the cast three-phase structures have prevented the preparation of such a specimen.

PRELIMINARY INVESTIGATION OF THE LATTICE SPACINGS OF THE ALPHA PHASE IN THE INDIUM-ZIRCONIUM SYSTEM

J. O. Betterton, Jr. R. Steele

The lattice spacings of a series of polycrystalline indium-zirconium alloys were determined with an x-ray spectrometer in order to obtain preliminary curves of the spacings and to determine the c/a variation with indium content. It was realized that this technique had low accuracy, but the method is convenient when a series of polished specimens is already available from microscopical work. The grain size of the alloys was large so that a distortion of the etched surface by grinding with 600-grit emery paper was required in order to produce satisfactory patterns.

The microscopical constitutions of the alloys have been reported previously. These alloys were prepared from iodide zirconium and were heat-treated for 20 to 30 days in the vicinity of 802°C. The change from one-phase to two-phase constitutions occurs between 7.2 and 7.5 at. % indium. The Vickers hardnesses of these alloys are given in Fig. 189 in order to provide an approximate check on the consistency of the impurity content of the specimens.

The lattice spacings are plotted in Fig. 190, and it is apparent from the figure that the accuracy of these data is only about 1 part in 1,000, and one point at 3 at. % indium deviates by 1 part in 500 for the c spacing measurement. Similar accuracy is indicated when the results for pure zirconium are compared with Debye-Sherrer values (a = 3.2330 Å, c = 5.1485 Å, and c/a = 1.5924) for iodide-zirconium batch No. 3 filed in air and annealed at 400°C. The relatively large experimental error is also indicated by the failure of the lattice-spacing data to indicate with any degree of accuracy the occurrence of the $\alpha/(\alpha + \gamma)$ phase boundary. On the other hand, the general effects of indium, contraction of the a spacings and expansion of the c spacings, can be seen from the curves. Further, the expansion of the axial ratio would seem to be established.

That some irregular effect exists in the lattice spacings of the alpha phase of indium-zirconium may be seen by plotting Vegard's law. This is shown by the dotted lines on Fig. 190, where it has been assumed that pure indium may be represented by a hexagonal structure with the same c/a as pure

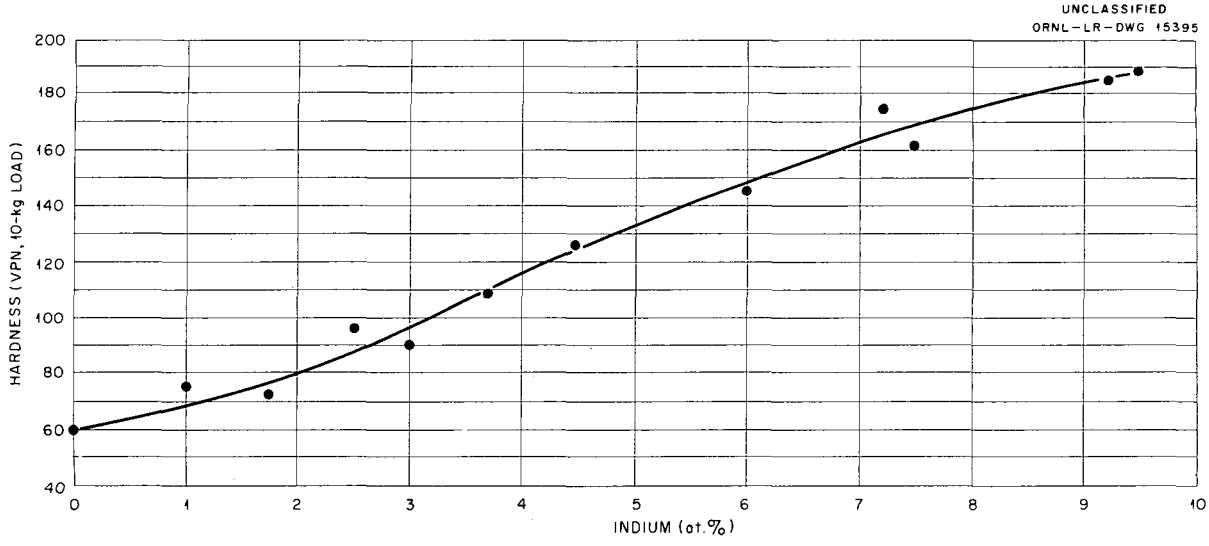

Fig. 189. Vickers Hardnesses of Indium-Zirconium Alloys Annealed at 802°C.

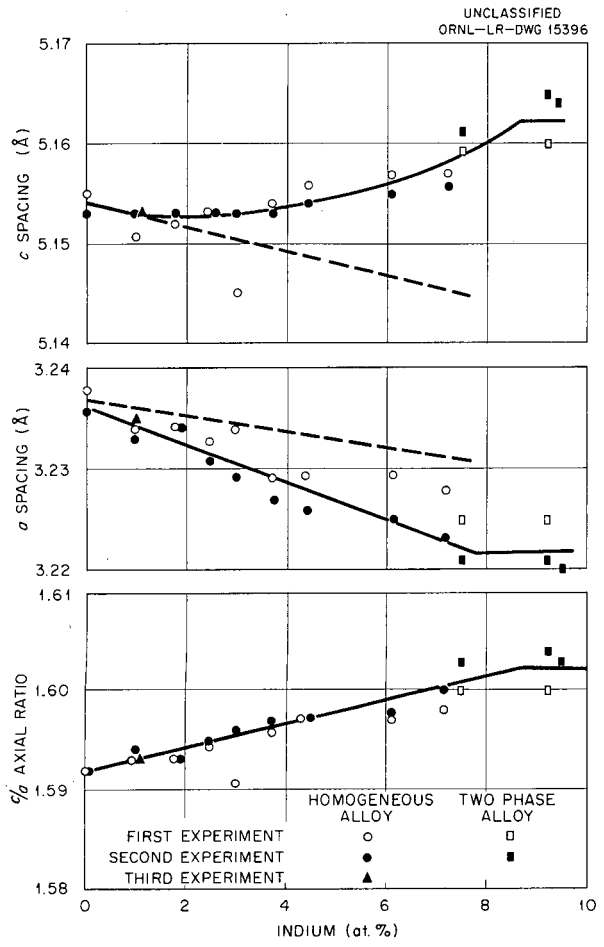

Fig. 190. Preliminary Lattice Spacings of the Alpha Phase of the Indium-Zirconium System.

zirconium but with a smaller atomic volume. The atomic volume actually used was obtained by extrapolation of data from copper, silver, and gold solid solutions containing indium,[18] since pure indium is generally considered to be incompletely ionized in the element structure. Both *a* and *c* curves deviate in opposite directions from the dotted lines; and, as discussed later, this effect may be related to an electron overlap across the *c* faces of the Brillouin zone.

DEPENDENCE OF THE AXIAL RATIO OF THE ALPHA PHASE OF ZIRCONIUM ALLOYS UPON ELECTRON CONCENTRATION

J. O. Betterton, Jr.

Jones[19] has shown that certain changes in the axial ratio of the hexagonal eta and epsilon phases in the copper-zinc system can be related to Fermi energy changes during alloying, providing the reasonable assumption is made that differences in the size of the ions and differences in the potential in which the electron exists during alloying, affect only the volume of the unit cell. The shearing strains or deviations from the ideal axial ratio are then functions only of the Fermi energy. The assumption is reasonable in systems where experiment has shown the axial ratios to depend upon electron concentration, rather than upon atomic concentration. This has been shown to be true to a good degree of approximation for dilute magnesium alloys,[20] and recently Denney[21] has contended that dilute alloys of alpha titanium are of this type.

In order to test the electron-concentration relationship in alpha-zirconium alloys, the preliminary axial ratios determined for the zirconium-indium system were compared to the axial ratios determined for the zirconium-tin system by Speich and Kulin.[22] The electron concentrations were calculated by using a valency of two for zirconium, three for indium, and four for tin. The result is shown in Fig. 191; and considering the experimental accuracy of the data, a fair agreement has been obtained.

Denney[21] has applied a modified form of the Jones theory to the lattice spacings and axial ratios of the hexagonal alpha phase in the Ti-Al, Ti-Ga, and Ti-Ag systems. In this treatment, the results are best explained by assuming that titanium is approximately divalent; and in this case the complication occurs, when the axial ratios are plotted against electron concentration, that both an increase and a decrease of electrons expand the axial ratio of pure titanium. Denney explained this on the basis of Brillouin-zone considerations in which he concludes that, if pure titanium had approximately 1.5 valency electrons per atom, the

---

[18] H. J. Axon and W. Hume-Rothery, *Proc. Roy. Soc. (London)* **193A**, 1 (1948).

[19] H. Jones, *Proc. Roy. Soc. (London)* **147A**, 396 (1934).

[20] H. Jones, *Phil. Mag.* **41**, 663 (1950).

[21] J. M. Denney, *A Study of Electron Effects in Solid Solution Alloys of Titanium. Sixth Technical Report to the Office of Naval Research. California Institute of Technology* (Jan. 1955).

[22] G. R. Speich and S. A. Kulin, "The Solid Solubility of Tin in Alpha Zirconium," *Zirconium and Zirconium Alloys*, p. 197, Am. Soc. Metals, Cleveland, Ohio, 1953.

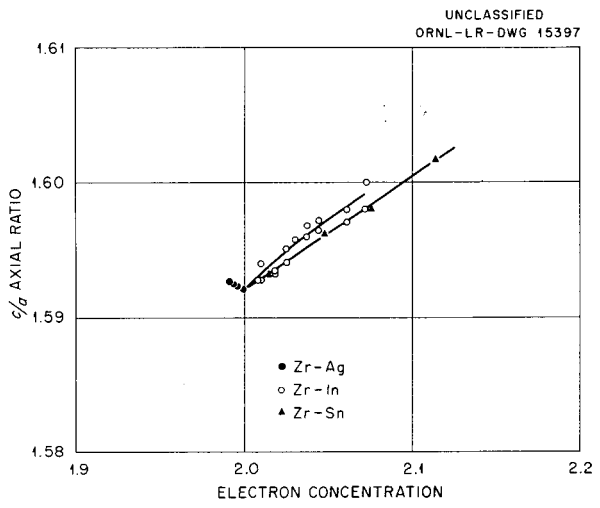

Fig. 191. Variation of the Axial Ratio of Alpha Zirconium in the Systems Zr-Ag, Zr-In, and Zr-Sn at Room Temperature.

Fermi surface of the pure metal would be in a critical condition, that is, just approaching tangency of the (00.1) faces of the first energy zone. The expansion of the axial ratio with increased electron concentration is, thus, due to an increased number of electrons overlapping the (00.1) faces; whereas the expansion with reduced electron concentration is due to a reduced number of electrons overlapping the (10.0) faces of the first energy zone.

Since the data on the axial ratios of alpha-titanium alloys can be plotted equally well in terms of electron concentration by using a valency of four for titanium, three for aluminum and gallium, and one for silver, it is desirable to test the correlation for a tetravalent solute. This has been done in Fig. 192, where the axial ratios of the alpha phase of the titanium-tin system[23] have been plotted by

[23]H. W. Worner, *J. Inst. Metals* 81, 521 (1953).

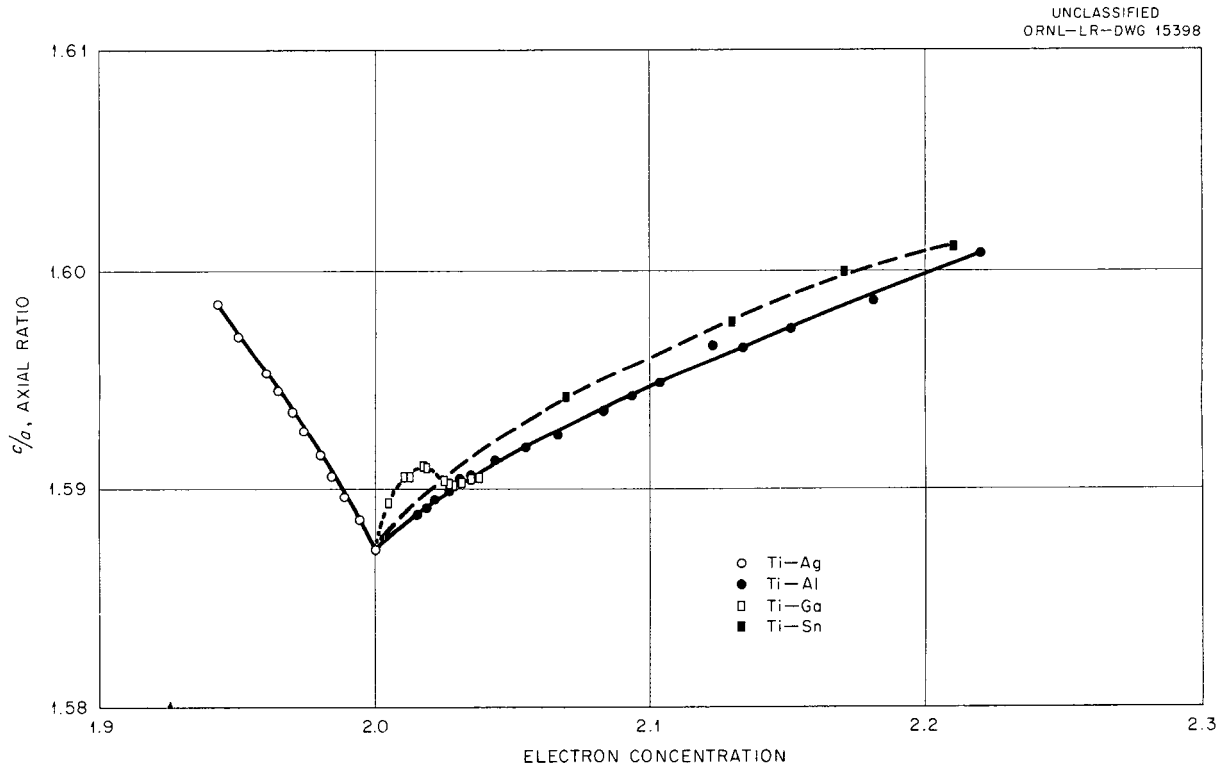

Fig. 192. Variation of the Axial Ratio of Alpha Titanium in the Systems Ti-Ag, Ti-Al, Ti-Ga, and Ti-Sn.

using the data determined by Denney. A valency of two for titanium was used, and the electron concentrations have been calculated. The agreement with an electron-concentration dependence is within the probable experimental accuracy of the titanium-tin data.

When the axial ratios determined for the zirconium-silver alpha phase are added to Fig. 191, the closely similar behavior of the axial ratios of zirconium and titanium alloys may be seen by comparison of Fig. 191 and Fig. 192. The agreement suggests that the energy-zone effects may be similar in titanium and zirconium and that a (001) face overlap may occur during the alloying of both metals. Experiments on the variations of electronic specific heat in these alloy systems will be a useful test of the above hypothesis.

ZONE REFINING OF ZIRCONIUM

G. D. Kneip, Jr. J. O. Betterton, Jr.
R. J. Bohnhoff

The impurities contained in zirconium made by the iodide-decomposition process are sufficient to cause the α/β transformation to take place over a considerable temperature range. For this reason it is unsuitable for use as the base material in studies of the effects of solutes on the α/β transformation. The trace amounts of impurities, such as iron and nickel, present in iodide zirconium have a pronounced effect on the temperature width of the transition region and, hence, are particularly injurious. Floating-zone refining[24] was chosen as a likely means of attaining the desired purification, since the chemical affinity of zirconium for other elements dictates the use of a purification process which can be carried out in an inert atmosphere and which introduces no crucible contamination. The theory of zone refining has been extended to the case of a finite-length bar and to a consideration of the limits imposed upon the calculations by the physical nature of the systems involved. The efficiency of purification from eutectoid-forming impurities has been evaluated qualitatively by annealing refined ingots slightly below the pure-zirconium transition temperature and observing the distribution of the high-temperature beta phase. The redistribution of iron and nickel has also been established by activation analyses.

[24]P. H. Keck and M. J. E. Golay, *Phys. Rev.* **89**, 1297 (1953).

Zone-Refining Theory for Finite-Length Passes

The zone-refining process[25] is based on the difference in solubility of an impurity in the liquid and solid phases. For impurities which lower the melting point and which are thus more soluble in the liquid phase, the first material to freeze as the liquid zone is put into motion contains less impurities than the liquid and, hence, is purer than the original solid. As the movement of the liquid zone is continued, the concentration of impurities in the liquid zone increases, and the composition of the material freezing behind the zone gradually returns toward its initial value. When the motion is stopped and the liquid is allowed to freeze, a region has been developed which has a higher impurity content than the original material. On the other hand, impurities which raise the melting point of the solute and, thus, are more soluble in the solid phase migrate in the opposite direction, since the material freezing behind the liquid zone has a higher impurity concentration than the liquid. In this case, the purified region is found in the last zone to solidify. Further purification can be attained by making successive passes over the same ingot. Analytical expressions for the impurity distribution in a semi-infinite bar after a single pass have been presented by Pfann[25] and for multiple passes by Reiss[26] and Lord.[27] Of these, the expression developed by Lord (Eq. 1) is perhaps the most useful, since it is exact and utilizes ordinary numerical computation procedures. The expression

$$(1)\quad C_n(a) = \left[\int_0^a C_{n-1}\cdot(a+1)\cdot e^{ka}\,da + \int_0^1 C_{n-1}\cdot(a)da\right] ke^{-ka}\,,\quad 0 \leqq a \leqq N-1\,;$$

is based on the assumptions that there is no diffusion in the solid phase, that the impurity concentration is uniform throughout the liquid region, that the ratio of solid-to-liquid solubilities is constant for the concentrations involved, and that the

[25]W. G. Pfann, *Trans. Am. Inst. Mining Met. Engrs.* **194**, 747 (1952).

[26]H. Reiss, *Trans. Am. Inst. Mining Met. Engrs.* **200**, 1053 (1954).

[27]N. W. Lord, *Trans. Am. Inst. Mining Met. Engrs.* **197**, 1531 (1953).

zone length does not vary. In this expression, $C_n(a)$ is the concentration of the impurity in the solid after n passes at a distance a measured in zone lengths from the starting point of the passes, and k is the distribution coefficient or the ratio of solid-to-liquid solubilities. It is valid for the region $0 \leqq a \leqq N - 1$, where N is the total length of the pass measured in zone lengths, since the final zone is excluded because of the changing zone length during its solidification.

The equation can be integrated pass by pass, starting with a uniform concentration prior to the first pass. In this case the integrated expressions are only valid over the region $0 \leqq a \leqq N - n$, since with successive passes the effects of the excluded final zone region are reflected back one zone length for each pass on account of the $C_{n-1}(a + 1)$ term in the equation.

For the region $N - n \leqq a \leqq N - 1$ this expression can be written

$$(2) \quad C_n(a) = C_n(N - n)e^{-k[a-(N-n)]} + ke^{-ka} \int_{N-n}^{a} C_{n-1}\cdot(a + 1)\cdot e^{ka}\, da \ , \qquad N - n \leqq a \leqq N - 1 \ ,$$

where $C_{n-1}(a + 1)$ is a complicated expression dependent upon the solidification of the final zone and its back reflection into the bar.

For floating-zone refining, the final zone is assumed to solidify from both ends, according to the normal solidification process described by Pfann[25] and others.[28,29,30] The expressions for the impurity concentration in the final zone are then

$$(3) \quad C_n(a) = C_n(N - 1)\left\{2\left[\left(N - \frac{1}{2}\right) - a\right]\right\}^{k-1} \ , \qquad N - 1 \leqq a \leqq \left(N - \frac{1}{2}\right) - A \ ,$$

$$(4) \quad C_n(a) = C_n(N - 1)\left\{2\left[a - \left(N - \frac{1}{2}\right)\right]\right\}^{k-1} \ , \qquad \left(N - \frac{1}{2}\right) + A \leqq a \leqq N \ ,$$

and the impurity distribution is seen to be symmetrical about $a = N - 1/2$. For values of k less than one, the concentration rises rapidly from both ends of the zone toward infinity. This is plainly inconsistent with the densities of physical materials, or more specifically with the solid-solubility limits. The applicability of Eqs. 3 and 4 must accordingly be limited to that part of the range where k is constant and where the solubility limit is not exceeded in the solid phase, as indicated by the parameter A in the limits for expressions 3 and 4. In many systems in which a eutectic reaction takes place, k is approximately constant from the melting point to the eutectic temperature, and the value of the solid solubility at the eutectic temperature then determines the parameter A.

When the distribution coefficient is greater than one, similar limitations on the maximum concentration apply to the region at the beginning of the bar. In this case, in the final zone, the parameter A has a value of zero, and expressions 3 and 4 are valid over the whole region.

As will be shown later, iron is one of the elements which has a very dominant effect on the temperature interval over which the allotropic transformation takes place in zirconium. For this reason, the ability of the zone-refining process to redistribute iron is of particular interest.

Figure 193 shows the iron distribution for a zone-refined ingot, as computed from Eqs. 1–4 and shows the distribution coefficient taken from the zirconium-iron phase diagram.[31] The concentration in the final zone rises rapidly from both ends of the zone until the composition of the solid reaches the maximum solid solubility, at which time the liquid has attained the eutectic composition and the center section of the zone has frozen as material of the eutectic composition. This rapid rise in concentration in the final zone is then reflected back one zone length in the succeeding pass. In the third pass both the peak in the final zone and the step in the next to the last zone of the second pass are reflected back into the purified region one zone length farther. In the initial region the shape of the curve is established by two parameters, the zone length and the distribution coefficient. The zone length establishes the rapidity with which the impurity concentration returns to its initial value.

[28] G. H. Gulliver, *Metallic Alloys* (Appendix) Charles Griffin, London, 1922.

[29] E. Scheuer, *Z. Metallkunde* **23**, 237 (1931).

[30] A. Hayes and J. Chipman, *Trans. Am. Inst. Mining Met. Engrs.* **135**, 85 (1939).

[31] E. T. Hayes, A. H. Roberson, and W. L. O'Brien, *Trans. Am. Soc. Metals* **43**, 888 (1951).

Hence, for purification processes which are limited by experimental conditions to a small number of passes and, thus, where the back-reflection effect in a finite-length pass does not affect the initial region, a long zone length is more effective in transporting impurities than a short one. The distribution coefficient establishes the purification which is attained at the starting point for $k < 1$, or establishes the increase of impurity for $k > 1$.

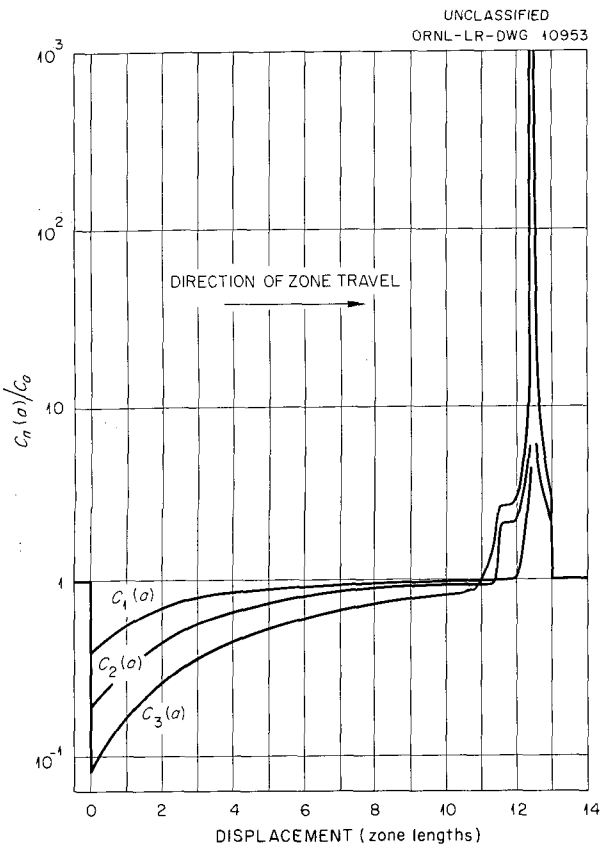

Fig. 193. Computed Distribution Curves for Iron in Zirconium After Passes of Finite Length. Maximum solid solubility 5.5%; Co = 45 ppm; k = 0.35; N = 13.

Experimental Method

In order to ascertain the degree of purification that is attainable by the floating-zone refining process, sufficient material was prepared (1) for chemical analyses for trace amounts of impurities and (2) in order that a metallographic study could be made of the temperature range over which the α/β transformation takes place. The details of the experimental apparatus have already been described.[32]

All the zirconium used for these experiments was prepared for a grade 1 iodide-zirconium crystal bar by swaging. This material contained 99.95 wt % zirconium, and the analytical values for the various impurities are given in Table 76. The rods were annealed at various stages in the reduction. Steps taken to prevent contamination during annealing included: chemical cleaning, use of protective zirconium-foil wrappings, and outgassing at 10^{-6} mm Hg in quartz tubes at 1000°C. No change in Vickers hardness was found between the crystal bar and the annealed rods, indicating little contamination by oxygen, nitrogen, or carbon. In addition, the outgassing was sufficient to reduce the hydrogen content to less than 5 ppm.

Although small quantities of zirconium have been refined by the floating-zone technique, the extension of this method to larger amounts of material is

[32] G. D. Kneip, Jr., and J. O. Betterton, Jr., *Met. Semiann. Prog. Rep. Oct. 10, 1955*, ORNL-1988, p 165.

TABLE 76. IMPURITY CONTENT OF GRADE 1 IODIDE ZIRCONIUM

Type of Analysis	Impurities (ppm)						
	Titanium	Hafnium	Chromium	Iron	Nickel	Silicon	All Others
Spectrographic	80 ± 50	120 ± 40	2 ± 2	15 ± 15	11 ± 7	38 ± 37	<5
Activation		132	7	45 ± 8	4.0 ± 1.0	6 ± 4	<5
		Carbon	Oxygen		Hydrogen	Nitrogen	
Chemical		20–175	105–340		4–50		
Vacuum-fusion			50–250		4–50	30–45	

limited by the inherent instability of the liquid zone.

Preliminary experiments using a $\frac{3}{4}$-in.-dia rod resting on a water-cooled copper hearth have been performed in the apparatus shown schematically in Fig. 194. It was shown that a liquid zone of large size can be formed and moved by induction heating on such a hearth.

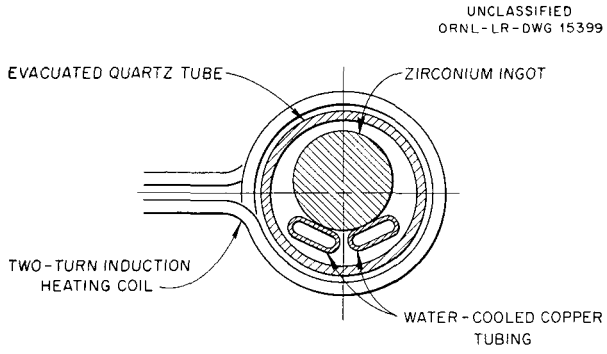

Fig. 194. Cross Section of Zone-Refining Apparatus.

Several experimental difficulties due to the large clearance necessary between the work and the heating coil were encountered, which must be overcome before actual zone refining of zirconium can be carried out in this fashion. The relatively large differences between the radii of the load and the work coil make efficient radio-frequency coupling difficult to attain. Thus, in order to put sufficient radio-frequency energy into a short length of the zirconium ingot, very high currents must be carried by the generator tank circuits and by the leads to the work coil which produce high I^2R losses in these parts.

Metallographic Evidence of Purification

Experiments with a number of lots of grade 1 iodide zirconium have indicated that the temperature intervals over which the alpha and beta phases coexist range from 16°C in the best lot to 70°C in the worst. The upper limit of this two-phase region is approximately constant at 873°C; while the lower limit varies from 800 to 857°C, suggesting the presence of eutectoid-forming impurities of limited solubility in alpha zirconium. If a zone-refined ingot is isothermally annealed slightly below the transformation temperature of the pure material and is rapidly cooled to room temperature, regions which are high in eutectoid-forming impurities will show that the alpha and beta phases[33] are distributed in proportion to the impurities. Accordingly, a zone-refined ingot was segmented and isothermally annealed for 100 hr at two temperatures in quartz capsules. The same precautions, as described previously, were taken to avoid contamination. A platinum–platinum + 10% rhodium thermocouple which had been calibrated at the melting points of aluminum, silver, and gold was used to measure the furnace temperature frequently during the annealing period. The temperature gradient over the specimens amounted to about ±0.3°C, and the variation in furnace temperature from time to time was ±0.2°C, so that the annealing temperatures reported are believed to be well within ±1°C. At the finish of the anneal, the specimens were quenched by breaking the quartz capsules under water.

Figure 195 shows the beta-phase distribution in a refined rod after isothermal annealing and indicates the concentration of the eutectoid-forming impurities in the final zone. The proportions of the alpha and beta phases were determined by the method of lineal analysis. If the impurity causing the broadening of the transition range is iron, then examination of the zirconium-iron phase diagram[31] will show that absence of the beta phase in the purified part of the rod after isothermal annealing at 860°C is an indication that the iron content is less than 30 ppm. The higher annealing temperature of 865°C provides increased sensitivity. In this case the homogeneous alpha region presumably contains less than 15 ppm iron, and the maximum beta region contains approximately 380 ppm iron. The hardness at various positions along the bar after annealing at 865°C is also shown in Fig. 195. The peak at the beginning of the pass is attributed to a concentration of oxygen and nitrogen which is more soluble in the solid than in the liquid phase and, thus, would be expected to move opposite to the direction of zone travel. The peak at the other end of the pass is assumed to be the result of the other impurities. Hardness measurements on two other rods show the same general trend but with increased scatter; and because of the uncertainty of hardness measurements on polycrystalline and

[33] The beta phase, of course, transforms martensitically to alpha prime during cooling, but the isothermal boundaries of the beta phase are easily recognized.

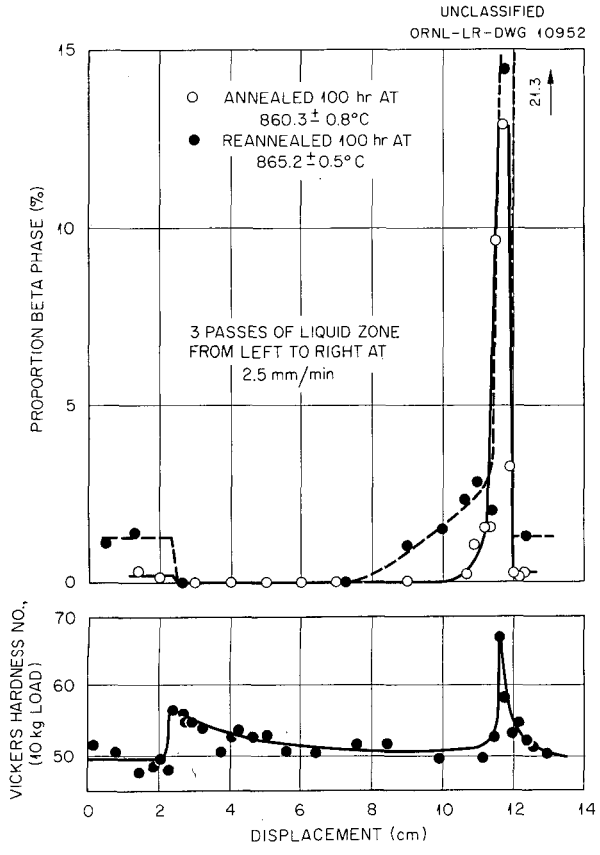

Fig. 195. Distribution of the Beta Phase and the Variation in Hardness for a Zone-Refined Zirconium Ingot After Isothermal-Annealing Treatments Near the Transition Temperature.

two phase metals, the results should be considered with caution. Since small amounts of oxygen and nitrogen markedly increase the hardness of zirconium, these data also indicate that very little contamination occurred during the 2 hr that a portion of the bar was molten.

The original material for these bars has a two-phase region extending from approximately 855 to 873°C, and after three passes of the molten zone the transformation range has been reduced to less than one-half of its original value, or from 865 to 873°C. This temperature interval for the transformation provides evidence supporting other experiments at ORNL which indicated that the allotropic transformation of zirconium takes place at 870 ± 3°C, instead of the lower value reported in the literature.

The actual microstructures observed after the 865°C anneal are shown in Fig. 196, and it can be appreciated that the iron content is essentially indicated by the amount of the beta phase. The unrefined ends of the bar contain about 1.2 vol % of the beta phase in the boundaries of the alpha grains, as shown in Fig. 196*a* and 196*f*. The interface between the upper end of the bar and the final zone is shown in Fig. 196*b*; and the center of the final zone, with a greatly increased amount of the high-temperature beta phase, is shown in Fig. 196*c*. The microphotographs, Fig. 196*d* and 196*e*, correspond to points approximately 2 cm apart in the purified region and show no traces of the high-temperature beta phase.

Activation Analyses of Purified Rods

The iron and nickel distributions in several zone-refined rods were determined by neutron-activation analyses in order to show that the above interpretation of the metallography is reasonable and, also, to provide an experimental test of the theory. Figure 197 shows the iron distribution after three passes of the molten zone. The analytical sample for each of these points was a segment, approximately 3 mm in length, of the refined ingot. In order to remove tool contamination, each specimen was chemically cleaned. After irradiation, each specimen was dissolved, and at least duplicate aliquots were taken for the analyses. The duplicate samples for the iron analyses all agreed to within ±3 ppm, except for the high values in the final zone for which the agreement was about ±13 ppm. The experimental points are in substantial agreement with the values predicted by the theory of zone refining; and, thus, in this system at least, the theoretical assumptions are experimentally realized. For the computation of the theoretical curve, a distribution coefficient of 0.35, as obtained from the zirconium-iron phase diagram,[31] and a zone length of 8 mm, as observed experimentally, were used. The experimental zone length is difficult to estimate, since there is no color distinction between the liquid and solid metals. Furthermore, for stable zones, the liquid region is very nearly cylindrical in shape, and, hence, its boundaries are not clearly defined. The agreement of the experimental points with the theoretical curve, however, indicates that the 8-mm length is approximately correct.

UNCLASSIFIED
Y-17140

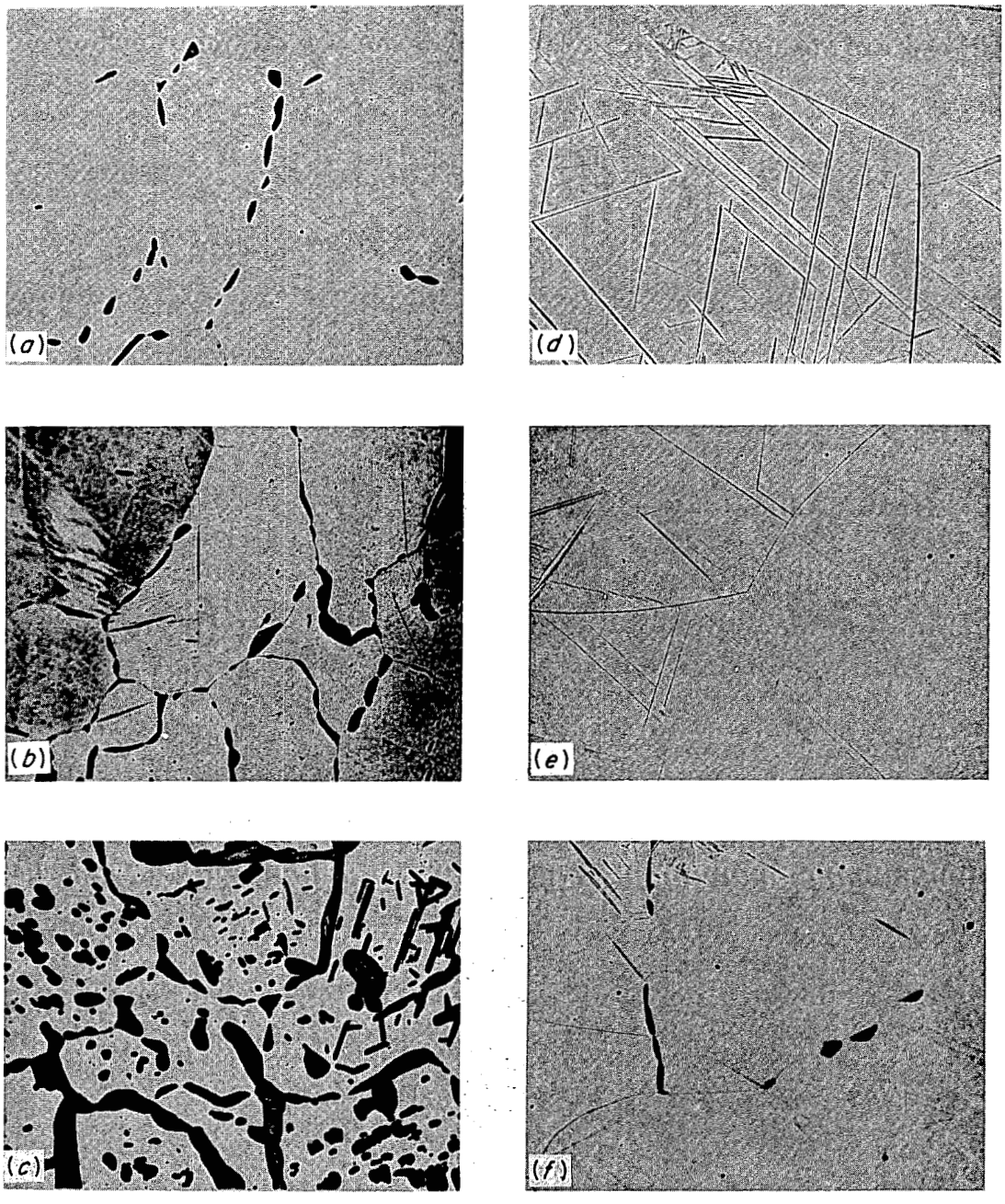

Fig. 196. Microstructures of Zone-Refined Zirconium After Isothermal Annealing at 865.2 ± 0.5°C for 100 hr. (*a*) Unrefined end of bar. (*b*) Interface between upper end of bar and final zone. (*c*) Center of final zone. (*d* and *e*) Specimens from purified region; taken from sites approximately 2 cm apart. (*f*) Unrefined end of bar. Etchant: 57% lactic acid, 40% nitric acid, 3% hydrofluoric acid. 50X.

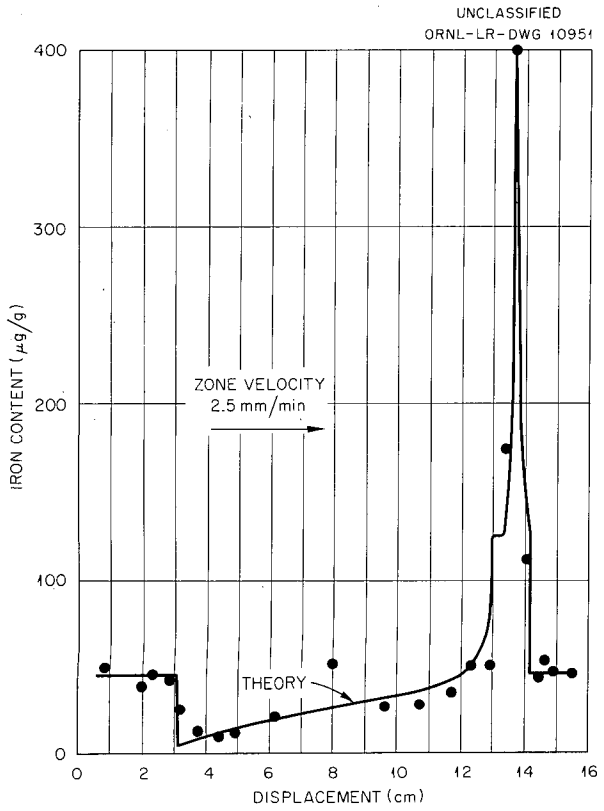

Fig. 197. Iron Distribution After Three Passes of the Liquid Zone.

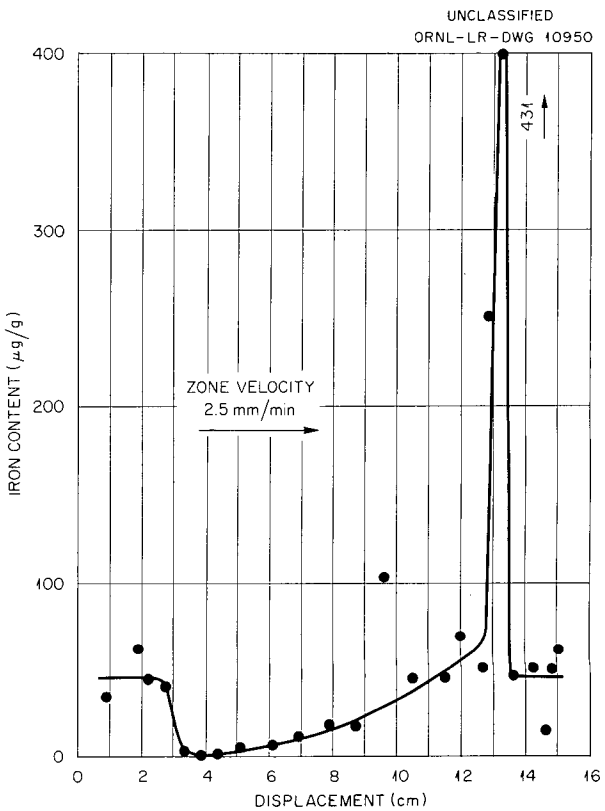

Fig. 198. Iron Distribution After Six Passes of the Liquid Zone.

The maximum and minimum iron contents, as determined by activation analysis, agree remarkably well with the estimates from isothermal-annealing experiments. This quantitative agreement indicates the marked effect of iron on the allotropic transformation of zirconium. In this zirconium, other impurities, such as carbon, are undoubtedly redistributed during the zone-refining process. However, they are either present in small quantities, or their effects on the allotropic transformation are small compared to the effect of iron.

In Fig. 198 the iron distribution after six passes of the molten zone is shown; the curve is similar in shape to the previous curve, except that it has a lower minimum value, as predicted by the theory. In each of the iron distribution curves, one of the experimental points does not agree with the rest of the data. These two values are higher than would be expected and may have been caused by a momentary solidification of the liquid zone, or they may be the result of tool contamination of the analytical samples which was not removed by the chemical-cleaning treatment. The latter explanation is favored, since no scatter of this nature was observed in the nickel data.

Nickel is another example of a eutectoid-forming impurity and is similar to iron in its limited solubility in alpha zirconium.[34] Since it is a relatively common impurity in zirconium, the ability of the zone-refining process to redistribute nickel is of interest. As shown in Fig. 199, nickel is distributed in much the same way as iron. After six passes of the molten zone, the minimum value of nickel was about three-quarters of a part per million, with an appreciable portion of the ingot containing less than 2 ppm. A three-pass rod was also analyzed for nickel. The shape of the distribution curve was the same as that of the six-pass curve; the minimum value in this case was 2 ppm. The nickel analyses were carried out in the same fashion as the iron analyses. The scatter in the duplicate analyses for the lower regions of the curve

[34] E. T. Hayes, A. H. Roberson, and O. G. Paasche, *Trans. Am. Soc. Metals* **45**, 893 (1953).

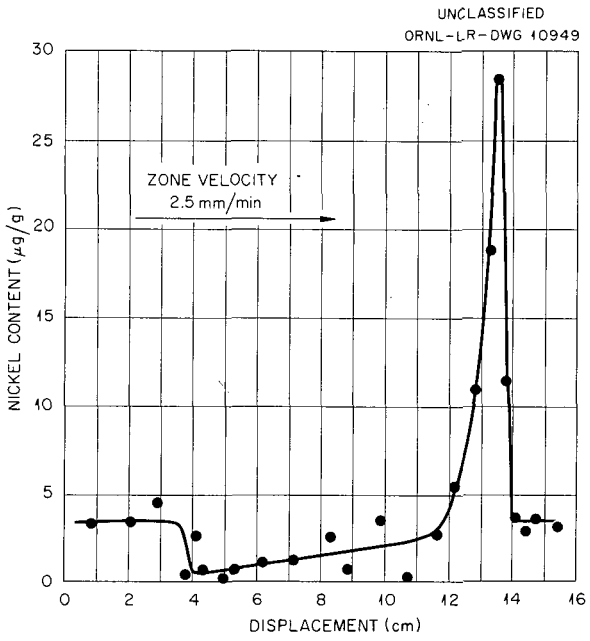

Fig. 199. Nickel Distribution After Six Passes of the Liquid Zone.

was between ±0.1 and ±0.5 ppm; while at the peak, the scatter was ±2.5 ppm. According to these curves, nickel is transported with an effective distribution coefficient of 0.3 to 0.4. This value for the distribution coefficient is only in qualitative agreement with the solubilities of nickel in liquid and solid zirconium, but this is not surprising because of the uncertain nature of this portion of the zirconium-nickel phase diagram. It is apparent that the redistribution of nickel in this particular lot of zirconium would not interfere significantly with the correlation between the metallographic results and the iron analyses because of the very low original concentration of the nickel.

While the general shape of the experimental impurity distribution curves is in agreement with theory, the distribution curves show a rounded instead of a sharp change in concentration at the beginning of the pass. This may be due either to diffusion of the impurities from the unmelted portion or to slight changes in the starting point of the successive passes.

Summary

It has been shown that the iron and nickel contents of iodide zirconium can be reduced to less than 2 ppm by the technique of floating-zone refining. The importance of these impurities on the temperature interval over which the α/β transformation takes place is indicated by the excellent quantitative agreement between the purification curves determined metallographically, assuming iron to be the major impurity, and the analytical iron-distribution curves. The purified metal has a transition range no greater than 865 to 873°C. This in good agreement with other experiments which indicate that the α/β transformation temperature in pure zirconium is 870 ± 3°C.

The absence of hardness changes during refining shows that contamination by oxygen, carbon, and nitrogen was substantially prevented. These measurements, however, are not sufficiently sensitive to permit conclusions to be drawn about the effect of zone refining on these impurities. The theory of zone refining was extended to include the effects of back reflection from the solidification of the final zone. In this case, restrictions imposed by the physical nature of the system must be considered. The agreement of the experimental and theoretical iron distributions provides, for this impurity, an experimental verification of the assumptions of the theory. The purified material, although produced in relatively small amounts, will permit the effects of a number of solutes on the zirconium α/β transformation to be established to a much greater degree of accuracy than was heretofore possible. Support of the molten zone by a water-cooled copper hearth appears to be a promising method for handling larger amounts of material.